From nonequilibrium phase transitions to topological interfaces in spinor Bose-Einstein condensates

Matthew Thomas Wheeler

A thesis presented for the degree of Doctor of Philosophy

Physics, Faculty of Science
Norwich, UK
January 28, 2024

ABSTRACT

Spinor Bose-Einstein condensates (BECs) present an experimentally accessible quantum emulator of universal phenomena that appear ubiquitously across physics, some of which are difficult or impossible to study in the laboratory. In this thesis, we investigate a variety of such phenomena in pseudospin-1/2, spin-1, and spin-2 BECs, ranging from quantum phase transitions to topological interfaces. Our investigations start with the relaxation dynamics of quantum turbulence in a two-component BEC containing half-quantum vortices. The temporal scaling of the number of vortices and the correlation lengths are shown to be, at early times, strongly dependent on the relative strength of the interspecies interaction. At later times, the scaling is observed to be universal, independent of the interspecies interaction, and follows scaling laws observed in the relaxation dynamics of scalar BECs, despite our system containing topologically distinct vortices. A spin-1 BEC is then used as an example system for investigating scaling behaviour in a discontinuous (first-order) quantum phase transition. We show how the Kibble-Zurek mechanism can be generalised and applied to our system, which gives associated scaling laws different from those observed in continuous quantum phase transitions. Our predictions are confirmed by mean-field numerical simulations and provide an experimentally accessible system for investigating properties of the decay of metastable states. Spin-2 BECs exhibit multiple ground state phases with continuous or discrete symmetries, making excellent candidates for studying topological interfaces. We analytically construct sets of spinor wave functions that continuously connect two distinct ground state phases, and show how topologically distinct defects and textures can be created that either terminate at the interface or continuously penetrate across it, connecting non-trivially to an object representing a different topology on the other side. Numerical simulations of select examples reveal a range of dynamics, including the formation of composite cores and splitting processes.

Access Condition and Agreement

Each deposit in UEA Digital Repository is protected by copyright and other intellectual property rights, and duplication or sale of all or part of any of the Data Collections is not permitted, except that material may be duplicated by you for your research use or for educational purposes in electronic or print form. You must obtain permission from the copyright holder, usually the author, for any other use. Exceptions only apply where a deposit may be explicitly provided under a stated licence, such as a Creative Commons licence or Open Government licence.

Electronic or print copies may not be offered, whether for sale or otherwise to anyone, unless explicitly stated under a Creative Commons or Open Government license. Unauthorised reproduction, editing or reformatting for resale purposes is explicitly prohibited (except where approved by the copyright holder themselves) and UEA reserves the right to take immediate 'take down' action on behalf of the copyright and/or rights holder if this Access condition of the UEA Digital Repository is breached. Any material in this database has been supplied on the understanding that it is copyright material and that no quotation from the material may be published without proper acknowledgement.

CONTENTS

LIST OF FIGURES

LIST OF TABLES

LIST OF ABBREVIATIONS

1D One-dimensional

2D Two-dimensional

3D Three-dimensional

BEC Bose-Einstein condensate

GPE Gross-Pitaevskii equation

FM Ferromagnetic

BA Broken-axisymmetry

UN Uniaxial nematic

BN Biaxial nematic

KZM Kibble-Zurek mechanism

DQCP Discontinuous quantum critical point

HQV Half-quantum vortex

ACKNOWLEDGEMENTS

I would like to thank the many people who helped make my PhD an enjoyable and unforgettable experience. Firstly, my heartfelt thanks go out to my supervisors Magnus Borgh and Hayder Salman for their invaluable support, wisdom, and enthusiasm as I traversed my PhD. Whether it was a simple chat over coffee or a multi-hour session at the blackboard, I walk away from the experience a better person and physicist. Thanks again to Hayder who hosted me at Cambridge and showed me a spectacular research environment outside the concrete of UEA. Thanks to Giuseppe and Dan who made the office an enjoyable place to be, in addition to making our small but brilliant physics team what it was. To Sophie and Luke, for keeping me sane throughout my years at UEA, hosting great dinner parties, and painful but always enjoyable runs. To Danny, Isaac, and Palmer for making my undergraduate experience what it was, there would be no PhD without your friendship. Thanks to my parents, Mel, and Mike, and their unrelenting love and support which made me who I am and allowed me to pursue physics. Lastly, to Pete, for your love, patience, and understanding as I have traversed this challenging but rewarding PhD journey.

Part I

Introduction and background

CHAPTER

1

INTRODUCTION

1.1 Bose-Einstein condensates

The first theoretical prediction of Bose-Einstein condensation occurred in 1924, when Indian physicist Satyendra Nath Bose, by re-deriving Planck's law of black-body radiation, developed a theory of statistical mechanics of photons by treating them as a collection of particles [1]. Einstein firstly helped Bose publish his work, before later going on to generalise the theory by applying it to a system of N interacting bosons [2]. This then led to the Bose-Einstein distribution, which describes the statistical distribution of bosons over single-particle energy states:

$$f(\epsilon_i) = \frac{1}{e^{(\epsilon_i - \mu)/k_B T} - 1}, \tag{1.1}$$

where ϵ_i is the energy of level i, μ is the chemical potential, k_B is the Boltzmann constant, and T is the temperature.

Since the average particle number is conserved, the chemical potential enters the above distribution. The chemical potential itself is calculated from the total particle number N and T by the condition that the total number of particles be equal to the sum of the particles in the individual levels. Mathematically, N is written as

$$N = \sum_i N_i = \sum_i g(\epsilon_i) f(\epsilon_i), \tag{1.2}$$

where N_i gives the mean occupation of level i and $g(\epsilon_i)$ gives the degeneracy of level i (i.e., the number of distinct states with energy level ϵ_i).

As $T \to 0$, Eq. (1.1) diverges. This implies that the total excited states must decrease in order to keep the number of particles fixed. At the precise point where the total excited states cannot accommodate the total number of particles, Bose-Einstein condensation occurs. At $T = 0$, all atoms must occupy the lowest energy level of the system, called the ground state.

1.1.1 Transition temperature

The critical temperature at which Bose-Einstein condensation occurs can be derived as follows. Let us consider a system of non-interacting bosons at thermal equilibrium at temperature T. According to de Broglie, particles behave like waves and as such have an associated wavelength termed the de Broglie wavelength. This wavelength characterises the length scale of the localised wave packet of the particles, and is conventionally written as

$$\lambda_{\mathrm{dB}} = \frac{h}{\sqrt{2\pi m k_B T}}, \tag{1.3}$$

where h is Planck's constant and m is the mass of the particle. Since $\lambda_{\mathrm{dB}} \propto 1/\sqrt{T}$, high temperatures ($T > T_c$) imply that the de Broglie wavelength is small compared to the average inter-particle spacing. In this limit, the system exhibits classical, particle-like behaviour and the particles closely follow the Boltzmann distribution. Conversely, as the temperature decreases, the de Broglie wavelength associated with each particle grows. At some critical temperature, T_c, the wavelength of each particle becomes comparable to the average inter-particle spacing and as such individual particles become indistinguishable. At this point the system exhibits quantum behaviour, and the particles form a degenerate gas. Assuming a uniform, three-dimensional system with volume $\mathcal{V}$ and number density $N/\mathcal{V}$, the Bose-Einstein transition for an ideal gas occurs when $n\lambda_{\mathrm{dB}}^3 \leq \zeta(3/2)$ [3], where ζ is the Riemann zeta function. Substituting in Eq. (1.3), we find the critical temperature for Bose-Einstein condensation:

$$T_c = \frac{h^2}{2\pi m k_B}\left(\frac{n}{\zeta(3/2)}\right)^{2/3}. \tag{1.4}$$

1.1.2 Experimental realisation

Alkali atoms, such as rubidium and sodium, present ideal candidates for Bose-Einstein condensate experiments due to being weakly-interacting, easily trapped magnetically, and their ability to be cooled using laser techniques. Cooling such atoms, however, can lead to a transition into a liquid or a solid. To prevent this, it is necessary to reduce the atomic density of the gas such that elastic, binary collisions dominate. Typical required densities for this to hold are around $n \sim 10^{-14}\mathrm{cm}^3$. Using the expression for the critical temperature quoted above, one can then estimate that Bose-Einstein condensation would occur at $T_c \sim 10^{-6}$K for such a system.

The first experimental realisations of Bose-Einstein condensates (BECs) occurred in 1995, where the groups at JILA [4], MIT [5], and Rice University [6] successfully cooled atoms of ^{87}Rb, ^{23}Na, and ^{7}Li, respectively, observing Bose-Einstein condensation. For their pioneering work on "the achievement of Bose-Einstein condensation in dilute gases of alkali atoms, and for early fundamental studies of the properties of the condensates", Carl Wieman, Eric Cornell, and Wolfgang Ketterle earned the 2001 Nobel Prize in Physics. These works gave birth to a whole new field of research, and today, interest in BECs has only accelerated further, with applications of such condensates ranging from precision measurements [7] to quantum computing [8].

1.1.3 Spin degree of freedom: Spinor Bose-Einstein condensates

In experiments, a consequence of strong magnetic trapping of the atoms is the "freezing" of the atomic spin, where such condensates are referred to as scalar (or spinless). An alternative method of trapping condensates is through the use of optical trapping potentials, which utilise the AC-Stark shift of atom to form a conservative potential that traps all the Zeeman sublevels equally. In this case, atoms can Bose-condense into each of the available component spin states, m_F, producing a multi-component condensate, and hence the atomic spin of the is no longer frozen out. Such a condensate is called a spinor Bose-Einstein condensate, and forms the main interest of this thesis.

The first experimental realisation of a spinor BEC occurred just three years after the pioneering work in scalar systems, where, in 1998, a group at MIT successfully produced a spin-1 condensate of ^{23}Na atoms [9]. Around the same time, seminal theory works by Ho [10] and Ohmi and Machida [11] were developed, which kickstarted a new wave of research into spinor BEC systems. Advances in optical trapping and laser cooling since then have led to the formation of spinor condensates in spin-1 and spin-2 ^{87}Rb [12, 13], spin-2 ^{23}Na [14], and even spin-3 ^{52}Cr [15].

1.2 Topological defects in Bose-Einstein condensates

Atomic BECs can support various topological excitations: Objects that are free to move in space and time without changing their characteristics that are defined by topological charges. An example that arises in scalar BECs is the quantum phase vortex, a singular line defect which carries mass circulation. The first experimental realisation of a quantum vortex in an

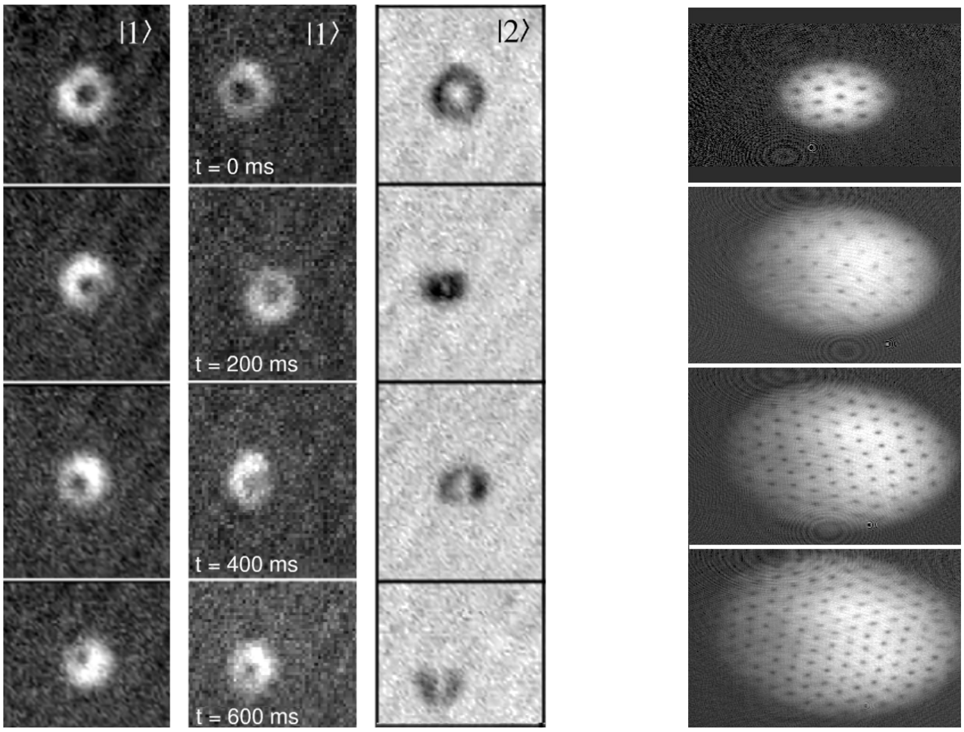

(a) (b)

Figure 1.1: Experimental images of quantum vortices in atomic BECs. (a): First experimental realisation of a quantum vortex in an atomic BEC, reproduced from Ref. [16]. (b): Quantum vortex lattice, reproduced from Ref. [18].

atomic BEC occurred in 1999 [16], which was achieved in a two-component ^{87}Rb condensate. The process of generating the vortex was based on imparting angular momentum to the condensate by rotating the trap in which it was held [17]. However, instead of rotating the trap, a laser was instead focused on a small region outside the condensate and rotated through a circular path. Images taken from the experiment are shown in Fig. 1.1a. Further theoretical work generalised this idea by allowing the amplitude of the rotating laser to spatially vary instead of being confined to a point [19].

Advances in experimental techniques led to the development of so-called stirring lasers, where an incident microwave field applied to the condensate causes it to stretch in the direction of the applied field. Vortices could then be produced dynamically from the edge of the rotating trap due to the slight asymmetries induced by the stirring laser. These advances led to the formation of the first vortices within scalar condensates [18, 20, 21]. Interestingly, rather than forming a single vortex with large angular momentum, vortices constructed in this way form vortex lattices, i.e., the condensate comprises many individual vortices of small angular momentum (see Fig. 1.1b).

A system containing many vortices, sometimes referred to as a vortex tangle in 3D systems, gives rise to a turbulent flow called quantum turbulence. Due to their accessibility, quantum turbulence in atomic BECs has attracted considerable theoretical [22–27] and experimental [28–33] attention. The rich family of topological defects in spinor and pseudospin-1/2 systems presents a new avenue for studying the properties of quantum turbulence and nonequilibrium dynamics [34–38]. In two-component condensates, when atomic mass and mean density of the components are equal, vortices may arise which are characterised by a phase winding in only one of the components, leading to what are known as half-quantum vortices (HQVs) due to their similarities with vortices carrying half a quantum of superfluid circulation in both ^{3}He [39] and spin-1 BECs [40, 41]. These vortices have very different dynamics to scalar vortices arising in scalar BECs, and cannot be described by simple point-vortex models [42, 43]. Chapter 4 is dedicated to the study of a 2D system filled with HQVs undergoing quantum turbulence.

The combination of a macroscopic condensate phase together with spin rotations leads to an even richer phenomenology of topological defects present within spinor BECs that are otherwise unseen in scalar and two-component condensates. The existence and type of topological defects allowed within spinor BECs can be found from the topology of the ground state manifold, and detailed constructions of some topological defects present within these systems are available in Chapter 3. Vortices, for example, are rich and varied in their characteristics within spinor BECs. Some examples are: Fractional vortices, which carry circulation in fractional units compared to vortices arising in scalar condensates, spin vortices, carrying a circulation of the condensate spin only, and nonsingular vortices, textures that carry mass and/or spin circulation. The existence of such vortices, however, does not imply their stability, and many numerical studies have investigated the energetic stability of both singular and nonsingular vortices in spinor condensates [44–50].

Since the expanded order parameter space of spinor BECs allows for a variety of different vortex states, including both singular and nonsingular vortices, if one applies a stirring laser to such a condensate to nucleate vortices then it is not always clear which types of vortices will nucleate. Thus, instead of stirring lasers, other experimental techniques exist for generating specific types of vortices in spinor systems. For example, a nonsingular vortex was generated in a spin-1 ^{23}Na condensate by methods of phase-imprinting [51], where the magnetic field bias was adiabatically reduced to zero along the trap axis. This distributed the atomic population across the three internal spin states, producing the required coreless spin texture. The same technique was used to realise both singly- and doubly-quantised vortices in a spin-polarised BEC, the latter of which was observed to undergo a splitting process into two singly quantised vortices [52, 53]. More recently, experimental techniques have been developed that allow for the controlled creation of vortices with internal point-group symmetries [54], further opening up experimental accessibility for investigating the unique properties of topological defects in spinor BECs.

Owing to their accessibility and high controllability, spinor BECs are also excellent candidates for studying a range of nonequilibrium physics [13], including relaxation dynamics [55, 56] and quantum quenches [35, 37, 57–62]. By continuously changing an external parameter, such as the linear or quadratic Zeeman shifts (see Sec. 2.3.4) through the use of applied magnetic fields, the system can be ramped across a quantum critical point [63] and undergo a quantum phase transition. Such a transition is defined as continuous (discontinuous) depending on whether the derivative of the internal energy of the system with respect to the changing external parameter is also continuous (discontinuous). Spinor BECs posses a number of both continuous and discontinuous quantum critical points between their ground state phases, making them an ideal test bed for studying both types of quantum phase transitions. An example of a second-order (continuous) quantum phase transition arises between the polar and broken-axisymmetry phases in spin-1 BECs (see Chapter 3). Naturally, they also make excellent candidates for investigating the Kibble-Zurek mechanism (KZM), which governs the observed scaling laws when the symmetry of a system is spontaneously broken after undergoing a continuous phase transition [64]. Much theoretical and experimental work has already confirmed Kibble-Zurek scaling in a multitude of continuous quantum phase transitions in spinor condensates [57, 61, 65–74]. Furthermore, there has been the first experimental evidence of observed scaling laws across a discontinuous quantum phase transition in a spinor BEC [75], showing their excellent eligibility for studying the lesser-known scaling laws associated with discontinuous phase transitions.

1.2.1 Topological interfaces

When a system contains multiple topologically distinct phases described by different order parameters, a topological interface may form between them. Such interfaces already arise in many areas of physics, from the context of domains walls in the early universe [76–78] to the A–B phase boundary in superfluid liquid ^{3}He [79–84]. The different bulk regions may also harbour topological defects, which either terminate on the interface or smoothly connect to a topologically distinct object on the other side. Due to their rich phase diagram exhibiting a range of symmetries and defects, spinor BECs provide an ideal testing ground for investigating topological interface physics in a highly-controllable system.

Topological interfaces in spin-1 systems can be engineered through spatial control of Zeeman shifts [85–87], leading to a condensate containing two topologically distinct bulk regions described by different symmetries. In [85], a topological interface was formed between the polar and ferromagnetic phases of a spin-1 BEC, and a range of topological defects were constructed. These defects ranged from simple singly-quantised vortices in both phases connecting across the interface, to the more complicated case of HQVs in the polar phase connecting to nonsingular vortices in the ferromagnetic phase, which may even exist together with monopoles. Interfaces may also form within vortex cores, where the bulk order parameter outside the core continuously transforms into a different symmetry within the core. Such interfaces have already been created experimental in spin-1 [88, 89] and spin-2 [54] BECs. Their even richer phase diagram and family of defects implies that spin-2 condensates offer an even greater avenue of study for topological interface physics. They additionally have ground state phases with discrete polytope point-group symmetries [54, 90–92] in which the defects are non-Abelian [93] and hence are dependent on other defects within the system, leading to intriguing interface physics.

1.3 Outline of the thesis

An outline of the structure of this thesis and a description of each chapter is given in this section. The thesis is split into three main parts: Part I introduces the mathematical models required to understand atomic BECs, and introduces the ground states, symmetries, and topological defects present in spin-1 and spin-2 BECs. Part II presents analytical and numerical work carried out to investigate various areas of physics in spinor and pseudospin-1/2 condensates. In particular, we cover three main areas: relaxation dynamics, discontinuous quantum phase transitions, and topological interfaces. Finally, part III is a collection of appendices relating to numerical methods or detailed derivations. The following publications partially feature results shown in this thesis:

- Relaxation dynamics of half-quantum vortices in a two-dimensional two-component Bose-Einstein condensate

  M. T. Wheeler, H. Salman, and M.O. Borgh, EPL **135** 30004 (2021).

  Contribution: All code development and numerical computation, contributed to analysis, analytical derivations and writing.

- Dynamics of a Nonequilibrium Discontinuous Quantum Phase Transition in a Spinor Bose-Einstein Condensate

  M. T. Wheeler, H. Salman, and M.O. Borgh, Submitted to Physical Review Letters.

Contribution: Code development and all numerical computation. Main contributor to analytical derivations and analysis. Contributed to writing.

- Topological interfaces crossed by defects and textures of continuous and discrete point group symmetries in spin-2 Bose-Einstein condensates

  G. Baio, M. T. Wheeler, D. S. Hall, J. Ruostekoski, and M.O. Borgh, Submitted to Physical Review Research.

  Contribution: Main contributor to numerical computation, contributed to analysis and writing.

Part I — Introduction and background

Chapter 1 introduces the notion of a Bose-Einstein condensate, as well as presenting an overview of the history of experimental techniques used to achieve them, before transitioning to spinor and pseudospin-1/2 condensates and their respective histories. We also present an overview of experimental techniques used to achieved different types of vortices within spinor and pseudospin-1/2 condensates, and show how spinor BECs are ideal test beds for investigate a wide range of different physics.

Chapter 2 introduces the mathematical models used to accurately describe scalar, two-component, and spinor Bose-Einstein condensate systems. We start with the scalar system, presenting the Hamiltonians using a quantum treatment, before introducing the mean-field theory and constructing the Gross-Pitaevskii equation. We then generalise to the two-component system and discuss the miscibility criterion. From here, we progress into the mathematical models of spinor BECs. We generally construct the interaction Hamiltonian of a spin-f system by linking projection operators to physical observables, and then discuss how the single-particle Hamiltonian differs between spinor and scalar systems. Finally, we introduce the mean-field equations for spinor systems, showing detailed derivations of their reduction to lower dimensionalities, and giving the equations in various dimensionless forms.

Chapter 3 discusses the ground states, symmetries, and topological defects present within spin-1 and spin-2 BECs. We first present the ground state phase diagram for both spin-1 and spin-2 systems, before discussing each phase that arises individually. In each case we give two different graphical representations of each phase, and discuss their respective symmetries. We finally introduce the topologically stable defects in each phase by constructing the homotopy groups, before presenting a dynamical discussion of a select few examples.

Part II — Numerical studies of spinor and pseudospinor condensates

Chapter 4 investigates the relaxation dynamics of HQVs in a two-component BEC. We first present the two-component BEC as a pseudospin-1/2 system, and analytically construct the form of the HQVs. We then present numerical simulations, investigating both the spatial and temporal aspects of the relaxation dynamics. In particular, we focus on the decay rate of the HQVs as the ratio of the inter- and intra-species interactions are varied.

Chapter 5 investigates a discontinuous quantum phase transition in a spin-1 BEC. We first discuss the notion of a discontinuous quantum critical point and how it applies to our system, thereby confirming we are working with a first-order phase transition. We then generalise the Kibble-Zurek theory to apply to our gapless spectrum, and derive a modified scaling for the density of defects. Additionally, separate from the KZM, we linearise the resulting Gross-Pitaevskii equations and derive scaling behaviour near the critical point. Finally, numerical studies are presented that confirm our analytical predictions.

Chapter 6 extends the work of Borgh and Ruostekoski [85–87] to spin-2 systems, and investigates a variety of topological interfaces that can be constructed in spin-2 BECs. In particular, four interfaces are studied: Uniaxial nematic to biaxial nematic, cyclic to nematic (both uniaxial nematic and biaxial nematic), cyclic to ferromagnetic, and finally ferromagnetic to biaxial nematic. We construct a variety of defects spanning the interface in each case, ranging from singular line defects to point defects such as monopoles. Finally, we present numerical work simulating the connection of a select few topological defects in both a uniaxial nematic to biaxial nematic interface, as we as a cyclic to ferromagnetic interface.

Finally, Chapter 7 ends with the overall conclusions of the thesis, before presenting avenues of future work.

Part III — Appendices

Appendix A presents the dimensionless form of the two-component Gross-Pitaevskii equations using the lattice length as our unit of length, which is relevant for Chapter 4. Finally, Appendix B discusses the derivation of the interpolating stationary solutions used within Chapter 6

CHAPTER 2

MATHEMATICAL MODELS OF BOSE-EINSTEIN CONDENSATES

In this chapter we provide the theoretical background necessary to understand the dynamics of ultracold atomic gases. We begin by introducing the most simple form of a BEC, the scalar condensate. This lays the framework for building to more complex systems. We then go on to discuss the two-component condensate, where additional interactions arise between atoms of differing components. Finally, we construct the framework needed to understand spinor BECs, which is the main focus of this thesis.

2.1 Mean-field description of scalar condensates

Consider a system of bosons which is dilute enough such that we may approximate interactions between bosons as two-body interactions only. Such a system is described by the Hamiltonian [94]

$$\hat{H} = \hat{H}_0 + \hat{H}_I. \tag{2.1}$$

Here, $\hat{H}_0$ is the single-particle Hamiltonian:

$$\hat{H}_0 = \int \hat{\Psi}^\dagger(\mathbf{r},t)\left[-\frac{\hbar^2\nabla^2}{2m} + V(\mathbf{r},t)\right]\hat{\Psi}(\mathbf{r},t)\,\mathrm{d}^3\mathbf{r}, \tag{2.2}$$

where $\hat{\Psi}(\mathbf{r},t)$ is the field operator that annihilates a boson at position $\mathbf{r}$ at time t. The first term represents the kinetic energy operator and $V(\mathbf{r},t)$ is a trapping potential. Additionally,

$\hat{H}_I$ represents the interacting part of the Hamiltonian, which describes binary collisions between bosons at positions $\mathbf{r}_1$ and $\mathbf{r}_2$ whose interactions are described by the interaction potential $\mathcal{U}(\mathbf{r}_1,\mathbf{r}_2)$:

$$\hat{H}_I = \frac{1}{2}\int\int \hat{\Psi}^\dagger(\mathbf{r}_1,t)\hat{\Psi}^\dagger(\mathbf{r}_2,t)\mathcal{U}(\mathbf{r}_1,\mathbf{r}_2)\hat{\Psi}(\mathbf{r}_2,t)\hat{\Psi}(\mathbf{r}_1,t)\,\mathrm{d}^3\mathbf{r}_1\,\mathrm{d}^3\mathbf{r}_2. \tag{2.3}$$

The dilute nature of the BEC justifies that any binary interaction between two particles at positions $\mathbf{r}_1,\mathbf{r}_2$ can be approximated by a contact interaction modelled by the following delta function:

$$\mathcal{U}(\mathbf{r}_1,\mathbf{r}_2) = g\delta(\mathbf{r}_1-\mathbf{r}_2), \tag{2.4}$$

where the interaction coefficient, g, is related to the s-wave scattering length, a_s, as

$$g = \frac{4\pi\hbar^2 a_s}{m}, \tag{2.5}$$

for a boson with atomic mass m.

2.1.1 The Gross-Pitaevskii equation

The Heisenberg picture states that the time evolution for the field operator $\hat{\Psi}(\mathbf{r},t)$ is given by [94]

$$i\hbar\frac{\partial\hat{\Psi}(\mathbf{r},t)}{\partial t} = \left[\hat{\Psi}(\mathbf{r},t),\hat{H}\right], \tag{2.6}$$

which, using Eq. (2.1), is calculated to be

$$i\hbar\frac{\partial\hat{\Psi}(\mathbf{r},t)}{\partial t} = \left[-\frac{\hbar^2\nabla^2}{2m}+V(\mathbf{r},t)\right]\hat{\Psi}(\mathbf{r},t)+g\hat{\Psi}^\dagger(\mathbf{r},t)\hat{\Psi}(\mathbf{r},t)\hat{\Psi}(\mathbf{r},t). \tag{2.7}$$

Now, since we consider a system close to absolute zero, we make the assumption that most atoms occupy the same quantum state, and hence we can decompose the field operator into a mean and fluctuation parts as [94]

$$\hat{\Psi}(\mathbf{r},t) = \psi(\mathbf{r},t)+\delta\hat{\psi}(\mathbf{r},t), \tag{2.8}$$

where $\psi \equiv \langle\hat{\Psi}(\mathbf{r},t)\rangle$ is a classical scalar field describing the wave function of the condensate, which describes the spatially-coherent condensed state. Here, $\delta\hat{\psi}(\mathbf{r},t)$ describes deviations from this mean and $\langle\delta\hat{\psi}(\mathbf{r},t)\rangle = 0$. Substituting the above form of the field operator into Eq. (2.7), taking the expectation and ignoring terms of $\delta\hat{\psi}^2$ or higher yields the equation of motion for the wave function of a Bose-Einstein condensate, the Gross-Pitaevskii equation (GPE):

$$i\hbar\frac{\partial\psi(\mathbf{r},t)}{\partial t} = \left(-\frac{\hbar^2}{2m}\nabla^2+V(\mathbf{r},t)+g|\psi(\mathbf{r},t)|^2\right)\psi(\mathbf{r},t). \tag{2.9}$$

Neglecting the fluctuation terms is only valid when considering a system at zero temperature, where there are no contributions from thermal fluctuations and contributions from quantum fluctuations are negligible in comparison to the classical field.

For $g > 0$ the interactions are repulsive and for $g < 0$ they are attractive. When $g = 0$ there are no interactions present and the system reduces to the Schrödinger equation. The wave function of the system is normalised to the number of particles

$$\int |\psi(\mathbf{r}, t)|^2 \, \mathrm{d}^3\mathbf{r} = N, \tag{2.10}$$

which remains conserved under the GPE. Finally, the total energy of the system is given by

$$E = \int \left[\frac{\hbar^2}{2m} |\nabla\psi(\mathbf{r}, t)|^2 + V(\mathbf{r}, t)|\psi(\mathbf{r}, t)|^2 + \frac{g}{2}|\psi(\mathbf{r}, t)|^4 \right] \mathrm{d}^3\mathbf{r} = E_{\mathrm{kin}} + E_{\mathrm{pot}} + E_{\mathrm{int}}, \tag{2.11}$$

where $E_{\mathrm{kin}}, E_{\mathrm{pot}}$ and E_{int} describes the kinetic, potential, and interaction energies, respectively.

2.2 Two-component Bose-Einstein condensates

We now generalise part of the theory introduced in the previous section to describe multi-component condensates. The time-dependent coupled Gross-Pitaevskii equations each describe a condensate similar to the standard GPE given in Eq. (2.9), but now with an additional non-linear term that describes the interactions of atoms between condensate components. The coupled GPEs are given as

$$\begin{aligned} i\hbar \frac{\partial \psi_1(\mathbf{r}, t)}{\partial t} &= \left[-\frac{\hbar^2}{2m_1}\nabla^2 + V_1(\mathbf{r}, t) + g_1|\psi_1(\mathbf{r}, t)|^2 + g_{12}|\psi_2(\mathbf{r}, t)|^2 \right] \psi_1(\mathbf{r}, t), \\ i\hbar \frac{\partial \psi_2(\mathbf{r}, t)}{\partial t} &= \left[-\frac{\hbar^2}{2m_2}\nabla^2 + V_2(\mathbf{r}, t) + g_2|\psi_2(\mathbf{r}, t)|^2 + g_{12}|\psi_1(\mathbf{r}, t)|^2 \right] \psi_2(\mathbf{r}, t), \end{aligned} \tag{2.12}$$

where $\psi_j(\mathbf{r}, t)$ corresponds to the wave function of component j with atomic mass m_j for $j = 1, 2$, and $V_j(\mathbf{r}, t)$ is an external trapping potential. The interaction terms are a generalised from of Eq. (2.5), given explicitly as

$$g_j = \frac{4\pi\hbar^2 a_j}{m_j}, \qquad g_{12} = \frac{2\pi\hbar^2 (m_1 + m_2) a_{12}}{m_1 m_2}, \tag{2.13}$$

which describe the intraspecies and interspecies interaction strengths, respectively. Similar to the scalar case, the wave function of each component is normalised to the number of atoms of that component

$$\int |\psi_j|^2 d^3\mathbf{r} = N_j. \tag{2.14}$$

The time-independent GPEs can be obtained by making the following substitution of the wave function $\psi_j(\mathbf{r},t) = \psi_j(\mathbf{r})e^{-i\mu_j t/\hbar}$ in Eq. (2.12), yielding

$$\begin{aligned} \mu_1\psi_1(\mathbf{r}) &= \left[-\frac{\hbar^2}{2m_1}\nabla^2 + V_1(\mathbf{r}) + g_1|\psi_1(\mathbf{r})|^2 + g_{12}|\psi_2(\mathbf{r})|^2\right]\psi_1(\mathbf{r}), \\ \mu_2\psi_2(\mathbf{r}) &= \left[-\frac{\hbar^2}{2m_2}\nabla^2 + V_2(\mathbf{r}) + g_2|\psi_2(\mathbf{r})|^2 + g_{12}|\psi_1(\mathbf{r})|^2\right]\psi_2(\mathbf{r}), \end{aligned} \tag{2.15}$$

where μ_j is the chemical potential of component j. The total energy of the two-component system comprises the same contributions to the energy as the scalar case given in Eq. (2.11), i.e., $E = E_{\text{kin}} + E_{\text{pot}} + E_{\text{int}}$, but with contributions from both components as

$$\begin{aligned} E = &\int \left[\frac{\hbar^2}{2m_1}|\nabla\psi_1|^2 + V_1(\mathbf{r})|\psi_1|^2 + \frac{g_1}{2}|\psi_1|^4\right] \mathrm{d}^3\mathbf{r} \\ &+ \int \left[\frac{\hbar^2}{2m_2}|\nabla\psi_2|^2 + V_2(\mathbf{r})|\psi_2|^2 + \frac{g_2}{2}|\psi_2|^4\right] \mathrm{d}^3\mathbf{r} \\ &+ \int \left[g_{12}|\psi_1|^2|\psi_2|^2\right] \mathrm{d}^3\mathbf{r}. \end{aligned} \tag{2.16}$$

2.2.1 Miscible and immiscible regimes

Two-component condensates can be either miscible or immiscible, depending on the interactions present within the system. Here, we derive the immiscibility criterion for two-component condensates following the procedure in Ref. [95]. We start by assuming, for simplicity, a BEC in the absence of a trapping potential such that $V_1(\mathbf{r}) = V_2(\mathbf{r}) = 0$. Assuming a homogeneous stationary solution where the kinetic energy terms can be neglected, Eq. (2.15) reduces to

$$\begin{aligned} \mu_1 &= g_1|\psi_1|^2 + g_{12}|\psi_2|^2, \\ \mu_2 &= g_2|\psi_2|^2 + g_{12}|\psi_1|^2. \end{aligned} \tag{2.17}$$

Let us consider a miscible regime, where, inside the trap, the densities of each component can be re-written as $n_j = N_j/\mathcal{V}$, where $\mathcal{V}$ is the volume of the condensate. The above equations then reduce to $g_1 n_1 + g_{12} n_2 = \mu_1$ and $g_2 n_2 + g_{12} n_1 = \mu_2$, and the energy becomes

$$E_{\text{misc}} = \frac{1}{2}\left[g_1\frac{N_1^2}{\mathcal{V}} + g_2\frac{N_2^2}{\mathcal{V}} + 2g_{12}\frac{N_1 N_2}{\mathcal{V}}\right]. \tag{2.18}$$

Provided g_{12} is small enough, any variation to this state will increase the system energy, implying that this state is stable. When g_{12} gets large enough, however, it can be shown that there exists a state with a lower energy.

Let us consider an immiscible regime, where the two condensates do not spatially overlap. The volume of condensate j is given as $\mathcal{V}_j$ and the densities subsequently become $n_j =$

$N_j/\mathcal{V}_j$. Assuming that the contribution to the energy arising from the interface between the two condensates is negligible in comparison to the contribution from the bulk, Eqs. (2.15) reduce to $g_j n_j = \mu_j$ with the total energy

$$E_{\text{immisc}} = \frac{1}{2}\left[g_1\frac{N_1^2}{\mathcal{V}_1} + g_2\frac{N_2^2}{\mathcal{V}_2}\right]. \tag{2.19}$$

Minimising the above energy with respect to $\mathcal{V}_1$ or $\mathcal{V}_2$ with $\mathcal{V} = \mathcal{V}_1 + \mathcal{V}_2$ results in the expressions for the volume of each component

$$\mathcal{V}_1 = \frac{1}{1+\sqrt{g_2/g_1}(N_2/N_1)}\mathcal{V}, \tag{2.20}$$

$$\mathcal{V}_2 = \frac{1}{1+\sqrt{g_1/g_2}(N_1/N_2)}\mathcal{V}. \tag{2.21}$$

The corresponding densities then become

$$n_1 = \left(1+\sqrt{\frac{g_2}{g_1}\frac{N_2}{N_1}}\right)\frac{N_1}{\mathcal{V}}, \quad n_2 = \left(1+\sqrt{\frac{g_1}{g_2}\frac{N_1}{N_2}}\right)\frac{N_2}{\mathcal{V}}. \tag{2.22}$$

Substituting the above densities into the expression for the total energy in Eq. (2.19) yields

$$E_{\text{immisc}} = \frac{1}{2}\left[g_1\frac{N_1^2}{\mathcal{V}} + g_2\frac{N_2^2}{\mathcal{V}} + 2\sqrt{g_1 g_2}\frac{N_1 N_2}{\mathcal{V}}\right], \tag{2.23}$$

and the difference between the energies of the miscible and immiscible phases is subsequently calculated as

$$\Delta E = E_{\text{misc}} - E_{\text{immisc}} = (g_{12} - \sqrt{g_1 g_2})\frac{N_1 N_2}{\mathcal{V}}. \tag{2.24}$$

Therefore, the condition $g_{12} > \sqrt{g_1 g_2}$ reveals that for large enough interspecies interactions the system favours an immiscible phase over a miscible one. This criterion only depends on the interactions within the system, and is not affected by condensate particle numbers or size. Fig. 2.1 shows the boundary between the two phases for $g_1 = 1$ in a parameter space of g_2, g_{12}.

2.3 Spinor Bose-Einstein condensates

Spinor systems are comprised of particles with total hyperfine spin f. The hyperfine spin is made up of contributions from the atoms' electron spin, s, the electron orbital angular momentum, l, and the nuclear spin, i [96]. Canonical examples include ^{23}Na and ^{87}Rb, which can be realised as both $f = 1$ and $f = 2$ systems, and ^{52}Cr, which can be realised as an $f = 3$

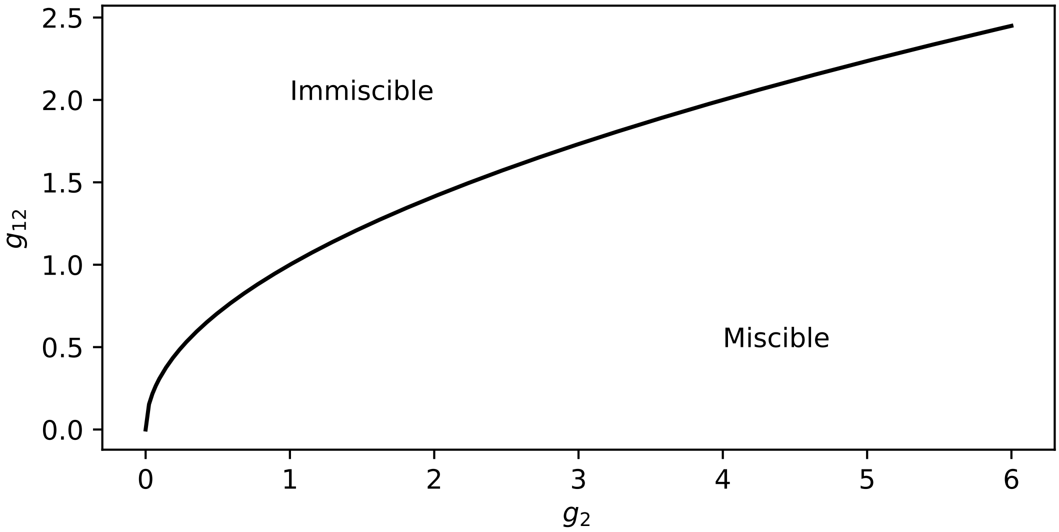

Figure 2.1: Boundary between the miscible and immiscible regimes for a two-component condensate with $g_1 = 1$.

system. A hyperfine spin f implies that there are $2f+1$ possible spin states along a given spin quantisation axis. Such a state is denoted $|f, m\rangle$, where $m \in \{-f, -f+1, \ldots, 0, \ldots, f-1, f\}$ denotes the magnetic sublevel for an atom with total spin f. A system of identical spin-f bosons is described by the field operators $\hat{\psi}_m(\mathbf{r})$ which satisfy the following commutation relations [96]:

$$\left[\hat{\psi}_m(\mathbf{r}_1), \hat{\psi}^\dagger_{m'}(\mathbf{r}_2)\right] = \delta_{mm'}\delta(\mathbf{r}_1 - \mathbf{r}_2), \tag{2.25}$$

$$\left[\hat{\psi}_m(\mathbf{r}_1), \hat{\psi}_{m'}(\mathbf{r}_2)\right] = \left[\hat{\psi}^\dagger_m(\mathbf{r}_1), \hat{\psi}^\dagger_{m'}(\mathbf{r}_2)\right] = 0. \tag{2.26}$$

To construct the relevant spinor Hamiltonians we follow the methodology in Refs [10, 11, 96–98] and make the following assumptions: We assume only elastic and binary collisions between atoms, implying that the total spin is conserved, as well as low incident collision energy so that only s-wave scattering is observed. Additionally, we assume no spin-orbit coupling and no mixing of hyperfine states.

2.3.1 Contributions from spin-channels

Collisions between two incoming spin-f atoms in magnetic sublevels m and m' can undergo spin-exchange interactions, where the outgoing particles can now be in entirely different magnetic sublevels. In the case of s-wave scattering, where the orbital angular momentum is zero, $\mathcal{M} \equiv m + m'$ is conserved [96]. For example, collisions between two spin-1 atoms located in sublevels $m = 1$ and $m' = -1$ must collide to form $\mathcal{M} = 0$, implying that the only allowed exchange is:

$$(1,-1) \leftrightarrows (0,0). \tag{2.27}$$

In general, a collision between two spin-f atoms can combine to have a total spin $\mathcal{F} \in \{0,1,\ldots,2f\}$ and $\mathcal{M} \equiv m+m' \in \{-\mathcal{F},\ldots,\mathcal{F}\}$. In the s-wave scattering limit, the total spin $\mathcal{F}$ of two colliding atoms must be a multiple of $2f$, i.e., $\mathcal{F} \in \{0,2,\ldots,2f\}$, since the wave function must remain symmetric under the exchange of the two atoms [3]. The total interaction Hamiltonian is constructed as a sum of each contribution from individual spin channels as [96]

$$\hat{H}_{\text{int}} = \sum_{\mathcal{F}=0,2,\ldots 2f} \hat{V}^{(\mathcal{F})}, \tag{2.28}$$

where $\hat{V}^{(\mathcal{F})}$ is the interaction Hamiltonian between two atoms with total spin $\mathcal{F}$, which is given as

$$\hat{V}^{(\mathcal{F})} = \frac{1}{2}\int\int \mathscr{U}^{(\mathcal{F})}(\mathbf{r}_1,\mathbf{r}_2) \sum_{\mathcal{M}=-\mathcal{F}}^{\mathcal{F}} \hat{A}^{\dagger}_{\mathcal{F}\mathcal{M}}(\mathbf{r}_1,\mathbf{r}_2)\hat{A}_{\mathcal{F}\mathcal{M}}(\mathbf{r}_1,\mathbf{r}_2)\,\mathrm{d}^3\mathbf{r}_1\mathrm{d}^3\mathbf{r}_2, \tag{2.29}$$

where $\mathscr{U}^{(\mathcal{F})}$ describes the interaction potential between two particles with total spin $\mathcal{F}$. Here, $\hat{A}_{\mathcal{F}\mathcal{M}}$ are projection operators that project two spin-f particles with total component $\mathcal{M}$ onto total spin $\mathcal{F}$ and component $\mathcal{M}$. They are defined, explicitly, as

$$\hat{A}_{\mathcal{F}\mathcal{M}}(\mathbf{r}_1,\mathbf{r}_2) = \hat{\psi}^T \mathscr{A}_{\mathcal{F}\mathcal{M}}\hat{\psi}, \tag{2.30}$$

where $\mathscr{A}_{\mathcal{F}\mathcal{M}}$ are matrices of Clebsch-Gordon coefficients which couple individual spins of atoms together to describe them using the total spin $\mathcal{F}$ [96]:

$$(\mathscr{A}_{\mathcal{F}\mathcal{M}})_{m,m'} = \langle \mathcal{F};\mathcal{M} | f,m;f,m' \rangle. \tag{2.31}$$

Since we are assuming binary collisions, we can make an assumption similar to the scalar case and model the interactions by a contact potential of the following form:

$$\mathscr{U}^{(\mathcal{F})} = g_{\mathcal{F}}\delta(\mathbf{r}_1 - \mathbf{r}_2), \tag{2.32}$$

where $g_{\mathcal{F}}$ is an interaction coefficient related to the s-wave scattering length of the total spin-$\mathcal{F}$ channel, $a_{\mathcal{F}}$, as

$$g_{\mathcal{F}} = \frac{4\pi\hbar^2}{M} a_{\mathcal{F}}. \tag{2.33}$$

This then reduces Eq. (2.29) to

$$\hat{V}^{(\mathcal{F})} = \frac{g_{\mathcal{F}}}{2} \int \sum_{\mathcal{M}=-\mathcal{F}}^{\mathcal{F}} \hat{A}^{\dagger}_{\mathcal{F}\mathcal{M}}(\mathbf{r},\mathbf{r}) \hat{A}_{\mathcal{F}\mathcal{M}}(\mathbf{r},\mathbf{r})\, \mathrm{d}^3\mathbf{r}. \tag{2.34}$$

From this, we can construct the full interaction Hamiltonian using Eq. (2.28). However, we first want to connect the projection operators $\hat{A}_{\mathcal{F}\mathcal{M}}(\mathbf{r},\mathbf{r})$ to physical observables of the system, so that we can construct the Hamiltonian in terms of these observables.

2.3.2 Physical observables

In this subsection we introduce useful quantities and operators that arise in spinor condensates, such as spinor Pauli-type matrices and the spin-singlet pair operator. In addition, we show how physical observables can be constructed from powers of the spinor Pauli-type matrices, and how these physical observables can be connected to the projection operators $\hat{A}_{\mathcal{F}\mathcal{M}}(\mathbf{r})$.

Spinor Pauli-type matrices

Spin-f Pauli-type matrices, $\mathbf{f} \equiv (f_x, f_y, f_z)$, form the basis for constructing useful quantities that arise in spinor BECs such as the condensate spin vector. Here we construct a general representation for these matrices as well as give the explicit Pauli-type matrices for spin-1 and spin-2 systems.

A spin-f Pauli-type matrix is a $(2f+1)\times(2f+1)$ matrix. The (m,m')-components of the spin matrices are defined generally as [96]

$$(f_x)_{mm'} = \frac{1}{2}\left[\sqrt{(f-m+1)(f+m)}\delta_{m-1,m'} + \sqrt{(f+m+1)(f-m)}\delta_{m+1,m'}\right], \tag{2.35}$$

$$(f_y)_{mm'} = -\frac{i}{2}\left[\sqrt{(f-m+1)(f+m)}\delta_{m-1,m'} - \sqrt{(f+m+1)(f-m)}\delta_{m+1,m'}\right], \tag{2.36}$$

$$(f_z)_{mm'} = m\delta_{mm'}. \tag{2.37}$$

The spin matrices act on a given spin state to transform it into a new spin state. For example, the action of f_z on a given state is

$$f_z\left|f,m\right\rangle = m\left|f,m\right\rangle. \tag{2.38}$$

The spin-1 Pauli-type matrices are given below in their irreducible representation as [96]

$$f_x = \frac{1}{\sqrt{2}}\begin{pmatrix} 0 & 1 & 0 \\ 1 & 0 & 1 \\ 0 & 1 & 0 \end{pmatrix}, \quad f_y = \frac{i}{\sqrt{2}}\begin{pmatrix} 0 & -1 & 0 \\ 1 & 0 & -1 \\ 0 & 1 & 0 \end{pmatrix}, \quad f_z = \begin{pmatrix} 1 & 0 & 0 \\ 0 & 0 & 0 \\ 0 & 0 & -1 \end{pmatrix}. \tag{2.39}$$

Similarly, the spin-2 Pauli-type matrices are

$$f_x = \begin{pmatrix} 0 & 1 & 0 & 0 & 0 \\ 1 & 0 & \sqrt{\frac{3}{2}} & 0 & 0 \\ 0 & \sqrt{\frac{3}{2}} & 0 & \sqrt{\frac{3}{2}} & 0 \\ 0 & 0 & \sqrt{\frac{3}{2}} & 0 & 1 \\ 0 & 0 & 0 & 1 & 0 \end{pmatrix}, \quad f_y = i \begin{pmatrix} 0 & -1 & 0 & 0 & 0 \\ 1 & 0 & -\sqrt{\frac{3}{2}} & 0 & 0 \\ 0 & \sqrt{\frac{3}{2}} & 0 & i\sqrt{\frac{3}{2}} & 0 \\ 0 & 0 & \sqrt{\frac{3}{2}} & 0 & -1 \\ 0 & 0 & 0 & 1 & 0 \end{pmatrix},$$
$$f_z = \begin{pmatrix} 2 & 0 & 0 & 0 & 0 \\ 0 & 1 & 0 & 0 & 0 \\ 0 & 0 & 0 & 0 & 0 \\ 0 & 0 & 0 & -1 & 0 \\ 0 & 0 & 0 & 0 & -2 \end{pmatrix}. \tag{2.40}$$

Spin-singlet pair

The quantity $\hat{A}_{00}$ is the spin-singlet pair operator, which describes interactions for atoms in a singlet state (zero total spin, i.e., $\mathcal{F} = 0$) and with $\mathcal{M} = 0$. Using Eq. (2.30) and Eq. (2.31), along with the substitution $\mathcal{F} = \mathcal{M} = 0$, yields the spin-singlet pair operator:

$$\hat{A}_{00}(\mathbf{r}_1, \mathbf{r}_2) = \frac{1}{\sqrt{2f+1}} \sum_{m=-f}^{f} (-1)^{f-m} \hat{\psi}_m(\mathbf{r}_1) \hat{\psi}_{-m}(\mathbf{r}_2). \tag{2.41}$$

Operator relations

Most physical observables can be constructed from powers of the spinor Pauli-type matrices, $\mathbf{f} \equiv (f_x, f_y, f_z)$ [96]. Firstly, the total density operator is defined as

$$\hat{n}(\mathbf{r}) = \sum_{m=-f}^{f} \hat{\psi}_m^\dagger(\mathbf{r}) \hat{\psi}_m(\mathbf{r}). \tag{2.42}$$

Secondly, the components of the condensate spin density operator, $\hat{\mathbf{F}} \equiv (\hat{F}_x, \hat{F}_y, \hat{F}_z)$, also known as the magnetisation operator, are constructed as

$$\hat{F}_\nu(\mathbf{r}) = \sum_{m,m'=-f}^{f} \left(f_\nu\right)_{mm'} \hat{\psi}_m^\dagger(\mathbf{r}) \hat{\psi}_{m'}(\mathbf{r}), \quad (\nu = x, y, z). \tag{2.43}$$

Finally, the general rank-k spin nematic tensor operator for $k \geq 2$ is given by

$$\mathcal{N}^{(k)}_{\nu_1 \nu_2 \cdots \nu_k} = \sum_{m,m'=-f}^{f} \left(f_{\nu_1} f_{\nu_2} \cdots f_{\nu_k}\right)_{mm'} \hat{\psi}_m^\dagger(\mathbf{r}) \hat{\psi}_{m'}(\mathbf{r}), \quad (\nu_1, \nu_2, \ldots, \nu_k = x, y, z). \tag{2.44}$$

Spin-channel operators to physical observables

To construct the spinor interaction Hamiltonian in terms of physical observables, we need to connect them to the projection operators, $\hat{A}_{\mathcal{F},\mathcal{M}}$. The relationship between the two is constructed using a completeness relation that joins the irreducible observables to the composition law of angular momentum, then taking the expectation value (see Ref. [96] for details). The result is the following relation [96, 98]:

$$\sum_{\nu_1\nu_2\cdots\nu_k} (\mathcal{N}_{\nu_1\nu_2\cdots\nu_k})^2 = \sum_{\mathcal{F}=0,2,\ldots,2f} \left[\frac{1}{2}\mathcal{F}(\mathcal{F}+1) - f(f+1)\right]^k \sum_{\mathcal{M}=-\mathcal{F}}^{\mathcal{F}} \hat{A}^\dagger_{\mathcal{F},\mathcal{M}}\hat{A}_{\mathcal{F},\mathcal{M}}, \tag{2.45}$$

where the left-hand side is a tensor inner product, reducing the tensor to a scalar energy term.

2.3.3 Spinor interaction Hamiltonian

Using the results of the previous subsection, namely, Eq. (2.45), we can now construct the full spinor interaction Hamiltonian for spin-f systems. In particular, we explicitly construct the interaction Hamiltonian for spin-1 and spin-2 systems, and then provide the general interaction Hamiltonian for a spin-f system. The Hamiltonian will provide us with the form of interaction strengths arising in spinor systems, and how they relate to the spin-channel scattering lengths, $a_\mathcal{F}$.

Spin-1

In spin-1 we have $\mathcal{F}=0$ or $\mathcal{F}=2$, which, using Eq. (2.28), implies an interaction Hamiltonian of the form

$$\hat{H}_{\text{int}} = \hat{V}^{(0)} + \hat{V}^{(2)}. \tag{2.46}$$

Then, using Eq. (2.34), this becomes

$$\hat{H}_{\text{int}} = \frac{1}{2}\int g_0 \hat{A}^\dagger_{00}(\mathbf{r})\hat{A}_{00}(\mathbf{r}) + g_2 \sum_{\mathcal{M}=-2}^{2} \hat{A}^\dagger_{2\mathcal{M}}(\mathbf{r})\hat{A}_{2\mathcal{M}}(\mathbf{r})\, \mathrm{d}^3\mathbf{r}. \tag{2.47}$$

To simplify the above expression, we set $f=1$ and $k=0,1$ in Eq. (2.45), which yields the following two expressions

$$\hat{n}^2(\mathbf{r}) = \hat{A}^\dagger_{00}(\mathbf{r})\hat{A}_{00}(\mathbf{r}) + \sum_{\mathcal{M}=-2}^{2} \hat{A}^\dagger_{2\mathcal{M}}(\mathbf{r})\hat{A}_{2\mathcal{M}}(\mathbf{r}), \tag{2.48}$$

$$\hat{\mathbf{F}}^2(\mathbf{r}) = -2\hat{n}^2(\mathbf{r}) + 3\sum_{\mathcal{M}=-2}^{2} \hat{A}^\dagger_{2\mathcal{M}}(\mathbf{r})\hat{A}_{2\mathcal{M}}(\mathbf{r}). \tag{2.49}$$

Solving the above simultaneous equations gives the following expressions for the projection operators:

$$\hat{A}^\dagger_{00}(\mathbf{r})\hat{A}_{00}(\mathbf{r}) = \frac{1}{3}\left[\hat{n}^2(\mathbf{r}) - \hat{\mathbf{F}}^2(\mathbf{r})\right], \tag{2.50}$$

$$\sum_{\mathcal{M}=-2}^{2}\hat{A}^\dagger_{2\mathcal{M}}(\mathbf{r})\hat{A}_{2\mathcal{M}}(\mathbf{r}) = \frac{1}{3}\left[\hat{n}^2(\mathbf{r}) + \hat{\mathbf{F}}^2(\mathbf{r})\right]. \tag{2.51}$$

Finally, substituting the above expressions into Eq. (2.47) gives the full interaction Hamiltonian for a spin-1 BEC:

$$\hat{H}_{\text{int}} = \frac{1}{2}\int c_0\hat{n}^2(\mathbf{r}) + c_1\hat{\mathbf{F}}^2(\mathbf{r})\,\mathrm{d}^3\mathbf{r}, \tag{2.52}$$

where

$$c_0 = \frac{1}{3}\left(g_0 + 2g_2\right), \tag{2.53}$$

$$c_1 = \frac{1}{3}\left(g_2 - g_0\right). \tag{2.54}$$

Here, c_0 gives the density, or spin-independent, interaction strength and c_1 gives the spin-dependent interaction strength. As we shall see in Chapter 3, the sign of the spin-independent interaction strength, c_1, determines the relevant ground states available in spin-1 systems. Since c_1 is the difference of two s-wave scattering lengths, which are comparable in magnitude experimentally, the spin-dependent interaction strength is usually much smaller than the spin-independent strength (see Sec. 2.5.3).

Spin-2

In a spin-2 system we have $\mathcal{F} = 0, 2, 4$. Eq. (2.28) then implies the interaction Hamiltonian for a spin-2 system has the form

$$\hat{H}_{\text{int}} = \hat{V}^{(0)} + \hat{V}^{(2)} + \hat{V}^{(4)}. \tag{2.55}$$

Using Eq. (2.34) the above becomes

$$\hat{H}_{\text{int}} = \frac{1}{2}\int g_0\hat{A}^\dagger_{00}(\mathbf{r})\hat{A}_{00}(\mathbf{r}) + g_2\sum_{\mathcal{M}=-2}^{2}\hat{A}^\dagger_{2\mathcal{M}}(\mathbf{r})\hat{A}_{2\mathcal{M}}(\mathbf{r}) + g_4\sum_{\mathcal{M}=-4}^{4}\hat{A}^\dagger_{4\mathcal{M}}(\mathbf{r})\hat{A}_{4\mathcal{M}}(\mathbf{r})\,\mathrm{d}^3\mathbf{r}. \tag{2.56}$$

Substituting $f = 2$ and $k = 0, 1, 2$ in Eq. (2.45) and solving the resulting equations for the projection operators gives the following relations

$$\sum_{\mathcal{M}=-2}^{2}\hat{A}^\dagger_{2\mathcal{M}}(\mathbf{r})\hat{A}_{2\mathcal{M}}(\mathbf{r}) = \frac{1}{7}\left[4\hat{n}^2(\mathbf{r}) - 10\hat{A}^\dagger_{00}(\mathbf{r})\hat{A}_{00}(\mathbf{r}) - \hat{\mathbf{F}}^2(\mathbf{r})\right], \tag{2.57}$$

$$\sum_{\mathcal{M}=-4}^{4}\hat{A}^\dagger_{4\mathcal{M}}(\mathbf{r})\hat{A}_{4\mathcal{M}}(\mathbf{r}) = \frac{1}{7}\left[3\hat{n}^2(\mathbf{r}) + 3\hat{A}^\dagger_{00}(\mathbf{r})\hat{A}_{00}(\mathbf{r}) + \hat{\mathbf{F}}^2(\mathbf{r})\right]. \tag{2.58}$$

Substituting the above relations into Eq. (2.56) yields the full interaction Hamiltonian for a spin-2 BEC:

$$\hat{H} = \frac{1}{2}\int c_0 \hat{n}^2(\mathbf{r}) + c_1 \hat{\mathbf{F}}^2(\mathbf{r}) + c_2 \hat{A}^\dagger_{00}(\mathbf{r})\hat{A}_{00}(\mathbf{r})\,\mathrm{d}^3\mathbf{r}, \tag{2.59}$$

where the interaction strengths are defined as

$$c_0 = \frac{1}{7}\left(4g_2 + 3g_4\right), \tag{2.60}$$

$$c_1 = \frac{1}{7}\left(g_4 - g_2\right), \tag{2.61}$$

$$c_2 = \frac{1}{7}\left(7g_0 - 10g_2 + 3g_4\right). \tag{2.62}$$

Here, c_0, c_1 are the spin-independent and spin-dependent interaction strengths, respectively. Since the spin-2 system has an extra contribution from the spin-channels compared to the spin-1 system, there arises an additional interaction strength, c_2, denoted the spin-singlet interaction strength.

Spin-f

Generally, the spin-f interaction Hamiltonian has $f+1$ non-linear interaction terms to account for the $f+1$ spin-channels. The process to construct higher spin interaction Hamiltonians is the same as for the spin-1 and spin-2 cases, making use of Eq. (2.45). For example, for a spin-3 system, we substitute $f = 3$ and $k = 0,1,2,3$ into Eq. (2.45) and follow the same methodology as before.

2.3.4 Single-particle Hamiltonian

When a magnetic field is applied to a spinor system, the field causes energy shifts in the spin components. When this field is aligned along the spin quantisation axis, linear, p, and quadratic, q, Zeeman shifts arise. In such a case, the single-particle (non-interacting) Hamiltonian is given by [96]

$$\hat{H}_0 = \int \sum_{m,m'=-f}^{f} \hat{\psi}^\dagger_m \left[-\frac{\hbar^2}{2M}\nabla^2 + V(\mathbf{r}) - p(f_z)_{mm'} + q(f_z^2)_{mm'}\right]\hat{\psi}_{m'}\,\mathrm{d}^3\mathbf{r}, \tag{2.63}$$

where $V(\mathbf{r})$ is a trapping potential. The linear Zeeman shift, p, introduces a Larmor precession of the condensate spin about the direction of the applied magnetic field, and hence can be removed by transforming to a rotating basis. The quadratic Zeeman shift, q, however, breaks the spin symmetry, and thus affects the non-linear spin dynamics. Throughout this thesis we consider a variety of applied magnetic fields providing different forms for the quadratic Zeeman shift. In Chapter 5 we consider a time-dependent but spatially-uniform quadratic Zeeman shift, i.e., $q = q(t)$. Additionally, Chapter 6 sees the application of a non-uniform magnetic field such that $q = q(z)$.

2.4 Spinor mean-field theory

The mean-field theory for spinor BECs is obtained by expanding the field operator $\hat{\psi}_m(\mathbf{r})$ into a complete orthonormal set of basis functions and taking the expectation (see Ref. [96] for details). The mean-field state of a spin-f system is then described by a $(2f+1)$-component order parameter of the form

$$\Psi(\mathbf{r}) = \begin{pmatrix} \psi_f(\mathbf{r}) \\ \psi_{f-1}(\mathbf{r}) \\ \vdots \\ \psi_{-f}(\mathbf{r}) \end{pmatrix} = \sqrt{n(\mathbf{r})} \begin{pmatrix} \zeta_f(\mathbf{r}) \\ \zeta_{f-1}(\mathbf{r}) \\ \vdots \\ \zeta_{-f}(\mathbf{r}) \end{pmatrix}, \tag{2.64}$$

where ψ_f is the wave function for magnetic sublevel $m = f$ which can be further decomposed into a normalised spinor ζ as $\psi_m = \sqrt{n}\zeta_m$, where

$$n(\mathbf{r}) = \sum_{m=-f}^{f} |\psi_m(\mathbf{r})|^2, \tag{2.65}$$

is the atomic density and $\zeta^\dagger \zeta = 1$. In this section we use the result of the mean-field theory to construct the energy functional of both spin-1 and spin-2 systems, and then derive the spinor Gross-Pitaevskii equations.

2.4.1 Spin-1 Gross-Pitaevskii equations

The mean-field wave function of a spin-1 system is given as a three-component vector of the form

$$\Psi(\mathbf{r}) = \begin{pmatrix} \psi_1(\mathbf{r}) \\ \psi_0(\mathbf{r}) \\ \psi_{-1}(\mathbf{r}) \end{pmatrix} = \sqrt{n(\mathbf{r})} \begin{pmatrix} \zeta_1(\mathbf{r}) \\ \zeta_0(\mathbf{r}) \\ \zeta_{-1}(\mathbf{r}) \end{pmatrix}. \tag{2.66}$$

Combining the results of the single-particle Hamiltonian in Eq. (2.63) and the spin-1 interaction Hamiltonian in Eq. (2.52) gives the full mean-field energy functional of the spin-1 system [96]:

$$E[\Psi] = \int \left\{ \sum_{m=-1}^{1} \psi_m^* \left[-\frac{\hbar^2 \nabla^2}{2M} + V(\mathbf{r}) - pm + qm^2 \right] \psi_m + \frac{c_0}{2} n^2 + \frac{c_1}{2} n^2 |\langle \hat{\mathbf{F}} \rangle|^2 \right\} \mathrm{d}^3\mathbf{r}, \tag{2.67}$$

where $\langle\hat{\mathbf{F}}\rangle \equiv (\langle\hat{F}_x\rangle, \langle\hat{F}_y\rangle, \langle\hat{F}_z\rangle)$ is the spin expectation density vector of which the components are defined as

$$\langle\hat{F}_\nu\rangle = \sum_{m,m'=-1}^{1} \zeta_m^*(\mathbf{r})(f_\nu)_{mm'}\zeta_m(\mathbf{r}), \quad (\nu = x, y, z). \tag{2.68}$$

Using the spin-1 Pauli-type matrices defined in Eq. (2.39), the individual components of the spin vectors for a spin-1 system are given explicitly as

$$\langle\hat{F}_x\rangle = \frac{1}{\sqrt{2}}\left(\zeta_1^*\zeta_0 + \zeta_0^*(\zeta_1 + \zeta_{-1}) + \zeta_{-1}^*\zeta_0\right), \tag{2.69}$$

$$\langle\hat{F}_y\rangle = \frac{i}{\sqrt{2}}\left(-\zeta_1^*\zeta_0 + \zeta_0^*(\zeta_1 - \zeta_{-1}) + \zeta_{-1}^*\zeta_0\right), \tag{2.70}$$

$$\langle\hat{F}_z\rangle = |\zeta_1|^2 - |\zeta_{-1}|^2. \tag{2.71}$$

The spin expectation $\langle\hat{\mathbf{F}}\rangle$ is related to the spin density vector $\hat{\mathbf{F}}$ as

$$\langle\hat{\mathbf{F}}\rangle = \frac{\hat{\mathbf{F}}}{n}. \tag{2.72}$$

The magnitude of the spin expectation takes values from $|\langle\hat{\mathbf{F}}\rangle| = 0$ to $|\langle\hat{\mathbf{F}}\rangle| = f$ in a spin-f system.

The mean-field equations that govern the time-evolution of the individual wave function components $\psi_m(\mathbf{r})$ are derived from a variational derivative of the energy functional in Eq. (2.67) as

$$i\hbar\frac{\partial\psi_m(\mathbf{r})}{\partial t} = \frac{\delta E}{\delta\psi_m^*(\mathbf{r})}. \tag{2.73}$$

This results in the spin-1 GPEs:

$$i\hbar\frac{\partial\psi_m}{\partial t} = \left[-\frac{\hbar^2\nabla^2}{2M} + V(\mathbf{r}) - pm + qm^2 + c_0 n\right]\psi_m + c_1 n \sum_{m'=-1}^{1}\langle\hat{\mathbf{F}}\rangle\cdot\mathbf{f}_{mm'}\psi_{m'}, \tag{2.74}$$

which describe the mean-field evolution of spin-1 Bose-Einstein condensates. The time-independent GPEs are found through the substitution $\psi_m = \psi_m(\mathbf{r})e^{-i\mu t/\hbar}$, where μ is the chemical potential. Substituting into Eq. (2.74) and writing the equation for each component explicitly gives

$$\left[-\frac{\hbar^2\nabla^2}{2M} + V(\mathbf{r}) - p + q + c_0 n + c_1 n\langle\hat{F}_z\rangle - \mu\right]\psi_1 + \frac{c_1}{\sqrt{2}}n\langle\hat{F}_-\rangle\psi_0 = 0, \tag{2.75}$$

$$\frac{c_1}{\sqrt{2}}n\langle\hat{F}_+\rangle\psi_1 + \left[-\frac{\hbar^2\nabla^2}{2M} + V(\mathbf{r}) + c_0 n - \mu\right]\psi_0 + \frac{c_1}{\sqrt{2}}n\langle\hat{F}_-\rangle\psi_{-1} = 0, \tag{2.76}$$

$$\left[-\frac{\hbar^2\nabla^2}{2M} + V(\mathbf{r}) + p + q + c_0 n - c_1 n\langle\hat{F}_z\rangle - \mu\right]\psi_{-1} + \frac{c_1}{\sqrt{2}}n\langle\hat{F}_+\rangle\psi_0 = 0, \tag{2.77}$$

where

$$\langle \hat{F}_\pm \rangle = \langle \hat{F}_x \rangle \pm i \langle \hat{F}_y \rangle. \tag{2.78}$$

These equations can be solved to reveal more about the ground states and stationary solutions of spinor BECs, which forms the basis of Chapter 3. Note that, in contrast to two-component BECs, spinor BECs have a common chemical potential, μ, rather than different chemical potentials per component. This is due to the fact that spin-dependent interactions lead to exchange of particles between the components and hence individual component atom numbers are not conserved, but the total atom number, N, is (see Sec. 2.4.3).

2.4.2 Spin-2 Gross-Pitaevskii equations

The mean-field wave function of a spin-2 system is given as a five-component vector of the form

$$\Psi(\mathbf{r}) = \begin{pmatrix} \psi_2(\mathbf{r}) \\ \psi_1(\mathbf{r}) \\ \psi_0(\mathbf{r}) \\ \psi_{-1}(\mathbf{r}) \\ \psi_{-2}(\mathbf{r}) \end{pmatrix} = \sqrt{n(\mathbf{r})} \begin{pmatrix} \zeta_2(\mathbf{r}) \\ \zeta_1(\mathbf{r}) \\ \zeta_0(\mathbf{r}) \\ \zeta_{-1}(\mathbf{r}) \\ \zeta_{-2}(\mathbf{r}) \end{pmatrix}. \tag{2.79}$$

As before, combining the results of the single-particle Hamiltonian in Eq. (2.63) and the spin-2 interaction Hamiltonian in Eq. (2.59) gives the full mean-field energy functional of the spin-2 system [96]:

$$E[\Psi] = \int \left\{ \sum_{m=-2}^{2} \psi_m^* \left[-\frac{\hbar^2 \nabla^2}{2M} + V(\mathbf{r}) - pm + qm^2 \right] \psi_m + \frac{c_0}{2} n^2 + \frac{c_1}{2} n^2 |\langle \hat{\mathbf{F}} \rangle|^2 + \frac{c_2}{2} n^2 |A_{00}|^2 \right\} \mathrm{d}^3\mathbf{r}. \tag{2.80}$$

In the spin-2 case the components of the expectation of the condensate spin vector can be constructed using the spin-2 Pauli-type matrices in Eq. (2.40) along with Eq. (2.68) to give

$$\langle \hat{F}_+ \rangle = \langle \hat{F}_-^* \rangle = 2\left(\zeta_2^* \zeta_1 + \zeta_{-1}^* \zeta_{-2}\right) + \sqrt{6}\left(\zeta_1^* \zeta_0 + \zeta_0^* \zeta_{-1}\right), \tag{2.81}$$

$$\langle \hat{F}_z \rangle = 2\left(|\zeta_2|^2 - |\zeta_{-2}|^2\right) + |\zeta_1|^2 - |\zeta_{-1}|^2. \tag{2.82}$$

The additional term in the spin-2 energy functional is the spin-singlet pair amplitude, defined in terms of the condensate spinor as

$$A_{00} = \frac{1}{\sqrt{5}} \left(2\zeta_2 \zeta_{-2} - 2\zeta_1 \zeta_{-1} + \zeta_0^2\right). \tag{2.83}$$

Similar to the spin-1 case, the spin-2 GPEs are obtained by substituting Eq. (2.80) into Eq. (2.73) resulting in five coupled equations that model the mean-field dynamics of spin-2 Bose-Einstein condensates:

$$i\hbar\frac{\partial\psi_{\pm2}}{\partial t}=\left[-\frac{\hbar^2\nabla^2}{2M}+V(\mathbf{r})\mp2p+4q+c_0n\pm2c_1n\langle\hat{F}_z\rangle\right]\psi_{\pm2}+c_1n\langle\hat{F}_\mp\rangle\psi_{\pm1}+\frac{c_2}{\sqrt{2}}nA_{00}\psi^*_{\mp2} \tag{2.84}$$

$$i\hbar\frac{\partial\psi_{\pm1}}{\partial t}=\left[-\frac{\hbar^2\nabla^2}{2M}+V(\mathbf{r})\mp p+q+c_0n\pm c_1n\langle\hat{F}_z\rangle\right]\psi_{\pm1}+c_1\left(\frac{\sqrt{6}}{2}n\langle\hat{F}_\mp\rangle\psi_0+n\langle\hat{F}_\pm\rangle\psi_{\pm2}\right) -\frac{c_2}{\sqrt{2}}nA_{00}\psi^*_{\mp1} \tag{2.85}$$

$$i\hbar\frac{\partial\psi_0}{\partial t}=\left[-\frac{\hbar^2\nabla^2}{2M}+V(\mathbf{r})+c_0n\right]\psi_0+\frac{\sqrt{6}}{2}c_1\left(n\langle\hat{F}_+\rangle\psi_1+n\langle\hat{F}_-\rangle\psi_{-1}\right)+\frac{c_2}{\sqrt{2}}nA_{00}\psi^*_{\mp2}. \tag{2.86}$$

Following the same procedure as in the spin-1 case, the time-independent GPEs can be found through the substitution $\psi_m(\mathbf{r},t)=\psi_m(\mathbf{r})e^{-\mu t/\hbar}$.

2.4.3 Conserved quantities

In spinor BECs, there are three conserved quantities. Firstly, assuming that the linear and quadratic Zeeman shifts as well as the external potential are independent of time, the total energy of the system [Eq. (2.67) and Eq. (2.80)] is conserved. In addition, the total atom number of the condensate

$$N=\int\sum_{m=-f}^{f}|\psi_m|^2\,\mathrm{d}^3\mathbf{r}, \tag{2.87}$$

is also conserved. Furthermore, the z-component of the magnetisation, defined as

$$M_z=\int\langle\hat{F}_z\rangle\,\mathrm{d}^3\mathbf{r}, \tag{2.88}$$

is also conserved. The conservation of the longitudinal magnetisation can be seen from the fact that spin-exchange interactions leave the wave function symmetric. For example, in a spin-1 system the only allowed exchanges are given in Eq. (2.27). Hence, having a particle that leaves (or enters) the $m=1$ component implies there is also an additional particle that leaves (or enters) the $m=-1$ component. Then, by the definition of $\hat{F}_z$ in Eq. (2.69), we see that the integral of the longitudinal spin vector, i.e., the longitudinal magnetisation defined above, would remain constant.

2.4.4 Reduction to lower dimensions

One can reduce the full 3D coupled GPEs to lower dimensions by considering sufficiently tight confinement of the condensate in one or more directions. Here, we reduce the spin-1 GPEs to their 2D and 1D counterparts.

Reduction to 2D

To begin, we start with the full 3D dimensional equations given in Eq. (2.74), written in matrix form as

$$i\hbar\frac{\partial\Psi}{\partial t}=\left[-\frac{\hbar^2\nabla^2}{2M}+V(\mathbf{r})+c_0n+c_1n\langle\hat{\mathbf{F}}\rangle\cdot\mathbf{f}-pf_z+qf_z^2\right]\Psi, \tag{2.89}$$

where $\Psi=(\psi_1,\psi_0,\psi_{-1})$ is the three-component wave function and $\mathbf{f}\equiv(f_x,f_y,f_z)$ are the spin-1 Pauli-type matrices defined in Eq. (2.39). To reduce the dimensionality, we assume the condensate has been tightly confined in the z-direction by means of a harmonic oscillator which has trapping frequencies $(\omega_x,\omega_y,\omega_z)$ in the (x,y,z) directions, respectively. A tight confinement in the z direction is achieved by having $\omega_z\gg\omega_x,\omega_y$. In addition, we assume the trapping frequencies are sufficiently such that only the ground state of the condensate is occupied. With these assumptions, we can write the wave function of the condensate in a separable form:

$$\Psi(x,y,z,t)=\tilde{\Psi}(x,y,t)\Phi(z), \tag{2.90}$$

where $\Phi(z)$ is normalised as $\int_{-\infty}^{\infty}|\Phi(z)|^2\,\mathrm{d}z=1$.

Substituting Eq. (2.90) into Eq. (2.89) we obtain

$$\begin{aligned}i\hbar\frac{\partial\tilde{\Psi}}{\partial t}\Phi=\Bigg[&-\frac{\hbar^2}{2M}\Phi\nabla_\perp^2-\frac{\hbar^2}{2M}\frac{\partial^2\Phi}{\partial z^2}+[V_\perp(x,y)+V_z(z)]\Phi+c_0\tilde{\Psi}^\dagger\tilde{\Psi}|\Phi|^2\Phi\\&+c_1\tilde{\Psi}^\dagger\tilde{\Psi}|\Phi|^2\Phi\langle\hat{\mathbf{F}}\rangle\cdot\mathbf{f}-p\Phi f_z+q\Phi f_z^2\Bigg]\tilde{\Psi}\Phi.\end{aligned} \tag{2.91}$$

To reduce the equation further, we multiply from the left by Φ^* and integrate over the z direction, which gives:

$$\begin{aligned}i\hbar\frac{\partial\tilde{\Psi}}{\partial t}=\Bigg[&-\frac{\hbar^2}{2M}\Phi\nabla_\perp^2-\frac{\hbar^2}{2M}\left(\int_{-\infty}^{\infty}\Phi^*\frac{\mathrm{d}^2\Phi}{\mathrm{d}z^2}\mathrm{d}z\right)+V_\perp(x,y)+\left(\int_{-\infty}^{\infty}V_z(z)|\Phi|^2\mathrm{d}z\right)\\&+c_0\tilde{n}\left(\int_{-\infty}^{\infty}|\Phi|^4\mathrm{d}z\right)+c_1\tilde{n}\langle\hat{\mathbf{F}}\rangle\cdot\mathbf{f}\left(\int_{-\infty}^{\infty}|\Phi|^4\mathrm{d}z\right)-pf_z+qf_z^2\Bigg]\tilde{\Psi},\end{aligned} \tag{2.92}$$

where $\tilde{n}=\tilde{\Psi}^\dagger\tilde{\Psi}$. In the above equation, the constant $C=-\frac{\hbar^2}{2M}\int_{-\infty}^{\infty}\Phi^*\frac{\mathrm{d}^2\Phi}{\mathrm{d}z^2}\mathrm{d}z+\int_{-\infty}^{\infty}V_z(z)|\Phi|^2\mathrm{d}z$ can be removed from the equation via the appropriate transformation $\tilde{\Psi}\to\tilde{\Psi}e^{-Ct/N}$, where

N is the total atom number. Now, we take $\Phi(z)$ to be the harmonic oscillator ground state, which has the form

$$\Phi(z) = \left(\frac{\beta}{\pi}\right)^{\frac{1}{4}} e^{-\frac{\beta}{2}z^2}, \tag{2.93}$$

where $\beta = M\omega_z/\hbar$. This then leads to the integral

$$\int_{-\infty}^{\infty} |\Phi(z)|^4 \mathrm{d}z = \sqrt{\frac{\beta}{2\pi}}. \tag{2.94}$$

We can then appropriately rescale the interaction strengths to obtain their 2D counterparts:

$$c_0^{\mathrm{2D}} = c_0\sqrt{\frac{\beta}{2\pi}}, \qquad c_1^{\mathrm{2D}} = c_1\sqrt{\frac{\beta}{2\pi}}. \tag{2.95}$$

Finally, substituting back into Eq. (2.92) yields the 2D GPEs for a spin-1 system:

$$i\hbar\frac{\partial\tilde{\Psi}}{\partial t} = \left[-\frac{\hbar^2}{2M}\nabla_\perp^2 + V_\perp + c_0^{\mathrm{2D}} n + c_1^{\mathrm{2D}} n\langle\hat{\mathbf{F}}\rangle\cdot\mathbf{f} - pf_z + qf_z^2\right]\tilde{\Psi}, \tag{2.96}$$

where we have dropped the tildes for notational convenience.

Reduction to 1D

A similar process can be used to reduce the full 3D equations into their 1D counterparts. We now assume that the condensate is tightly confined in two directions, which we will take to be the x, y directions ($\omega_x, \omega_y \gg \omega_z$). This time, we separate the wave function according to

$$\Psi(x, y, z, t) = \tilde{\Psi}(z, t)\Phi(x, y), \tag{2.97}$$

and once again assuming $\Phi(x, y)$ to be normalised as $\int_{-\infty}^{\infty}\int_{-\infty}^{\infty}|\Phi(x, y)|^2 \mathrm{d}x\mathrm{d}y = 1$. We substitute the above expression into the GPEs in Eq. (2.89) and find

$$\begin{aligned} i\hbar\frac{\partial\tilde{\Psi}}{\partial t}\Phi = \Bigg[&-\frac{\hbar^2}{2M}\Phi\frac{\partial^2}{\partial z^2} - \frac{\hbar^2}{2M}\nabla_\perp^2\Phi + [V_\perp(x, y) + V_z(z)]\Phi + c_0\tilde{\Psi}^\dagger\tilde{\Psi}|\Phi|^2\Phi \\ &+ c_1\tilde{\Psi}^\dagger\tilde{\Psi}|\Phi|^2\Phi\langle\hat{\mathbf{F}}\rangle\cdot\mathbf{f} - p\Phi f_z + q\Phi f_z^2\Bigg]\tilde{\Psi}\Phi. \end{aligned} \tag{2.98}$$

Following a similar procedure to before, we multiply from the left by Φ^* and integrate over x and y which yields

$$\begin{aligned} i\hbar\frac{\partial\tilde{\Psi}}{\partial t} = \Bigg[&-\frac{\hbar^2}{2M}\Phi\frac{\partial^2}{\partial z^2} - \frac{\hbar^2}{2M}\left(\int_{-\infty}^{\infty}\int_{-\infty}^{\infty}\Phi^*\frac{\mathrm{d}^2\Phi}{\mathrm{d}z^2}\mathrm{d}x\mathrm{d}y\right) + V_\perp(x, y) + \left(\int_{-\infty}^{\infty}\int_{-\infty}^{\infty}V_z(z)|\Phi|^2\mathrm{d}x\mathrm{d}y\right) \\ &+ c_0\tilde{n}\left(\int_{-\infty}^{\infty}\int_{-\infty}^{\infty}|\Phi|^4\mathrm{d}x\mathrm{d}y\right) + c_1\tilde{n}\langle\hat{\mathbf{F}}\rangle\cdot\mathbf{f}\left(\int_{-\infty}^{\infty}\int_{-\infty}^{\infty}|\Phi|^4\mathrm{d}x\mathrm{d}y\right) - pf_z + qf_z^2\Bigg]\tilde{\Psi}. \end{aligned} \tag{2.99}$$

Now, the constant term $C = -\hbar^2/2M \int_\infty^\infty \int_\infty^\infty |\nabla_\perp^2 \Phi|^2 \mathrm{d}x\mathrm{d}z + \int_\infty^\infty \int_\infty^\infty V_\perp |\Phi|^2 \mathrm{d}x\mathrm{d}y$ can again be dropped from the equation via the appropriate substitution $\tilde{\Psi} = \tilde{\Psi} e^{-iCt/N}$. We then take $\tilde{\Psi}$ to be the lowest harmonic oscillator ground state, which in 2D becomes

$$\Phi(x, y) = \left(\frac{\beta}{\pi}\right)^{1/2} e^{-\frac{\beta}{2}(x^2+y^2)}, \tag{2.100}$$

where $\beta = m\omega_\perp/\hbar$, which leads to the relation

$$\int_{-\infty}^{\infty} \int_{-\infty}^{\infty} |\Phi(x, y)|^4 \mathrm{d}x\mathrm{d}y = \frac{\beta}{2\pi}. \tag{2.101}$$

This then leads to the 1D rescaled interaction strengths

$$c_0^{1\mathrm{D}} = c_0 \frac{\beta}{2\pi}, \qquad c_1^{1\mathrm{D}} = c_1 \frac{\beta}{2\pi}. \tag{2.102}$$

Finally, we arrive at the 1D GPE given in matrix form:

$$i\hbar \frac{\partial \Psi}{\partial t} = \left[-\frac{\hbar^2}{2M} \frac{\partial^2}{\partial z^2} + V_z(z) + c_0^{1\mathrm{D}} n + c_1^{1\mathrm{D}} \langle \hat{\mathbf{F}} \rangle \cdot \mathbf{f} - p f_z + q f_z^2 \right] \Psi, \tag{2.103}$$

again dropping the tildes for notational convenience.

2.5 Dimensionless spinor Gross-Pitaevskii equations

Systems that can undergo Bose-Einstein condensation, and hence become a superfluid, can form at a variety of length scales, ranging from Bose-Einstein condensates at the micron scale all the way to the cores of neutron stars, which are theorised to be superfluid on the kilometre scale [99]. In addition, atomic BECs in experiment take on a wide range of variable parameters and geometries. Such geometries include box-like potentials [100], toroidal ring geometries [101, 102], both quasi-2D [103] and quasi-1D systems [104], and even arbitrary potentials [105]. Due to these reasons, rescaling the quantities used in the corresponding GPEs allows one to reformulate any calculation into a desired scale and parameter regime.

In practice, this is done by casting the GPEs into a dimensionless form, where each dimensional parameter in the equation is rescaled using an appropriate quantity such that it becomes dimensionless. An advantage of using a dimensionless form is that the parameters used within numerical computation become normalised on the scale of unity, which, when compared to values in the dimensional equation such as $\hbar = 1.054 \times 10^{-34}$, can reduce numerical errors that arise due to the floating point representation used by computers. The process of making the GPEs dimensionless can be carried out in different ways, where the scaling parameters chosen typically depend on whether the system is trapped or not. Here, we derive the dimensionless 3D GPEs for both a homogeneous spin-1 BEC and a trapped spin-2 BEC, which will aid in the analysis of subsequent chapters.

2.5.1 Homogeneous spin-1 BEC

Consider a homogeneous system in the absence of a trapping potential $V(\mathbf{r}) = 0$. In a spin-1 system, there are two choices of length scales one can choose as their unit of length: the density healing length $\xi_d = \hbar/\sqrt{2Mc_0n_0}$, or the spin healing length $\xi_s = \hbar/\sqrt{2M|c_1|n_0}$, where n_0 is the background density of the uniform system. Both choices are valid, but for this thesis we shall choose the spin healing length, ξ_s. Then, an appropriate unit of energy is the spin energy: $E_s = 2|c_1|n_0$, which leads to the spin time $\tau_s = \hbar/E_s$. Now we have found appropriate units for length, time, and energy, we can rescale each quantity as

$$\mathbf{r} \to \xi_s\tilde{\mathbf{r}}, \qquad t \to \tau_s\tilde{t}, \qquad \Psi \to \sqrt{n_0}\tilde{\Psi}, \tag{2.104}$$

where a tilde denotes the dimensionless quantity. Substituting these into Eq. (2.89) leads to the dimensionless spin-1 GPEs:

$$i\frac{\partial\tilde{\psi}_1}{\partial\tilde{t}} = \left[-\frac{1}{2}\tilde{\nabla}^2 + \tilde{c}_0\tilde{n} + \tilde{c}_1\tilde{n}\tilde{F}_z - \tilde{p} + \tilde{q}\right]\tilde{\psi}_1 + \frac{\tilde{c}_1}{\sqrt{2}}\tilde{n}\tilde{F}_-\tilde{\psi}_0, \tag{2.105}$$

$$i\frac{\partial\tilde{\psi}_0}{\partial\tilde{t}} = \left[-\frac{1}{2}\tilde{\nabla}^2 + \tilde{c}_0\tilde{n}\right]\tilde{\psi}_0 + \frac{\tilde{c}_1}{\sqrt{2}}\tilde{n}\left(\tilde{F}_+\tilde{\psi}_1 + \tilde{F}_-\tilde{\psi}_{-1}\right), \tag{2.106}$$

$$i\frac{\partial\tilde{\psi}_{-1}}{\partial\tilde{t}} = \left[-\frac{1}{2}\tilde{\nabla}^2 + \tilde{c}_0\tilde{n} - \tilde{c}_1\tilde{n}\tilde{F}_z + \tilde{p} + \tilde{q}\right]\tilde{\psi}_{-1} + \frac{\tilde{c}_1}{\sqrt{2}}\tilde{n}\tilde{F}_+\tilde{\psi}_0, \tag{2.107}$$

where the rescaled interaction strengths and Zeeman shifts are

$$\tilde{c}_0 = \frac{n_0c_0}{E_s} = \left|\frac{c_0}{2c_1}\right|, \quad \tilde{c}_1 = \frac{n_0c_1}{E_s} = \frac{1}{2}\cdot\operatorname{sgn}(c_1), \quad \tilde{p} = \frac{q}{E_s}, \quad \tilde{q} = \frac{q}{E_s}. \tag{2.108}$$

By choosing our unit of length and time as ξ_s and τ_s, respectively, the dimensionless spin-dependent interaction strength is fixed at $|\tilde{c}_1| = 1/2$. Therefore, to set the spin-independent interaction strength, $\tilde{c}_0$, we need the ratio of the interaction strengths, c_0/c_1, which is set by the atomic species itself.

2.5.2 Trapped spin-2 BEC

Consider now a spin-2 BEC trapped by a uniform harmonic trap $V(\mathbf{r})$. Now, instead of choosing the healing length as our unit of length, it makes more sense to instead choose the harmonic oscillator length $\ell = \sqrt{\hbar/(M\omega)}$, where ω is the trapping frequency. Then, time is measured in units of ω^{-1} and energy in $\hbar\omega$, which leads to the rescaling of the following units: $\mathbf{r} \to \ell\tilde{\mathbf{r}}$, $t \to \omega\tilde{t}$. To construct the dimensionless wave function, it is conventional to define the dimensionless wave function as being normalised to unity $\int_{-\infty}^{\infty}|\tilde{\Psi}|^2\mathrm{d}^3\tilde{\mathbf{r}} = 1$. Then, recalling that the dimensional wave function is normalised to the number of atoms $\int_{-\infty}^{\infty}|\Psi|^2\mathrm{d}^3\mathbf{r} = N$, and that $\mathrm{d}^3\mathbf{r} = \ell^3 \mathrm{d}^3\tilde{\mathbf{r}}$, it follows that the dimensional wave function can be rescaled as

$$\Psi \to \sqrt{\frac{N}{\ell^3}}\tilde{\Psi}. \tag{2.109}$$

Substituting these rescaled quantities into Eqs. (2.84) - (2.86) yields the dimensionless spin-2 GPEs for a trapped system

$$i\frac{\partial\tilde{\psi}_{\pm2}}{\partial\tilde{t}} = \left[-\frac{1}{2}\tilde{\nabla}^2 + V(\tilde{\mathbf{r}})\tilde{c}_0\tilde{n} \pm 2\tilde{c}_1\tilde{n}\tilde{F}_z \mp 2\tilde{p} + 4\tilde{q}\right]\tilde{\psi}_{\pm2} + \tilde{c}_1\tilde{n}\tilde{F}_{\mp}\tilde{\psi}_{\pm1} + \frac{\tilde{c}_2}{\sqrt{2}}\tilde{n}\tilde{A}_{20}\tilde{\psi}^*_{\mp2} \tag{2.110}$$

$$i\frac{\partial\tilde{\psi}_{\pm1}}{\partial\tilde{t}} = \left[-\frac{1}{2}\tilde{\nabla}^2 + V(\tilde{\mathbf{r}})\tilde{c}_0\tilde{n} \pm \tilde{c}_1\tilde{n}\tilde{F}_z \mp 2\tilde{p} + 4\tilde{q}\right]\tilde{\psi}_{\pm1} + \tilde{c}_1\tilde{n}\left(\frac{\sqrt{6}}{2}\tilde{F}_{\mp}\tilde{\psi}_0 + \tilde{F}_{\pm}\tilde{\psi}_{\pm2}\right) - \frac{\tilde{c}_2}{\sqrt{2}}\tilde{n}\tilde{A}_{20}\tilde{\psi}^*_{\mp1} \tag{2.111}$$

$$i\frac{\partial\tilde{\psi}_0}{\partial\tilde{t}} = \left[-\frac{1}{2}\tilde{\nabla}^2 + V(\tilde{\mathbf{r}}) + \tilde{c}_0\tilde{n}\right]\tilde{\psi}_0 + \frac{\sqrt{6}}{2}\tilde{c}_1\tilde{n}\left(\tilde{F}_+\tilde{\psi}_1 + \tilde{F}_-\tilde{\psi}_{-1}\right) + \frac{\tilde{c}_2}{\sqrt{2}}\tilde{n}\tilde{A}_{20}\tilde{\psi}^*_{\pm2}, \tag{2.112}$$

where now the rescaled interaction strengths and Zeeman shifts are

$$\tilde{c}_0 = \frac{Nc_0}{\hbar\omega\ell^3}, \quad \tilde{c}_1 = \frac{Nc_1}{\hbar\omega\ell^3}, \quad \tilde{c}_2 = \frac{Nc_2}{\hbar\omega\ell^3}, \quad \tilde{p} = \frac{p}{\hbar\omega}, \quad \tilde{q} = \frac{q}{\hbar\omega}. \tag{2.113}$$

2.5.3 Mapping to experimental parameters

Numerical simulations are an extremely useful tool for gaining insight into what experiments of BEC systems might look like. Therefore, it is useful to calculate the values of the interaction strengths for different atomic species so that they can be mapped to our dimensionless parameters. In particular, we investigate both the spin-1 and spin-2 atoms of ^{23}Na and ^{87}Rb. Here, we are taking our unit of length and time to be the harmonic oscillator length ℓ and inverse trap frequency ω^{-1}, respectively.

Spin-1

Recall that the dimensional interaction strengths for a spin-1 system are given as

$$c_0 = \frac{4\pi\hbar^2}{3M}(a_0 + 2a_2), \qquad c_1 = \frac{4\pi\hbar^2}{3M}(a_2 - a_0), \tag{2.114}$$

where $a_{\mathscr{F}}$ is the s-wave scattering length for the spin-$\mathscr{F}$ channel. To calculate the dimensional interaction strengths, we list the scattering lengths obtained by Crubellier [106] for ^{23}Na and Ho [10] for ^{87}Rb in Table 2.1. With these values, we are free to calculate the dimensional interaction strengths using Eq. (2.114). To calculate the numerical, dimensionless interaction strengths we assume an atom number of $N = 2 \times 10^5$ and a trapping frequency of $\omega = 2\pi \times 130$Hz. Both the dimensional (with uncertainties) and dimensionless values for

	a_0	a_2
^{23}Na	50.0 ± 1.6	55.0 ± 1.7
^{87}Rb	110.0 ± 4.0	107.0 ± 4.0

Table 2.1: Table of scattering lengths for spin-1 atomic species ^{23}Na and ^{87}Rb in units of the Bohr radius.

^{23}Na	Dimensional (units of $\mathrm{kg\,m^5 s^{-2}}$)	Dimensionless
c_0	$1.03 \pm 0.00321 \times 10^{-50}$	3.91×10^3
c_1	$3.21 \pm 0.0640 \times 10^{-52}$	122

Table 2.2: Dimensional (with uncertainties) and dimensionless interaction strengths of ^{23}Na.

^{87}Rb	Dimensional (units of $\mathrm{kg\,m^5 s^{-2}}$)	Dimensionless
c_0	$5.43 \pm 0.201 \times 10^{-51}$	2.10×10^3
c_1	$-5.03 \pm 10.3 \times 10^{-53}$	-19.1

Table 2.3: Dimensional (with uncertainties) and dimensionless interaction strengths of ^{87}Rb.

a spin-1 ^{23}Na system are given in Table 2.2. Calculating the ratio of interaction parameters gives $c_0/c_1 = 32.0$, which predicts the ground state of ^{23}Na to be polar (see Sec 3.2 for details on spin-1 ground states).

For the ^{87}Rb system, we again assume an atom number of $N = 2 \times 10^5$ with a trapping frequency of $\omega = 2\pi \times 130$Hz. The dimensional (with uncertainties) and dimensionless interaction strengths for a spin-1 ^{87}Rb are given in Table 2.3. Calculating the ratio of interaction strengths for this system gives $c_0/c_1 = -110$, which predicts the ground state of ^{87}Rb to be ferromagnetic (see Sec 3.2 for details on spin-1 ground states).

Spin-2

Recall that the dimensional interaction strengths for a spin-2 system are given as

$$c_0 = \frac{4\pi\hbar^2}{7M}(4a_2 + 3a_4), \qquad c_1 = \frac{4\pi\hbar^2}{7M}(a_4 - a_2), \qquad c_2 = \frac{4\pi\hbar^2}{7M}(7a_0 - 10a_2 + 3a_4), \tag{2.115}$$

To determine the values of the interaction strengths, we first list the s-wave scattering lengths in units of the Bohr radius given by Ciobanu [107] for ^{23}Na and Klausen [108] for ^{85}Rb and ^{87}Rb in Table 2.4. With these scattering lengths we can calculate the dimensional interaction strengths using Eq. (2.115). To calculate the corresponding dimensionless interaction strength, we assume $N = 2 \times 10^5$ and $\omega = 2\pi \times 130$ Hz. Both the dimensional (with uncertainties) and dimensionless values for a spin-2 ^{23}Na system are given in Table 2.5. The ratios of

	a_0	a_2	a_4
^{23}Na	34.9 ± 1.0	45.8 ± 1.1	64.5 ± 1.3
^{85}Rb	-740 ± 60.0	-570 ± 50.0	-390 ± 20.0
^{87}Rb	86.2 ± 1.0	90.2 ± 1.0	97.4 ± 1.0

Table 2.4: Table of scattering lengths for spin-2 atomic species ^{23}Na, ^{85}Rb, and ^{87}Rb in units of the Bohr radius.

^{23}Na	Dimensional (units of $\mathrm{kg\,m^5 s^{-2}}$)	Dimensionless
c_0	$1.03 \pm 0.00654 \times 10^{-50}$	3.91×10^3
c_1	$5.10 \pm 0.654 \times 10^{-52}$	195
c_2	$-5.51 \pm 0.927 \times 10^{-52}$	-210

Table 2.5: Dimensional (with uncertainties) and dimensionless interaction strengths of ^{23}Na.

^{87}Rb	Dimensional (units of $\mathrm{kg\,m^5 s^{-2}}$)	Dimensionless
c_0	$4.71 \pm 0.0144 \times 10^{-51}$	1.32×10^4
c_1	$5.19 \pm 1.44 \times 10^{-53}$	146
c_2	$-4.61 \pm 2.16 \times 10^{-53}$	-129

Table 2.6: Dimensional (with uncertainties) and dimensionless interaction strengths of ^{87}Rb.

interaction parameters are

$$\frac{c_0}{c_1} = 20.1, \qquad \frac{c_0}{c_2} = -18.6, \tag{2.116}$$

which predicts the ground state of ^{23}Na to be nematic (see Sec 3.3 for details on spin-2 ground states).

For ^{87}Rb we once again assume an atom number of $N = 2 \times 10^5$ with a trapping frequency $\omega = 2\pi \times 130$Hz. The dimensional (with uncertainties) and dimensionless parameters for a spin-2 ^{87}Rb system are listed in Table 2.6. In this case, the interaction strength ratios are

$$\frac{c_0}{c_1} = 90.7, \qquad \frac{c_0}{c_2} = -102.0, \tag{2.117}$$

which again predict the ground state to be nematic (see Sec 3.3 for details on spin-2 ground states).

CHAPTER

3

GROUND STATES AND TOPOLOGICAL DEFECTS IN SPINOR BOSE-EINSTEIN CONDENSATES

Spinor BECs offer a rich phase diagram, where the ground states of each system exhibit different symmetry properties. In this chapter we investigate the ground states of spin-1 and spin-2 BECs, which are obtained by minimizing the corresponding mean-field energy functional. In particular, we construct the phase diagram for both cases in the presence of Zeeman shifts. Additionally, we investigate the symmetry properties of each ground state using different graphical representations: namely Majorana and spherical harmonics. Finally, we delve into the topological defects that can arise in spinor BECs. In particular, we first introduce the homotopy theory used to describe the types of stable defects allowed in each phase. From here we construct the wave functions of some illustrative examples of vortices arising in both spin-1 and spin-2 condensates, and, using the spherical harmonic representation of the order parameter, visualise the properties of each vortex. There are numerous references (e.g., see [96, 97, 107, 109]) that already provide most of these results, but we reproduce them here to provide reference for subsequent chapters.

3.1 Graphical representations of spinor ground states

Graphical representations help us to visual the symmetry properties of different ground states in spinor systems. In particular, they can provide valuable insight to what is occurring within the order parameter when, e.g., topological defects form or the symmetry of the system is spontaneously broken. Here we focus on two types of graphical representation: spherical harmonics and Majorana representations. Spherical harmonics in particular are widely used in Chapter 6, where the system exhibits multiple ground states, and hence different symmetries at once. Before we discuss individual ground states in depth, we first mathematically define the different graphical representations. Then, throughout the subsequent sections we shall provide both the spherical harmonic and Majorana representations of the discussed ground states and discuss the symmetries that arise in each phase.

3.1.1 Spherical harmonic representation

We first consider the spherical harmonic representation, which maps the order parameter onto spherical harmonics using the relation

$$Z(\hat{s}) = \sum_m \zeta_m Y_f^m(\hat{s}), \tag{3.1}$$

where $\hat{s}$ is a unit vector in 3D spin space, and Y_f^m are the spherical harmonics for a spin-f state. Then, by taking a surface plot of $|Z(\hat{s})|^2$, the symmetry of the order parameter can be visualised, where the surface colour is represented by the argument of $Z(\hat{s})$.

As we shall see, the orientation of the spherical harmonics corresponds to the condensate spin, and so as the spin vector rotates, the orientation of spherical harmonics rotates to match. In addition, the colour of the spherical harmonics corresponds to the global phase, τ. Therefore, the spherical harmonics give an accurate description of the physical symmetries of the wave function, along with a pictorial representation of how the phase is changing. Throughout this thesis we will use the spherical harmonics to construct a picture of what is happening to the wave function at different locations in space, where the symmetry of the wave function can rapidly transform in a non-trivial manner (see Chapter 6). In spin-1, there are three ($f = 1$) spherical harmonics given by

$$Y_1^0(\theta,\phi) = \frac{1}{2}\sqrt{\frac{3}{\pi}}\cos\theta, \tag{3.2}$$

$$Y_1^{\pm 1}(\theta,\phi) = \frac{1}{2}\sqrt{\frac{3}{2\pi}}e^{\pm i\phi}\sin\theta, \tag{3.3}$$

and in spin-2 there are five ($f = 2$) spherical harmonics given by

$$Y_2^0(\theta,\phi) = \frac{1}{4}\sqrt{\frac{5}{\pi}}(3\cos^2\theta - 1), \tag{3.4}$$

$$Y_2^{\pm 1}(\theta,\phi) = \mp\frac{1}{2}\sqrt{\frac{15}{2\pi}}e^{\pm i\phi}\sin\theta\cos\theta, \tag{3.5}$$

$$Y_2^{\pm 2}(\theta,\phi) = \frac{1}{4}\sqrt{\frac{15}{2\pi}}e^{\pm 2i\phi}\sin^2\theta. \tag{3.6}$$

3.1.2 Majorana representation

An alternative description to visualising the symmetries of spinor BECs is through the use of the Majorana representation [110, 111], where a spin-f system can be represented as $2f$ points on the Bloch sphere. The points on the sphere are numerically calculated as the $2f$ roots z_j of the polynomial equation

$$P^{(f)}(z) = \sum_{\alpha=0}^{2f} \sqrt{\binom{2f}{\alpha}} \zeta^*_{f-\alpha} z^\alpha = 0, \tag{3.7}$$

where each root represents a stereographic mapping $z_j = \tan(\theta/2)e^{i\phi}$ of the spherical coordinates (θ, ϕ). The disadvantage of this representation, however, is that one is not able to visualise the condensate phase. The individual polynomials for both spin-1 and spin-2 systems are listed below. For the spin-1 system, we calculate the $2f = 2$ roots of the polynomial

$$P^{(1)}(z) = \zeta^*_1 z^2 + \sqrt{2}\zeta^*_0 z + \zeta^*_{-1}, \tag{3.8}$$

and for the spin-2 system we calculate the $2f = 4$ roots of the polynomial

$$P^{(2)}(z) = \zeta^*_2 z^4 + 2\zeta^*_1 z^3 + \sqrt{6}\zeta^*_0 z^2 + 2\zeta^*_{-1} z + \zeta^*_{-2}. \tag{3.9}$$

3.2 Ground states of spin-1 BECs

To obtain ground states for a spin-1 BEC, we consider the interaction part of the energy functional given as (see Sec. 2.3.3)

$$E_{\text{int}} = \frac{1}{2} \int c_0 n^2 + c_1 n^2 |\langle \hat{\mathbf{F}} \rangle|^2 \mathrm{d}^3\mathbf{r}, \tag{3.10}$$

which contains two independent non-linear interaction terms, namely the condensate density and the condensate spin. Here, $|\langle \hat{\mathbf{F}} \rangle| = \sqrt{|\langle \hat{F}_x \rangle|^2 + |\langle \hat{F}_y \rangle|^2 + |\langle \hat{F}_z \rangle|^2}$ is the magnitude of the spin expectation, where the spin vectors $\langle \hat{F}_\nu \rangle$ for $\nu = (x, y, z)$ are defined in Eq. (2.68). To simplify our analysis we assume a uniform ground state where the condensate density remains fixed, and so only the spin term remains relevant for determining ground states. This then implies that the sign of c_1 determines the energetic ground state in a spin-1 system.

In the absence of a magnetic field, the energy of a given spinor is degenerate with respect to a global U(1) phase $e^{i\tau}$ and an SO(3) spin rotation $U(\alpha, \beta, \gamma)$ parameterized by three Euler angles α, β, and γ, as

$$\zeta \to e^{i\tau} U(\alpha, \beta, \gamma)\zeta. \tag{3.11}$$

A spin rotation can be defined generally as a rotation around the $z-y-z$ axes as

$$U(\alpha,\beta,\gamma)=e^{-i\hat{F}_z\alpha}e^{-i\hat{F}_y\beta}e^{-i\hat{F}_z\gamma}. \tag{3.12}$$

For a spin-1 system the above spin rotation can be cast explicitly in matrix form [96]:

$$U(\alpha,\beta,\gamma)=\begin{pmatrix} e^{-i(\alpha+\gamma)}\cos^2\frac{\beta}{2} & -\frac{e^{-i\alpha}}{\sqrt{2}}\sin\beta & e^{-i(\alpha-\gamma)}\sin^2\frac{\beta}{2} \\ \frac{e^{-i\gamma}}{\sqrt{2}}\sin\beta & \cos\beta & -\frac{e^{i\gamma}}{\sqrt{2}}\sin\beta \\ e^{i(\alpha-\gamma)}\cos^2\frac{\beta}{2} & \frac{e^{i\alpha}}{\sqrt{2}}\sin\beta & e^{i(\alpha+\gamma)}\sin^2\frac{\beta}{2} \end{pmatrix}. \tag{3.13}$$

3.2.1 Ferromagnetic phase

Consider the case $c_1<0$, sometimes referred to as ferromagnetic interactions. Then, Eq. (3.10) is minimised when $|\langle\hat{\mathbf{F}}\rangle|$ takes its maximal value of $|\langle\hat{\mathbf{F}}\rangle|=1$. This type of ground state, where the spin is maximised, is referred to as a ferromagnetic state. The wave function of the ferromagnetic state takes the form

$$\psi=\sqrt{n}\zeta^{\mathrm{FM}}, \tag{3.14}$$

where the representative spinor, i.e., a spinor that minimises the energy, is given as [96]

$$\zeta^{\mathrm{FM}}=\begin{pmatrix}1\\0\\0\end{pmatrix}. \tag{3.15}$$

Substitution of the above spinor into the expression for the condensate spin indeed reveals that $|\langle\hat{\mathbf{F}}\rangle|=1$. Note that $\zeta^{\mathrm{FM}}=(0,0,1)^T$ is an equally valid representative spinor. However, in this case, the magnetisation now becomes negative [see Eq. (2.88)]. The general ferromagnetic wave function is constructed by applying the spin rotation in Eq. (3.13), coupled with a condensate phase, to the representative spinor as

$$\psi^{\mathrm{FM}}=\sqrt{n}e^{i\tau}U(\alpha,\beta,\gamma)\zeta^{\mathrm{FM}}=\sqrt{n}e^{i\tau'}\begin{pmatrix} e^{-i\alpha}\cos^2\frac{\beta}{2} \\ \frac{1}{\sqrt{2}}\sin\beta \\ e^{i\alpha}\sin^2\frac{\beta}{2} \end{pmatrix}, \tag{3.16}$$

where $\tau'=\tau-\gamma$, which describes all possible ferromagnetic states.

Both the spherical harmonic and Majorana representations of the spin-1 ferromagnetic ground states are shown in Fig. 3.1. We see that the ferromagnetic order parameter has an SO(2) symmetry about the direction of magnetisation, which in this case is the z-axis. The order parameter space, which describes the symmetries associated with the order parameter of the system, is $\mathscr{M}_{\mathrm{FM}}=\mathrm{SO}(3)_{\hat{\mathbf{F}},\tau}$, i.e., the full 3D rotation group, where τ and $\hat{\mathbf{F}}$ denote contributions to the symmetry from the global phase and spin, respectively.

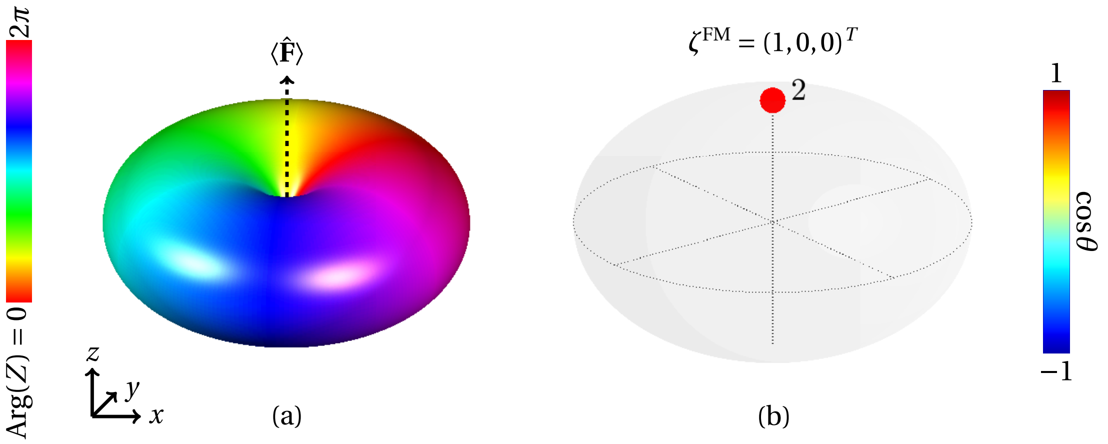

Figure 3.1: Graphical representation of the spin-1 ferromagnetic phase, with the representative spinor given by Eq. (3.15). (a): Spherical harmonic representation, $|Z(\hat{\mathbf{s}})|^2$, using Eq. (3.1), where the black dashed arrow represents the direction of the condensate magnetisation. (b): Majorana representation, where the colour of the points represent $\cos\theta = (1-|z|^2)/(1+|z|^2)$ and a number next to a point represents the root when the polynomial $P^{(1)}(z)$ has an n-multiple root.

3.2.2 Polar phase

Now consider the case of $c_1 > 0$, typically referred to as polar (or antiferromagnetic) interactions. Then, Eq. (3.10) becomes minimised by having the spin magnitude vanish $|\langle \hat{\mathbf{F}} \rangle| = 0$. For this case, the ground state is called polar, with a representative spinor given as

$$\zeta^{\mathrm{EAP}} = \begin{pmatrix} 0 \\ 1 \\ 0 \end{pmatrix}. \tag{3.17}$$

Similar to the FM case, a general polar wave function is constructed as

$$\psi^{\mathrm{P}} = \sqrt{n} e^{i\tau} U(\alpha,\beta,\gamma)\zeta^{\mathrm{EAP}} = \sqrt{n} e^{i\tau} \begin{pmatrix} -\frac{e^{-i\alpha}}{\sqrt{2}} \sin\beta \\ \cos\beta \\ \frac{e^{i\alpha}}{\sqrt{2}} \sin\beta \end{pmatrix}. \tag{3.18}$$

It is also often useful to characterise the polar state using the condensate phase and an unoriented unit vector, $\hat{\mathbf{d}} \equiv (d_x, d_y, d_z)$, referred to as the nematic director [112]. A wave function in this representation is given as

$$\psi^{\mathrm{P}} = \frac{\sqrt{n} e^{i\tau}}{\sqrt{2}} \begin{pmatrix} -d_x + i d_y \\ \sqrt{2} d_z \\ d_x + i d_y \end{pmatrix}. \tag{3.19}$$

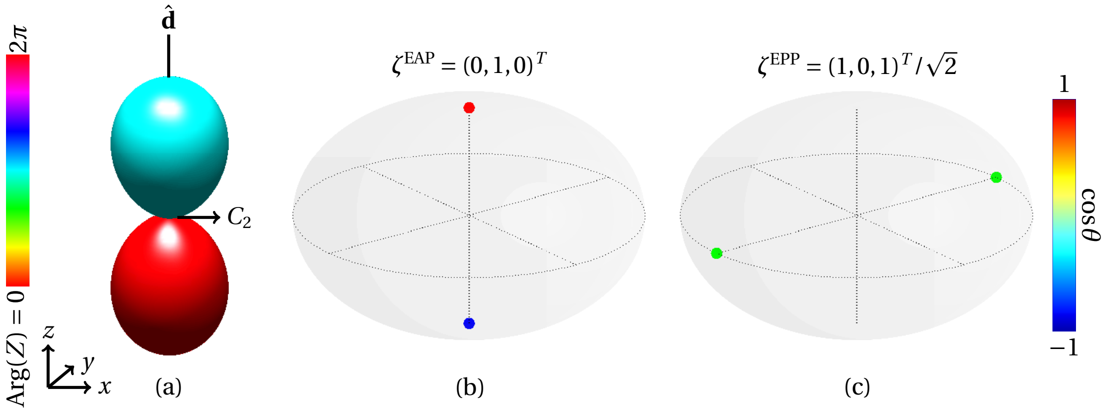

(a) (b) (c)

Figure 3.2: Graphical representation of the EAP and EPP polar ground states. (a): Spherical harmonic representation of the EAP phase, with the representative spinor given as $\zeta^{\mathrm{P}}=(0,1,0)^T$. The nematic director $\hat{\mathbf{d}}$ is aligned with the z-axis. Note that the EPP phase looks equivalent, but with the nematic director now laying in the xy-plane. The order parameter remains unchanged about π rotations about the C_2 axis coupled with a π change of the condensate phase as $\left(\hat{\mathbf{d}},\tau\right)\to\left(-\hat{\mathbf{d}},\tau+\pi\right)$. (b) and (c): Majorana representation of the EAP and EPP phase, respectively.

The nematic director can, in the absence of a magnetic field, be used to distinguish between the state given in Eq. (3.17) and an alternative representative spinor of

$$\zeta^{\mathrm{EPP}}=\frac{1}{\sqrt{2}}\begin{pmatrix}1\\0\\1\end{pmatrix}. \tag{3.20}$$

The former has the nematic director aligned with the z-axis, and is typically referred to as the easy-axis polar (EAP) phase. The latter instead has the nematic director perpendicular to the z-axis, and is either referred to as the easy-plane polar (EPP) phase or the antiferromagnetic phase. Throughout this thesis we shall prefer the term EPP when describing an unmagnetised polar spinor of the form of Eq. (3.20).

Both the spherical harmonic and Majorana representations of the EAP and EPP polar ground states are shown in Fig. 3.2. The polar state is distinguished by two nematic lobes which have a π phase difference, hence the name polar. These lobes are aligned along an axis of symmetry given by the nematic director, $\hat{\mathbf{d}}$. In the above figure, the EPP phase is distinguished from the EPP phase by having the nematic director lay in the xy-plane. There is a further axis of symmetry about the C_2 axis, about which π rotations preserve the symmetry, but not the phase. It can be seen that the order parameter will remain invariant under a change of $\zeta\left(\hat{\mathbf{d}},\tau\right)\to\zeta\left(-\hat{\mathbf{d}},\tau+\pi\right)$. The corresponding order parameter space is given as

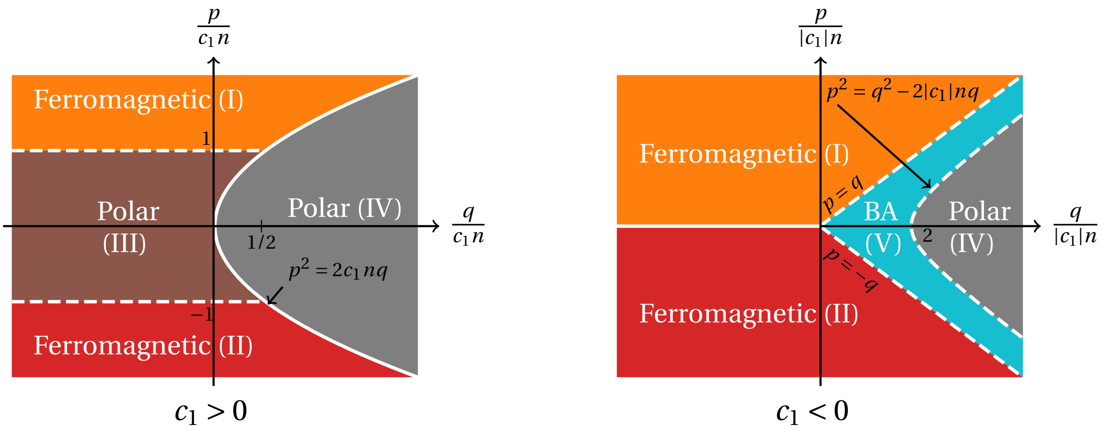

Figure 3.3: Ground state phase diagrams of spin-1 BECs for $c_1 > 0$ (left) and $c_1 < 0$ (right) interactions in a parameter space of (p, q). Solid or dashed white lines represent discontinuous and continuous phase transitions, respectively.

$\mathcal{M} = \left[S^2_{\hat{\mathbf{F}}} \times U(1)_\tau\right] / (\mathbb{Z}_2)_{\hat{\mathbf{F}},\tau}$ [96]. Note that the $\mathbb{Z}_2$ factor in the order parameter space arises from the fact that the polar order parameter described in Eq. (3.18) remains invariant under the transformation described above.

3.2.3 Ground states in the presence of magnetic fields

The presence of an external magnetic field drastically changes the ground state phase diagram of the spin-1 system. Fig. 3.3 shows the ground state phase diagram for spin-1 BECs with $c_1 > 0$ (left) and $c_1 < 0$ (right) in the presence of a magnetic field. The full derivation of the ground state phase diagram can be found in reviews [96, 97]. There are five total ground states shown in Fig. 3.3, which are summarised in Table 3.1.

There exists a fully magnetised ferromagnetic state with $\zeta = (1,0,0)^T$ and $\langle \hat{F}_z \rangle = 1$ (state I) or $\zeta = (0,0,1)^T$ and $\langle \hat{F}_z \rangle = -1$ (state II), depending on the sign of the linear Zeeman shift p. A non-magnetised polar phase (state IV) arises with $\zeta = (0,1,0)^T$ and $\langle \hat{F}_z \rangle = 0$. For polar interactions $c_1 > 0$, there exists a partially-magnetised polar phase (state III) with

$$\zeta^{\text{PMP}} = \left(\sqrt{\frac{1 + p/(c_1 n)}{2}}, 0, \sqrt{\frac{1 - p/(c_1 n)}{2}}\right)^T, \tag{3.21}$$

and $\langle \hat{F}_z \rangle = p/(c_1 n)$. At $p = 0$, this state transforms into the non-magnetised EPP phase given in Eq. (3.20), equivalent to state IV with the nematic director in the xy-plane. As $p \to \pm c_1 n$ this state tends toward the ferromagnetic states I or II, respectively. Finally, a broken-axisymmetry

Ground state	Spinor, ζ^T	$\langle\hat{F}_z\rangle$
Ferromagnetic (I)	$(1,0,0)$	1
Ferromagnetic (II)	$(0,0,1)$	-1
Polar (III)	$\left(\sqrt{\frac{1+p(c_1n)}{2}},0,\sqrt{\frac{1-p(c_1n)}{2}}\right)$	$\frac{p}{c_1n}$
Polar (IV)	$(0,1,0)$	0
Broken-axisymmetry (V)	Eq. (3.22)	$\frac{p(-p^2+q^2+2qc_1n)}{2c_1nq^2}$

Table 3.1: Summary of the ground state phases in a spin-1 BEC with their respective spinors and magnetisation.

(BA) phase (state V) occurs in a condensate with $c_1 > 0$ which has a spinor of the form

$$\begin{aligned}\zeta^{\mathrm{BA}}_{\pm1} &= \frac{q\pm p}{2q}\sqrt{\frac{-p^2+q^2+2c_1nq}{2c_1nq}},\\ \zeta^{\mathrm{BA}}_{0} &= \sqrt{\frac{(q^2-p^2)(-p^2-q^2+2c_1nq)}{4c_1nq^3}}.\end{aligned} \tag{3.22}$$

This corresponds to a magnetisation that tilts against the quantisation axis, given by

$$\langle\hat{F}_z\rangle = \frac{p(-p^2+q^2+2qc_1n)}{2c_1nq^2}. \tag{3.23}$$

These five ground states fully encapsulate the phase diagram of spin-1 BECs in a magnetic field.

The spherical harmonic representations of the partially-magnetised polar (state III) and broken-axisymmetry (state V) phases are shown in Fig. 3.4. For the partially-magnetised polar state, we see the effect of the linear Zeeman shift breaking the symmetry of the spin when compared to the polar state shown in Fig. 3.2a. The broken-axisymmetry phase is seen to tilt against the z-axis, which arises due to the linear Zeeman shift, p.

3.3 Ground states of spin-2 BECs

To find the ground states of a spin-2 system we follow a similar procedure to the spin-1 case. The interacting part of the spin-2 Hamiltonian reads (see Sec. 2.3.3)

$$E_{\mathrm{int}} = \frac{1}{2}\int c_0n^2 + c_1n^2|\langle\hat{\mathbf{F}}\rangle|^2 + c_2n^2|A_{00}|^2\mathrm{d}^3\mathbf{r}. \tag{3.24}$$

As before, we assume a uniform ground state so that the density remains fixed. Therefore, different ground states arise from the competition between the spin-dependent, c_1, and singlet-dependent, c_2, interaction strengths. The magnitude of the spin expectation is now defined

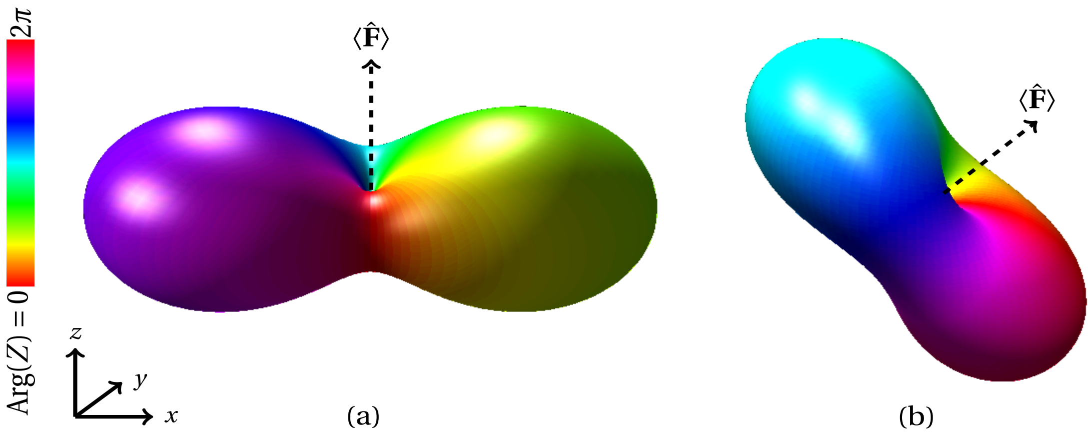

(a) (b)

Figure 3.4: Spherical harmonics representation of both the partially-magnetised polar state and the broken-axisymmetry phase calculated using the appropriate representative spinor in Eq. (3.1). (a): The partially-magnetised polar state given by Eq. (3.21) with $p \neq 0$. Note that for this state the direction of the spin vector is aligned with the applied magnetic field. (b): The broken-axisymmetry state given by Eq. (3.22) with $p, q \neq 0$. The direction of the spin vector is tilted away from the magnetic field axis, which is assumed to be along the z-axis.

in terms of the spin-2 spin vectors given in Eqs. (2.81) and (2.82), and the spin-singlet pair amplitude, A_{00}, given in Eq. (2.83).

As in the spin-1 case, the energy of a given spinor in the absence of a magnetic field is degenerate following the application of a global $U(1)$ phase and an $SO(3)$ spin rotation. In a spin-2 system, a general spin rotation is instead represented as a 5×5 matrix of the form [96]

$$U(\alpha,\beta,\gamma) =$$
$$\begin{pmatrix} e^{-2i(\alpha+\gamma)}C^4 & -2e^{-i(2\alpha+\gamma)}C^3S & \sqrt{6}e^{-2i\alpha}C^2S^2 & -2e^{-i(2\alpha-\gamma)}CS^3 & e^{-2i(\alpha-\gamma)}S^4 \\ 2e^{-i(\alpha+2\gamma)}C^3S & e^{-i(\alpha+\gamma)}C^2(C^2-3S^2) & -\sqrt{\frac{3}{8}}e^{-i\alpha}\sin 2\beta & -e^{-i(\alpha-\gamma)}S^2(S^2-3C^2) & -2e^{-i(\alpha-2\gamma)}CS^3 \\ \sqrt{6}e^{-2i\gamma}C^2S^2 & \sqrt{\frac{3}{8}}e^{-i\gamma}\sin 2\beta & \frac{1}{4}(1+3\cos 2\beta) & -\sqrt{\frac{3}{8}}e^{-i\gamma}\sin 2\beta & \sqrt{6}e^{2i\gamma}C^2S^2 \\ 2e^{i(\alpha-2\gamma)}CS^3 & -e^{i(\alpha-\gamma)}S^2(S^2-3C^2) & \sqrt{\frac{3}{8}}e^{i\alpha}\sin 2\beta & e^{i(\alpha-\gamma)}C^2(C^2-3S^2) & -2e^{i(\alpha+2\gamma)}C^3S \\ e^{2i(\alpha-\gamma)}C^4 & 2e^{i(2\alpha-\gamma)}CS^3 & \sqrt{6}e^{2i\alpha}C^2S^2 & 2e^{i(2\alpha+\gamma)}C^3S & e^{2i(\alpha+\gamma)}C^4 \end{pmatrix}, \tag{3.25}$$

where $S \equiv \sin(\beta/2)$ and $C \equiv \cos(\beta/2)$.

The ground states of the spin-2 system in a parameter space of (c_1, c_2) are summarised in Fig. 3.5. In the following subsections we shall discuss each phase individually, along with their respective graphical representations and order parameter spaces. Note, for the case of $c_1, c_2 < 0$, there is a competition between the ferromagnetic and nematic phases. For this case, the energy functional is minimised by either having maximal spin density and $|A_{00}|^2 = 0$

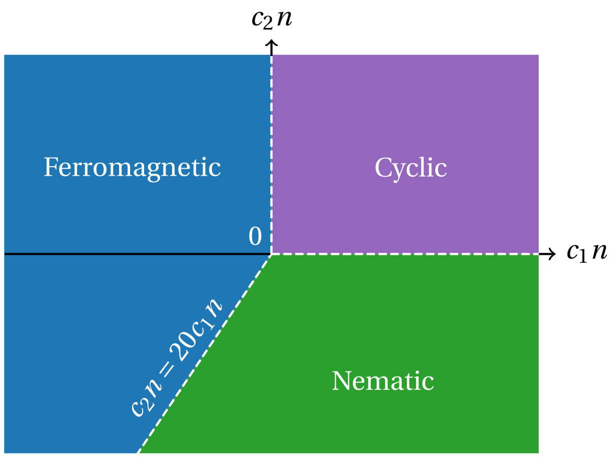

Figure 3.5: Ground state phase diagram for spin-2 BECs in a parameter space of (c_1, c_2) in the absence of a magnetic field. White dashed lines indicate a first-order phase transition region between the phases.

as in the ferromagnetic phase, or by having minimal spin density and $|A_{00}|^2 = 1/5$ as in the nematic phase, which leads to a phase boundary at $c_2 n = 20 c_1 n$ (see below).

3.3.1 Ferromagnetic phase

If we first consider $c_1 < 0$ and $c_2 > 0$, then the energy functional is minimised when the spin density is maximised, $|\langle \hat{\mathbf{F}} \rangle| = 2$, and the singlet-duo amplitude is minimised, $|A_{00}| = 0$. This state is denoted as the spin-2 ferromagnetic phase, where $|\langle \hat{\mathbf{F}} \rangle|$ is now $|\langle \hat{\mathbf{F}} \rangle| = 2$ for this ground state, as opposed to $|\langle \hat{\mathbf{F}} \rangle| = 1$ in the spin-1 system. Note that there exists a ferromagnetic state in a spin-2 BEC with $|\langle \hat{\mathbf{F}} \rangle| = 1$, but this state is not the ground state since the $|\langle \hat{\mathbf{F}} \rangle| = 2$ state has lower energy. To avoid confusion, we refer to the ferromagnetic state with $|\langle \hat{\mathbf{F}} \rangle| = 2$ as the FM_2 state, and the state with $|\langle \hat{\mathbf{F}} \rangle| = 1$ as the FM_1 state. It should be noted, however, that the FM_1 state can remain stable in certain situations, such as in the cores of vortices (see Chapter 6). The representative spinors for the spin-2 ferromagnetic states have the form

$$\zeta^{\text{FM}_2} = \begin{pmatrix} 1 \\ 0 \\ 0 \\ 0 \\ 0 \end{pmatrix}, \qquad \zeta^{\text{FM}_1} = \begin{pmatrix} 0 \\ 1 \\ 0 \\ 0 \\ 0 \end{pmatrix}. \tag{3.26}$$

Following the same procedure as the spin-1 case, applying a general spin rotation $U(\alpha, \beta, \gamma)$ with a global phase τ and condensate density n yields the general FM_2 wave function which

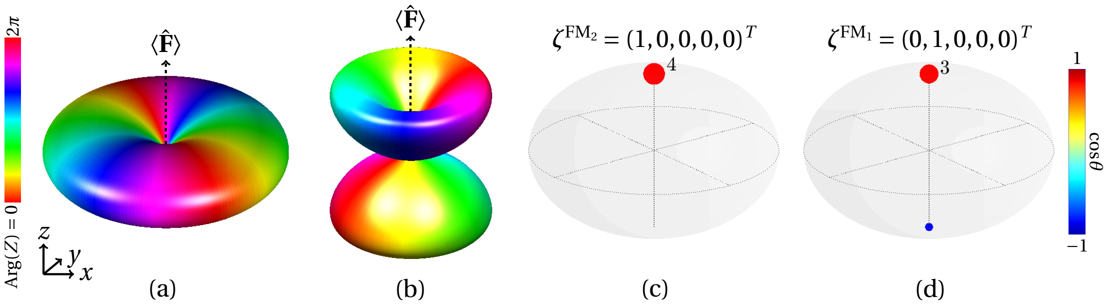

Figure 3.6: Spherical harmonic and Majorana representations of the spin-2 ferromagnetic ground states, with representative spinors given in Eq. (3.26). (a) and (b): Spherical harmonic representation for the ferromagnetic states with $|\langle\hat{\mathbf{F}}\rangle| = 2$ and $|\langle\hat{\mathbf{F}}\rangle| = 1$, respectively, where the dashed line represents the direction of the magnetisation. (c) and (d): Equivalent Majorana representations.

describes all ferromagnetic states that have $|\langle\hat{\mathbf{F}}\rangle| = 2$ in a spin-2 system:

$$\psi^{\mathrm{FM}_2} = \sqrt{n}e^{i(\tau-2\gamma)}\begin{pmatrix} e^{-2i\alpha}\cos^4\frac{\beta}{2} \\ 2e^{-i\alpha}\cos^3\frac{\beta}{2}\sin\frac{\beta}{2} \\ \sqrt{6}\cos^2\frac{\beta}{2}\sin^2\frac{\beta}{2} \\ 2e^{i\alpha}\cos\frac{\beta}{2}\sin^3\frac{\beta}{2} \\ e^{2i\alpha}\sin^4\frac{\beta}{2} \end{pmatrix}. \tag{3.27}$$

Equivalently, the general spinor for the FM_1 phase is given as

$$\zeta^{\mathrm{FM}_1} = \sqrt{n}e^{i(\tau-\gamma)}\begin{pmatrix} -2e^{-2i\alpha}\cos^3\frac{\beta}{2}\sin\frac{\beta}{2} \\ e^{-i\alpha}\cos^2\frac{\beta}{2}\left[\cos^2\frac{\beta}{2}^2 - 3\sin^2\frac{\beta}{2}\right] \\ \sqrt{\frac{3}{8}}\sin 2\beta \\ -e^{i\alpha}\sin^2\frac{\beta}{2}\left[\sin^2\frac{\beta}{2} - 3\cos^2\frac{\beta}{2}\right] \\ 2e^{2i\alpha}\cos\frac{\beta}{2}\sin^3\frac{\beta}{2} \end{pmatrix}. \tag{3.28}$$

Fig. 3.6 shows the spherical harmonic and Majorana representations of the spin-2 ferromagnetic ground states. It is clear from Figs 3.6a, b that the ferromagnetic order parameters have the same SO(2) symmetry about the direction of the magnetisation as in the spin-1 case. However, the difference between the FM_2 phase of the spin-2 system and the FM phase of the spin-1 system is apparent in the phase: the FM_2 state winds by 4π about the spherical harmonic as opposed to 2π (see Fig. 3.1). Therefore, the order parameter space of the FM_2 phase is slightly different, and given as $\mathscr{M}_{\mathrm{FM}_2} = \mathrm{SO}(3)_{\hat{\mathbf{F}},\tau}/(\mathbb{Z}_2)_{\hat{\mathbf{F}},\tau}$. The $(\mathbb{Z}_2)_{\hat{\mathbf{F}},\tau}$ factor arises from the double winding of the condensate phase seen above.

3.3.2 Nematic phases

Instead, let us now consider the case of $c_1 > 0$ and $c_2 < 0$. We see that the energy functional is minimised when the spin is minimised, $|\langle\hat{\mathbf{F}}\rangle| = 0$, but the singlet-duo amplitude is maximised, $|A_{00}|^2 = 1/5$. Such a state is called nematic, and takes two forms: the uniaxial nematic (UN) or biaxial nematic (BN), depending on the sign of the quadratic Zeeman shift, q. A representative spinor for the UN state, where the nematic director $\hat{\mathbf{d}}$ is aligned along the z-axis, is given as

$$\zeta^{\mathrm{UN}} = \begin{pmatrix} 0 \\ 0 \\ 1 \\ 0 \\ 0 \end{pmatrix}, \tag{3.29}$$

and a representative spinor for the BN state reads

$$\zeta^{\mathrm{BN}} = \frac{1}{\sqrt{2}} \begin{pmatrix} 1 \\ 0 \\ 0 \\ 0 \\ 1 \end{pmatrix}. \tag{3.30}$$

Applying a general spin rotation and condensate phase leads to the general wave functions for the UN and BN states, respectively, as

$$\psi^{\mathrm{UN}} = \frac{\sqrt{6n}}{4} e^{i\tau} \begin{pmatrix} e^{-2i\alpha} \sin^2\beta \\ -2e^{-i\alpha} \sin\beta\cos\beta \\ \sqrt{\frac{2}{3}}(3\cos^2\beta - 1) \\ 2e^{i\alpha} \sin\beta\cos\beta \\ e^{2i\alpha} \sin^2\beta \end{pmatrix}, \tag{3.31}$$

$$\psi^{\mathrm{BN}} = \sqrt{\frac{n}{2}} e^{i\tau} \begin{pmatrix} e^{-2i\alpha} \left[\left(1 - \frac{1}{2}\sin^2\beta\right)\cos 2\gamma - i\cos\beta\sin 2\gamma\right] \\ e^{-i\alpha} \sin\beta(\cos\beta\cos 2\beta - i\sin 2\gamma) \\ \sqrt{\frac{3}{2}} \sin^2\beta\cos 2\gamma \\ -e^{i\alpha} \sin\beta(\cos\beta\cos 2\gamma + i\sin 2\gamma) \\ e^{2i\alpha} \left[\left(1 - \frac{1}{2}\sin^2\beta\right)\cos 2\gamma + i\cos\beta\sin 2\gamma\right] \end{pmatrix}. \tag{3.32}$$

In the absence of a magnetic field, these two states are degenerate. However, a quadratic Zeeman shift, q, can be used to manipulate the system into choosing one or the other, since

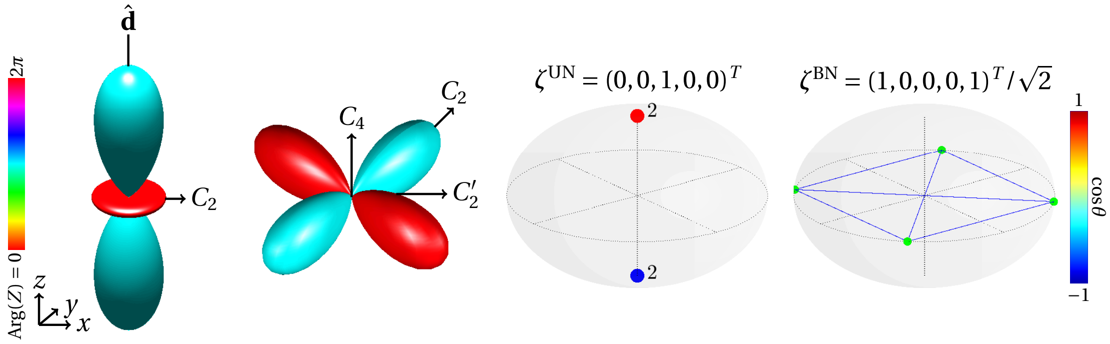

(a) (b) (c) (d)

Figure 3.7: Spherical harmonic and Majorana representations of the spin-2 nematic ground states. (a): Spherical harmonic representation of the uniaxial nematic spinor given in Eq. (3.29) where $\hat{\mathbf{d}}$ is the nematic director. The order parameter exhibits a two-fold symmetry about the C_2 axis. (b) Spherical harmonic representation of the biaxial nematic state given by Eq. (3.30) which has a four-fold symmetry about the C_4 axis, and two additional two-fold symmetries about the C_2, C_2' axes. (c) and (d): Equivalent Majorana representations.

the energies of each ground state now change (energetic stability of these states is discussed in Sec. 6.2.1).

The spherical harmonics and Majorana representation of both nematic states are plotted in Fig. 3.7. The UN phase is seen to differ slightly from the polar phase of spin-1 (see Fig. 3.2a) in that the nematic lobes have the same phase. This implies that a π spin rotation about the C_2 axis leaves the order parameter unchanged, and no appropriate transformation of the condensate phase has to occur. In addition, this order parameter also has an $SO(2)$ symmetry about the nematic director. The order parameter space for this phase is then calculated as $\left[S^2_{\hat{\mathbf{F}}} \times U(1)_\tau\right]/(\mathbb{Z}_2)_{\hat{\mathbf{F}}}$. This is identical to the polar phase of the spin-1 BEC, except now the $(\mathbb{Z}_2)_{\hat{\mathbf{F}}}$ arises only from the condensate spin due to the nematic lobes having the same phase. The BN phase, shown in Fig. 3.7b, breaks the SO(2) symmetry due to the perpendicular nematic lobes, which have a π phase difference. The symmetry of the order parameter is preserved under $\pi/4$ rotations about the C_4 axis and π rotations about both the C_2 and C_2' axes. The order parameter space for this phase is calculated as $\left[\mathrm{U}(1)_\tau \times \mathrm{SO}(3)_{\hat{\mathbf{F}}}\right]/(\mathrm{D}_4)_{\hat{\mathbf{F}},\tau}$, where D_4 is the fourth dihedral group [113].

3.3.3 Cyclic phase

Now consider $c_1, c_2 > 0$. The energy functional is minimised when both the spin magnitude and singlet-duo amplitude is minimised: $|\langle\hat{\mathbf{F}}\rangle| = 0, |A_{00}|^2 = 0$. Such a state is referred to as the cyclic state and has the representative spinor

$$\zeta^{\mathrm{C}_1} = \frac{1}{2}\begin{pmatrix} 1 \\ 0 \\ i\sqrt{2} \\ 0 \\ 1 \end{pmatrix}. \tag{3.33}$$

The general wave function is calculated as

$$\psi^{\mathrm{C}} = \frac{\sqrt{n}}{2} e^{i\tau} \begin{pmatrix} e^{-2i(\alpha+\gamma)} C^4 + 2i\sqrt{3} e^{-2i\alpha} C^2 S^2 + e^{-2i(\alpha-\gamma)} S^4 \\ 2e^{-i(\alpha+2\gamma)} C^3 S - \frac{\sqrt{3}}{2} i e^{-i\alpha} \sin 2\beta - 2e^{-i(\alpha-2\gamma)} C S^3 \\ \sqrt{6} e^{-2i\gamma} C^2 S^2 + i\frac{\sqrt{2}}{4}(1 + 3\cos 2\beta) + \sqrt{6} e^{2i\gamma} C^2 S^2 \\ 2e^{i(\alpha-2\gamma)} C S^3 + \frac{\sqrt{3}}{2} i e^{i\alpha} \sin 2\beta - 2e^{i(\alpha+2\gamma)} C^3 S \\ e^{2i(\alpha-\gamma)} S^4 + 2i\sqrt{3} e^{2i\alpha} C^2 S^2 + e^{2i(\alpha+\gamma)} C^4 \end{pmatrix}. \tag{3.34}$$

In addition to the three-component cyclic state, there is also a two-component cyclic state that is useful for understanding the general cyclic state:

$$\zeta^{\mathrm{C}_2} = \frac{1}{\sqrt{3}}\begin{pmatrix} 1 \\ 0 \\ 0 \\ \sqrt{2} \\ 0 \end{pmatrix}, \tag{3.35}$$

which is obtained from Eq. (3.33) via the spin rotation [96]

$$\zeta^{\mathrm{C}_2} = -i e^{i\frac{\pi}{4}\hat{F}_z} \exp\left[i\frac{\hat{F}_x - \hat{F}_y}{\sqrt{2}} \arccos\left(\frac{1}{\sqrt{3}}\right)\right] \zeta^{\mathrm{C}_1}. \tag{3.36}$$

The spherical harmonic and Majorana representations of both orientations of the cyclic state are plotted in Fig. 3.8. The cyclic order parameter has the symmetry of a tetrahedron, where each nematic lobe has a two-fold symmetry about each C_2 axis. Furthermore, the order parameter has a three-fold symmetry about the C_3 axis, of which $2\pi/3$ rotations about this axis preserve the symmetry of the order parameter. In Fig. 3.8a, this axis is the $(1,1,1)$-axis, whereas in Fig. 3.8b the three-fold axis of symmetry is the z-axis. The order parameter space of the cyclic phase can be written as $\left[\mathrm{U}(1)_\tau \times \mathrm{SO}(3)_{\hat{\mathbf{F}}}\right]/\mathrm{T}_{\hat{\mathbf{F}},\tau}$ [96], where $\mathrm{T}_{\hat{\mathbf{F}},\tau}$ is the tetrahedral group [113].

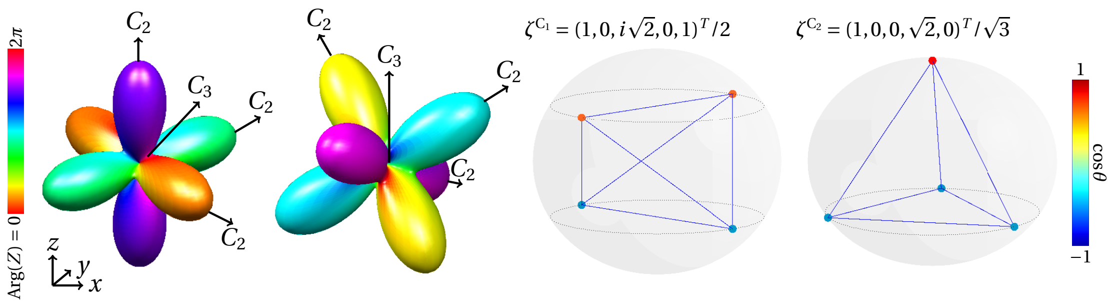

(a) (b) (c) (d)

Figure 3.8: Spherical harmonic and Majorana representations of two different orientations of the spin-2 cyclic ground state. (a): Cyclic state given by Eq. (3.33) which has a two- and three-fold symmetry about the C_2, C_3 axes, respectively. (b): Alternative, two-component cyclic state, given by Eq. (3.35) which is obtained from (a) by the spin rotation given in Eq. (3.36). (c) and (d): Equivalent Majorana representations.

3.4 Topologically stable defects in spinor BECs

Due to their rich phase diagrams discussed in the previous sections, spinor BECs give rise to multiple different types of topological defects. Such defects range from vortices, both singular [45, 48, 50, 54, 57, 88–90, 114–116], including singular fractional vortices [40, 41, 48, 50, 54, 89, 90, 116–120], and nonsingular [10, 11, 46, 49, 51, 88, 121–124], to point defects such as monopoles [112, 125–131].

The types of topologically stable defects within a given system can be found from a group-theoretical approach using homotopy theory [93, 96]. The theory states that the nth homotopy group, π_n, classifies topological excitations with dimension of homotopy n, where $n = d - \nu - 1$ for singular excitations and $n = d - \nu$ for nonsingular excitations [113]. Here, d and ν describe the dimensionality of the system and the dimensionality of the excitation, respectively. To calculate whether a given defect is stable in a particular system, one needs to first find the relevant order parameter space, $\mathcal{M}$, that describes the symmetries associated with the order parameter of that system. Then, calculating a given homotopy group, $\pi_n(\mathcal{M})$, states whether the types of topological defects described by π_n are stable in that order parameter space. For example, given an order parameter space $\mathcal{M}$, one can calculate whether point defects ($n = 2$) are stable within the system by seeing if $\pi_2(\mathcal{M}) \neq 0$. Homotopy groups and the topological excitations they describe are listed in Table 3.2 [96].

In this section, we list the order parameter space for each ground state in both spin-1 and spin-2 systems, which we then use to deduce the possible stable defect structures in each phase by calculating the homotopy groups of the space.

π_n	Defects	Solitons
π_1	Vortices	Nonsingular domain walls
π_2	Monopoles	2D Skyrmions
π_3		(3D) Skyrmions, knots

Table 3.2: A list of different homotopy groups and the corresponding topological defects/solitons they describe [96].

Spin-1 phase	$\mathscr{M}$	π_1	π_2	π_3
Polar	$\left[S^2_{\hat{\mathbf{F}}} \times U(1)_\tau\right] / (\mathbb{Z}_2)_{\hat{\mathbf{F}},\tau}$	$\mathbb{Z}$	$\mathbb{Z}$	$\mathbb{Z}$
Ferromagnetic	$\mathrm{SO}(3)_{\hat{\mathbf{F}},\tau}$	$\mathbb{Z}_2$	0	$\mathbb{Z}$

Table 3.3: Spin-1 phases and their relative order parameter space, $\mathscr{M}$ along with the corresponding first (π_1), second (π_2), and third (π_3) homotopy groups [113]. Here, $\hat{\mathbf{F}}$ and τ indicate contributions from the condensate spin and phase, respectively.

3.4.1 Homotopy groups for a spin-1 system

Recall that a spin-1 system has two phases in the absence of a magnetic field: ferromagnetic and polar. The order parameter space and the first three homotopy groups for these phases are calculated and listed in Table 3.3 [93, 96, 113].

We start with the polar phase, with the representative spinor defined as in Eq. (3.18). The first homotopy group is calculated to be the additive group of integers, $\pi_1(\mathscr{M}_{\text{polar}}) = \mathbb{Z}$, which indicates vortices are stable and classified by integers within this phase. It is worth noting that the first homotopy group for a scalar BEC system, which has an order parameter space of $\mathscr{M}_{\text{scalar}} = \mathrm{U}(1)$, is the same: $\pi_1(\mathscr{M}_{\text{scalar}}) = \mathbb{Z}$. However, due to the $\mathbb{Z}_2$ symmetry, the minimum unit of circulation becomes half that of a scalar U(1) vortex, giving rise to what are known as half-quantum vortices (HQVs) [96] (see Sec. 3.5.1). In addition, the polar phase supports stable point defects since $\pi_2(\mathscr{M}_{\text{UN}}) = \mathbb{Z}$, where the point defects are classified by integers.

The FM phase, described generally by Eq. (3.16), has an order parameter space consisting of the full 3D rotation group: $\mathscr{M}_{\text{FM}} = \mathrm{SO}(3)_{\hat{\mathbf{F}},\tau}$. This leads to a first homotopy group of $\pi_1(\mathscr{M}_{\text{FM}}) = \mathbb{Z}_2$, which states that vortices are classified one of two ways in this phase. One class represents singular vortices and the other nonsingular, where the vortex is classified by a fountain-like texture of the condensate spin vector (see Sec. 3.5.1). Additionally, unlike the polar phase, the FM phase does not support stable point defects since $\pi_2(\mathscr{M}_{\text{FM}}) = 0$.

Spin-2 phase	$\mathscr{M}$	π_1	π_2	π_3
Uniaxial nematic	$\left[S^2_{\hat{\mathbf{F}}} \times U(1)_\tau\right] / (\mathbb{Z}_2)_{\hat{\mathbf{F}}}$	$\mathbb{Z} \times \mathbb{Z}_2$	$\mathbb{Z}$	$\mathbb{Z}$
Biaxial nematic	$\left[\mathrm{U}(1)_\tau \times \mathrm{SO}(3)_{\hat{\mathbf{F}}}\right] / (\mathrm{D}_4)_{\hat{\mathbf{F}},\tau}$	$\mathbb{Z} \times_h (\mathrm{D}^*_4)_{\hat{\mathbf{F}}}$	0	$\mathbb{Z}$
Cyclic	$\left[\mathrm{U}(1)_\tau \times \mathrm{SO}(3)_{\hat{\mathbf{F}}}\right] / \mathrm{T}_{\hat{\mathbf{F}},\tau}$	$\mathbb{Z} \times_h \mathrm{T}_{\hat{\mathbf{F}},\tau}$	0	$\mathbb{Z}$
Ferromagnetic	$\mathrm{SO}(3)_{\hat{\mathbf{F}},\tau} / (\mathbb{Z}_2)_{\hat{\mathbf{F}},\tau}$	$\mathbb{Z}_4$	0	$\mathbb{Z}$

Table 3.4: Spin-2 phases and their relative order parameter space, $\mathscr{M}$, along with the corresponding first (π_1), second (π_2), and third (π_3) homotopy groups. Here, $\hat{\mathbf{F}}$, τ indicate contributions from the condensate spin and phase, respectively. Additionally, D_4 and T represent the fourth dihedral and tetrahedral groups, respectively, and a $*$ denotes a lift of that particular group [93]. Finally, $\times_h$ is the h-product (see [113] for details).

3.4.2 Homotopy groups for a spin-2 system

As shown in Sec. 3.3, spin-2 BECs have a richer phase diagram, and with that an even richer family of topological defects. The order parameter spaces along with the first three homotopy groups are given in Table 3.4 [93, 96, 113].

Firstly, note that the order parameter space for the FM phase is slightly different from the spin-1 case in that it is now divided by a $(\mathbb{Z}_2)_{\hat{\mathbf{F}},\tau}$ factor. This contribution arises from the double winding of the condensate phase seen in the spherical harmonic representation in Fig. 3.6a. The first homotopy group is also different, allowing now for an additional two classes of line defects as $\pi_1(\mathscr{M}_{\mathrm{FM}}) = \mathbb{Z}_4$, but the second and third homotopy groups are the same.

The UN phase has an identical order parameter space to the polar phase of a spin-1 BEC, except now the $(\mathbb{Z}_2)_{\hat{\mathbf{F}}}$ factor arises only from the condensate spin since the nematic lobes are no longer π out of phase (see Fig. 3.7a and Fig. 3.2b). In addition, the first homotopy group differs slightly as now it reads $\pi_1(\mathscr{M}_{\mathrm{UN}}) = \mathbb{Z} \times \mathbb{Z}_2$ [113], which allows for the creation of additional types of line defects such as spin vortices, which are vortices which carry no mass circulation, but instead only carry a circulation of the condensate spin (see Sec. 3.5.2).

The BN phase has an order parameter space of $\left[\mathrm{U}(1)_\tau \times \mathrm{SO}(3)_{\hat{\mathbf{F}}}\right] / (\mathrm{D}_4)_{\hat{\mathbf{F}},\tau}$, where D_4 is the fourth dihedral group [113]. This leads to a first homotopy group that is non-Abelian: $\pi_1(\mathscr{M}_{\mathrm{BN}}) = \mathbb{Z} \times_h (\mathrm{D}^*_4)_{\hat{\mathbf{F}}}$, where $\times_h$ is the h-product (see [113] for details). A non-Abelian group, by definition, has members which do not commute [93], which implies that the BN phase can host non-Abelian vortices, i.e., vortices whose topological charges do not commute. A reconnection between two non-Abelian vortices leaves a trace of the reconnection in the form of a rung vortex [93].

The cyclic phase has an order parameter space of $\mathscr{M}_{\mathrm{C}} = \left[\mathrm{U}(1)_\tau \times \mathrm{SO}(3)_{\hat{\mathbf{F}}}\right] / \mathrm{T}_{\hat{\mathbf{F}},\tau}$, where $\mathrm{T}_{\hat{\mathbf{F}},\tau}$

is the tetrahedral group [113]. Like the BN phase, this leads to a non-Abelian fundamental group: $\pi_1(\mathscr{M}_{\mathrm{C}}) = \mathbb{Z} \times_h \mathrm{T}_{\hat{\mathbf{F}},\tau}$, and hence the cyclic phase also supports non-Abelian vortices. One class of non-Abelian vortex is the fractional vortex, where the mass circulation is quantised in different fractional units to other fractional vortices arising in, e.g., the BN phase (see Sec. 3.5.2).

3.5 Spinor vortices and their hydrodynamic properties

The properties of a vortex can be characterised by determining how the order parameter changes on a loop, C, encircling the vortex. Let us first take the example of a scalar BEC, described by the order parameter $\psi = \sqrt{n}e^{i\tau}$ for condensate density n and phase τ. The superfluid velocity, $\mathbf{v}$, for a scalar system with atomic mass M is [132]

$$n\mathbf{v} = \frac{\hbar}{2Mi}\left(\psi^*\nabla\psi - (\nabla\psi^*)\psi\right), \tag{3.37}$$

which, upon substitution of the general scalar order parameter into the above, leads to the relation $\mathbf{v} = (\hbar/M)\nabla\tau$. The mass circulation is then calculated as the integral of the superfluid velocity around the loop as [132]

$$\oint_C \mathbf{v}\cdot \mathrm{d}\ell = \frac{\hbar}{M}\oint_C \nabla\tau\cdot\mathrm{d}\ell, \tag{3.38}$$

where $\mathrm{d}\ell$ is the line element of integration. The single-valuedness of the wave function states that $\psi(r_0) = \psi(r_1)$, where r_0, r_1 are points denoting the start and the end of the loop, respectively. This implies that the change in phase around the loop is $\Delta\tau = 2\pi n_w$, where $n_w \in \mathbb{Z}$, showing that the circulation is quantised in scalar BECs, with the unit of circulation given as $\kappa = h/M$. For $n_w \neq 0$ a phase defect arises, where at a point in space the phase simultaneously takes on every value and therefore, to avoid this singularity, the density must vanish at this point.

In spinor BECs, the situation becomes more complex. Consider the general spinor wave function given as $\psi = \sqrt{n}e^{i\tau}U(\alpha,\beta,\gamma)\zeta_{\mathrm{rep}}$, where the spin rotation $U(\alpha,\beta,\gamma)$ is defined in Eq. (3.12) and ζ_{rep} is a representative spinor. If we consider a closed loop in space with the start and end points denoted r_0 and r_1, respectively, then the single-valuedness condition for the wave function of a spinor BEC states [96]

$$\sqrt{n(r_0)}e^{i\tau(r_0)}U(\alpha(r_0),\beta(r_0),\gamma(r_0))\zeta_{\mathrm{rep}}(r_0) = \sqrt{n(r_1)}e^{i\tau(r_1)}U(\alpha(r_1),\beta(r_1),\gamma(r_1))\zeta_{\mathrm{rep}}(r_1). \tag{3.39}$$

Following a similar procedure as the scalar case, the superfluid velocity for a spin-f system, $\mathbf{v}_s$, is given as [96]:

$$n\mathbf{v}_s = \frac{\hbar}{2Mi}\sum_{m=-f}^{f}\left(\psi_m^*\nabla\psi_m - (\nabla\psi_m^*)\psi_m\right). \tag{3.40}$$

Substituting the general spinor wave function into the above equation yields the following expression for the superfluid velocity

$$\mathbf{v}_s = \frac{\hbar}{M}\left[\nabla\tau - |\hat{\mathbf{F}}|(\cos\beta\nabla\alpha + \nabla\gamma)\right]. \tag{3.41}$$

When $|\hat{\mathbf{F}}| = 0$, as is the case for non-ferromagnetic ground states in spin-1 and spin-2 BECs, then the superfluid velocity results in $\mathbf{v}_s = (\hbar/M)\nabla\tau$, similar to the scalar BEC case. This implies circulation is quantised in these phases, but as we shall see, the circulation can be quantised in fractional units of κ. On the other hand, Eq. (3.41) implies that $\nabla\times\mathbf{v}_s \neq 0$ when $|\hat{\mathbf{F}}| \neq 0$ due to the $\cos\beta\nabla\alpha$ term. Hence, ferromagnetic spinor BECs do not have quantised mass circulation, which can lead to some interesting vortex structures such as coreless vortices (see the below sections).

3.5.1 Vortices in spin-1 systems

Here, we analytically construct wave functions corresponding to different classes of vortices arising in spin-1 condensates, and investigate their properties using spherical harmonics. We begin with the polar phase, and construct a wave function that corresponds to a HQV. If we consider a vortex that is oriented along the z-axis, and the nematic director is oriented in the (x,y)-plane, then such a vortex corresponds to the choice of $\tau = \alpha = \varphi/2$ and $\beta = \pi/2$ in Eq. (3.18) to yield the wave function

$$\psi^{\mathrm{P}}_{\mathrm{hqv}} = \sqrt{\frac{n}{2}}\begin{pmatrix}-1\\0\\e^{i\varphi}\end{pmatrix}, \tag{3.42}$$

where φ is the azimuthal angle about the vortex core. Similar, but topologically distinct vortices arise in the A phase of superfluid ^{3}He [81, 133]. In experiment, for the vortex constructed as in Eq. (3.42), the vortex consists of density depletion along the core in the ψ_{-1} component, where the phase winding is located. This core is then filled with atoms of the ψ_1 component, which lifts the core out of the polar phase and into the ferromagnetic phase. Fig. 3.9a shows the spherical harmonic representation of the HQV. By substituting $\tau = \varphi/2$ in Eq. (3.41), and

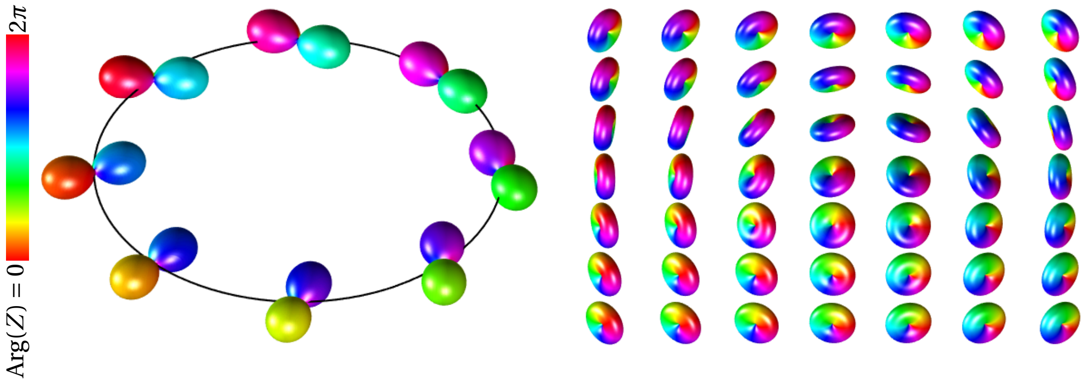

(a) (b)

Figure 3.9: Spherical harmonic representation of vortices in a spin-1 BEC. (a): Spin-1 polar HQV defined by Eq. (3.42). A complete circuit of the vortex results in a π spin rotation of the nematic director coupled with a π change to the condensate phase. (b): Ferromagnetic coreless vortex. The vortex takes on a characteristic fountain-like texture of the condensate spin vector.

taking $|\hat{\mathbf{F}}| = 0$ since this is the polar phase, the superfluid velocity becomes $\mathbf{v}_s = \hbar/(2M)\nabla\varphi$. It immediately follows that the mass circulation is calculated as

$$\oint_C \mathbf{v}_s \cdot \mathrm{d}\ell = \frac{\kappa}{2}, \tag{3.43}$$

showing that the unit of circulation is quantised in units of $\kappa/2$ for this system, and hence the name HQV.

For the case of the ferromagnetic phase, recall that the first homotopy group is calculated as [96] $\pi_1(\mathscr{M}_{\mathrm{FM}}) = \mathbb{Z}_2$, which corresponds to two different classes of line defects: singular and nonsingular. The singular vortex configuration can be constructed from Eq. (3.16) using the choice $\tau' = 0$ along with $\alpha = \varphi$, which leads to the wave function

$$\psi^{\mathrm{FM}}_{\mathrm{pcv}} = \sqrt{n}\begin{pmatrix} e^{-i\varphi}\cos^2\frac{\beta}{2} \\ \frac{1}{\sqrt{2}}\sin\beta \\ e^{i\varphi}\sin^2\frac{\beta}{2} \end{pmatrix}. \tag{3.44}$$

In this configuration, the single-valuedness condition could be satisfied by having the condensate density vanish along the vortex core. However, in spinor BECs, we typically have $c_0 \gg |c_1|$, which implies that it is more energetically favourable to vary the condensate spin instead. Therefore, the condensate can instead choose to lift atoms out of the ferromagnetic state and into the polar state (i.e., occupy the $m = 0$ component) within the vortex core. For this reason, such a vortex is referred to as a polar-core vortex [96].

An example of a nonsingular vortex arising in the FM phase is the coreless vortex [51, 121], which can be constructed from Eq. (3.16) by choosing $\tau' = \alpha = \varphi$ and having $\beta = \beta(\rho)$ be a function of the transverse radial coordinate, $\rho = \sqrt{x^2 + y^2}$, as:

$$\psi_{\text{cl}}^{\text{FM}} = \sqrt{n}\begin{pmatrix} \cos^2\frac{\beta}{2} \\ \frac{e^{i\varphi}}{\sqrt{2}}\sin\beta \\ e^{2i\varphi}\sin^2\frac{\beta}{2} \end{pmatrix}. \tag{3.45}$$

The single-valuedness condition of the wave function is satisfied by choosing $\beta(\rho)$ in one of two ways, resulting in slightly different configurations of a coreless vortex. If we choose $\beta(\rho)$ such that $\beta(\rho = 0) = 0$ and $\beta(\rho = \rho_0) = \pi/2$, where ρ_0 is the radius of the system, then we have what is known as a Mermin-Ho vortex [46, 134]. In this configuration, the spin starts aligned with the z-axis at $\rho = 0$, then gradually tilts away as $\rho \to \rho_0$ until the spin lies in the xy-plane at $\rho = \rho_0$. A different configuration is obtained if instead one chooses $\beta(\rho)$ such that $\beta(\rho = 0) = 0$ and now $\beta(\rho = \rho_0) = \pi$, leading to what is known as an Anderson-Toulouse-Chechetkin vortex [135, 136]. In this configuration, the spin follows a similar path, but now tilts through the xy-plane, and ends up aligned with the z-axis once more at $\rho = \rho_0$, with the spin now pointing in the opposite direction to the spin at $\rho = 0$. A spherical harmonic representation of the Mermin-Ho vortex is shown in Fig. 3.9b, where the characteristic fountain-like spin texture is apparent.

3.5.2 Vortices in spin-2 systems

Like the subsection before, we construct a few illustrative examples of vortices arising in the spin-2 phases and investigate them using spherical harmonics. We start with the UN phase, as given by Eq. (3.31). Unlike the spin-1 polar phase, the UN phase does not support fractional vortices with mass circulation. This is apparent from the spherical harmonic representation given in Fig. 3.7a, where the two-fold symmetry about the C_2 axis is not coupled to the condensate phase, τ. This phase instead accommodates a spin vortex, i.e., a vortex which carries only spin circulation. Such a vortex is constructed from Eq. (3.31) with the choice $\tau = 0, \alpha = -\varphi/2, \beta = \pi/2$:

$$\psi_{\text{sv}}^{\text{UN}} = \frac{\sqrt{6n}}{4}\begin{pmatrix} e^{i\varphi} \\ 0 \\ -\sqrt{\frac{2}{3}} \\ 0 \\ e^{-i\varphi} \end{pmatrix}. \tag{3.46}$$

The spherical harmonic representation of this vortex state is shown in Fig. 3.10a. Indeed,

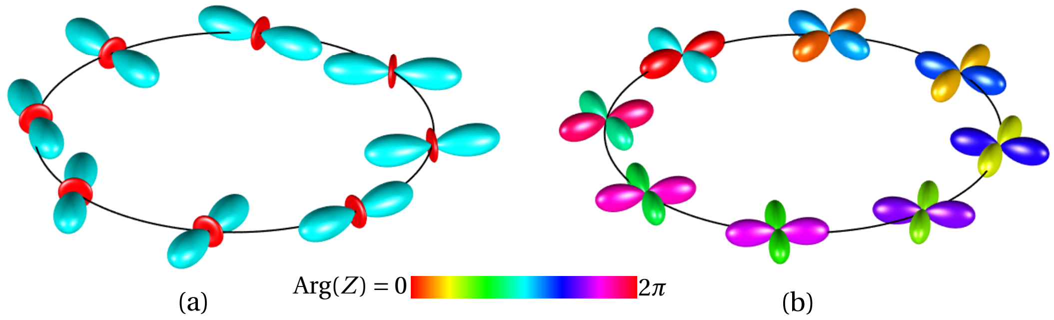

(a) (b)

Figure 3.10: Spherical harmonic representation of select vortices in the spin-2 nematic phases. (a): A spin vortex in the UN phase. A complete circuit of the vortex results in a π winding of the condensate spin vector, with no change to the condensate phase, and hence this vortex has no mass circulation. (b): One type of half-quantum vortex in the BN phase. The condensate phase winds by π about the vortex core which is coupled to a $\pi/2$ spin rotation.

we see that as the core of the vortex is traversed, the spin vector winds by π about the axis perpendicular to the nematic director (see Fig. 3.7a), but the condensate phase remains unchanged.

Recall that the first homotopy group of the BN phase ($\pi_1(\mathscr{M}_{\mathrm{BN}}) = \mathbb{Z} \times_h (\mathrm{D}^*)_{\hat{\mathbf{F}}}$) is non-Abelian, and hence supports non-Abelian vortices. Unlike the UN phase, the BN phase can support fractional vortices with mass circulation. One such example is of the BN HQV, which, due to the differing first homotopy group, is topologically distinct from that of the spin-1 polar case presented in Fig. 3.9a. Such a vortex can be constructed from Eq. (3.32) using the choice $\tau = 2\alpha = \varphi/2$ and $\beta = \gamma = 0$:

$$\psi^{\mathrm{BN}}_{\mathrm{hqv}} = \sqrt{\frac{n}{2}} \begin{pmatrix} 1 \\ 0 \\ 0 \\ 0 \\ e^{i\varphi} \end{pmatrix}. \tag{3.47}$$

The spherical harmonic representation of this vortex is shown in Fig. 3.10b. It is clear this vortex has the typical π phase winding about the vortex core associated with HQVs, which is also coupled to a $\pi/2$ spin rotation. When a vortex consists of a $2\pi w$ winding of the condensate phase coupled to a $2\pi\sigma$ winding of the spin vector about some axis of symmetry, the vortex charge can be described as (w, σ). The particular case of the vortex shown in Fig. 3.10b is classed as a $(1/2, 1/4)$ vortex, where the $1/2$ and $1/4$ denote the phase and spin windings, respectively. Additionally, there exists a half-quantum spin vortex, also called a $(0, 1/2)$ vortex,

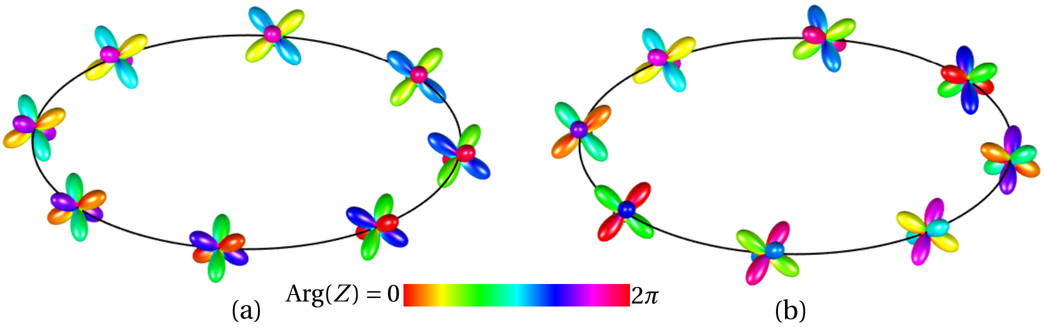

Figure 3.11: Spherical harmonic representations of cyclic fractional vortices. (a): A one-third vortex. A complete circuit reveals a $2\pi/3$ winding of the condensate phase, coupled with a $\pi/2$ spin rotation. (b): A two-third vortex. Similarly, a complete circuit of the vortex results in a $4\pi/3$ winding of the condensate phase, again coupled to a $\pi/2$ spin rotation.

in this phase, in which the condensate spin winds by π about the core, but the condensate phase remains unchanged [96].

Like the BN phase, the cyclic phase also supports non-Abelian vortices. Additionally, this phase also supports fractional vortices, but instead of the half-quantum of circulation that arises in the nematic phases, the cyclic phase has circulation that is quantised in units of $\kappa/3$, leading to one-third and two-third vortices. These vortices can be constructed from Eq. (3.34) by applying a condensate phase and general spin rotation, where a one-third vortex is constructed from the choice $\tau = -\alpha = \varphi/3$ with $\gamma = 0$ and a two-third vortex is constructed by choosing $\tau = 2\varphi/3$, $\alpha = \varphi/3$ and $\gamma = 0$. The result is a phase winding in the ψ_2 and ψ_{-1} components for the one-third and two-third vortices, respectively:

$$\psi^{\mathrm{C}}_{\frac{1}{3}} = \sqrt{\frac{n}{3}}\begin{pmatrix} e^{i\varphi} \\ 0 \\ 0 \\ \sqrt{2} \\ 0 \end{pmatrix}, \qquad \psi^{\mathrm{C}}_{\frac{2}{3}} = \sqrt{\frac{n}{3}}\begin{pmatrix} 1 \\ 0 \\ 0 \\ \sqrt{2}e^{i\varphi} \\ 0 \end{pmatrix}. \tag{3.48}$$

Spherical harmonic representations are plotted in Fig. 3.11. As we did for the spin-1 HQV in the polar phase, one can use the above wave function to see that the circulation is now quantised in units of $\kappa/3$. Substituting $\tau = \varphi/3$ in Eq. (3.41), and taking $|\hat{\mathbf{F}}| = 0$ since this is the cyclic phase, the superfluid velocity becomes $\mathbf{v}_s = \hbar/(3M)\nabla\varphi$. It then immediately follows that the mass circulation is calculated as

$$\oint_C \mathbf{v}_s \cdot \mathrm{d}\ell = \frac{\kappa}{3}, \tag{3.49}$$

showing the mass circulation in this phase is quantised in units of $\kappa/3$.

Part II

Numerical studies of spinor and pseudospinor condensates

CHAPTER 4

RELAXATION DYNAMICS OF HALF-QUANTUM VORTICES IN A TWO-COMPONENT SYSTEM

Since the realization of superfluidity, quantum turbulence has been studied in systems ranging from superfluid liquid Helium [137, 138] to quasi-particle condensates in solid-state systems [139]. Due to their unprecedented experimental accessibility, quantum turbulence in dilute, ultra-cold atomic gases has attracted considerable theoretical [22–27] and experimental [28–33] interest in both 2D and 3D configurations. In a scalar BEC, the quantum turbulence state is typically made up of many vortices with quantised circulation. The collective behaviour of the vortices plays a key role in the hydrodynamics, recovering features of classical turbulence that can exhibit the characteristic Kolmogorov power-law spectrum [140].

In contrast to the scalar superfluids, multi-component and spinor BECs are described by multi-component order parameters and allow for a wider range of topological defects, which give rise to novel dynamics [43, 88, 119, 141]. Consequently, there has been increasing interest in the properties of quantum turbulence and non-equilibrium dynamics in such systems [34–38]. The simplest non-scalar topological excitation appears in a two-component BEC, described by two complex fields, as the appearance of a phase singularity in only one component. When the atomic mass and mean density of the components are equal, such vortices are often referred to as HQVs, due to their similarities with vortices carrying half a quantum of superfluid circulation in superfluid ^{3}He [39] and spin-1 BECs [40, 41]. These vortices are sometimes also referred to as coreless vortices in a pseudospin-1/2 system, but note that the vortex is still singular when the order parameter space is $\mathrm{U}(1)\times\mathrm{U}(1)$ (which is the case in two-component systems, see below), different from, e.g., the coreless vortices that arise in the spin-2 ferromagnetic phases (see Sec. 3.5.2). Throughout this thesis we shall prefer the HQV terminology when discussing this class of vortex in a pseudospin-1/2 system.

The study of quantum turbulence in BECs can be separated into two distinct categories. Firstly, there is forced turbulence, where a statistically stationary state is established. Secondly, there is decaying turbulence, where a non-equilibrium initial condition, typically involving vortices, relaxes towards equilibrium. In this chapter, we focus on the latter case, and investigate the relaxation dynamics of HQVs in a two-dimensional, two-component condensate. Our interest is in studying the scaling laws that govern the decay rate of the vortices, and consequently the growth of the length scales associated with domains in the system, whilst varying the ratio of inter- to intra-species interactions. We study these scales by starting from an initially turbulent state containing HQVs and subsequently letting the system relax in time. Upon relaxation, vortices will annihilate leading to domain growth within the system.

To extract the appropriate length scales of these domains, we construct correlation functions, originally defined for an antiferromagnetic spin-1 system [60], which then allow us to extract relevant length scales associated with spin and mass order. By investigating these length scales temporally, we reveal interesting, novel dynamics occurring at early times for a sufficiently high ratio of inter- to intra-species interactions. This result is then confirmed by considering the total vortex number of the system. Furthermore, we contrast our observations for this system with similar simulations that have been performed for scalar BECs and reported in [142–144]. Finally, we discuss how our observations of anomalous vortex decay can be explained by relating to previous work [42, 43].

4.1 The two-component Bose-Einstein condensate as a pseudospin-1/2 system

4.1.1 Mapping of a spin-1 Bose-Einstein condensate to a two-component system

In order to treat the two-component BEC as a pseudospin-1/2 system, we discuss how a spin-1 condensate can be directly mapped to a two-component configuration for particular ground states. Recall from Sec. 3.2 that the spin-1 condensate with polar interactions ($c_1 > 0$) supports a polar ground state with $|\langle\hat{\mathbf{F}}\rangle| = 0$. This state can be categorized in two different ways depending on the sign of the quadratic Zeeman shift, q. The first occurs when $q > 0$, in which case the nematic director, is aligned along the spin quantisation axis (which we take to be the z-axis without loss of generality), and has a representative spinor of the form in

Eq. (3.17) called the EAP phase. The second case has $q > 0$, in which the nematic director is perpendicular to the spin quantisation axis, with a representative spinor of the form in Eq. (3.20) called the EPP phase. Due to the unpopulated middle component, the EPP phase presents a configuration of a spin-1 BEC that can be mapped directly to a two-component condensate, assuming that scattering into and out of the ζ_0 component can be neglected.

To begin the mapping procedure, recall the spin-1 GPEs listed in Eq. (2.74), in which the time-independent GPEs can be found using the substitution $\psi_m = \psi_m(\mathbf{r})e^{-i\mu t/\hbar}$. Since we're considering the EPP phase, we construct the time-independent GPEs for the spin-1 system with a wave function that assumes an empty middle component:

$$\begin{aligned}\left[-\frac{\hbar^2\nabla^2}{2M} + (c_0+c_2)|\psi_1|^2 + (c_0-c_2)|\psi_{-1}|^2 + q - \mu\right]\psi_1 = 0,\\ \left[-\frac{\hbar^2\nabla^2}{2M} + (c_0+c_2)|\psi_{-1}|^2 + (c_0-c_2)|\psi_1|^2 + q - \mu\right]\psi_{-1} = 0,\end{aligned} \tag{4.1}$$

where we have taken $p = 0$. Now, one can compare the above spin-1 GPEs to the equivalent two-component time-dependent GPEs, given here as (see Sec. 2.2)

$$\begin{aligned}\left(-\frac{\hbar^2\nabla^2}{2m_1} + g_1|\psi_1|^2 + g_{12}|\psi_2|^2 - \mu_1\right)\psi_1 = 0,\\ \left(-\frac{\hbar^2\nabla^2}{2m_2} + g_2|\psi_2|^2 + g_{12}|\psi_1|^2 - \mu_2\right)\psi_2 = 0.\end{aligned} \tag{4.2}$$

Using these time-independent equations, we can map the two-component system to that of the spin-1 by comparing the coefficients of the above with that of Eq. (4.1). Doing this we find

$$g_1 = g_2 = c_0 + c_2, \;\; g_{12} = c_0 - c_2, \;\; \mu_1 = \mu_2 = \tilde{\mu}, \;\; m_1 = m_2 = M, \tag{4.3}$$

where $\tilde{\mu} = \mu - q$. The above equations then directly maps the EPP phase of a spin-1 BEC to the equivalent two-component system, hence providing a pseudospin-1/2 description of the two-component BEC.

4.1.2 Hydrodynamic properties of a pseudospin-1/2 condensate

The wave function for a two-component BEC can be written generally as

$$\begin{pmatrix}\psi_1\\ \psi_2\end{pmatrix} = \begin{pmatrix}|\psi_1|e^{i\theta_1}\\ |\psi_2|e^{i\theta_2}\end{pmatrix} = e^{i\Theta}\begin{pmatrix}|\psi_1|e^{i\Phi}\\ |\psi_2|e^{-i\Phi}\end{pmatrix}, \tag{4.4}$$

where $\theta_j = \mathrm{Arg}(\psi_j)$ for component $j = 1, 2$ and

$$\Theta = \frac{\theta_1+\theta_2}{2}, \qquad \Phi = \frac{\theta_1-\theta_2}{2}. \tag{4.5}$$

Since there are two condensates, each with a global U(1) symmetry, the order parameter space for a two-component system is $\mathrm{U}(1)_1 \times \mathrm{U}(1)_2$, where $\mathrm{U}(1)_j$ denotes the contribution from the phase θ_j of component j. In the pseudospin-1/2 picture, this can be thought of as a contribution from the global condensate phase, Θ, and pseudospin, Φ, leading to the order parameter space [42]

$$\mathcal{M}_{2\mathrm{C}} = \frac{\mathrm{U}(1)_\Theta \times \mathrm{U}(1)_\Phi}{\mathbb{Z}_2}. \tag{4.6}$$

The $\mathbb{Z}_2$ factor comes from the fact that the order parameter remains invariant under the choice $\Theta = \Phi = \pi$ in Eq. (4.4), and hence gets factored out.

To understand the dynamical role that Θ and Φ play, it is useful to construct a hydrodynamic picture. In a two-component system, each component has an associated mass current given by the formula

$$(n\mathbf{v})_j = \frac{\hbar}{2im_j}\left[\psi_j^*\nabla\psi_j - (\nabla\psi_j^*)\psi_j\right]. \tag{4.7}$$

for component $j = 1,2$. Substituting Eq. (4.4) into the above expressions yields the mass current for both components:

$$\mathbf{v}_1 = \frac{\hbar}{m_1}\nabla(\Theta+\Phi), \qquad \mathbf{v}_2 = \frac{\hbar}{m_2}\nabla(\Theta-\Phi). \tag{4.8}$$

If we consider the total superfluid mass current, i.e., $\mathbf{v} = \mathbf{v}_1 + \mathbf{v}_2$, for our case of $m_1 = m_2 = m$, then we arrive at

$$\mathbf{v} = \frac{2\hbar}{m}\nabla\Theta. \tag{4.9}$$

This reveals that gradients in Θ are associated with a total, superfluid mass current. We can perform a similar analysis to determine the importance of Φ. Instead of looking at the total mass current, we instead take the difference of the individual mass currents, resulting in the expression

$$\mathbf{v}_2 - \mathbf{v}_1 = \frac{2\hbar}{m}\nabla\Phi. \tag{4.10}$$

The difference of the two mass currents, and hence gradients of Φ, are interpreted as a pseudospin current.

4.1.3 Vortices in two-component systems

As we have seen in Chapter 3, the types of stable topological defects within a system can be obtained using homotopy theory. For a pseudospin-1/2 system, the first homotopy group is calculated as [42]

$$\pi_1(\mathcal{M}_{2\mathrm{c}}) = \mathbb{Z}\times\mathbb{Z}, \tag{4.11}$$

which specifies that two types of vortices are topological stable within this system. The first is integer vortices, which are described by a 2π winding of the global phase, Θ, with no winding in the pseudospin, Φ. This is achieved in Eq. (4.4) by having $\theta_1 = \theta_2 = \varphi$, where φ is the azimuthal angle about the core. These vortices share similarities with U(1) vortices arising in scalar condensates, due to their both having a 2π winding of the condensate phase. The second class of vortex can be distinguished as a π winding of the condensate phase, Θ, which is coupled to a $\pm\pi$ winding of the pseudospin Φ, where the sign of the winding in Φ is determined by which component the phase singularity is located. For example, consider a vortex state which consists of a phase singularity in the ψ_1 component such that about the singularity θ_1 winds by 2π and θ_2 remains unchanged, i.e., it is a smooth phase field. Such a state can be written as

$$\begin{pmatrix}\psi_1\\ \psi_2\end{pmatrix} = \begin{pmatrix}|\psi_1|e^{i\varphi}\\ |\psi_2|\end{pmatrix} = e^{\varphi/2}\begin{pmatrix}|\psi_1|e^{i\varphi/2}\\ |\psi_2|e^{-i\varphi/2}\end{pmatrix}. \tag{4.12}$$

By comparing the above to Eq. (4.4), we have $\Theta = \Phi = \varphi/2$. Due to the global phase winding by π, we call such a vortex a HQV. Note however that this vortex is different from, e.g., the HQV arising in the polar phase of spin-1 condensates [40, 41] (see Sec. 3.5.1). One key difference arises in the quantisation of circulation. Using Eq. (4.9), the mass circulation along a closed contour C about the vortex can be calculated as

$$\oint_C \mathbf{v}\cdot d\ell = \kappa, \tag{4.13}$$

where $\kappa = h/m$ is the quantum of circulation. This shows that, despite being classed as a HQV, the circulation of such a vortex is still quantised in the typical units of κ, similar to U(1) vortices in scalar condensates. Here, however, we use the term HQV for convenience to distinguish it from the integer vortex also arising in the psueodspin-1/2 system.

4.2 Investigating half-quantum vortex relaxation dynamics

To begin studying the relaxation dynamics of HQVs in a turbulent system, we numerically solve the two-component Gross-Pitaevskii equations, given here in dimensionless form (see Appendix A.1 for details):

$$\begin{aligned} i\frac{\partial\psi_1}{\partial t} &= (-\nabla^2 + g|\psi_1|^2 + \gamma|\psi_2|^2)\psi_1,\\ i\frac{\partial\psi_2}{\partial t} &= (-\nabla^2 + g|\psi_2|^2 + \gamma|\psi_1|^2)\psi_2, \end{aligned} \tag{4.14}$$

where we have assumed each component has the same atomic mass ($m_1 = m_2 = m$) and interspecies interaction strength ($g_1 = g_2 = g$) to comply with the mapping of the spin-1

EPP phase to a two-component system. This type of condensate, with equal mass and inter-species interactions, can be achieved experimentally using two hyperfine states of the same atom [145, 146]. The key parameter is the ratio of inter- to intra-species interaction

$$\gamma = \frac{g_{12}}{g}. \tag{4.15}$$

We consider the case $0 < \gamma < 1$, with all interactions repulsive such that the condensate is stable against the separation of the components. Throughout our simulations we treat γ as a free parameter within this range.

The inter- and intra-component interactions give rise to two important length scales within the system. These are, respectively, associated with variations in the total superfluid density and the difference in density between the components. The density and spin healing lengths are then defined as [42]

$$\xi_d = \frac{\hbar}{\sqrt{2mgn_0}}, \qquad \xi_s = \xi_d\sqrt{\frac{1+\gamma}{1-\gamma}}, \tag{4.16}$$

where n_0 is the background number density, which we assume to be the same in each component. The size of the HQV core can be understood from the energetic hierarchy of these healing lengths. Since a HQV consists of a phase singularity in one component and not the other, the vortex core is free to fill with the atoms in the component with no phase singularity. This corresponds to spatial variations in the z-component of the pseudospin, the size of which is set by the pseudospin healing length, ξ_s. The vortex core can expand when $\xi_s \gtrsim \xi_d$, which lowers the total energy. We see from Eq. (4.16) that γ directly determines the core sizes within our systems. Similar energetic hierarchies exist in spinor BECs, which can facilitate deformations of vortex cores such as the splitting of singly quantised vortices into fractional vortices [41].

4.2.1 Numerical setup

Our numerical setup is as follows. We solve Eq. (4.14) on a periodic domain with $N_s^2 = 1024^2$ grid points which has dimensionless area $L^2 = N_s^2$ with side length $L = N_s$. We take $N = 3.2 \times 10^9$ atoms per component and fix dimensionless $g = L^2/4N$. The dimensionless density healing length is then fixed at $\xi_d = N_s/\sqrt{gN} = 2$ in our system. Our goal is to explore the effect of the inter-component interaction on HQV relaxation dynamics by varying γ within the range $0 < \gamma < 1$.

We first need to construct an initial state that consists of many HQVs, which we can subsequently relax. Our numerical procedure for generating such a system is outlined here. We

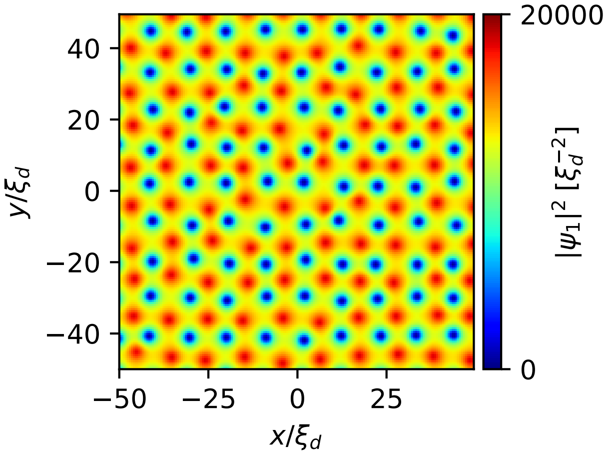

Figure 4.1: Density of ψ_1 component in a $100\xi_d \times 100\xi_d$ subregion of the initial state after imaginary time propagation. We see the HQVs in this component by the density depletion. The density peaks correspond to the location of HQV cores in the other component, which have been filled by atoms in this component.

start with a grid of positions such that the i-th vortex is to be constructed at position (x_i, y_i). The grid in each component is offset by some amount in both the x and y directions to avoid overlapping vortex positions, which would subsequently generate a system of integer vortices. To generate a random distribution of vortices, we displace each position by some small amount $(x_i, y_i) \to (x_i + \delta x_i, y_i + \delta y_i)$, where δx_i,δy_i are random number drawn from a uniform distribution and $|\delta x_i|, |\delta y_i| < 3\xi_d$. The phase of each component is then constructed to contain a 2π phase winding about each vortex position using the method described in [25]. To ensure that the overall circulation is zero, each position alternates the winding of the phase, leading to an equal number of HQVs with positive and negative charge. For our system in particular, we imprint 48^2 HQVs each component. Finally, the vortices themselves are constructed using a short imaginary time propagation of Eq. (4.14), whilst keeping the phase profile of each component fixed to not alter the positions of the vortices. This imaginary time propagation imprints the cores of the vortices, and therefore results in an initially turbulent system of HQVs.

The HQV cores correspond to a density depletion in one component at the position of the phase singularity with a corresponding density peak at the same position in the other component (see Fig. 4.1). Previous work has shown that clustering of vortices can lead to anomalously slow coarsening dynamics [144] and thus constructing the initial state this way ensures that there is no clustering of like-signed vortices. From this initial state, the system evolves according to Eq. (4.14). Two HQVs in the same component with opposite winding

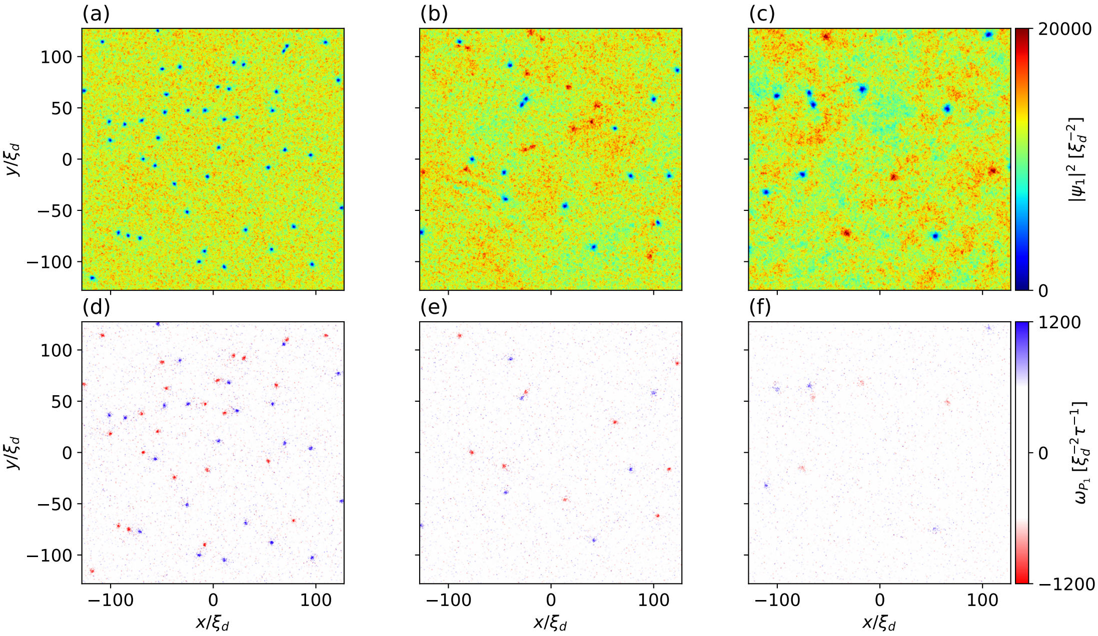

Figure 4.2: Density (a) – (c) and pseudo-vorticity (d) – (f) of the ψ_1 component in a $256\xi_d \times 256\xi_d$ subregion at a time $t/\tau = 2.5 \times 10^4 \xi_d^2$ for $\gamma = 0.1$ (left), $\gamma = 0.6$ (middle), and $\gamma = 0.8$ (right). The density depletions correspond to HQVs in this component. For $\gamma \gtrsim 0.6$, density peaks reveal the locations of HQVs with the phase singularity in the other component, where the vortex cores have filled with atoms in this component. Vortices with positive (blue) and negative (red) circulation are identifiable in the pseudo-vorticity field.

can annihilate, leading to a decay of the total vortex number within the system.

4.3 Spatial aspects of half-quantum vortex decay

We begin our investigations by considering the spatial aspects of the relaxation dynamics. Firstly, we wish to investigate how γ affects the HQVs within our systems. Fig. 4.2 shows the density field of the ψ_1 component for $\gamma = 0.1, 0.6, 0.8$. One sees that as γ increases, the core size (i.e., the radial size of the density depletion) also increases. From Eq. (4.16) we see that the size of the HQV core is dependent on γ, where $\xi_s \to \xi_d$ as $\gamma \to 0$. The healing lengths can explain why, for $\gamma \geq 0.6$, bright density peaks also appear within the ψ_1 field. For small γ, the density and spin healing lengths become comparable, $\xi_d \sim \xi_s$. However, an increasing γ implies a larger spin healing length. Consequently, atoms of the other component will fill the vortex core as the resulting lowering of the kinetic energy offsets the cost of interaction energy. This results in the expansion of the vortex cores to the size of the spin healing length.

Hence, bright density peaks in Fig. 4.2 correspond to atoms in the ψ_1 component that have filled the core of an HQV in the ψ_2 component.

To locate the HQVs in the system, we make use of the pseudo-vorticity [147], given as:

$$\omega_{\mathrm{p_j}} = \frac{1}{2}\nabla \times (n\mathbf{v})_j, \tag{4.17}$$

where $(n\mathbf{v})_j$ is the mass current of component $j = 1,2$ defined as in Eq. (4.7). The pseudo-vorticity has the unique property of remaining regular and non-zero within the vortex cores, and, on length scales greater than the spin healing length away from a vortex core, quickly relaxes to zero. Therefore, this becomes a useful tool to identify where vortices are in the system by checking for regions of non-zero pseudo-vorticity. Fig. 4.2 (d) – (f) shows the pseudo-vorticity for the same systems in (a) – (c). We see that non-zero regions of pseudo-vorticity are in alignment with the density depletions, confirming the cores of vortices. Additionally, the sign of the pseudo-vorticity also determines the charge of the vortex, where positive pseudo-vorticity corresponds to a vortex with a positive charge and vice versa.

4.3.1 Investigating the kinetic energy spectrum

A useful property to investigate in turbulent systems is the kinetic energy spectrum, which provides useful insights into the spatial aspects of the relaxation dynamics. We start with the kinetic energy of the two-component system which is written in terms of the density n_j and velocity $\mathbf{v}_j$ of the j-th component as

$$E_{\mathrm{kin}} = \int \left(|\nabla\sqrt{n_1}|^2 + |\nabla\sqrt{n_2}|^2\right) \mathrm{d}^2\mathbf{r} + \frac{1}{4}\int \left(|\sqrt{n_1}\mathbf{v}_1|^2 + |\sqrt{n_2}\mathbf{v}_2|^2\right) \mathrm{d}^2\mathbf{r}. \tag{4.18}$$

The kinetic energy can be further decomposed into quantum pressure (E^q) and classical velocity (E^v) contributions:

$$E^v = \frac{1}{4}\int \left(|\sqrt{n_1}\mathbf{v}_1|^2 + |\sqrt{n_2}\mathbf{v}_2|^2\right) \mathrm{d}^2\mathbf{r}, \tag{4.19}$$

$$E^q = \int \left(|\nabla\sqrt{n_1}|^2 + |\nabla\sqrt{n_2}|^2\right) \mathrm{d}^2\mathbf{r}. \tag{4.20}$$

To extract energy spectra from these contributions we define the generalized velocities for the incompressible (i), compressible (c), and quantum pressure (q) parts as [35]

$$\mathbf{w}^{i,c} = \sqrt{n_1}\mathbf{v}_1^{i,c} + \sqrt{n_2}\mathbf{v}_2^{i,c} \tag{4.21}$$

$$\mathbf{w}^q = 2(\nabla\sqrt{n_1} + \nabla\sqrt{n_2}). \tag{4.22}$$

Here, the incompressible and compressible parts of the velocity field, $\mathbf{v}$, are extracted from a Helmholtz decomposition which splits the velocity into a divergence-free incompressible part, $\nabla \cdot \mathbf{v}^i = 0$, and an irrotational, compressible part, $\nabla \times \mathbf{v}^c = \mathbf{0}$. Hence, in Fourier space, the kinetic energy spectrum can be calculated by taking the Fourier transform of the generalized velocities and integrating over the k-space angle as

$$E^\delta(k) = \frac{1}{4}\int_0^{2\pi} |\tilde{\mathbf{w}}^\delta(\mathbf{k})|^2 \,\mathrm{d}\Omega_k \qquad (\delta = i, c, q), \tag{4.23}$$

where $\tilde{\mathbf{w}}^\delta$ denotes the Fourier transform of the generalised velocity $\mathbf{w}^\delta$ for wave number $k = |\mathbf{k}|$. The total kinetic energy is then given by the sum of each contribution, integrated over all k

$$E_{\text{kin}} = \sum_\delta \int E^\delta(k)\,\mathrm{d}k \qquad (\delta = i, c, q). \tag{4.24}$$

The occupation numbers of each contribution are extracted as

$$n^\delta(k) = k^{-2}E^\delta(k) \qquad (\delta = i, c, q). \tag{4.25}$$

Finally, the total occupation number of the system is given as

$$n(k) = \int_0^{2\pi} \left[\tilde{\psi}_1^*(k)\tilde{\psi}_1(k) + \tilde{\psi}_2^*(k)\tilde{\psi}_2(k)\right] \mathrm{d}\Omega_k. \tag{4.26}$$

We plot the occupation number for each energy contribution, as well as total occupation number, at a late time for $\gamma = 0.6$ in Fig. 4.3. The total occupation number exhibits two different scaling: A k^{-4} in the ultraviolet (UV), and k^{-2} in the infrared (IR). The same scaling have been found in some 2D, turbulent, scalar BEC systems containing scalar vortices [143]. The decomposition of the kinetic energy into its respective contributions allows us to see that the incompressible contribution dominates the spectrum in the IR region, and is therefore responsible for the transition to the k^{-4} scaling. This incompressible contribution is directly associated with the vortices in the system, as vortices are the only excitations that can arise in an incompressible, irrotational superfluid [3, 132]. Similarly, we see it is both the compressible and quantum pressure contributions that dominate in the UV region, facilitating the transition to the k^{-2} scaling, which is characteristic of weak-wave-turbulence [148–150]. This scaling of the kinetic energy was observed throughout all values of γ tested, indicating that it is quantitatively insensitive to variations in γ. The investigation into the kinetic energy spectrum thus reveals that γ has negligible effects on the spatial aspects of the relaxation dynamics. In addition, it shows that, despite containing a different type of vortex, the dynamics follow quantitatively similar behaviour to some turbulent scalar BEC systems containing scalar vortices [143].

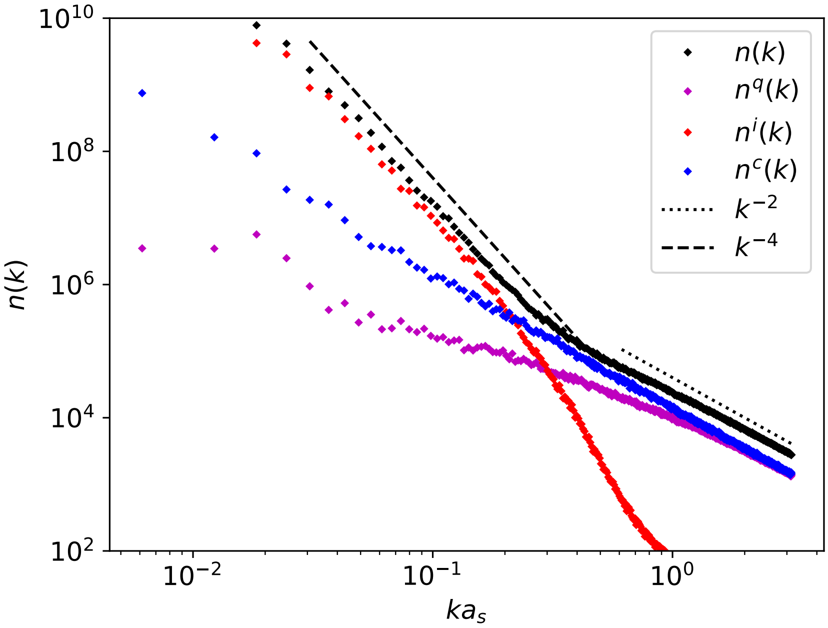

Figure 4.3: Occupation numbers for the quantum pressure (purple), incompressible (red diamonds), and compressible (blue) contributions for $\gamma = 0.6$. The total occupation number (black) is obtained from the sum of each contribution. The total occupation number has two distinct scaling: a k^{-2} (dotted line) in the ultraviolet region, and a k^{-4} scaling (dashed line) in the infrared.

4.4 Temporal aspects of half-quantum vortex decay

4.4.1 Growth of correlation lengths

To measure the temporal aspect of the relaxation dynamics, we will consider correlation functions. Since our pseudospin-1/2 order parameter is composed of a mass part and a spin part [c.f. Eq. (4.5)], it is natural to then construct both a mass and spin correlation function. To begin, we need to identify appropriate quantities that serve as order parameters for our system. Motivated by the form of the EPP phase in spinor BECs, one such quantity is the planar tensor [60]

$$\mathrm{Q} = \begin{pmatrix} Q_{xx} & Q_{xy} \\ Q_{xy} & -Q_{xx} \end{pmatrix}, \tag{4.27}$$

where $Q_{xx} = \mathrm{Re}(\psi_1^*\psi_2)$ and $Q_{xy} = \mathrm{Im}(\psi_1^*\psi_2)$. The eigenvalues of Q are given by $\{-\frac{1}{2}|\alpha|, \frac{1}{2}|\alpha|\}$, where $\alpha = -2\psi_1\psi_2$. If we consider the general wave function defined in Eq. (4.4), then evaluating Q and α gives

$$Q_{xx} = |\psi_1||\psi_2|\cos(2\Phi), \qquad Q_{xy} = -|\psi_1||\psi_2|\sin(2\Phi), \tag{4.28}$$

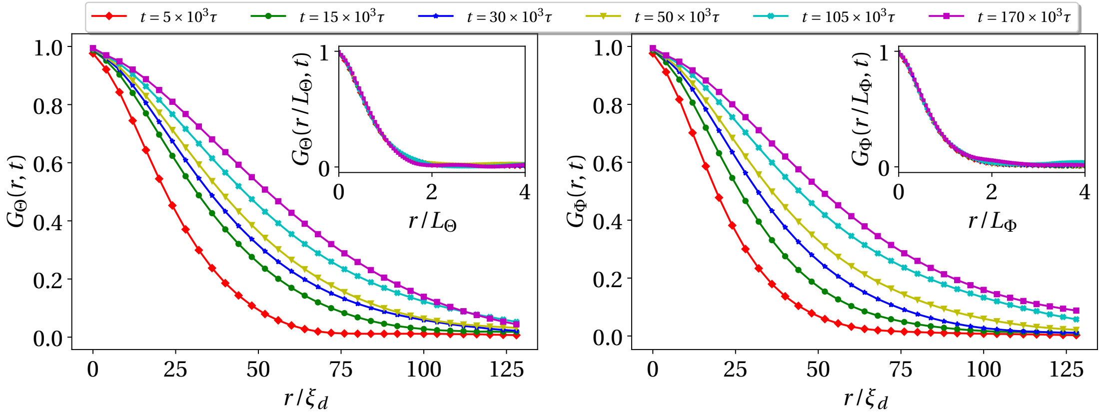

Figure 4.4: Correlation functions for the mass (left) and spin (right) parts of a two-component system as functions of time for $\gamma = 0.6$. As time increases the correlation functions decay over a larger range, indicating long-rang ordering within the system. Insets: Collapse of the mass (left) and spin (right) correlation functions when scaled by the appropriate correlation length.

$$\alpha = -2|\psi_1||\psi_2|e^{2i\Theta}. \tag{4.29}$$

This shows that Q is dependent on the phase of the spin, Φ, whereas α is dependent upon the global phase, Θ.

Armed with these quantities, we can then construct correlation functions related to the mass and spin parts of our pseudo-spinor order parameter. These are defined, respectively, as

$$G_\Theta(\mathbf{r},t) = \frac{1}{n^2}\langle\alpha^*(\mathbf{0})\alpha(\mathbf{r})\rangle, \tag{4.30}$$

$$G_\Phi(\mathbf{r},t) = \frac{2}{n^2}\mathrm{Tr}[\langle \mathrm{Q}(\mathbf{0})\mathrm{Q}(\mathbf{r})\rangle], \tag{4.31}$$

where $\langle\cdot\rangle$ denotes ensemble averaging. By exploiting the fact that our system is homogeneous, we can replace ensemble averages with spatial averages. To obtain the 1D spectrum, we perform an angular integration in k-space. The spin correlation function is then computed as

$$G_\Phi(r,t) = \int d\Omega_k \int \frac{d^2\mathbf{r}'}{L^2}\frac{2}{n^2}\mathrm{Tr}[\langle \mathrm{Q}(\mathbf{r}')\mathrm{Q}(\mathbf{r}'+\mathbf{r})\rangle], \tag{4.32}$$

where $\int d\Omega_k$ denotes integration over the k-space angle, whilst $\int d^2\mathbf{r}'/L^2$ is spatial averaging. We perform the same averaging for the mass correlation function.

Fig. 4.4 shows both correlation functions for $\gamma = 0.6$ for various times through the simulation. We see that as time increases, the correlation functions extend over larger distances which indicates that the respective domains are growing over time, showing long-range order is being established. From these correlation functions, we may extract a correlation length, L_δ

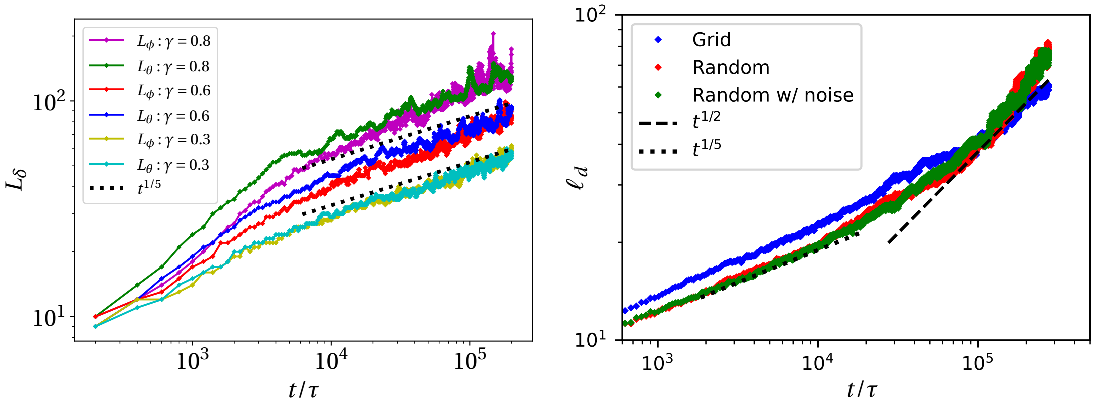

(a) (b)

Figure 4.5: (a): Mass and spin correlation lengths as a function of time for $\gamma = 0.3, 0.6, 0.8$. For early-time dynamics, a larger γ is associated with a faster growth of the correlation length. At late times, however, all correlation lengths tend to a universal $t^{1/5}$ scaling. (b): Inter-vortex spacing, ℓ_d, as a function of time for scalar systems prepared using different initial conditions. Grid corresponds to a grid of vortices, similar to the setup in (a), random (with noise) corresponds to a random distribution of vortices where each position is drawn from a uniform distribution (with numerical noise added to the initial state). For early-time dynamics the inter-vortex spacing follows a $t^{1/5}$ for each initial state. At late times, this scaling transition to $t^{1/2}$, which is typically observed in scalar vortex relaxation dynamics [143].

with $\delta \in \{\Theta, \Phi\}$, that enables us to determine a length scale over which the correlation function decays. We take the correlation length to be the value at which the corresponding correlation function decays to a quarter of its value at $r = 0$: $G_\delta(L_\delta, t) = \frac{1}{4} G_\delta(0, t)$. Using the correlation length, we can determine whether the correlation functions exhibit dynamical scaling, which implies the form of the functions remains self-similar at different times throughout the simulation. This means the function collapses to a universal, time-independent function when scaled by the correlation length: $H_\delta(r) = G(r/L_\delta(t), t)$. The insets of Fig. 4.4 show the scaling of the correlation functions when scaled by the respective correlation length. This confirms that the correlation functions within our system do exhibit dynamical scaling.

Fig. 4.5 shows the correlation lengths for $\gamma = 0.3$, $\gamma = 0.6$, and $\gamma = 0.8$ as functions of time. We see that at late times in the evolution, all correlation lengths tend to a universal $t^{1/5}$ scaling. However, the early-time dynamics are remarkably different for the various γ. As γ increases, there is a faster growth of the correlation lengths at early times, which signifies the correlation length being γ-dependent. We investigate this behaviour by considering the total vortex number of the system as a function of time. We can then extract the mean distance between the vortices as $\ell_d = 1/\sqrt{N_{\text{vort}}}$, where N_{vort} is the total number of vortices in the two components. In a scalar BEC containing an initially large number of vortices, it has been observed that $\ell_d \sim t^{\beta}$ [144], where β characterizes the annihilation rate of vortices. In particular, there were two distinct β observed: Firstly, a $\beta = 1/5$ scaling after some short period of evolution. This scaling is included in Fig. 4.5a as a comparison. Secondly, after a much longer period of evolution, a $\beta = 1/2$ scaling emerges. This second scaling can be delayed if the initial vortex distribution is highly clustered [144].

Fig. 4.5b is a reproduction of both the early- and late-time scaling of the mean vortex distance, ℓ_d, for a scalar system using the parameters of [144]. We consider three initial conditions: Firstly, we constructed a grid of vortices analogous to our two-component system (see Sec. 4.2.1). Secondly, we considered a random distribution of vortices; one with noise added to the energy spectrum, and one without. We see that at early and intermediate times, there is a clear $t^{1/5}$ scaling in all the initial states tested. Furthermore, at late times we recover the $t^{1/2}$ scaling for all initial states. This indicates the scaling is robust and insensitive to the initial conditions.

4.4.2 Vortex decay rate

Motivated by this previous work in scalar BECs [144], we conduct a similar analysis on our two-component system containing HQVs, and determine how γ affects the vortex decay rate. In particular, we consider the early-time evolution in which Fig. 4.5a suggests interesting dynamics. The variation of the total vortex number with time is plotted in Fig. 4.6 for $\gamma = 0.3$, $\gamma = 0.7$, and $\gamma = 0.9$. We see that for $\gamma = 0.3$, the vortex decay rate is mostly consistent throughout the evolution, which tends to a $t^{-2/5}$ ($\ell_d \sim t^{1/5}$) scaling at later times. More interesting dynamics are revealed for $\gamma = 0.7, 0.9$ where two different scaling regimes emerge at early times ($2.5 \times 10^2 \xi_d^2 \lesssim t/\tau \lesssim 2.5 \times 10^3 \xi_d^2$) with $N_{\text{vort}} \sim t^{-1}$ for $\gamma = 0.7$ and $N_{\text{vort}} \sim t^{-3/2}$ for $\gamma = 0.9$. After the initial differing early-time dynamics, the systems then tend to a universal $t^{-2/5}$ scaling, which corresponds to $\ell_d \sim t^{1/5}$ similar to the scalar BEC simulation shown. These results show a better fit to the theoretical $t^{1/5}$ scaling than indicated by the correlation lengths shown in Fig. 4.5. This further suggests that $L_{\Phi,\Theta}$ differs slightly from ℓ_d, even though the growth of the correlation lengths is driven by vortex annihilation. Fig. 4.6 only extends up to $t/\tau = 5 \times 10^4 \xi_d^2$, and we expect to see a universal transition to $N_{\text{vort}} \sim t^{-1}$ ($\ell_d \sim t^{1/2}$) at much later times for sufficiently small γ. For large γ, due to the rapid annihilation of vortices at early times, there may not be enough vortices left within the system to facilitate the transition to the $N_{\text{vort}} \sim t^{-1}$ regime.

We wish to investigate further the effect of γ on the initial decay rate of the vortices. We

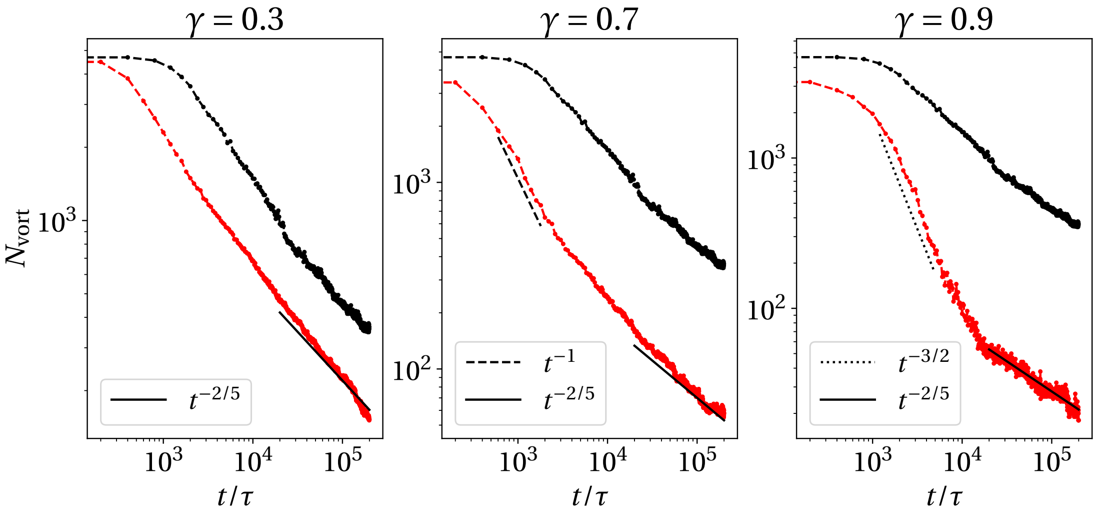

Figure 4.6: Total vortex number as a function of time for $\gamma = 0.3, 0.7, 0.9$ (red circles). Larger γ leads to a faster decay rate of vortices at early times due to the rapid annihilation of opposite-signed vortices within the same component. Despite vastly different early-time dynamics, the vortex decay rates tend to a universal $t^{-2/5}$ at late times. For comparison the vortex decay rate of a scalar system is shown (black circles). This system is set up using the grid method as defined in Sec. 4.2.1, with 48^2 vortices in total. Note that the black line is multiplied by two to have it be the same total vortex number as the two-component system.

can model the vortex decay rate as a simple kinetic-like equation of the form

$$\frac{\partial N_{\mathrm{vort}}}{\partial t} \sim N_{\mathrm{vort}}^{\eta}, \tag{4.33}$$

where $\eta > 1$. The form of this equation states that the decay rate of the vortices is dependent on the total number of vortices facilitating the annihilation. Using this simple model, we can extract a scaling for the total vortex number as

$$N_{\mathrm{vort}} \sim t^{-2/z}, \tag{4.34}$$

where $z = -2(1-\eta)$. An exponent of $z = 2$ corresponds to a two-body collision process, in which only two vortices are required to annihilate. On the contrary, an exponent of $z = 5$ corresponds to a three-body collision process, where three vortices are necessary to facilitate annihilation. Fig. 4.7 shows the exponent, z, as a function of γ where z is extracted within the time interval $2.5 \times 10^2 \xi_d^2 < t/\tau < 2.5 \times 10^3 \xi_d^2$. We see a rapid decrease of the exponent after $\gamma \gtrsim 0.6$, in which Fig. 4.6 shows the rapid annihilation of vortices is prevalent. The decrease of the exponent in our simulations signals an additional vortex interaction mechanism not present in scalar BEC systems.

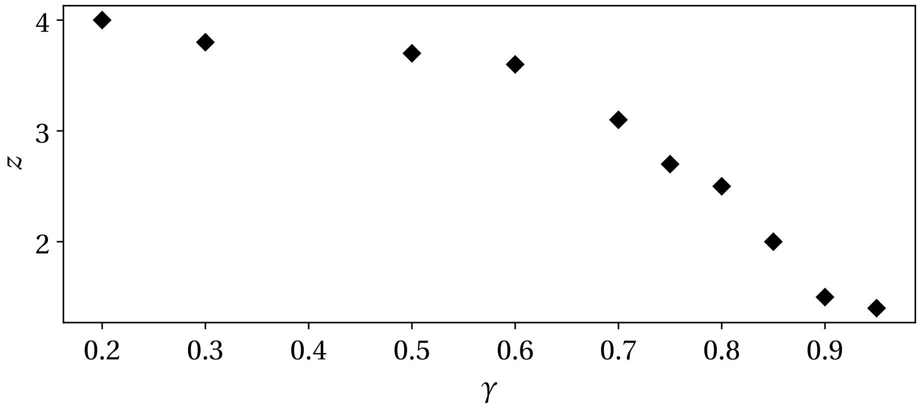

Figure 4.7: The exponent z in Eq. (4.34) as a function of γ. Here, z is calculated in the region $2.5\times10^2\xi_d^2 < t/\tau < 2.5\times10^3\xi_d^2$, where early-time dynamics take place. We see that after $\gamma \gtrsim 0.6$ a rapid decrease of the exponent occurs, signalling a rapid change in vortex dynamics.

Numerous studies have been conducted to try to understand the inter-vortex forces between HQVs in two-component systems [42, 43]. In particular, Kasamatsu *et al.* [43] tried to derive a point vortex model to explain the dynamics shown in Fig. 4.7, but found that the model failed to accurately predict the resulting vortex dynamics. They conducted simple tests involving a dipole of HQVs in which they found that an increase in γ dramatically changes the motion of the dipole. For $\gamma >= 0.6$, it was found that the individual vortices move together and undergo annihilation. For weaker γ, the two vortices move in parallel, similar to the behaviour observed for dipoles consisting of scalar U(1) vortices. The strength of γ also determines the rate at which the vortices annihilate (see Fig. 11 of Ref. [43]).

4.5 Conclusions

In this chapter we have investigated the relaxation dynamics of HQVs in a two-dimensional, two-component BEC. After detailing the numerical set up, we first investigated the spatial aspects of the relaxation dynamics. In particular, we investigated the kinetic energy spectrum by splitting it into incompressible, compressible, and quantum pressure parts. We found that the kinetic energy spectrum exhibits two different scaling in the infrared and ultraviolet regions. The former had a scaling of k^{-2}, whilst the latter had k^{-4}. The splitting of the spectrum into its constituent parts revealed that the transition to the k^{-2} scaling was due to the incompressible component, whilst the k^{-4} arose due to the compressible component. Similar scaling has been observed in scalar BEC systems containing scalar vortices [143]. This shows that, despite being an entirely different class of vortex, relaxation dynamics of HQVs exhibit similar spatial aspects to those observed in scalar systems with scalar vortices

After considering the spatial aspects, we then considered the temporal aspects of the relaxation dynamics. We started with investigating the correlation functions, for which we constructed both a mass and spin part. It was revealed that the correlation functions extended over larger regions as time increased, which indicates long-range order within our systems. We also showed our system exhibits dynamical scaling, by showing that the correlation functions collapsed to a universal, time-independent function when scaled by the appropriate correlation length. Investigations into these correlation lengths suggested anomalous early-time dynamics was taking part. It was revealed that the correlation lengths had a faster initial growth for larger γ, but at late times all correlation lengths scaled as $t^{1/5}$.

Motivated by the previous scalar BEC work in [144], we investigated the decay rate of the vortices. We showed that for sufficiently high $\gamma \gtrsim 0.6$ the vortices had an increasingly steeper decay rate at early times, which then tended to a universal $t^{-2/5}$ at late times in all γ tested. We tested this theory further by modelling the vortex decay rate as a simple kinetic-like equation, for which we then manually extracted the scaling of the total vortex number. Plotting the exponent of the scaling against γ confirmed that after $\gamma \sim 0.6$ there is a rapid increase the exponent, and therefore the decay rate of the vortices.

CHAPTER

5

GENERALISED KIBBLE-ZUREK SCALING IN A SPIN-1 BOSE-EINSTEIN CONDENSATE

Nonequilibrium phase transitions are ubiquitous, arising in many areas of physics, including cosmology [78, 151], condensed matter [152–157], and ultracold atomic gases [158–161]. A quantum phase transition (QPT), in contrast to its classical counterpart, is a zero-temperature transition driven by quantum fluctuations [63]. In such a transition, a fundamental change of ground state occurs as an external parameter is varied across the quantum critical point. For a continuous phase transition, as this critical point is passed, the timescale governing the dynamics diverges, resulting in the system no longer adiabatically following the ground state. This non-adiabatic evolution implies that the symmetry of the system is broken independently in causally disconnected regions, which typically results in the formation of topological defects. The Kibble-Zurek mechanism (KZM) is a theory that describes the resulting dynamics and predicts the scaling properties of the excitations from the details of the universality class of the transition. It was first introduced by Kibble in the context of cosmological phase transitions in the early universe [77, 78], before being extended by Zurek to condensed matter systems [162–164].

Any continuous phase transition can be modelled using the KZ theory, and due to this robustness, it has been successfully applied to both classical [165, 166] and quantum [67, 167, 168] phase transitions. Whilst the theory has had great success in applications to continuous, second-order transitions, direct application to discontinuous phase transitions does not typically give an accurate description of observed scaling laws. This is due to the fact that at the critical point of a continuous phase transition the energy spectrum is gapped, in which well-defined correlation lengths and time scales can be derived. In a first-order, discontinuous phase transition, the energy spectrum at the critical point is gapless, and hence the traditional KZ theory breaks down. Recently, there has been the first experimental evidence of the existence of scaling laws for a first-order QPT [75], where standard KZ theory failed to predict the observed scaling. However, the KZM was generalised by considering the energy gap between the metastable state and its first corresponding excited state, which then gave an accurate prediction of the observed scaling laws. There is current interest in trying to generalise the KZM and applying it to discontinuous transitions and deriving appropriate scaling laws [169, 170].

The seminal work of Fisher and Berker [171], in the classical case, first discussed a particular type of discontinuous, first-order transition and introduced the notion of a discontinuous critical point (DCP). Such a DCP separates two distinct phases, characterized by a discontinuous jump in the order parameter. Despite the discontinuity, the transition can still be characterized by a diverging length scale and hence critical exponents can be derived. This framework was then extended to the quantum case, specifying the conditions for a discontinuous quantum critical point (DQCP) [170]. The DQCP leads to a prediction of the scaling of the defect density that is modified from the typical KZ scenario.

Spinor BECs offer a highly controllable platform for studying non-equilibrium physics, ranging from topological defects [49, 116] to quantum quenches [35, 37, 60]. In addition, their rich phase diagram has seen the KZM applied both numerically and experimentally in various continuous phase transitions [66, 68, 69, 71–73]. For a ferromagnetic spin-1 BEC, there exists a first-order QPT between a three-component broken-axisymmetry (BA) phase and a ferromagnetic (FM) phase, making this system an ideal platform for investigating the KZM across discontinuous transitions.

In this Chapter we analytically and numerically investigate the KZM in a 1D FM spin-1 BEC. By quenching the quadratic Zeeman shift, we are able to quench the system through both continuous and discontinuous phase transitions. In particular, we first examine the resulting scaling laws associated with quenching through the continuous phase transition from the polar phase to the BA phase, and confirm that these are in excellent agreement with the KZ theory. Then, we extend the KZM to predict the scaling laws of the discontinuous, first-order phase transition between the BA and FM phases. Quenching the quadratic Zeeman shift allows the system to change from the BA phase into a phase-separated FM phase, where domains with opposing condensate-spin projection develop [96]. We show that, despite this particular transition having a gapless spectrum, the standard KZ theory can be generalised and extended to cover discontinuous, first-order transitions. In addition, scaling behaviour near the critical point is derived by means of linearising the mean-field equations for the spin-1 condensate [66, 172]. Predicted scaling laws are then confirmed by direct numerical simulations.

5.1 The Kibble-Zurek mechanism

Consider a system that undergoes a spontaneous breaking of symmetry when a control parameter, λ, is ramped across a phase transition that occurs at the critical point, λ_c. A continuous, second-order phase transition can be characterized by a divergence of the equilibrium correlation length [64]

$$\xi(\epsilon) \sim |\epsilon|^{-\nu}, \tag{5.1}$$

and an equilibrium relaxation time

$$\tau(\epsilon) \sim \xi^{z} \sim |\epsilon|^{-\nu z}, \tag{5.2}$$

where

$$\epsilon = \frac{\lambda - \lambda_c}{\lambda_c} \tag{5.3}$$

is the dimensionless distance from the critical point. The equilibrium relaxation time τ describes the time it takes for the system to react to an external change of a parameter. In a quantum phase transition, the relaxation time is set by the inverse of an energy gap Δ between the ground state and the first excited state [65, 173]

$$\tau \simeq \Delta^{-1}. \tag{5.4}$$

As we approach the critical point, the energy gap vanishes as

$$\Delta \sim |\epsilon|^{\nu z}. \tag{5.5}$$

The system is initially prepared in a high-symmetry phase ($\epsilon > 0$), but breaks that symmetry as the critical point is crossed ($\epsilon < 0$). In the above equations, the exponents z and ν are the dynamical and correlation length critical exponents, respectively. Different systems which have the same critical exponents are said to belong to the same universality class [63, 64].

The KZM describes the dynamics of crossing the critical point when λ is continually varied. We assume the form of a linear quench (cases concerning non-linear quenches are discussed in Refs. [174, 175]), such that the control parameter can be written as

$$\lambda(t) = \lambda_c \left[1 - \epsilon(t)\right], \tag{5.6}$$

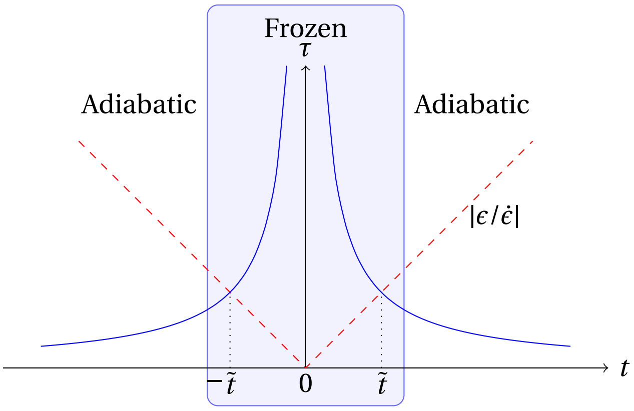

Figure 5.1: A schematic representation of the dynamics of a system during a linear quench. The system starts in a high-symmetry phase ($t > 0$) and is quenched across a critical point to a low symmetry phase ($t < 0$) by the reduced control parameter (red dashed line) $\epsilon(t) = t/\tau_Q$. As the critical point is approached, the equilibrium relaxation time (blue line) diverges, and the order parameter can no longer follow the ground state, leading to frozen dynamics in the interval $t \in [-\tilde{t}, \tilde{t}]$

.

where the distance to the critical point is

$$\epsilon(t) = \frac{t}{\tau_Q}, \tag{5.7}$$

for a quench time τ_Q. This form gives a transition rate $|\dot{\epsilon}/\epsilon| = t^{-1}$ which diverges as we approach the critical point. Here, $t \in [-\tau_Q, \tau_Q]$, where the critical point is reached at $t = 0$. The dynamics of the system can be broken into three stages as ϵ is ramped from $\epsilon > 0$ to $\epsilon < 0$: adiabatic, frozen, and adiabatic again (see Fig. 5.1 for a schematic representation).

Far from the critical point, the equilibrium relaxation time is small compared to the inverse transition rate $|\epsilon/\dot{\epsilon}|$, meaning the system adiabatically follows the instantaneous ground state for $\epsilon(t)$. This stage of adiabaticity lasts until the relaxation time becomes comparable to $|\epsilon/\dot{\epsilon}|$:

$$\tau \approx |\epsilon/\dot{\epsilon}| = \tilde{t}. \tag{5.8}$$

Using Eqs. (5.5) and (5.7), the above equation can be solved to yield the freeze-out time, $\tilde{t}$:

$$\tilde{t} \sim \tau_Q^{\frac{z\nu}{1+z\nu}}. \tag{5.9}$$

After the freeze-out time is passed, however, the relaxation time diverges and the system can no longer keep up with the externally imposed changes. The system then enters the so-called impulse regime, where the dynamics are frozen and remains in this regime until $-\tilde{t}$, when the relaxation time becomes faster than the transition rate once again. The consequence of the impulse region, however, is that the system arrives at $-\tilde{t}$, in which the true ground state is in a broken-symmetry phase, whilst remaining in the state set at $\tilde{t}$, which corresponds to a symmetric phase. This state at $\tilde{t}$ then becomes the initial state for the last adiabatic stage of evolution beginning at $-\tilde{t}$. At this point, the system is no longer in its current ground state and rectifies this by breaking the symmetry of the initial state. This results in the formation of distinct domains in the system whose size is set by the value of the equilibrium correlation length at the freeze-out time

$$\hat{\xi} = \xi(\tilde{t}) \sim \tau_Q^{\frac{\nu}{1+z\nu}}. \tag{5.10}$$

If the system supports topological defects such as vortices, then the defect density is given by

$$N_d \simeq \hat{\xi}^{-d} \sim \tau_Q^{\frac{-d\nu}{1+z\nu}}, \tag{5.11}$$

where d is the number of spatial dimensions. This key result provides a foundation in testing the KZM in subsequent sections, and has already been successfully applied to numerous spinor BEC systems [66, 68, 69, 71, 73] to determine the validity of the KZM.

5.2 Numerical studies of the Kibble-Zurek mechanism across a second-order quantum phase transition

To verify the key results of the KZ theory presented in the previous section, we perform numerical simulations using a spin-1 BEC. As shown in Sec. 3.2, there are four ground state phases of spin-1 BECs; namely, the ferromagnetic, partially-magnetised polar, polar, and broken-axisymmetry phases, where each ground state phase has an associated symmetry. The Kibble-Zurek mechanism can be studied in spin-1 BECs by considering how the change of a control parameter causes the order parameter to change from one ground state to another. As it does this, the symmetry of the system is spontaneously broken, and hence the Kibble-Zurek theory can be applied.

Spin-1 BECs support numerous first- and second-order quantum phase transitions when the linear, p, or quadratic, q, Zeeman shifts are ramped across a critical point [96]. A second-order quantum phase transition is characterised by the continuous first derivatives of the internal energy with respect to variations in p and q at the critical point. In this section, we aim to test the predictions of the Kibble-Zurek mechanism for a second-order quantum phase transition in a spin-1 BEC.

5.2.1 Polar to broken-axisymmetry quench

Motivated by previous work [66], we will investigate the Kibble-Zurek mechanism across the second-order phase transition occurring between the polar and broken-axisymmetry phases in a ferromagnetic spin-1 BEC. The polar phase is the energetic ground state when $Q = q/|c_1|n > 2$. The critical point $Q = 2$ (for $p = 0$) represents the second-order phase transition to the BA phase. The BA phase contains three Bogoliubov modes [172], but only one is non-zero in the long wavelength limit (see Sec. 5.3.2 for further details on Bogoliubov modes in a spin-1 BEC). This mode is gapped, and has the scaling form

$$\Delta \sim \sqrt{4 - Q^2}. \tag{5.12}$$

We temporally vary Q according to

$$Q(t) = 2 - \frac{t}{\tau_Q}, \tag{5.13}$$

where τ_Q^{-1} is the quench rate. To investigate Kibble-Zurek scaling, we consider the freeze-out time, $\tilde{t}$, which occurs when the equilibrium relaxation time is equal to the rate of change of the control parameter [see Eq. (5.8)]. Using the above form of the linear quench, the freeze-out time is calculated as [66]

$$\tilde{t} \sim \tau_Q^{1/3}. \tag{5.14}$$

We now analyse the resulting dynamics when linearly decreasing Q according to Eq. (5.13), starting from the polar phase ($t < 0$) and end the simulation precisely at $Q = 0$ ($t = 2\tau_Q$) in the BA phase. The initial state is a polar wave function that is slightly perturbed:

$$\psi = \left(\delta\psi_1, \frac{1}{\sqrt{L}} + \delta\psi_0, \delta\psi_{-1}\right), \tag{5.15}$$

where $|\delta\psi_m| \ll 1/\sqrt{L}$ are small noise terms and L is the length of the computational domain. The real and imaginary parts of these terms at individual grid points are drawn from the probability distribution $p(x) = \exp\left(-x^2/2\sigma^2\right)/\sqrt{2\pi}\sigma$. To ensure we remain close to the polar ground state, we take $\sigma = 10^{-4}$. We consider a 1D system with $N_x = 2048$ grid points with $L = 78$ and choose dimensionless spin-independent interaction $c_0 = 1.4 \times 10^5$ and $c_0/c_1 = -222$. Note that these choice of parameters give a condensate close to that of ^{87}Rb, in which $c_0/c_1 \approx -111$ (see Sec. 2.5.3). We start with the initial state in Eq. (5.15) and integrate the spin-1 Gross-Pitaevskii equations using a symplectic integrator [176] (see Appendix A.2 for details on the numerical integration scheme).

5.2.2 Evolution of the transverse magnetisation

To determine the freeze-out time within our system, we need to find a quantity that grows as the transition point is crossed. This freeze-out time is then measured by the time it takes for

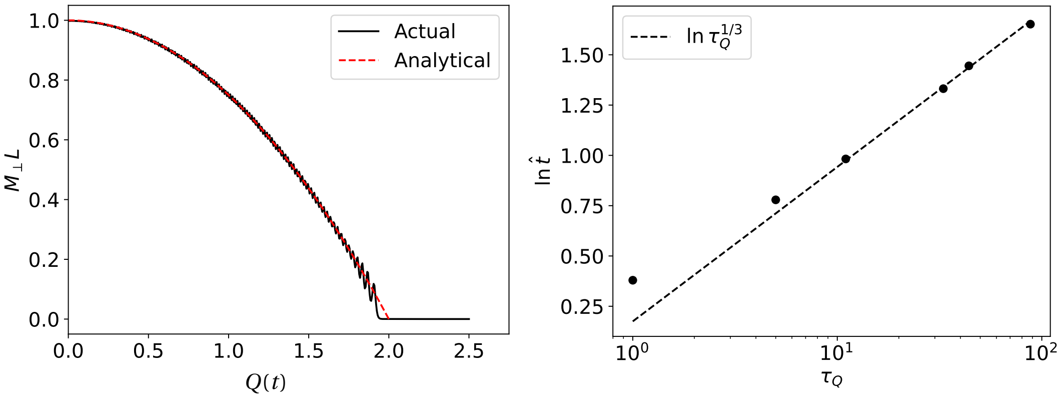

(a) (b)

Figure 5.2: (a) The transverse magnetisation as a function of $Q(t)$ for $\tau_Q = 11$. Plotted are the numerical values (black line) and the analytical prediction (red line). (b) The extracted value of $\tilde{t}$ versus the quench time. Overlaid is the power-law scaling $\tau_Q^{1/3}$.

the onset of that growth to occur. The quantity that satisfies this condition in the polar to BA transition is the transverse magnetisation

$$M_\perp = \int \langle \hat{F}_x^2 \rangle + \langle \hat{F}_y^2 \rangle \, dz, \tag{5.16}$$

where $\hat{F}_x$ and $\hat{F}_y$ are the x, y components of the condensate spin vector, respectively. In the polar phase this quantity is zero, but becomes non-zero in the BA limit where it is $M_\perp = (1 - Q^2/4)/L$. Fig. 5.2a shows a typical evolution of the transverse magnetisation for $\tau_Q = 11$. One sees that after the critical point is crossed at $Q = 2$, the transverse magnetisation grows in a non-trivial fashion. This growth starts precisely after the system exits the freeze-out stage, which occurs at $t = \tilde{t}$. The magnetisation then grows rapidly, exceeding the analytical prediction at certain time intervals, and begins to oscillate with the amplitude of the oscillation decaying over time. Using this quantity, we can test the Kibble-Zurek prediction in Eq. (5.9).

We define $\tilde{t}$ as the instant when $M_\perp L$ intersects 1% of the maximum value given by $M_\perp L = 1$. Fig 5.2b shows the extracted value of $\tilde{t}$ for a range of τ_Q. We see an unambiguous power-law scaling of $\tau_Q^{1/3}$ for $\tau_Q \geq 10$. The gradual departure from the $\tilde{t} \sim \tau_Q^{1/3}$ scaling indicates that the quench has to be sufficiently slow to capture the Kibble-Zurek scaling. We note that the choice of the 1% threshold used here is arbitrary. We have tested a range of values up to a maximum of 10%, and obtain quantitatively similar behaviour for all values tested.

5.3 Extending the Kibble-Zurek theory to first-order quantum phase transitions

The preceding sections were concerned with the KZM across second-order phase transitions. Describing the KZM across discontinuous, first-order transitions, however, has been difficult due to lack of universality [177–179]. More recent work has aimed to bridge the gap between the KZM and first-order transitions [170], and here we present an overview of how the KZM can be adapted to describe a discontinuous phase transition that will form the focus in the remainder of this chapter.

Fisher and Berker [171] demonstrated that first-order phase transitions occurring at a DCP can also give rise to scaling behaviour. Such a DCP results in a discontinuity in the order parameter as the critical point is passed. Despite this, the transition can still be characterised by a divergent length scale, and hence, critical exponents can be derived. Suzuki *et al.* [170] aimed to extend the notion of a DCP to a DQCP, of which we will summarise here. Let us consider a system that contains a critical point at $q = q_c$, where q is a tunable parameter and contains the presence of a symmetry-breaking field, p. For one to have a DQCP five conditions need to be satisfied. Firstly, the energy density $\epsilon(q,p)$ must be a continuous function of q and p across the critical point

$$\epsilon(q_c+0,0)=\epsilon(q_c-0,0). \tag{5.17}$$

The derivative of this energy density, however, is discontinuous

$$\frac{\partial\epsilon(q_c+0,0)}{\partial q}\neq\frac{\partial\epsilon(q_c-0,0)}{\partial q}. \tag{5.18}$$

The order parameter $m(q,p)$, where $m=-\frac{\partial\epsilon(q,p)}{\partial p}$, has a discontinuous jump as a function of q as the critical point is passed

$$|m(q_c-0,0)|>|m(q_c+0,0)|=0, \tag{5.19}$$

whilst also having a discontinuous jump as a function of p

$$|m(q_c,\pm 0)|>0. \tag{5.20}$$

Finally, we require that the derivative of the energy density be bounded as $q\to q_c\pm 0$

$$\left|\frac{\partial\epsilon(q_c\pm 0,0)}{\partial q}\right|<\infty. \tag{5.21}$$

These five conditions encapsulate a DQCP.

5.3.1 The Broken-axisymmetry to ferromagnetic transition as a discontinuous quantum critical point

Let us now consider a specific example. We are interested in the phase transition that occurs between the BA and FM phases. The energy densities for the two states are given by [96]

$$\epsilon_{\mathrm{BA}} = \frac{(-p^2+q^2+2qc_1n)^2}{8c_1nq^2} + \frac{1}{2}c_0n, \qquad \epsilon_{\mathrm{FM}_\pm} = \mp p + q + \frac{1}{2}n(c_0+c_1), \tag{5.22}$$

where $\epsilon_{\mathrm{FM}_\pm}$ corresponds to the energy density in the FM phase for the spinor $\zeta = (1,0,0)^T$ (+) and $\zeta = (0,0,1)^T$ (-). One sees that at the critical point $q = q_c = 0$ and $p = 0$ the energy is continuous. On the other hand, the derivative of the above energies with respect to q yields

$$\frac{\partial\epsilon_{\mathrm{BA}}}{\partial q} = \frac{1}{4c_1n}\left(q - \frac{p^4}{q^3}\right) - \frac{p^2}{q^2} + \frac{1}{2}, \qquad \frac{\partial\epsilon_{\mathrm{FM}_\pm}}{\partial q} = 1. \tag{5.23}$$

Indeed, there is a discontinuity in these derivatives at $q = p = 0$, although they still remain bounded. The relevant order parameters for this transition are given by

$$m_{\mathrm{BA}} = \frac{p(p^2-q^2-2qc_1n)}{8c_1nq}, \qquad m_{\mathrm{FM}_\pm} = \pm 1, \tag{5.24}$$

which is precisely the local magnetisation, $\hat{F}_z = |\psi_1|^2 - |\psi_{-1}|^2$, in both phases (see Sec. 3.2). Again, one sees that at the critical point and for $p = 0$ the order parameter becomes zero in the BA phase whilst becoming non-zero in the FM phase. In addition, as the linear Zeeman shift p is varied both above and below zero, the order parameter becomes non-zero. We have shown that the BA to FM phase transition satisfies all conditions specified in Eqs. (5.17) - (5.21) and therefore is a DQCP.

5.3.2 Determining the relevant Bogoliubov mode

In order to determine the relevant energy spectrum for our system, we consider the Bogoliubov modes of the BA phase of a spin-1 BEC, which we derive explicitly from the relevant Bogoliubov transformations. The broken-axisymmetry phase can be parameterised as [172]

$$\zeta^{\mathrm{BA}} = \left(\frac{\sin\theta}{\sqrt{2}}, \cos\theta, \frac{\sin\theta}{\sqrt{2}}\right), \tag{5.25}$$

where $\sin\theta = \sqrt{1/2 + q/(4nc_1)}$. Then, the fluctuation operators for this state are then defined as [172]:

$$\hat{a}_{\mathbf{k},d} = \frac{\sin\theta}{\sqrt{2}}(\hat{a}_{\mathbf{k},1} + \hat{a}_{\mathbf{k},-1}) + \cos\theta\,\hat{a}_{\mathbf{k},0}, \tag{5.26}$$

$$\hat{a}_{\mathbf{k},f_z} = \frac{1}{\sqrt{2}}(\hat{a}_{\mathbf{k},1} - \hat{a}_{\mathbf{k},-1}), \tag{5.27}$$

$$\hat{a}_{\mathbf{k},\theta} = \frac{\cos\theta}{\sqrt{2}}(\hat{a}_{\mathbf{k},1} + \hat{a}_{\mathbf{k},-1}) - \sin\theta\,\hat{a}_{\mathbf{k},0}, \tag{5.28}$$

where on the right-hand side $\hat{a}_{\mathbf{k},m}$ is the annihilation operator for a spin-1 boson in magnetic level m (for $m = -1, 0, +1$), determined by expanding the wave function field operator as

$$\hat{\psi}_m(\mathbf{x}) = \frac{1}{\sqrt{V}}\sum_{\mathbf{k}} \hat{a}_{\mathbf{k},m} e^{i\mathbf{k}\cdot\mathbf{x}}, \tag{5.29}$$

where V is the volume of the system.

The sub-Hamiltonian for the spin fluctuation mode $\hat{a}_{\mathbf{k},f_z}$ can be diagonalised using the transformation

$$\hat{b}_{\mathbf{k},f_z} = \sqrt{\frac{\epsilon_{\mathbf{k}} + q/2 + E_{\mathbf{k},f_z}}{2E_{\mathbf{k},f_z}}}\,\hat{a}_{\mathbf{k},f_z} + \sqrt{\frac{\epsilon_{\mathbf{k}} + q/2 - E_{\mathbf{k},f_z}}{2E_{\mathbf{k},f_z}}}\,\hat{a}^{\dagger}_{-\mathbf{k},f_z}, \tag{5.30}$$

where $\epsilon_{\mathbf{k}} = \hbar^2|\mathbf{k}|^2/2M$ is the kinetic energy. The Bogoliubov spectrum is then given by

$$E_{\mathbf{k},f_z} = \sqrt{\epsilon_{\mathbf{k}}(\epsilon_{\mathbf{k}} + q)}. \tag{5.31}$$

The sub-Hamiltonians for the density fluctuation mode $\hat{a}_{\mathbf{k},d}$ and the θ mode $\hat{a}_{\mathbf{k},\theta}$ can be similarly diagonalised using operators $\hat{b}_{\mathbf{k},+}$ and $\hat{b}_{\mathbf{k},-}$, which yields the remaining two Bogoliubov modes [172]:

$$E_{\mathbf{k},\pm} = \sqrt{\epsilon_{\mathbf{k}}^2 + n(c_0 - c_1)\epsilon_{\mathbf{k}} + 2(nc_1)^2(1 - \tilde{q}^2) \pm E_1(\mathbf{k})}, \tag{5.32}$$

where $\tilde{q} = -q/2c_1 n$ and

$$E_1(\mathbf{k}) = \sqrt{\left[n(c_0 + 3c_1)\epsilon_{\mathbf{k}} + 2(c_1 n)^2(1 - \tilde{q}^2)\right]^2 - 4c_1(c_0 + 2c_1)(n\tilde{q}\epsilon_{\mathbf{k}})^2}. \tag{5.33}$$

The final, diagonalised Hamiltonian then reads

$$\hat{H}^{\mathrm{BA}} = E_0^{\mathrm{BA}} + \sum_{\mathbf{k}\neq 0}\left[E_{\mathbf{k},f_z}\hat{b}^{\dagger}_{\mathbf{k},f_z}\hat{b}_{\mathbf{k},f_z} + E_{\mathbf{k},-}\hat{b}^{\dagger}_{\mathbf{k},-}\hat{b}_{\mathbf{k},-} + E_{\mathbf{k},+}\hat{b}^{\dagger}_{\mathbf{k},+}\hat{b}_{\mathbf{k},+}\right], \tag{5.34}$$

where E_0^{BA} is the ground state energy for the BA phase [172].

For simplicity, we now consider a 1D system. In the long-wavelength limit ($k \to 0$), the only non-zero (gapped) mode is given by $E_{k,+} = \sqrt{4(c_1 n)^2(1 - \tilde{q})}$, which has the form $E_{k,+} \sim$

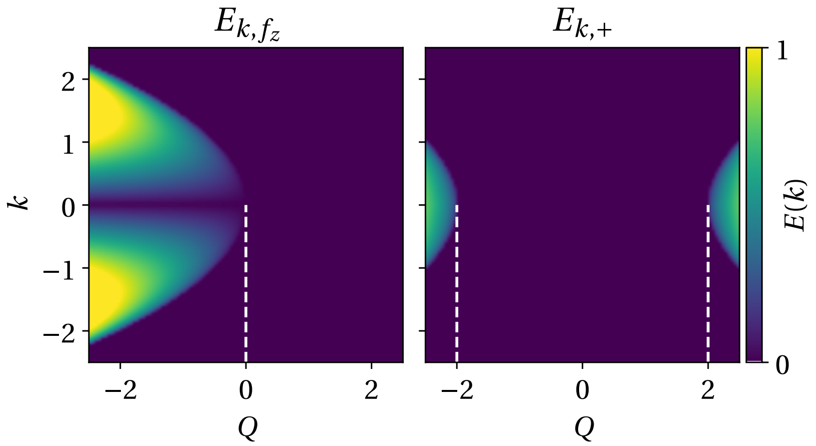

Figure 5.3: Imaginary parts of the energies defined in Eq. (5.31) and Eq. (5.32) in a parameter space of mode k and $Q = q/|c_1|n$. Note that $E_{k,-} = 0$ for our range of k and hence is not shown.

$\sqrt{q_c'^2 - q^2}$, where $q_c' = 2c_1 n$. The relevant mode for the BA to FM transition can be found by considering the imaginary parts of the derived Bogoliubov energies (see Fig. 5.3). For $|Q| > 2$, $\mathrm{Im}(E_{k,+})$ becomes non-zero, indicating an instability. The critical point $Q = 2$ corresponds to the second-order phase transition from the polar to the BA phase, indicating that $E_{k,+}$ is the desired Bogoliubov energy for that particular transition. However, we see that for $Q < 0$ the imaginary part of E_{k,f_z} becomes non-zero, and hence unstable. This critical point corresponds to the transition between the BA and FM phases, which precisely describes our transition of interest. Therefore, E_{k,f_z} is the correct Bogoliubov mode for our transition. Note that for $k = 0$ an instability does not occur in the E_{k,f_z} mode, and so studies focussing on this mode in particular (the so-called uniform mode approximation) will not capture the phase transition that occurs at $Q = 0$ [75, 180, 181]. In contrast, choosing the $k = 0$ mode is sufficient to capture the phase transition at $Q = 2$ since it is the most unstable mode indicated in $E_{k,+}$. In practice, the $Q = -2$ transition is not realised since the instability at $Q = 0$ for any $k \neq 0$ will typically arise and take precedent when Q is quenched from positive to negative values.

5.3.3 Predicting the density of defects

Recall from Sec 5.1 that the density of defects takes the form $N_d \simeq \xi^{-d}$. Therefore, to predict the density of defects for the BA to FM transition, we need to find the appropriate form for the correlation length, ξ. With the relevant Bogoliubov mode found, we can predict the scaling of the density of defects for a BA to FM phase transition. Since our relevant mode is gapless, it is instructive to consider a generalisation of the spectrum, given by

$$E_k^2 \sim |q(t) - q_c|^\alpha \epsilon_k^\eta + \epsilon_k^{2z}. \tag{5.35}$$

We focus on the case of approaching the critical point from the BA phase, since this determines the crossover from the adiabatic regime to the impulse regime which sets the metastable state after the DQCP is crossed. To be consistent with the KZM, where $E_k \sim |q(t) - q_c|^z$, we make the ansatz $k \sim \xi^{-1} \sim |q(t) - q_c|^\nu$, equivalent to $k \sim \xi^{-1}$. For a scaling solution to arise that is consistent with the relaxation time, we require $E_k \sim k^z$. This, combined with Eq. (5.35), leads us to the relation

$$\alpha = \nu(2z - \eta). \tag{5.36}$$

Now, in our system, we have $q_c = 0$ and $q = -t/\tau_Q$ and thus Eq. (5.35) simplifies to

$$E_k^2 \sim \frac{|t|^\alpha}{\tau_Q^\alpha} k^\eta. \tag{5.37}$$

Recall now the adiabatic-impulse approximation described in Sec. 5.1, with an energy gap given by $\Delta(t)$. In this case, the relaxation time scales as $\tau \sim 1/\Delta$, which implies that far from the critical point the relaxation time is small, and the system adiabatically follows the instantaneous ground state. However, as the critical point is approached $\Delta \to 0$, and the relaxation time then diverges. At some time $\tilde{t}$ the relaxation time becomes comparable to the transition time, $\Delta/\dot{\Delta}$, and the system can no longer adiabatically follow the ground state. This time (often denoted the freezing time), $\tilde{t}$, signifies the onset of the impulse regime, where the system becomes frozen. Therefore, the freezing time can be evaluated from the expression

$$\frac{1}{\Delta(\tilde{t})} \sim \frac{\Delta(\tilde{t})}{\dot{\Delta}(\tilde{t})}. \tag{5.38}$$

For our gapless spectrum, we work with a dispersion relation of the form given by Eq. (5.37). Then, the adiabatic-impulse approximation states that $E_k^2 = \dot{E}_k$, which leads to

$$\frac{\alpha}{2\tau_Q^{\alpha/2}} |\tilde{t}|^{(\alpha/2-1)} \tilde{k}^{\eta/2} \sim \frac{|\tilde{t}|^\alpha}{\tau_Q^\alpha} \tilde{k}^\eta, \tag{5.39}$$

which then leads us directly to the freezing time

$$|\tilde{t}| \sim \tau_Q^{\alpha/(2+\alpha)} \tilde{k}^{-\eta/(2+\alpha)} \sim \tau_Q^{\nu z/(1+\nu z)}. \tag{5.40}$$

Now, to obtain the characteristic momentum scale, we substitute Eq. (5.40) back into Eq. (5.37), which yields

$$\tilde{k} \sim \tau_Q^{-\nu/(z\nu+1)}. \tag{5.41}$$

The density of defects is then finally calculated as

$$N_d \sim \tilde{k}^d \sim \tau_Q^{-d\nu/(z\nu+1)}, \tag{5.42}$$

where d is the dimensionality of the system. Hence, we have shown how the density of defects can be predicted for a system containing a gapless spectrum.

For the BA to FM transition specifically, Eq. (5.31) implies that $\alpha = 1$, $\eta = 2$, and $z = 2$. Considering a 1D system ($d = 1$), that leads to a scaling of the density of defects as

$$N_d \sim \tau_Q^{-1/4}, \tag{5.43}$$

which corresponds to choosing $z = 2$ and $\nu = 1/2$ in Eq. (5.11). Despite the Hamiltonian of our model being the same as previous works, this scaling obtained is different from that reported in previous studies on the KZM in spinor BECs [66, 68, 69, 71, 182]. These studies focused on continuous phase transitions through a QCP, and our results indicate a new scaling regime that is associated specifically with the DQCP of this system.

5.3.4 Extracting a power-law scaling near the critical point

Having identified the relevant mode of the transition, we now follow a procedure similar to Damski [66] and analytically determine the scaling behaviour of the system near the critical point by linearising our system of equations. To begin, we start with a wave function close to the BA state

$$\Psi^T = \left(\frac{\sqrt{2n_0}}{4}\sqrt{2-Q_0} + \delta\psi_1(t), \frac{\sqrt{n_0}}{2}\sqrt{2+Q_0} + \delta\psi_0(t), \frac{\sqrt{2n_0}}{4}\sqrt{2-Q_0} + \delta\psi_{-1}(t)\right) e^{-i\mu t}, \tag{5.44}$$

where $0 < Q_0 < 2$ is a constant, μ is the chemical potential and $|\delta\psi_m| \ll 1$ are time-dependent noise terms. The noise terms must satisfy $\int \sum_m \delta\psi_m + \delta\psi_m^* \, \mathrm{d}z$ to ensure normalisation of the wave function. Additionally, they must also satisfy $\int (\delta\psi_1 + \delta\psi_1^* \delta\psi_{-1} + \delta\psi_{-1}^*) \mathrm{d}z = 0$ to ensure that magnetisation is conserved.

Recall the spin-1 GPEs are given as (see Sec. 2.4.1):

$$i\hbar\frac{\partial\Psi}{\partial t} = \left[-\frac{\hbar^2\nabla^2}{2M} - pf_z + qf_z^2 + c_0 n + c_1 n\langle\hat{\mathbf{F}}\rangle\cdot\hat{\mathbf{F}}\right]\Psi. \tag{5.45}$$

Substituting Eq. (5.44) into the above equations and keeping terms linear in $\delta\psi_m$ yields the following two equations for $\delta\psi_{\pm1}$ $(p=0)$

$$\begin{aligned} i\hbar\frac{\partial\delta\psi_1}{\partial t} = &\left[-\frac{\hbar^2}{2M}\frac{\partial^2}{\partial z^2}+q-\mu+\frac{n_0(10c_0+6c_1-(c_0-c_1)Q)}{8}\right]\delta\psi_1 \\ &+\frac{n_0\sqrt{2(4-Q^2)}}{8}\left[(c_0+3c_1)\delta\psi_0+(c_0+c_1)\delta\psi_0^*\right] \\ &+\frac{n_0(2-Q)}{8}\left[(c_0-c_1)\delta\psi_{-1}+(c_0+c_1)\delta\psi_1^*\right]+\frac{n_0}{8}\left[(2-Q)c_0+(2+3Q)c_1\right]\delta\psi_{-1}^*, \end{aligned} \tag{5.46}$$

$$\begin{aligned} i\hbar\frac{\partial\delta\psi_{-1}}{\partial t} = &\left[-\frac{\hbar^2}{2M}\frac{\partial^2}{\partial z^2}+q-\mu+\frac{n_0(10c_0+6c_1-(c_0-c_1)Q)}{8}\right]\delta\psi_{-1} \\ &+\frac{n_0\sqrt{2(4-Q^2)}}{8}\left[(c_0+3c_1)\delta\psi_0+(c_0+c_1)\delta\psi_0^*\right] \\ &+\frac{n_0(2-Q)}{8}\left[(c_0-c_1)\delta\psi_1+(c_0+c_1)\delta\psi_{-1}^*\right]+\frac{n_0}{8}\left[(2-Q)c_0+(2+3Q)c_1\right]\delta\psi_1^*. \end{aligned} \tag{5.47}$$

Now, subtracting Eq. (5.47) from Eq. (5.46) results in the partial differential equation

$$i\hbar\frac{\partial G_y}{\partial t}=\left[-\frac{\hbar^2}{2M}\frac{\partial^2}{\partial z^2}+q-\mu+n_0(c_0+c_1)\right]G_y-\frac{c_1n_0Q}{2}G_y^*, \tag{5.48}$$

where $G_y=\delta\psi_1-\delta\psi_{-1}$. The chemical potential of the system is calculated from the ψ_0 component of Eq. (5.45) by keeping leading order terms and assuming a stationary state which leads to $\mu=c_0n_0+c_1n_0(2-Q_0)/2$. Using this expression for the chemical potential and $q(t)=-c_1n_0Q(t)$ Eq. (5.48) simplifies to

$$i\hbar\frac{\partial G_y}{\partial t}=\left[-\frac{\hbar^2}{2M}\frac{\partial^2}{\partial z^2}-c_1n_0\left(Q-\frac{Q_0}{2}\right)\right]G_y-\frac{c_1n_0Q}{2}G_y^*. \tag{5.49}$$

To proceed with our analysis, we now split G_y into real and imaginary parts and make use of Fourier transforms, $a_y=\int\mathrm{Re}(G_y)e^{ikz}dz$ and $b_y=\int\mathrm{Im}(G_y)e^{ikz}dz$ to progress our analysis. Substituting these expressions in Eq. (5.49) yields the following matrix equation

$$\frac{\mathrm{d}}{\mathrm{d}t}\begin{bmatrix}a_y\\ b_y\end{bmatrix}=\begin{pmatrix}0 & \frac{\hbar k^2}{2M}-\frac{c_1n_0}{2\hbar}(Q-Q_0)\\ \frac{c_1n_0}{2\hbar}(3Q-Q_0)-\frac{\hbar k^2}{2M} & 0\end{pmatrix}\begin{bmatrix}a_y\\ b_y\end{bmatrix}. \tag{5.50}$$

To solve the above system of equations, we rewrite the equation in terms of a single $\frac{\mathrm{d}^2a_y}{\mathrm{d}t^2}$ and substitute the critical point value $Q=0$ to obtain

$$\frac{\mathrm{d}^2a_y}{\mathrm{d}t^2}=\frac{c_1n_0}{2\hbar\tau_Q}b_y+\left(\frac{\hbar^2k^2}{2M}-\frac{c_1n_0Q}{2\hbar}\right)\frac{\mathrm{d}b_y}{\mathrm{d}t}. \tag{5.51}$$

Now, expressions for b_y and $\frac{\mathrm{d}b_y}{\mathrm{d}t}$ can be found from Eq. (5.50), which transforms the above equation to

$$\frac{\mathrm{d}^2 a_y}{\mathrm{d}t^2} = \frac{1}{\tau_Q\left(\frac{\hbar^2 k^2}{Mc_1 n_0} - Q\right)}\frac{\mathrm{d}a_y}{\mathrm{d}t} - \left(\frac{\hbar^2 k^4}{4M^2} - \frac{k^2 c_1 n_0 Q}{M} + \frac{3c_1^2 n_0^2 Q^2}{4\hbar^2}\right)a_y. \tag{5.52}$$

Finally, to simplify the above expression, we use the spin healing length $\xi_s = \hbar/\sqrt{2|c_1|n_0}$ and the spin time $\tau_s = \hbar/(|c_1|n_0)$, along with the substitution $Q = -t/\tau_Q$:

$$\frac{\mathrm{d}^2 a_y}{\mathrm{d}t^2} = \frac{-1}{\left(2\xi_s^2 k^2 \tau_Q - t\right)}\frac{\mathrm{d}a_y}{\mathrm{d}t} - \left(\frac{\xi_s^4 k^4}{4\tau_s^2} - \frac{\xi_s^2 k^2 t}{2\tau_s^2\tau_Q} + \frac{3t^2}{16\tau_s^2\tau_Q^2}\right)a_y. \tag{5.53}$$

Now, to extract scaling solutions, we rescale time as $t \to t\lambda$ where $\lambda = \sqrt{\tau_s\tau_Q}$, which leads to the final differential equation

$$\frac{\mathrm{d}^2 a_y}{\mathrm{d}t^2} = \frac{-1}{\left(2\kappa^2 - t\right)}\frac{\mathrm{d}a_y}{\mathrm{d}t} - \frac{1}{4}\left(\kappa^4 - 2\kappa^2 t + \frac{3t^2}{4}\right)a_y, \tag{5.54}$$

where $\kappa^2 = \xi_s^2 k^2 \sqrt{\tau_Q/\tau_s}$. This scaling ensures that the last term of the above equation is independent of τ_Q. Then, the remaining dependence on τ_Q is eliminated if we require that κ is constant, implying that $k \sim \tau_Q^{-1/4}$. Under these conditions, we have now, independent of the KZM, derived scaling solutions for k, which are seen to be consistent with the alternatively derived scaling of the density of defects following the KZ theory (compare the above scaling for k with the density of defects given in Eq. (5.43)). The main advantage of this approach over the KZM is in treating the time-dependence of the quadratic Zeeman shift directly rather than working with instantaneous dispersion relation as in the standard KZM. The agreement of the scaling obtained from the two methods provides further verification of the validity of the arguments used to extend the KZM to our gapless spectrum.

5.4 Numerical studies of the Kibble-Zurek mechanism across a discontinuous quantum phase transition

5.4.1 Broken-axisymmetry to ferromagnetic quench

To check our predictions, we perform numerical simulations of a spin-1 Bose-Einstein condensate crossing a DQCP. We start from the BA wave function with ($p = 0$):

$$\psi_{\pm 1} = \frac{\sqrt{2n_0}}{4}\sqrt{2 - Q(t)}, \qquad \psi_0 = \frac{\sqrt{n_0}}{2}\sqrt{2 + Q(t)}, \tag{5.55}$$

where $Q(t) = q(t)/|c_1|n$ and n_0 is the background density in a uniform system. The BA wave function is the ground state for $c_1 < 0$ and $0 < Q < 2$. There exists a critical point at $Q = 0$

where the ground state changes from the BA phase to the ferromagnetic phase. To check our predictions of the previous section we perform mean-field numerical simulations of this quench by integrating the spin-1 GPEs using a symplectic integrator [176] (see Appendix A.2 for details on the numerical integration scheme). We measure length and time in units of the spin healing length, ξ_s, and the spin time, τ_s, respectively. Our simulations are performed on a 1D grid of $N_z = 16384$ grid points with a grid spacing of $\Delta_z = 0.125\xi_s$, and we consider a ring-shaped geometry by assuming periodic boundary conditions and $V(z) = 0$. We follow the same methodology as in the continuous QPT discussed in Sec. 5.2.1 and perturb the initial BA state by adding small noise, δ_m, to each component where $|\delta_m| \ll 1$. Then, we generate the real and imaginary parts of δ_m for each grid point using the probability distribution $p(z) = e^{-z^2/2\sigma^2}(\sqrt{2\pi}\sigma)^{-1}$, choosing $\sigma = 10^{-4}$ so that we start close to the BA ground state.

5.4.2 Phase boundaries in the ferromagnetic phase

As the system is quenched across the critical point at $Q = 0$, the ground state changes to the ferromagnetic phase. The order parameter for this phase takes the form $\psi = (\sqrt{n_0}, 0, 0)^T$ or $\psi = (0, 0, \sqrt{n_0})^T$ depending on the orientation of the spin. From Eq. (5.55), however, we have $\psi_{\pm1} = \frac{\sqrt{n_0}}{2}$ and $\psi_0 = \frac{\sqrt{2n_0}}{2}$ at $Q = 0$. The question that remains is: Which state will the system choose after the critical point is passed?

Fig. 5.4 shows the full evolution of the density of each component for a quench time $\tau_Q = 1000\tau_s$. As the Zeeman shift is quenched, we see the density of the ψ_0 component linearly decrease as the $\psi_{\pm1}$ components increase. After the critical point at $t/\tau_s = 0$ is passed, there is a freeze-out time (see Sec. 5.1) before the system crosses into the ferromagnetic phase. During this new phase, we see the formation of ferromagnetic domain walls (characterised by the bright density peaks) in the $\psi_{\pm1}$ components as the order parameter adjusts to the new ground state. These domains are spatially separated and where there is zero density in one of the components, there is maximal density in the other, so that overall the total density $n = \sum_m \psi_m^* \psi_m$ is uniform.

The KZM predicts in Eq. (5.10) that the size of the domains grow as the quench rate decreases. Fig. 5.5a shows the average domain size for two different simulations with $\tau_Q = 500$ and $\tau_Q = 5000$. We see that the quench with larger τ_Q produces domains that have a larger width than those of faster quenches, supporting the Kibble-Zurek theory. In addition, we plot the time evolution of $|\psi_1|^2$ for $\tau_Q = 500$ and $\tau_Q = 1000$ in Fig. 5.5b. We see the ferromagnetic domain formation is delayed in the simulation with a slower quench rate, again supporting the prediction in Eq. (5.9).

One can count the number of ferromagnetic domains in the system and see the depen-

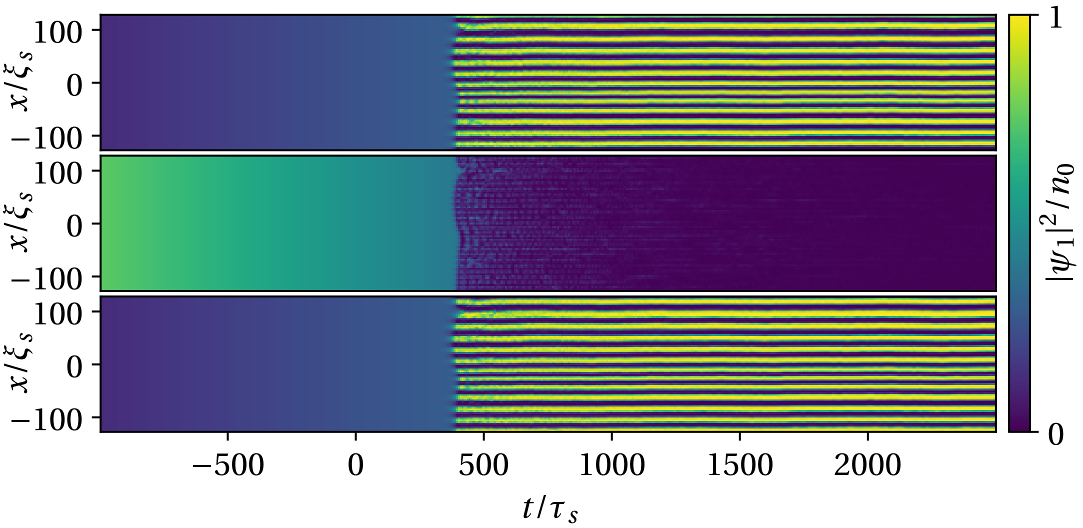

Figure 5.4: Plots of $|\psi_1|^2$ (top) $|\psi_0|^2$ (middle) and $|\psi_{-1}|^2$ (bottom) as a function of time for a $256\xi_s$ spatial subregion of the condensate for $\tau_Q = 1000\tau_s$. After the critical point is passed ($t/\tau_s = 0$), FM domains form in the $\psi_{\pm1}$ components, indicated by the bright density peaks. The location of a bright density peak in one component matches with a density minimum in the other component, showcasing the opposite spin-projection.

dence on τ_Q. To do this, we identified that each domain is associated with a corresponding density peak, and subsequently developed a numerical algorithm that counts the number of density peaks in each component and sums the result to give the total number of domains, N_d. We calculate this quantity at the end of each simulation to ensure that the domains are frozen and avoid the early-time coarsening taking place which could affect the total number of domains present. In Fig. 5.6 we plot the total number of domains as a function of the quench time, where each point represents fifty ensemble runs for each simulation. We find excellent agreement with the predicted value of $N_d \sim \tau_Q^{-1/4}$ for sufficiently fast quenches ($\tau_Q < 2 \times 10^3$). However, for slower quenches, a clear deviation from the predicted scaling occurs. Similar deviation from the predicted KZM scaling has been observed in other works where the quantities investigated were measured far past the critical point [71, 183]. The deviation observed in our system can be attributed to a crossover into a different regime that follows the predictions of a Landau-Zener model [168, 169, 173, 184].

5.4.3 Power-law scaling near the critical point

Since we know the relevant unstable mode within our system, we can investigate power-law scaling near the critical point. To begin, we start with the fluctuation operator associated

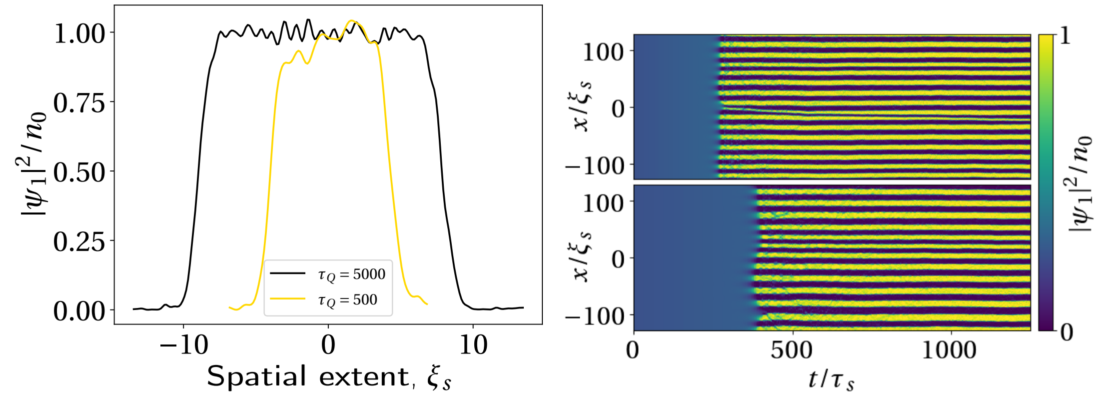

(a) (b)

Figure 5.5: (a): Density profile of the ψ_1 component across an average domain in a simulation with $\tau_Q = 5000\tau_s$ (black line) and $\tau_Q = 500\tau_s$ (gold line). Domain size appear proportional to the quench time τ_Q, with slower quenches having large domains, which supports the KZ theory (see Eq. (5.10)). (b): Time evolution of $|\psi_1|^2$ for a $256\xi_s$ spatial subregion for $\tau_Q = 500\tau_s$ (top) and $\tau_Q = 1000\tau_s$ (bottom) showcasing the difference in the time it takes for domain formation to occur, which faster quenches leading to an earlier onset of domain formation when compared with slower quenches.

with the Bogoliubov spectrum $E_{k,fz}$ given in Eq. (5.27). Fig. 5.7a shows the above quantity for a quench time of $\tau_Q = 5000$ with $k = 1$. The quantity remains zero until after the critical point is passed, where a rapid period of growth occurs. This onset of this growth corresponds to the ferromagnetic domains forming within the system (see Fig. 5.4). Motivated by previous work [66, 75], we define a time, $\tilde{t}$, which is the time when $|\hat{a}_{k,f_z}|$ first exceeds 1% of its maximum value: $|\hat{a}_{k,f_z}(\tilde{t})| = 0.01 \times \max|\hat{a}_{k,f_z}(t)|$. Using this time, we can extract the critical value of q that this growth occurs at, $Q(\tilde{t}) = Q_a$. Fig. 5.7b shows $|Q_a|$ as a function of the quench time. We see a clear power-law scaling of $Q_a \sim \tau_Q^{-\frac{1}{2}}$ for all values of τ_Q tested. This exponent differs from observed results in previous works investigating second-order phase transitions [66, 71, 73] where an exponent of $-1/3$ is observed. Our observation of a $-1/2$ exponent signifies a deviation from the Kibble-Zurek theory which appears to be a consequence of the properties of the DQCP.

5.4.4 Crossing two phase transitions

To test the robustness of the observed scaling, we combine the effort of the previous two numerical studies into one. Namely, we investigate the scaling of the density of defects using a simulation that spans two phase transitions. Starting from the polar phase at $Q = 2.5$, we quench the quadratic Zeeman shift such that we cross over to the BA phase at $Q = 2$ and

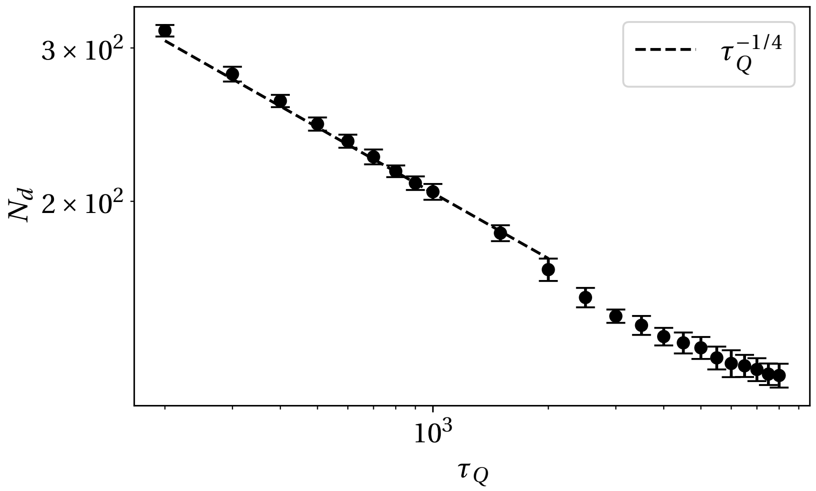

Figure 5.6: The number of ferromagnetic domains as a function of the quench time. Each point represents 50 simulations and the error bar gives one standard deviation. Overlaid is the scaling line $\tau_Q^{-1/4}$ (black dashed line), which confirms the prediction in Eq. (5.43) for $\tau_Q \lesssim 10^3$.

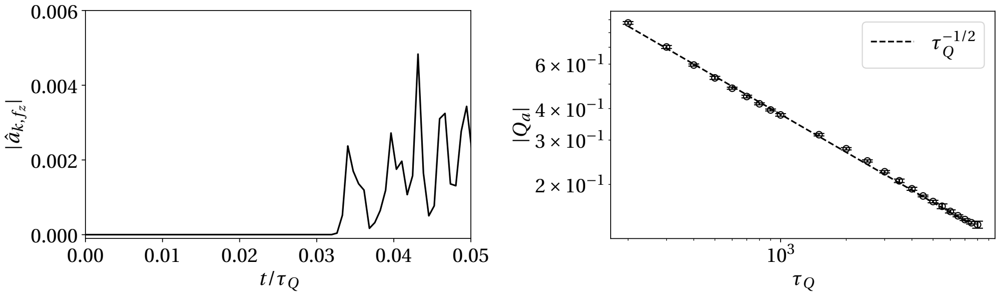

(a) (b)

Figure 5.7: (a): The modulus of the fluctuation operator in Eq. (5.27) for $k = 1$ and $\tau_Q = 5000$. The plot shown is obtained by averaging over all runs in the ensemble. (b): The critical value $|Q_a|$ as a function of the quench time. Each point represents an ensemble of 50 runs, and the error bars give ±1 standard deviation.

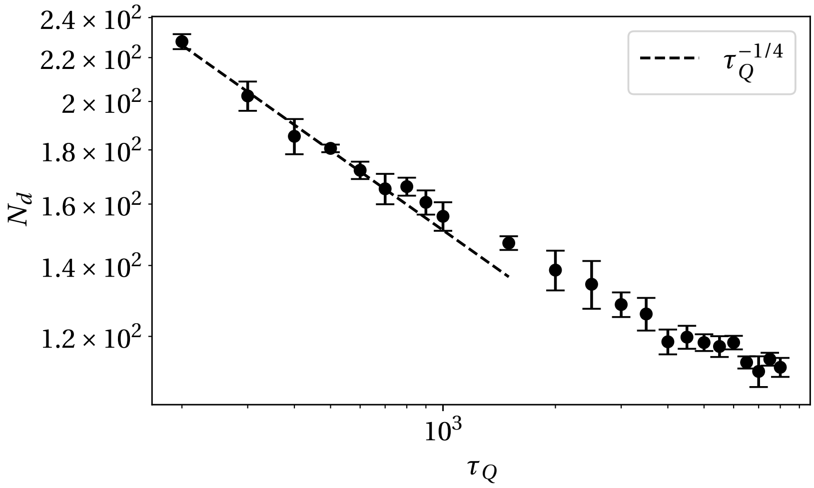

Figure 5.8: Number of ferromagnetic domains as a function of the quench time, τ_Q, after the system has crossed two phase transitions. Each point is averaged over 5 runs, with the error bars giving ±1 standard deviation.

finally the FM phase at $Q = 0$. This quench then evidently spans two phase transitions: one second-order, and one first-order. Our numerical set up is exactly the same as the previous section.

We once again count the number of ferromagnetic domains present at the end of the simulation when the system is in the FM phase. Results for the density of defects are plotted in Fig. 5.8. Despite passing through two phase transitions, we observe qualitatively similar behaviour to that of previous transition crossing only the first-order phase transition (see Fig. 5.6). For fast quenches ($\tau_Q \lesssim 10^3$), the scaling of the density of defects follows closely to $N_d \sim \tau_Q^{-1/4}$. Similar to the previous case, there is a deviation from this scaling when the quench time becomes slower ($\tau_Q > 10^3$). This shows that the scaling of the density of defects for fast quenches is robust, and is unaffected by passing through other phase transitions.

5.5 Conclusions

In this chapter we have investigated the KZM across both second-order, continuous QPTs and first-order, discontinuous QPTs using a spin-1 BEC with $c_1 < 0$as a test bed system. We initially reproduced a known result, and showed that the KZM accurately predicted observed scaling laws across a second-order, continuous QPT in a spin-1 BEC between the polar and BA phases. In particular, we measured the freeze-out time directly by measuring the time at which the transverse magnetisation (initially zero in the polar phase) became non-zero after crossing to the BA phase.

The primary work of this chapter consisted of analytical and numerical investigations into a first-order, discontinuous QPT across the BA and FM phases in a spin-1 BEC with $c_1 < 0$. We showed that by accounting for a gapless dispersion relation, the KZM can be generalised to such a discontinuous QPT, which, for our spin-1 system in question, lead to a scaling of the density of defects as $N_d \sim \tau_Q^{-1/4}$. The observed scaling laws of our generalised KZM differed from those observed across continuous quantum critical points for the same spin-1 BEC model discussed initially. Furthermore, by linearising the resulting spinor GPEs, we obtained scaling laws governing the growth of the unstable excitations as the system transitions to the FM phase.

Numerical simulations provided excellent agreement for both the short-time growth of unstable excitations in addition to the number of FM domains formed after the critical point was passed. The robustness of our theory was confirmed by performing similar simulations which crossed both a second-order QPT (polar to BA) and a first-order QPT (BA to FM), which gave quantitatively similar results to the previously observed scaling laws.

CHAPTER 6

TOPOLOGICAL INTERFACES IN SPIN-2 BOSE-EINSTEIN CONDENSATES

In this chapter, we both analytically and numerically investigate the physics of topological defects when connected across topological interfaces in spin-2 Bose-Einstein condensates. We begin by introducing the concept of a topological interface, and discuss systems where they can arise. We then construct interpolating spinor wave functions for a spin-2 system that smoothly connect states with different symmetries, forming a topological interface. Such interfaces include connections between the UN and BN phases, cyclic to both nematic (UN/BN) phases, cyclic to FM phases, and also between the FM and BN phases. With these interpolating solutions, we then construct a rich phenomenology of different defect states connecting across the interface. These defects range from singular phase vortices, spin vortices, nonsingular textures, and even to point defects such as monopoles. Additionally, we also perform numerical simulations for select examples, highlighting the interesting physics occurring at the interface.

6.1 Introduction to topological interfaces

Topological interfaces may form at the phase boundary between topologically distinct phases that are described by different order parameters. In such an interface, the phases can coexist in such a way that the different symmetries connect smoothly across the boundary. These interfaces arise in many areas of physics, such as in the context of domain walls in the early universe [76–78], the *A*–*B* phase boundary in superfluid liquid ^{3}He [79–84], and in atomic BECs [85–87, 185–187]. When the order parameters on either side of the interface exhibit point-group symmetries [54], families of vastly different defects and textures may exist, where the topological charges of each defect depends on other defects within the system [93, 188]. An example is the cyclic and BN phases of spin-2 BECs, which, as we calculated in Sec. 3.4.2, have non-Abelian first homotopy groups, and hence support non-Abelian defects whose topological charges do not commute. Due to the different symmetries on either side of the interface, defects cannot typically cross the interface unchanged. Instead, the defect must either terminate at the boundary, or continuously and non-trivially connect to an object representing a different topology on the other side of the interface.

As shown in Chapter 3, spin-1 and spin-2 systems offer a rich ground state phase diagram with a myriad of different order parameter symmetries. In spin-1 systems, methods have already been proposed to engineer topological interfaces between the different order parameter symmetries by use of Zeeman shifts [85–87]. Naturally, since the spin-2 system offers even more choice of order parameter symmetry, they make an excellent candidate for further investigating topological interfaces. Additionally, spinor BECs support wide family of topological defects exhibiting different order parameter symmetries, cementing them as an ideal test bed for connections of topological defects across such interfaces. A small selection of vortices in the spin-2 system has already been considered in Sec. 3.5.2. However, spin-2 systems support a much larger family of vortices and higher order topological defects. These include, but are not limited to, integer vortices [45, 48, 50, 54, 57, 88–90, 114–116], vortices with fractional charges [40, 41, 48, 50, 54, 89, 90, 116–120], nonsingular vortices such as 2D Skyrmions [10, 11, 46, 49, 51, 88, 121–124] and point defects such as monopoles [112, 125–131, 189].

6.1.1 Engineering topological interfaces in spinor Bose-Einstein condensates

In a continuous spinor superfluid, it is possible for distinct phases with varying order parameter symmetry to coexist. A spinor BEC may be engineered such that separate regions of the condensate have distinct ground state phases, e.g., nematic or cyclic, and hence have different order parameter symmetries, creating a topological interface within the condensate itself. This can be achieved through variation of parameters in the Hamiltonian, such as the linear and quadratic Zeeman shifts, which locally stabilise the different regions. If the parameter fluctuation is sufficiently acute, then the wave function will interpolate between the bulk phases across a distance given by an appropriate healing length. In addition, as proposed for the spin-1 system [87], linear p and quadratic q Zeeman shifts form the basis for engineering interpolating solutions that model the topological interface. Such steady-state solutions are found from the mean-field Hamiltonian density functional discussed in Chapter 2 for a uniform system in the presence of an external magnetic field using the relation $\delta\mathscr{H}/\delta\zeta_m^* = 0$ [96]:

$$\left[-p\hat{F}_z + q\hat{F}_z^2 + c_0 n\zeta^\dagger\zeta + c_1 n\langle\hat{\mathbf{F}}\rangle\cdot\mathbf{f} + \frac{c_2 n}{5}(\hat{\mathscr{T}}\zeta)^\dagger\zeta\hat{\mathscr{T}} - \mu\right]\zeta = 0, \tag{6.1}$$

where μ is the chemical potential and $\hat{\mathscr{T}}$ is a time-reversal operator defined as $(\hat{\mathscr{T}}\zeta)_m = (-1)^m\zeta_{-m}^*$. Eq. (6.1) presents a non-linear system of equations that can be solved for the unknown ζ_m [96, 107]. Detailed derivations of each interpolating solution used in the subsequent sections can be found in Appendix B.

Using the constructed interpolating stationary states, defect states for a given spin-2 phase can, in principle, be constructed from the representative spinor by defining an appropriate azimuthal phase winding, χ_m, in each component, i.e., $\mathrm{Arg}(\zeta_m) = \chi_m = k_m\varphi$, where k_m is an integer which denotes a generalisation to multiple quantisation, and φ is the azimuthal angle around the vortex core. In addition, we also create a unitary framework which is applicable for constructing other types of defect states across topological interfaces in a spin-2 BEC, such as monopoles or nonsingular textures. A given defect state can be constructed from the uniform interpolating state by applying a global phase winding, τ, coupled with a spin rotation defined by three Euler angles (α,β,γ) as in Eq. (3.25). When the same transformation is supported by two phases, A and B, of a spin-2 condensate, a general defect connection across an interface between the two phases is given as

$$\zeta = e^{i\tau}U(\alpha,\beta,\gamma)\zeta^{\text{A-B}}. \tag{6.2}$$

Through the subsequent sections we provide various steady-state solutions that interpolate between the different phases of a spin-2 BEC. Using these solutions, we then construct interesting defect states that connect across the topological interface, by using either the component phase windings χ_m, or by applying a spin rotation with specified Euler angles to construct a particular state.

6.1.2 Interfaces arising within defect cores

In addition to the topological interface within the condensate itself, interfaces may also form within the cores of topological defects. This situation can arise, for example, due to energy relaxation in vortex core structures [48, 50, 54, 88, 89, 112, 116, 190]. In a spin-2 BEC, the three contributions to the interaction energy each give rise to a healing length, which describe, respectively, the length scale over which perturbations of the superfluid density, condensate spin, and singlet duo amplitude heal to the bulk value:

$$\xi_d = \ell\sqrt{\frac{\hbar\omega}{2nc_0}},\ \ \xi_s = \ell\sqrt{\frac{\hbar\omega}{2n|c_1|}},\ \ \xi_a = \ell\sqrt{\frac{\hbar\omega}{2n|c_2|}}, \tag{6.3}$$

where $\ell = (\hbar/M\omega)^{1/2}$ is the harmonic oscillator length. Typically, $\xi_s, \xi_a > \xi_d$, allowing the core of a singular vortex to reduce its energy by expanding and filling with a different superfluid phase [112]. The condensate wave function then smoothly interpolates between the coexisting phases in the superfluid and the phases within the defect core, establishing a topological interface between them. This type of interface can be described by the interpolating spinor when the interpolation parameter, η, is a function of the radial distance from the singular defect line, ρ, as $\eta = \eta(\rho)$. Such a vortex core interface is investigated in Sec. 6.3.1.

6.2 Interface crossing solutions in a spin-2 Bose-Einstein condensate

In this section we analytically construct interpolating spinor solutions that model connections between different ground states of spin-2 systems. In particular, we focus on four different topological interfaces, which are: UN to BN, cyclic to nematic (either UN or BN), cyclic to FM, and FM to BN. For each case we construct various topological defects connecting across the interface, ranging from simple phase vortex connections to more complicated connections involving monopoles and nonsingular textures.

6.2.1 Uniaxial nematic to biaxial nematic

We first focus on a family of solutions interpolating between the UN and BN phases (see Sec 3.3 for details on these ground states). Such an interpolating solution is given as

$$\zeta^{\text{UN-BN}} = \frac{1}{2}\begin{pmatrix} e^{i\chi_2}\sqrt{1-\eta} \\ 0 \\ e^{i\chi_0}\sqrt{2(1+\eta)} \\ 0 \\ e^{i\chi_{-2}}\sqrt{1-\eta} \end{pmatrix}, \tag{6.4}$$

where $\eta = 10q/|c_2|n \in [-1,1]$ and $\chi_m = \text{Arg}(\zeta_m)$ for component m. Here, χ_m are arbitrary phase coefficients that can either take fixed values, or be spatially wound in order to produce different vortex states. This solution depends only on the quadratic Zeeman shift, which can alter the spinor between the different phases: When $q = |c_2|n/10$ the system is in the UN phase with only the $\zeta_0 = 1$ component occupied, where the nematic director is aligned with the z-axis. In the opposite limit, when $q = -|c_2|n/10$, the system is in the BN phase with the $\zeta_{\pm 2} = 1/\sqrt{2}$ components occupied. This spinor therefore provides interpolating solutions between the UN and BN phases, engineered through manipulation of the quadratic Zeeman shift.

To determine the energetic stability of this interpolating spinor, we compare the energy per particle given by [96]

$$E = \hat{H}\left[\Psi^{\text{UN-BN}}\right] - \frac{c_0 n}{2}, \tag{6.5}$$

where $\hat{H} = \hat{H}_0 + \hat{H}_{\text{int}}$ is the spin-2 Hamiltonian where $\hat{H}_0$ and $\hat{H}_{\text{int}}$ are defined in Eq. (2.63) and Eq. (2.59), respectively. The energy of the interpolating spinor given in Eq. (6.4) reads $E^{\text{UN-BN}} = \frac{c_2 n}{10} + 2q(1-\eta)$. Comparing this energy with that of the UN phase ($E^{\text{UN}} = c_2 n/10$) and the BN phase ($E^{\text{BN}} = c_2 n/10 + 4q$) reveals that the ground state is UN for $q \geq 0$ and BN for $q \leq 0$. Therefore, the UN-BN interface can be stabilised through careful choice of a longitudinal quadratic Zeeman shift $q(z)$ such that $q(z)$ changes sign at some transverse plane, which we typically take to be $z = 0$.

A consequence of a spatially-dependent η is revealed from the spin singlet-duo and -trio amplitudes, given in terms of the spinor ζ, respectively, as

$$|A_{00}|^2 = \frac{1}{5}\left|2\zeta_2\zeta_{-2} - 2\zeta_1\zeta_{-1} + \zeta_0^2\right|^2, \tag{6.6}$$

$$|A_{30}|^2 = \left|\frac{3\sqrt{6}}{2}\left(\zeta_1^2\zeta_{-2} + \zeta_{-1}^2\zeta_2\right) + \zeta_0\left(\zeta_0^2 - 3\zeta_1\zeta_{-1} - 6\zeta_2\zeta_{-2}\right)\right|^2. \tag{6.7}$$

Upon substitution of Eq. (6.4) into the above, we get

$$\begin{aligned} |A_{00}|^2 &= \frac{1}{10}\left[(\eta^2 - 1)\cos\chi + \eta^2 + 1\right], \\ |A_{30}|^2 &= \frac{1+\eta}{4}\left[3\left(\eta^2 - 1\right)\cos\chi + \eta(5\eta - 8) + 5\right], \end{aligned} \tag{6.8}$$

where $\chi = \chi_2 + \chi_{-2} - 2\chi_0$ is the relative phase difference between the components. We plot both the singlet-duo and -trio amplitudes in Fig. 6.1 in a parameter space of (η, χ). Upon investigation, we see interesting behaviour arise in both quantities. In particular, we see that this spinor can interpolate between the different phases of UN, BN and cyclic depending on both η and the relative phase difference χ. For example, if one were to maintain $\chi = 0$ and interpolate η, then there would be multiple transitions between the UN ($|A_{00}|^2 = 1$) and BN ($|A_{00}|^2 = 0$) phases. In addition, maintaining a relative phase difference of $\chi = \pi$, the singlet-trio amplitude reveals that a cyclic phase is present when $-0.5 \lesssim \eta \lesssim 0.5$. As we shall see in our numerical investigations, this has profound effects on the structure of topological defects connecting across such an interface.

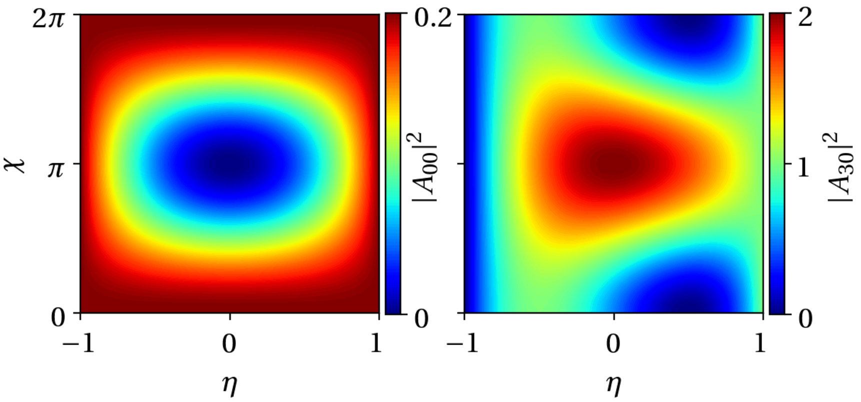

Figure 6.1: Spin singlet-duo (left) and -trio (right) amplitudes for the interpolating spinor in Eq. (6.4). Due to the spatially-dependent η, this spinor continuously interpolates between the UN, BN, and cyclic phases depending on the relative phase difference $\chi = \chi_2 + \chi_{-2} - 2\chi_0$.

Connections involving phase vortices

To begin our investigations of defects connecting across topological interfaces, we first consider vortex connections. We start by constructing a connection of k-quantised phase vortices on either side of the interface, which can be achieved by allowing $\chi_m = k\varphi$ in Eq. (6.4), which results in a spatially overlapping $2k\pi$ phase winding in each component. Such a spinor is given explicitly as

$$\zeta^{\text{UN-BN}}_{\text{pv-pv}} = \frac{1}{2}\begin{pmatrix} e^{ik\varphi}\sqrt{1-\eta} \\ 0 \\ e^{ik\varphi}\sqrt{2(1+\eta)} \\ 0 \\ e^{ik\varphi}\sqrt{1-\eta} \end{pmatrix}. \tag{6.9}$$

Note that an alternative construction of the above interface is achieved using Eq (6.2) with$\tau = k\varphi$ and the Euler angles kept constant, which then acts on the uniform spinor in Eq. (6.4) with $\chi_m = 0$. One can see that in the above spinor we recover the individual phase vortex case in both the UN $\zeta^{\text{UN}}_{\text{pv}} = (0,0,e^{ik\varphi},0,0)^T$ and BN $\zeta^{\text{BN}}_{\text{pv}} = (e^{ik\varphi},0,0,0,e^{ik\varphi})^T/\sqrt{2}$ limits when $\eta = \pm 1$, respectively. It is important to note that, despite being characterised by the same phase winding, the phase vortices on either side of the interface represent entirely different objects due to the differing topologies of the UN and BN phases.

Instead of connecting two vortices on either side of the interface, one can instead construct a vortex that terminates on the interface itself, essentially connecting to a vortex-free region on the other side. This can be achieved by selectively removing the phase winding from particular components. For example, to achieve a k-quantised phase vortex in the UN limit that connects to a vortex-free region in the BN limit, we can set $\chi_0 = 0$ and $\chi_{\pm 2} = k\varphi$ in Eq. (6.4), which gives

$$\zeta^{\text{UN-BN}}_{\text{pv-vf}} = \frac{1}{2}\begin{pmatrix} \sqrt{1-\eta} \\ 0 \\ e^{ik\varphi}\sqrt{2(1+\eta)} \\ 0 \\ \sqrt{1-\eta} \end{pmatrix}. \tag{6.10}$$

Similarly, by reversing this and setting the winding $\chi_{\pm 2} = 0$ and $\chi_0 = k\varphi$ one instead constructs a k-quantised phase vortex in the BN phase which connects to a vortex-free region in the UN limit, given by the spinor

$$\zeta^{\text{UN-BN}}_{\text{vf-pv}} = \frac{1}{2}\begin{pmatrix} e^{ik\varphi}\sqrt{1-\eta} \\ 0 \\ \sqrt{2(1+\eta)} \\ 0 \\ e^{ik\varphi}\sqrt{1-\eta} \end{pmatrix}. \tag{6.11}$$

Connections involving spin vortices

Vortices other than singular phase vortices may also be connected across the interface. One such example is of singular spin vortices, which, allowing for the fact that spinor BECs support the non-dissipative flow of spin, carry a circulation only in the condensate spin and not the mass (see Sec. 3.5.2). An example containing a k-quantised spin vortex in the BN phase can be constructed by considering opposite phase windings in the outer components, i.e., choosing $\chi_{\pm 2} = \pm\varphi$ in Eq. (6.4), resulting in the spinor

$$\zeta^{\text{UN-BN}}_{\text{vf-sv}} = \frac{1}{2}\begin{pmatrix} e^{ik\varphi}\sqrt{1-\eta} \\ 0 \\ \sqrt{2(1+\eta)} \\ 0 \\ e^{-ik\varphi}\sqrt{1-\eta} \end{pmatrix}. \tag{6.12}$$

Since there is no condensate phase winding in the ζ_0 component in the above equation, this implies that the spin vortex exists only within the BN limit, and therefore smoothly connects to a vortex-free state in the UN limit. It is, however, possible to construct a k-quantised spin vortex on both sides of the interface using spin rotations. Applying the spin rotation $U(\alpha =$

$k\varphi/2, \beta = \pi/2, \gamma = 0)$ to the initial interpolating spinor in Eq. (6.4) results in

$$\zeta^{\text{UN-BN}}_{\text{sv-sv}} = \frac{1}{4}\begin{pmatrix} e^{-ik\varphi}(\sqrt{1-\eta}+\sqrt{3(1+\eta)}) \\ 0 \\ \sqrt{6(1-\eta)}-\sqrt{2(1+\eta)} \\ 0 \\ e^{ik\varphi}(\sqrt{1-\eta}+\sqrt{3(1+\eta)}) \end{pmatrix}. \tag{6.13}$$

The result of the spin rotation means that in the UN ($\eta = 1$) and BN ($\eta = -1$) limits we now have three-component spinors given, respectively, as

$$\zeta^{\text{UN}}_{\text{sv}} = \begin{pmatrix} e^{-ik\varphi}\sqrt{6} \\ 0 \\ 2 \\ 0 \\ e^{ik\varphi}\sqrt{6} \end{pmatrix}, \quad \zeta^{\text{BN}}_{\text{sv}} = \begin{pmatrix} e^{-ik\varphi}\sqrt{2} \\ 0 \\ 2\sqrt{3} \\ 0 \\ e^{ik\varphi}\sqrt{2} \end{pmatrix}, \tag{6.14}$$

thereby allowing spin vortices to appear in both phases, and hence connect across the topological interface.

Connections involving half-quantum vortices

As discussed in Sec. 3.5.2, the BN phase supports vortices which have a fractional winding of the condensate phase, the spin, or a combination of both. The charge of such a vortex can be described as (w, σ), where $2\pi w$ denotes the winding of the condensate phase, τ, and $2\pi\sigma$ denotes the winding of the spin about some axis of symmetry. A $(1/2, 1/4)$ HQV in the BN phase can be constructed from Eq. (6.4) using the choice $\chi_2 = \chi_0 = 0$ and $\chi_{-2} = \varphi$, which connects it to a vortex-free state in the UN limit. Such an interpolating spinor reads

$$\zeta^{\text{UN-BN}}_{\text{vf-hqv}} = \frac{1}{2}\begin{pmatrix} \sqrt{1-\eta} \\ 0 \\ \sqrt{2(1+\eta)} \\ 0 \\ e^{i\varphi}\sqrt{1-\eta} \end{pmatrix}. \tag{6.15}$$

Note that $\chi_2 = \varphi$ and $\chi_0 = \chi_{-2} = 0$ would also connect a HQV in the BN phase to a vortex-free region in the UN phase. The same $(1/2, 1/4)$ HQV in the BN phase can connect to a singly quantised phase vortex in the UN limit by allowing $\chi_2 = 0$ and $\chi_0 = \chi_{-2} = \varphi$, resulting in the

UN-BN — Vortices from spinor-component phase winding				
UN limit	BN limit	χ_2/φ	χ_0/φ	χ_{-2}/φ
Phase vortex	Phase vortex	k	k	k
Vortex-free	Phase vortex	k	0	k
Phase vortex	Vortex-free	0	k	0
Vortex-free	Spin vortex	$-k$	0	k
Phase vortex	Spin vortex	$-k$	k	k
Vortex-free	Half-quantum vortex	0	0	1
Phase vortex	Half-quantum vortex	0	± 1	1

Table 6.1: Representative examples of different vortex connections possible across a UN-BN interface, constructed from the winding of the phase coefficients χ_m in Eq. (6.4). Additionally, generalisations to multiply quantised vortices are given by $k \in \mathbb{Z}$.

spinor

$$\zeta^{\text{UN-BN}}_{\text{pv-hqv}} = \frac{1}{2}\begin{pmatrix} \sqrt{1-\eta} \\ 0 \\ e^{i\varphi}\sqrt{2(1+\eta)} \\ 0 \\ e^{i\varphi}\sqrt{1-\eta} \end{pmatrix}. \tag{6.16}$$

A summary of the possible phase, spin, and half-quantum vortex connections across a UN-BN interface are listed in Table 6.1.

Connections involving monopoles and nonsingular textures

So far, we have considered only singular vortices connecting across the interface. It is, however, possible to construct interpolating solutions that contain other types of defects, such as monopoles and nonsingular textures. For example, the UN phase supports nonsingular spin vortices, which are defined by a fountain-like texture of the nematic director, $\hat{\mathbf{d}} = (\cos\alpha\sin\beta, \sin\alpha\sin\beta, \cos\beta)$. The nonsingular fountain-like texture can be achieved by having β be a monotonically increasing function of the radial coordinate, ρ. Applying the spin rotation $U(\alpha = \varphi, \beta = \beta(\rho), \gamma = 0)$ to Eq. (6.4) with $\chi_m = 0$ results in the spinor

$$\zeta^{\text{UN-BN}} = \frac{1}{\sqrt{2}}\left(\sqrt{1+\eta}\,\zeta^{\text{UN}}_{\text{nsv}} + \sqrt{1-\eta}\,\zeta^{\text{BN}}_{\text{sv}}\right), \tag{6.17}$$

where the UN and BN single phase limits are given, respectively, as

$$\zeta_{\text{nsv}}^{\text{UN}} = \sqrt{\frac{3}{8}}\begin{pmatrix} e^{-2i\varphi}\sin^2\beta(\rho) \\ -e^{-i\varphi}\sin 2\beta(\rho) \\ \frac{1}{\sqrt{6}}\left[1+3\cos 2\beta(\rho)\right] \\ e^{i\varphi}\sin 2\beta(\rho) \\ e^{2i\varphi}\sin^2\beta(\rho) \end{pmatrix}, \tag{6.18}$$

$$\zeta_{\text{sv}}^{\text{BN}} = \frac{1}{\sqrt{8}}\begin{pmatrix} e^{-2i\varphi}\left(\cos^2\beta(\rho)+1\right) \\ e^{-i\varphi}\sin 2\beta(\rho) \\ \sqrt{6}\sin^2\beta(\rho) \\ -e^{i\varphi}\sin 2\beta(\rho) \\ e^{2i\varphi}\left(\cos^2\beta(\rho)+1\right) \end{pmatrix}. \tag{6.19}$$

This spinor now represents a connection between a nonsingular spin vortex in the UN limit which smoothly connects to a singular spin vortex in the BN limit.

Since $\pi_2(\mathscr{M}_{\text{UN}}) \neq 0$ (see Sec. 3.4.2), an interesting example can be constructed by thinking about a monopole placed in the UN side of the interface. In such an interface, a monopole may form at the termination point of a singular line vortex. Similar structures, called boojums, have been observed in ^{3}He [84, 191]. A monopole can be realised as a radial hedgehog texture of the nematic director, $\hat{\mathbf{d}}$. This achieved via the spin rotation $U(\alpha=\varphi, \beta=\theta, \gamma=0)$, where θ is the polar angle in spherical coordinates. Applying this spin rotation to the state in Eq. (6.4) with $\chi_m = 0$ results in

$$\zeta^{\text{UN-BN}} = \frac{1}{\sqrt{2}}\left(\sqrt{1+\eta}\zeta_{\text{mp}}^{\text{UN}} + \sqrt{1-\eta}\zeta_{\text{sv}}^{\text{BN}}\right), \tag{6.20}$$

where the UN and BN single phase limits are given, respectively, as

$$\zeta_{\text{mp}}^{\text{UN}} = \sqrt{\frac{3}{8}}\begin{pmatrix} e^{-2i\varphi}\sin^2\theta \\ -e^{-i\varphi}\sin 2\theta \\ \frac{1}{\sqrt{6}}(1+3\cos 2\theta) \\ e^{i\varphi}\sin 2\theta \\ e^{2i\varphi}\sin^2\theta \end{pmatrix}, \tag{6.21}$$

$$\zeta_{\text{sv}}^{\text{BN}} = \frac{1}{\sqrt{8}}\begin{pmatrix} e^{-2i\varphi}\left(\cos^2\theta+1\right) \\ e^{-i\varphi}\sin 2\theta \\ \sqrt{6}\sin^2\theta \\ -e^{i\varphi}\sin 2\theta \\ e^{2i\varphi}\left(\cos^2\theta+1\right) \end{pmatrix}. \tag{6.22}$$

UN-BN — Vortices, textures, and monopoles using Euler angles				
UN limit	BN limit	α/φ	γ/φ	β
Spin half-quantum vortex	Spin half-quantum vortex	1	0	$\pi/2$
Nonsingular spin vortex	Spin vortex	1	0	$\beta(\rho)$
Monopole	Spin vortex	1	0	θ
Spin vortex	Monopole	1	-1	θ

Table 6.2: Summary of other types of defect connections possible in a UN-BN interface. Given solutions are characterised by winding of the condensate phase, τ, and Euler angles (α,β,γ), expressed in units of the azimuthal angle φ. Here, k is an integer which provides a generalisation to higher quantisation. Additionally, θ is the polar angle in spherical coordinates, and β describes a monotonically increasing function of the transverse radius ρ.

This interpolating spinor describes a monopole in the UN limit that terminates on a singular spin vortex in the BN limit. A summary of types of defects one can construct using Euler angles in a UN-BN interface is given in Table 6.2.

6.2.2 Cyclic to nematic

As we have discussed already in the context of vortex cores, topological interfaces can arise between the cyclic and nematic phases. From Fig. 6.1, we see that by maintaining a constant $\chi = \pi$ one can interpolate between the UN, cyclic and BN states. This can be achieved by the following family of spinors

$$\zeta^{\text{C-N}} = \frac{1}{2}\begin{pmatrix} e^{i\chi_2}\sqrt{1-\eta} \\ 0 \\ ie^{i\chi_0}\sqrt{2(1+\eta)} \\ 0 \\ e^{i\chi_{-2}}\sqrt{1-\eta} \end{pmatrix}, \tag{6.23}$$

where we now require that $\chi_2 + \chi_{-2} - 2\chi_0 = 0$. Then, due to the i term in the middle component, this leads to a constant phase difference of $\chi_2 + \chi_{-2} - 2(\chi_0 + \pi/2) = -\pi$, and hence allows us to use the quadratic Zeeman shift to interpolate the above solution between the different phases. At $\eta = 0$ the above solution becomes the three component cyclic state with a spinor of the form $\zeta_C = (1, 0, i\sqrt{2}, 0, 1)^T/2$. The sign of the quadratic Zeeman shift determines which nematic state is chosen, where $\eta = \pm 1$ recovers the familiar UN and BN states, respectively.

The uniform mean-field energy of Eq. (6.23) reads

$$E^{\text{C-N}} = \frac{c_2 n}{10}\eta^2 + 2q(1-\eta). \tag{6.24}$$

The energy becomes minimised at $\eta = 10q/c_2 n$ for $c_2 > 0$ and fixed q. Since the interpolating spinor $\zeta^{\text{C-N}}$ is a function of q only, the stability of the interface is guaranteed since $E^{\text{C-N}} = 2q - 10q^2/c_2 \le E^{\text{C}}, E^{\text{UN}}, E^{\text{BN}}$ for $|q| < c_2 n/10$.

Connections involving phase and spin vortices

Firstly, one can construct the same phase vortex and spin vortex connections considered in the UN-BN interface upon the substitution $\sqrt{1+\eta} \to i\sqrt{1+\eta}$. For example, a connection between k-quantised phase vortices is obtained from Eq. (6.9), where the resulting spinor reads

$$\zeta^{\text{C-N}}_{\text{pv-pv}} = \frac{1}{2}\begin{pmatrix} e^{ik\varphi}\sqrt{1-\eta} \\ 0 \\ ie^{ik\varphi}\sqrt{2(1+\eta)} \\ 0 \\ e^{ik\varphi}\sqrt{1-\eta} \end{pmatrix}, \tag{6.25}$$

identifying the cyclic limit as $\eta = 0$. This is obtained from Eq. (6.23) by the choice $\chi_2 = \chi_0 = \chi_{-2} = k\varphi$. Additionally, a connection involving spin vortices is constructed as

$$\zeta^{\text{C-N}}_{\text{sv-sv/vf}} = \frac{1}{2}\begin{pmatrix} e^{-ik\varphi}\sqrt{1-\eta} \\ 0 \\ i\sqrt{2(1+\eta)} \\ 0 \\ e^{ik\varphi}\sqrt{1-\eta} \end{pmatrix}, \tag{6.26}$$

which equates to spin vortices in the cyclic and BN limits, connecting to a vortex-free state in the UN limit. These connections can be achieved from Eq. (6.23) with the choice $\chi_{\pm 2} = \mp k\varphi$ and $\chi_0 = 0$. Vortices that can be constructed from component phase windings are summarised in Table 6.3. It is worth noting that choosing the phase windings χ_m in Eq. (6.23) such that $\chi \neq 0$ leads to defect states which are undefined in the cyclic limit, and hence we omit them from the discussion.

In addition to these connections, it is also possible to construct topologically distinct spin vortex connection between the cyclic and both nematic phases. This arises from the common axis of symmetry between the cyclic and BN phases (see C_2' axis in Fig. 3.7b). A spin rotation around this particular axis can be achieved by using the following spin rotation, given here in axis-angle representation:

$$U(C_2', \delta) = \exp\left\{-i\frac{\hat{F}_x + \hat{F}_y}{\sqrt{2}}\delta\right\}, \tag{6.27}$$

C-N — Vortices from spinor-component phase winding					
Cyclic limit	UN limit	BN limit	χ_2/φ	χ_0/φ	χ_{-2}/φ
Phase vortex	Phase vortex	Phase vortex	k	k	k
Spin vortex	Vortex-free	Spin vortex	$-k$	0	k

Table 6.3: Summary of the phase and spin vortices possible in a cyclic to nematic interface. Different vortices are constructed from appropriate choices of the phase windings χ_m. Note that $\chi = 0$ for all cases considered as to ensure identifiable vortices within the cyclic limit.

where C_2' represents the axis being rotated about and δ represents the angle of rotation. When δ is chosen to be the azimuthal angle such that it winds by 2π about a vortex core ($\delta = \varphi$), then the above spin rotation applied the general cyclic to nematic spinor in Eq. (6.23) results in the following spinor:

$$\zeta^{\text{C-N}}_{\text{sv}-\text{sv}} = \frac{1}{\sqrt{2}}\left(i\sqrt{1+\eta}\,\zeta^{\text{UN}}_{\text{sv}} + \sqrt{1-\eta}\,\zeta^{\text{BN}}_{\text{sv}}\right), \tag{6.28}$$

where the spinors in the UN and BN limits are given as

$$\zeta^{\text{UN}}_{\text{sv}} = \sqrt{\frac{3}{8}}\begin{pmatrix} -i\sin^2\varphi \\ -e^{-\frac{i\pi}{4}}\,i\sin 2\varphi \\ \frac{1}{\sqrt{6}}\left(1+3\cos 2\varphi\right) \\ e^{\frac{i\pi}{4}}\sin 2\varphi \\ i\sin^2\varphi \end{pmatrix}, \tag{6.29}$$

$$\zeta^{\text{BN}}_{\text{sv}} = \frac{1}{\sqrt{2}}\begin{pmatrix} \cos\varphi \\ e^{-\frac{3i\pi}{4}}\sin\varphi \\ 0 \\ e^{-\frac{i\pi}{4}}\sin\varphi \\ \cos\varphi \end{pmatrix}. \tag{6.30}$$

This yields a connection between singular, singly quantised spin vortices in all three limits.

Connections involving monopoles and nonsingular textures

As discussed in the previous section, the nematic phases give rise to nonsingular spin vortices and point defects such as monopoles. Those same defect connections can be constructed in this interface by using the transformation $\sqrt{1+\eta} \rightarrow i\sqrt{1+\eta}$ in Eq. (6.17) and Eq. (6.17). This then still results in, for example, the nonsingular vortex/monopole in the UN limit, which now also connects/terminates to a singular spin vortex in the cyclic and BN limits. These defects are summarised in Table 6.4.

C-N — Vortices, textures, and monopoles using Euler angles				
Cyclic / BN limits	UN limit	α/φ	γ/φ	β
Spin vortex	Spin vortex	$\alpha=\pi/4$	$\gamma=-\alpha$	$k\varphi$
Spin vortex	Nonsingular spin vortex	1	0	$\beta(\rho)$
Spin vortex	Monopole	1	0	θ

Table 6.4: Summary of other types of defect structures possible in a cyclic to nematic interface. Each defect is identified by windings of the condensate phase τ and Euler angles (α,β,γ), expressed in terms of the azimuthal angle φ. For nonsingular vortices, β denotes a monotonically increasing function of the transverse radius ρ. Additionally, for the monopole case, θ is the polar angle in spherical coordinates.

6.2.3 Cyclic to ferromagnetic

Since spin-2 BECs support an FM phase, which has inherent magnetisation, one can construct an interface between this state and one with zero magnetisation. This would then result in spatially distinct regions which have different values of the spin magnitude, and hence would create a spatially-dependent magnetisation. By restricting ourselves to the case of zero transverse magnetisation, $\hat{\mathbf{F}}=\hat{F}_z$, one such case that arises is between the cyclic and FM phases, given by the following family of spinors:

$$\zeta^{\text{C-FM}}=\frac{1}{\sqrt{3}}\begin{pmatrix} e^{i\chi_2}\sqrt{1+\eta} \\ 0 \\ 0 \\ e^{i\chi_{-1}}\sqrt{2-\eta} \\ 0 \end{pmatrix}, \tag{6.31}$$

where η now becomes the longitudinal magnetisation, $\langle\hat{F}_z\rangle$. At zero magnetisation, $\langle\hat{F}_z\rangle=0$, equivalent to setting $\eta=0$, this solution becomes the two-component cyclic state given in Eq. (3.35) which naturally has no magnetisation. Then, since this is a spin-2 system, the condensate spin is free to vary between $\langle\hat{F}_z\rangle=0$ and $\langle\hat{F}_z\rangle=2$. Recall from Chapter 3 that the spin-2 system supports two FM ground states, one with $|\langle\hat{\mathbf{F}}\rangle|=1$, which we denote $\text{FM}_1^{\pm}$, and another with $|\langle\hat{\mathbf{F}}\rangle|=2$, which we denote $\text{FM}_2^{\pm}$. Here, the + (-) represents the FM state with spin pointing up (down). Therefore, this spinor can interpolate between the cyclic and both FM phases, depending on the value of the condensate spin, $\langle\hat{F}_z\rangle$.

The uniform mean-field energy of the above spinor reads

$$E^{\text{C-FM}}=\frac{c_1 n}{2}\eta^2-(p-q)\eta+2q, \tag{6.32}$$

which becomes minimised upon the choice $\eta = (p-q)/c_1 n$ for $c_1 > 0$ and fixed p, q. The interface is expected to be stable within the range $-c_1 n \leq p \leq 2c_1 n$ since $E^{\text{C-FM}} \leq E^{\text{C}} = 0, E^{\text{FM}_1} = c_1 n/2 + p$. Therefore, assuming, e.g., $q = 0$, we can stabilise the interface by an appropriate choice of a longitudinally-dependent linear Zeeman shift $p(z)$, where $p(z) = 0$ represents the cyclic phase, whilst $p(z) = -c_1 n$ and $p(z) = 2c_1 n$ represent the FM_1 and FM_2 phases, respectively.

Connections involving phase, spin, and fractional vortices

Following the procedure similar to the previous interfaces, we first focus on constructing phase vortices connecting across this topological interface, which can be obtained by appropriate winding of χ_2 and χ_{-1}. Again, one can construct k-quantised phase vortices connecting in all three limits by crossing $\chi_2 = \chi_{-1} = k\varphi$, which yields

$$\zeta^{\text{C-FM}}_{\text{pv-pv}} = \frac{e^{ik\varphi}}{\sqrt{3}} \begin{pmatrix} \sqrt{1+\eta} \\ 0 \\ 0 \\ \sqrt{2-\eta} \\ 0 \end{pmatrix}, \tag{6.33}$$

In addition to these singly quantised vortices, the cyclic phase supports vortices with fractional charges, such as one-third and two-third vortices (see Sec. 3.5.2). One can then construct such a vortex in the cyclic limit by limiting the winding of the phase to only one component. Due to the spin-gauge symmetry of the FM phase, this choice of winding would then lead to either singular phase vortices and vortex-free regions in this limit. For example, the following spinor connects a one-third vortex in the cyclic limit to a singular phase vortex in the FM_2^+ and a vortex-free region in the FM_1^- limit:

$$\zeta^{\text{C-FM}}_{\frac{1}{3}\text{-pv}} = \frac{1}{\sqrt{3}} \begin{pmatrix} e^{i\varphi}\sqrt{1+\eta} \\ 0 \\ 0 \\ \sqrt{2-\eta} \\ 0 \end{pmatrix}, \tag{6.34}$$

which corresponds to the choice of $\chi_2 = \varphi$ and $\chi_{-1} = 0$ in Eq. (6.31). Similarly, a two-third vortex in the cyclic limit can connect to a vortex-free region in the FM_2^+ limit or a singular

C-FM — Vortices from spinor-component phase winding				
Cyclic limit	FM_2 limit	FM_1 limit	χ_2/φ	χ_{-1}/φ
Phase vortex	Phase vortex	Phase vortex	k	k
One-third vortex	Phase vortex	Vortex-free	1	0
Two-third vortex	Vortex-free	Phase vortex	0	1
Spin vortex	Phase vortex	Phase vortex	$-2k$	k

Table 6.5: Summary of the vortex connections possible in a cyclic to FM interface. Each vortex can be constructed by choosing the appropriate phase winding χ_m, expressed in terms of the azimuthal angle φ. Here, k is an integer that allows one to represent vortices of arbitrary quantisation.

phase vortex in the FM_1^- limit, given by the spinor

$$\zeta^{\text{C-FM}}_{\frac{2}{3}\text{-pv}} = \frac{1}{\sqrt{3}}\begin{pmatrix} e^{i\varphi}\sqrt{1+\eta} \\ 0 \\ 0 \\ \sqrt{2-\eta} \\ 0 \end{pmatrix}, \tag{6.35}$$

equivalent to setting $\chi_2 = 0$ and $\chi_{-1} = \varphi$ in Eq. (6.31). Note that equivalent constructions can be made for the above two spinors using Eq. (6.2) with $\tau = -\gamma = \varphi/3$ and $\tau = 2\gamma = 2\varphi/3$, respectively. A summary of the phase vortex connections possible in this interface are summarised in Table 6.5.

Connections involving monopoles and nonsingular textures

In addition to phase vortices, the FM phase also supports nonsingular vortices, which are identified from a characteristic fountain-like texture of the condensate spin (see Fig. 3.9b for the spin-1 analogue.) To construct such a defect across an interface, we first construct the most general C-FM interface spinor by applying the general spin rotation $U(\alpha,\beta,\gamma)$ to the interpolating spinor in Eq. (6.31), which results in

$$\zeta^{\text{C-FM}} = \frac{1}{\sqrt{3}}\left(\sqrt{1+\eta}\,\zeta^{\mathrm{FM}_2^+} + \sqrt{2-\eta}\,\zeta^{\mathrm{FM}_1^-}\right), \tag{6.36}$$

where the individual FM limits are given as

$$\zeta^{\mathrm{FM}_2^+} = e^{i(\tau-2\gamma)} \begin{pmatrix} e^{-2i\alpha}\cos^4\frac{\beta}{2} \\ 2e^{-i\alpha}\cos^3\frac{\beta}{2}\sin\frac{\beta}{2} \\ \sqrt{6}\cos^2\frac{\beta}{2}\sin^2\frac{\beta}{2} \\ 2e^{i\alpha}\cos\frac{\beta}{2}\sin^3\frac{\beta}{2} \\ e^{2i\alpha}\sin^4\frac{\beta}{2} \end{pmatrix}, \tag{6.37}$$

$$\zeta^{\mathrm{FM}_1^-} = e^{i(\tau+\gamma)} \begin{pmatrix} -2e^{-2i\alpha}\cos\frac{\beta}{2}\sin^3\frac{\beta}{2} \\ e^{-i\alpha}\sin^2\frac{\beta}{2}\left(3\cos^2\frac{\beta}{2}-\sin^2\frac{\beta}{2}\right) \\ \sqrt{6}\left(\cos\frac{\beta}{2}\sin^3\frac{\beta}{2}-\cos^3\frac{\beta}{2}\sin\frac{\beta}{2}\right) \\ e^{i\alpha}\cos^2\frac{\beta}{2}\left(\cos^2\frac{\beta}{2}-3\sin^2\frac{\beta}{2}\right) \\ 2e^{2i\alpha}\cos^3\frac{\beta}{2}\sin\frac{\beta}{2} \end{pmatrix}. \tag{6.38}$$

To construct the characteristic fountain-like spin texture, we choose β as a monotonically increasing function of the transverse radius, ρ. In the FM_2 and FM_1 cases, the order-parameter is kept single-valued by a combined winding of the condensate phase coupled to a winding of the spin vector, achieved, respectively, by

$$\tau - 2\gamma = \pm 2\alpha = \pm 2\varphi, \tag{6.39}$$

$$\tau + \gamma = \pm\alpha = \pm\varphi. \tag{6.40}$$

Choosing these Euler angles results in nonsingular vortices in the FM limits connecting to singular vortices in the cyclic limit. The type of singular vortex present in the cyclic limit depends on how γ and τ are specifically chosen. Choosing $\gamma = 0$ or $\tau = 0$ results in phase vortices or spin vortices, respectively. Additionally, the choice of $\tau = \varphi/3$ or $\tau = 2\varphi/3$ results in fractionally quantised vortices in the cyclic limit connecting to nonsingular vortices in the FM phases. The spherical harmonic representation of the nonsingular vortices arising in the FM phases are shown in Fig. 6.2, where we see the characteristic fountain-like texture emerge.

A generalisation of the Dirac monopole, which consists of a hedgehog texture of the condensate spin, $\langle\hat{\mathbf{F}}\rangle$, that terminates on a singular vortex, can be constructed in the FM phases. Similar generalisations have already been constructed in spin-1 systems [85, 126]. Such a structure is achieved by taking $\beta = \theta$ in Eqs. (6.37) and (6.38), where θ is the polar angle in spherical coordinates, along with the same required limits on the Euler angles given in Eqs. (6.39) and (6.40). This creates the required hedgehog texture of the condensate spin and embeds a singular vortex line terminating on the monopole. These choices of angles then

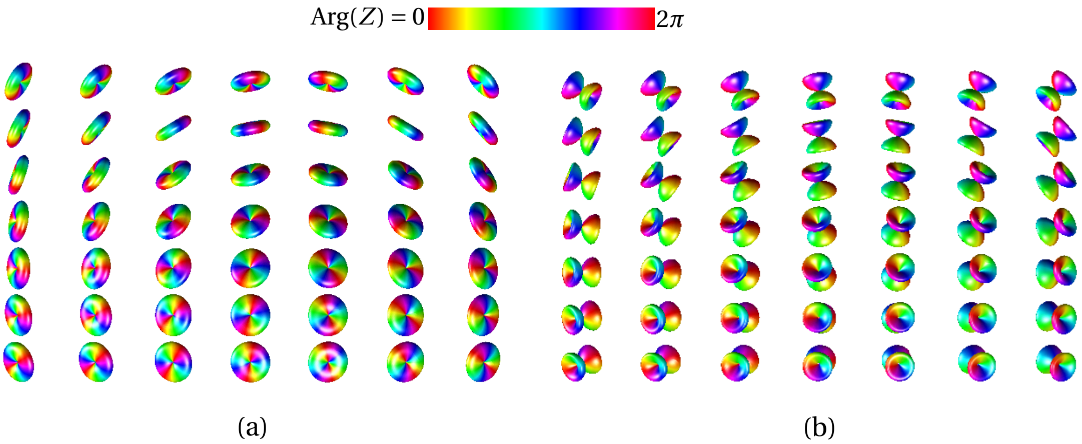

Figure 6.2: Spherical harmonic representation of the nonsingular vortices constructed in Eq. (6.36). (a): Nonsingular vortex in the FM_2^+ limit given by Eq. (6.37) with the choice $\tau - 2\gamma = 2\alpha = 2\varphi$. (b): Nonsingular vortex in the FM_1^- limit given by Eq. (6.38) with the choice $\tau + \gamma = \alpha = \varphi$.

connect the generalisation of the Dirac monopole in the FM limits to either phase, spin, or fractional vortices in the cyclic limit using the choice of angles discussed for the nonsingular case. A table of vortices, textures, and monopoles that can be constructed using Euler angles in the C-FM interface are presented in Table 6.6.

6.2.4 Ferromagnetic to biaxial nematic

Another interface containing non-zero magnetisation is that between the FM and BN phases, given by the following family of spinors:

$$\zeta^{\text{FM-BN}} = \frac{1}{2}\begin{pmatrix} e^{i\chi_2}\sqrt{2+\eta} \\ 0 \\ 0 \\ 0 \\ e^{i\chi_{-2}}\sqrt{2-\eta} \end{pmatrix}, \tag{6.41}$$

where η relates to the longitudinal magnetisation as $\eta = \langle \hat{F}_z \rangle$. This state then interpolates between the BN state at $\eta = 0$, to an FM state with spin pointing up (down) for $\eta = 2(-2)$. The energy of this interpolating spinor is obtained by substituting the above into Eq. (6.5), which reads

$$E^{\text{FM-BN}} = \frac{n}{2}\left(c_1 - \frac{c_2}{20}\right)\eta^2 - p\eta + 4q + \frac{nc_2}{10}. \tag{6.42}$$

C-FM — Vortices, textures and monopoles using Euler angles

C limit	FM_2 limit	τ/φ	α/φ	γ/φ	β
Phase vortex	Nonsingular vortex	2	1	0	$\beta(\rho)$
Spin vortex	Nonsingular vortex	0	1	±1	$\beta(\rho)$
Two-third vortex	Nonsingular vortex	2/3	1	-2/3, 4/3	$\beta(\rho)$
Phase vortex	Dirac monopole	2	1	0	θ
Spin vortex	Dirac monopole	0	1	±1	θ
Two-third vortex	Dirac monopole	2/3	1	-2/3, 4/3	θ

C limit	FM_1 limit	τ/φ	α/φ	γ/φ	β
Phase vortex	Nonsingular vortex	1	1	0	$\beta(\rho)$
Spin vortex	Nonsingular vortex	0	1	±1	$\beta(\rho)$
One-third vortex	Nonsingular vortex	1/3	1	-4/3, 2/3	$\beta(\rho)$
Phase vortex	Dirac monopole	1	1	0	θ
Spin vortex	Dirac monopole	0	1	±1	θ
One-third vortex	Dirac monopole	1/3	1	-4/3, 2/3	θ

Table 6.6: List of vortices, textures, and monopoles that can be constructed in a cyclic to FM interface using a combination of the condensate phase τ and the Euler angles α, β, γ. Here, τ, α, γ are given as multiples of the azimuthal angle φ, whilst β is either a multiple of the polar angle θ, or a monotonically increasing function of the transverse radius, ρ.

This energy becomes minimised precisely when $\eta = p/[(c_1 - c_2/20)n]$ for $c_1 \geq c_2/20$ and fixed p and q. Substitution of $\eta = p/[(c_1 - c_2/20)n]$ into Eq. (6.42) reveals that $E^{\text{FM-BN}} \leq E^{\text{BN}}, E^{\text{FM}_2}$ for $|p| < (2c_1 - c_2/10)n$. Thus, as in the previous FM interface, we can stabilise the interface by relying on a longitudinal dependence of the linear Zeeman shift, $p(z)$. One can see that at $p = \pm 2(c_1 - c_2/20)n$ the above solution becomes the FM state with spin $\langle \hat{F}_z \rangle = \pm 2$. Alternatively, the solution becomes the BN state precisely when $p = 0$, and hence has zero magnetisation. Therefore, this spinor provides an interpolating solution between the FM and BN phases, which is controlled by a longitudinal dependence of the linear Zeeman shift, $p(z)$.

Connections involving phase, spin, and half-quantum vortices

We start from the interpolating spinor between the FM and BN phases in Eq. (6.41) and first construct various vortex states using different combinations of the phase windings $\chi_{\pm 2}$. Again, similar to the previous cases, k-quantised phase vortices are connected across the interface by the choice $\chi_{\pm 2} = k\varphi$. An interesting case arises between a k-quantised phase vortex in the FM phases connecting to a spin vortex in the BN phase. This can be achieved by again allowing opposite phase windings in the outer components, i.e., $\chi_{\pm 2} = \pm k\varphi$, where the

Ferromagnetic to biaxial nematic — Vortices				
FM_2^+ limit	FM_2^- limit	BN limit	χ_2/φ	χ_{-2}/φ
Phase vortex	Phase vortex	Phase vortex	k	k
Phase vortex	Vortex-free	Half-quantum vortex	1	0
Vortex-free	Phase vortex	Half-quantum vortex	0	1
Phase vortex	Phase vortex	Spin vortex	$-k$	k

Table 6.7: Summary of possible vortex connections across an FM to BN interface. Each vortex is given in terms of the winding χ_m, given in multiples of the azimuthal angle φ. The FM limits are specified by the direction of the condensate spin, where a spin pointing up denotes a spinor of the form $\zeta = (1,0,0,0,0)^T$, and a spin pointing down denotes a spinor of the form $\zeta = (0,0,0,0,1)^T$. Additionally, k is an integer that allows one to generalise to higher quantisation.

interpolating spinor reads

$$\zeta^{\text{FM-BN}}_{\text{pv-sv}} = \frac{1}{\sqrt{2}} \begin{pmatrix} e^{ik\varphi}\sqrt{1+\eta} \\ 0 \\ 0 \\ 0 \\ e^{-ik\varphi}\sqrt{1-\eta} \end{pmatrix}. \tag{6.43}$$

As observed in Fig. 3.10, the BN phase allows for the creation of a HQV, characterised by a half-winding of the condensate phase. Such a vortex can be constructed by allowing a phase winding in only one of the outer components, i.e., $\chi_2 = \varphi$ and $\chi_{-2} = 0$ or vice versa. Using this first choice in Eq. (6.41) leads to the spinor

$$\zeta^{\text{FM-BN}}_{\text{pv-hqv}} = \frac{1}{\sqrt{2}} \begin{pmatrix} e^{i\varphi}\sqrt{1+\eta} \\ 0 \\ 0 \\ 0 \\ \sqrt{1-\eta} \end{pmatrix}, \tag{6.44}$$

which connects a HQV in the BN limit to a phase vortex in the FM_2 limit when $\eta = 2$, or a vortex-free state when $\eta = -2$. Choosing $\chi_{\pm 2}$ the opposite way around would reverse this connection. A summary of possible vortex connections constructed using the component phase windings is provided in Table 6.7.

Connections involving monopoles and nonsingular textures

As in the previous subsection discussing a cyclic to FM interface, we can apply the same logic and construct nonsingular defects in the FM phase that connect to singular defects in the BN

FM-BN — Vortices, textures and monopoles from Euler angles					
FM_2 limit	BN limit	τ/φ	α/φ	γ/φ	β
Nonsingular vortex	Phase vortex	2	1	0	$\beta(\rho)$
Nonsingular vortex	Spin vortex	0	1	±1	$\beta(\rho)$
Nonsingular vortex	Half-quantum vortex	1/2	1	-3/4	$\beta(\rho)$
Dirac monopole	Phase vortex	2	1	0	θ
Dirac monopole	Spin vortex	0	1	±1	θ
Dirac monopole	Half-quantum vortex	1/2	1	-3/4	θ

Table 6.8: List of vortices, textures, and monopoles that can be constructed in an FM to BN interface using a combination of the condensate phase τ and the Euler angles α,β,γ. Here, τ,α,γ are given as multiples of the azimuthal angle φ, whilst β is either a multiple of the polar angle θ, or a monotonically increasing function of the transverse radius, ρ.

phase, as well as Dirac monopoles that form the termination point of vortices. We begin by re-writing Eq. (6.41) in the general form

$$\zeta^{\text{FM-BN}} = \frac{1}{\sqrt{2}}\begin{pmatrix} \sqrt{1+\eta}\zeta^{\text{FM}_2^+} \\ 0 \\ 0 \\ 0 \\ \sqrt{1+\eta}\zeta^{\text{FM}_2^-} \end{pmatrix}, \tag{6.45}$$

where FM_2^+ is defined in Eq. (6.37) and FM_2^- is similarly obtained by applying a general spin rotation to $\zeta = (0,0,0,0,1)^T$. Then, choosing the Euler angles according to Eq. (6.39) results in $\text{FM}_2^\pm$ becoming

$$\zeta^{\text{FM}_2^+} = \begin{pmatrix} e^{-4i\varphi}\cos^4\frac{\beta}{2} \\ 2e^{-3i\varphi}\cos^3\frac{\beta}{2}\sin\frac{\beta}{2} \\ \sqrt{6}e^{-2i\varphi}\cos^2\frac{\beta}{2}\sin^2\frac{\beta}{2} \\ 2e^{-i\varphi}\sin^3\frac{\beta}{2}\cos\frac{\beta}{2} \\ \sin^4\frac{\beta}{2} \end{pmatrix}, \tag{6.46}$$

$$\zeta^{\text{FM}_2^-} = \begin{pmatrix} e^{-4i\varphi}\sin^4\frac{\beta}{2} \\ -2e^{-3i\varphi}\sin^3\frac{\beta}{2}\cos\frac{\beta}{2} \\ \sqrt{6}e^{-2i\varphi}\cos^2\frac{\beta}{2}\sin^2\frac{\beta}{2} \\ -2e^{-i\varphi}\cos^3\frac{\beta}{2}\sin\frac{\beta}{2} \\ \cos^4\frac{\beta}{2} \end{pmatrix}, \tag{6.47}$$

respectively. Then, choosing β as a monotonically increasing function of the transverse radius results in nonsingular vortices in both FM limits which connect to either phase, spin, or HQVs in the BN limit ($\eta = 0$) depending on whether $\tau = 2\varphi, 0, \varphi/2$, respectively. Similarly, choosing $\beta = \theta$ represents a generalisation of the Dirac monopole in both FM limits, which connects to either phase, spin, or HQVs in the BN limit depending on the choice of τ. A summary of vortices, textures, and monopoles that can be constructed using the Euler angles in an FM-BN interface is given in Table 6.8.

6.3 Numerical investigations of defect crossing physics

In this section we numerically investigate some topological interfaces defined in the preceding section, along with a subset of the possible defect connections. Our numerical setup is as follows. We numerically evolve the spin-2 GPEs defined in Eqs. (2.84) - (2.86) using a symplectic integrator [192] (see Appendix A.2 for details on the numerical integration scheme) with, for simplicity, a purely isotropic trapping potential $V = M\omega^2 r^2/2$. We simulate the energy loss during experiments by introducing a phenomenological damping coefficient, ν, through the substitution $t \to (1 - i\nu)t$. In all simulations considered, we choose $\nu = 1e{-}2$. We perform our simulations on a 3D of $N_s^3 = 128^3$ points, with side lengths $L = 20\ell$, where $(\ell = \hbar/M\omega)^{1/2}$ is the (isotropic) harmonic oscillator length. We choose parameters that correspond to a ^{87}Rb condensate [108] with $c_0 n = 1.32\times10^4 \hbar\omega\ell^3$, $c_0/c_1 = 90.7$, and $c_0/c_2 = -102$, where the ground state is predicted to be nematic (see Sec. 2.5.3 for details on the choice of numerical parameters). In each simulation, we perform a small spin rotation to the initial state to avoid components that are identically zero. Additionally, when constructing states with defects, the position of each defect is perturbed slightly to avoid artificial stability when placed at exactly the centre of the trap. Details of the trapped, dimensionless units can be found in Sec. 2.5.2.

6.3.1 Uniaxial nematic to biaxial nematic interface

The first interface we consider is that between the UN and BN phases, considered in Sec. 6.2.1. Since the UN and BN phases are energetically degenerate in the absence of a magnetic field, we introduce a spatially-dependent quadratic Zeeman shift $q(z)$ such that $q(z) > 0$ on the UN side and $q(z) < 0$ on the BN side to lift the degeneracy, and the maximum strength of our quadratic Zeeman shift is set to $q_{\max} = 0.1\hbar\omega$. The quadratic Zeeman shift linearly interpolates over a small transition region (which we take to be small compared to the spin-dependent healing lengths) from $q = -0.1\hbar\omega$ in the BN phase to $q = 0.1\hbar\omega$ in the UN phase.

Our investigation begins with that of the phase vortex connection, where the initial state is constructed as in Eq. (6.9). To imprint the vortices, we perform a short imaginary time propagation, then proceed to numerically evolve the spin-2 GPEs. The dynamics of this con-

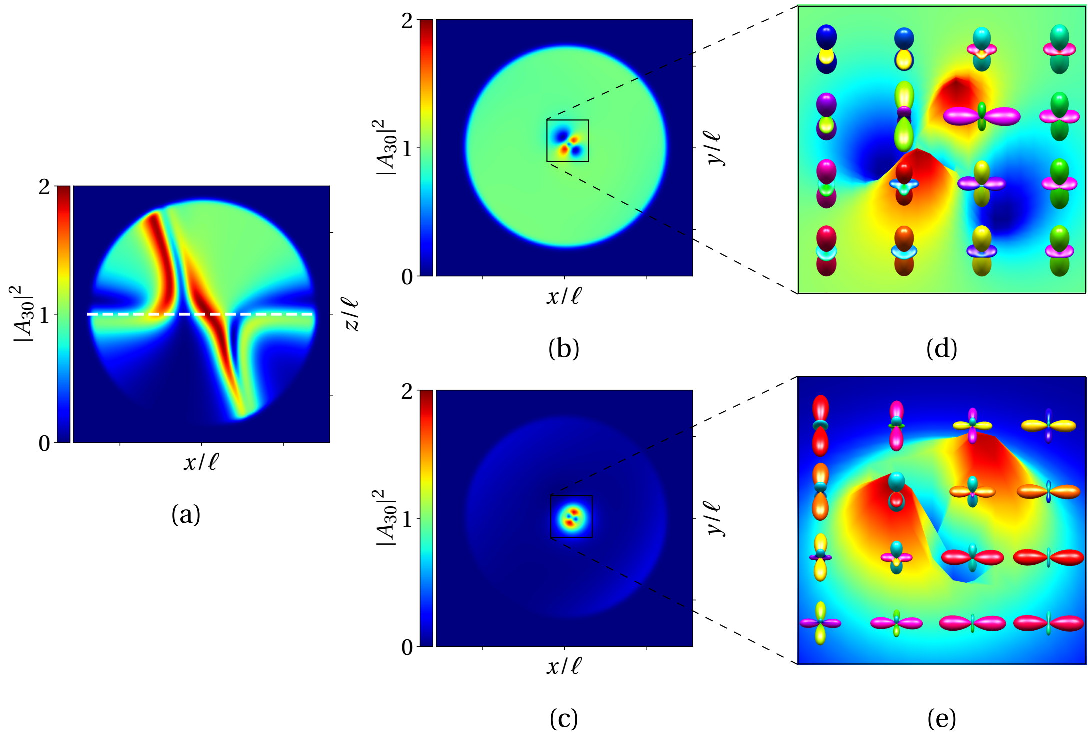

(a) (b) (c) (d) (e)

Figure 6.3: Spin singlet-trio amplitude for the UN-BN phase vortex connection given in Eq. (6.9) at $\tilde{t} = 300$. (a): Longitudinal cut showing the spatial separation of the two vortex lines. (b) and (c): Transverse cut on the UN ($z/\ell = 3.125$) and BN ($z/\ell = -3.125$) sides, respectively, showing the phase vortices and their composite core structure. (d) and (e): Magnified transverse cuts with an overlay of the spherical harmonics, showing the non-trivial change of symmetry of the order parameter within the vortex cores.

nection is split into two distinct parts, which are plotted in Fig. 6.3. Firstly, upon evolution, the two overlapping SQVs spatially separate due to an instability occurring at the interface $z \approx 0$. Each phase vortex then connects to a vortex-free state on the other side of the interface shown in Fig. 6.3a. After the initial separation, the cores of the vortices fill with atoms occupying different ground states, drastically altering the order parameter symmetry within the cores. In the UN case, the initially empty core fills with atoms occupying both the cyclic and BN phases, generating a topological interface within the core itself. This likely arises due to the differing phases factors between the spinor components, as seen in Fig. 6.1. The phase vortex on the BN side undergoes a similar filling of the empty vortex core, filling with atoms in the UN, BN and cyclic phases, also generating an interface within the core. The development of this composite core structure signifies the start of a splitting process, whereby the phase vortex is expected to split into two HQVs [41, 89]. Since our system has no rotation of the trapping potential to stabilise the vortices, the timescales considered here reveal that both vortices eventually leave the condensate cloud. Additionally, the phase vortex on the BN side of the interface is observed to leave the condensate before the splitting into two HQVs has occurred.

Note that it is possible to use the UN-BN interpolating spinor given in Eq. (6.4) to predict the topological interface formed within the core structures. For example, consider that η now has a radial dependence, with the radial distance given as $\rho = \sqrt{x^2 + y^2}$. Then vortex on the UN side can be modelled using Eq. (6.10) by requiring $\eta(0) = -1$ along the vortex core, which then interpolates smoothly to $\eta(\rho) = 1$ away from the vortex core, where we have assumed the vortex to be located at $\rho = 0$. This then results in the core taking on the BN phase, which smoothly interpolates back to the UN phase far from the vortex core. In addition, the phase difference arising between the components becomes $\chi = \mp 2\varphi$, which implies that χ can take values between 0 and 4π about the vortex line. Comparing this with Fig. 6.1 we see that at some point this phase difference will cross $\chi = \pi$ (and also $\chi = 3\pi$) in a region about the interface ($\eta = 0$), which implies that a transition to the cyclic phase will occur within the vortex core. This results in an interface forming within the vortex core itself, containing the BN, UN, and cyclic phases, which is clearly observed in Fig. 6.3. Similar analysis can be performed for the state in Eq. (6.11) to model the core on the BN side.

We next investigate a vortex connection that terminates on the interface. We start with the initial state in Eq. (6.11), which contains no phase winding in the middle component. The result is a phase vortex in the BN phase that smoothly connects to a vortex-free state in the UN phase. The resulting spin magnitude and singlet-trio amplitude after purely imaginary-time relaxation are plotted in Fig. 6.4. The dynamics of this connection closely resembles what the later dynamics of the BN side of the phase vortex connection would look like, provided that the vortices were stabilised against leaving the condensate. We see that the initial phase vortex on the BN side has undergone a splitting process into two HQVs, each of which can be seen to terminate at the interface. The cores of the HQVs are easily identified from the $|\langle\hat{\mathbf{F}}\rangle| = 2$ regions. Similar splitting of a phase vortex into HQVs has been observed in the polar phase of spin-1 condensates [41, 89]. For the timescales considered, the resulting HQVs remain stable against leaving the condensate. Additionally, we see the clear presence of the cyclic phase emerging at the interface $z/\ell \sim 0$, arising due to the phase difference between the spinor components (see Fig. 6.1).

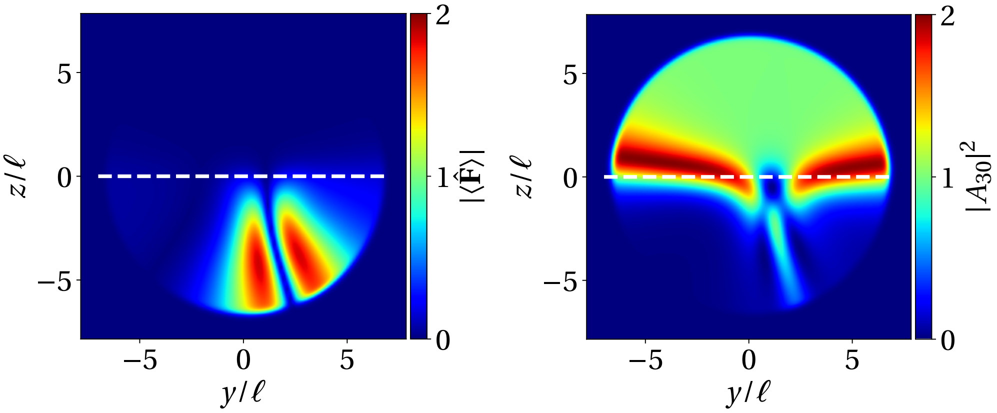

(a) (b)

Figure 6.4: Vortex-free to phase vortex connection defined by Eq. (6.9) with $\beta = 0$ and no winding in the middle component. (a): Spin magnitude at $\tilde{t} = 5$. The HQV cores are identified where $|\langle\hat{\mathbf{F}}\rangle| = 2$. (b): Spin-singlet trio amplitude at $\tilde{t} = 5$. A cyclic region is revealed where $|A_{30}|^2 = 2$, which arises due to phase differences (see Fig 6.1).

6.3.2 Cyclic to ferromagnetic interface

We numerically investigate vortex connections across a topological interface between the cyclic and FM_2 phases, given by Eq. (6.31). Since our numerical simulations use parameters that predict a nematic ground state, we introduce a spatially-dependent c_1 term such that $c0/c_1 = 90.7$ on the cyclic side but $c_0/c_1 = -90.7$ on the FM side, effectively changing the sign of the c_1 term [193, 194]. Now, in the FM region, the parameters ensure that the FM region remains stable. Despite the cyclic state not being the predicted ground state, the interface is observed to remain stable for the timescales considered in our simulations.

We firstly investigate the connection of a third vortex in the cyclic phase connecting to a singular phase vortex in the FM_2 phase using Eq. (6.34) as the initial state. This initial state is then propagated using a short imaginary-time evolution to imprint the vortex cores and, once the core is imprinted, we switch to complex-time simulations using a damping coefficient of $\nu = 10^{-2}$. The resulting spin magnitude and spin-singlet duo amplitude for this interface after time $\tilde{t} = 5$ are plotted in Fig. 6.5. Here, $|\langle\hat{\mathbf{F}}\rangle|$ reveals non-trivial core structures emerging. Clearly one can see the third vortex on the cyclic side of the interface ($z/\ell < 0$) evidenced by the $|\langle\hat{\mathbf{F}}\rangle| = 1$ core. However, unlike the previous case where the vortices spatially separated, this $|\langle\hat{\mathbf{F}}\rangle| = 1$ region then extends throughout the longitudinal extent of the condensate, and penetrates into the FM region, revealing that the initial phase vortex of the FM phase has developed a composite core structure. This composite core structure is separated into three distinct parts: Inside is the $|\langle\hat{\mathbf{F}}\rangle| = 1$ region, which is then encased in a cyclic shell as

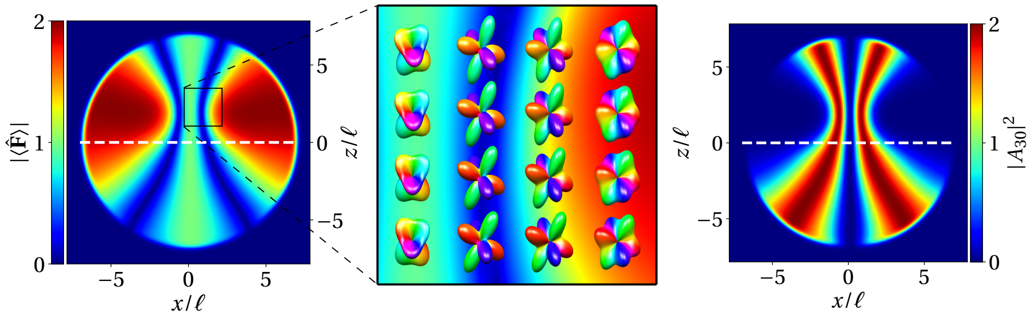

(a) (b) (c)

Figure 6.5: One-third vortex to phase vortex connection in an interface between the cyclic and FM_2 phases given by Eq. (6.34) at $\tilde{t} = 50$. (a): Longitudinal cut of $|\langle\hat{\mathbf{F}}\rangle|$ at $y/\ell = 0$. The third vortex on the cyclic side ($z/\ell < 0$) is evident from the $|\langle\hat{\mathbf{F}}\rangle| = 1$ core which extends throughout the FM region. (b): Zoomed transverse cut of $|\langle\hat{\mathbf{F}}\rangle|$ inside the core in the FM region. Overlaid are the spherical harmonics showing the non-trivial change of order parameter symmetry inside the core. (c): Longitudinal cut of $|A_{30}|^2$ at $y/\ell = 0$. Cyclic regions are identified from $|A_{30}|^2 = 2$.

seen from the $|A_{30}|^2 = 2$ regions in Fig. 6.5c. Then, far away from the vortex core, the system smoothly interpolates back to a $|\langle\hat{\mathbf{F}}\rangle| = 2$ region in the bulk of the condensate. The spherical harmonics of the internal core structure plotted in Fig. 6.5b reveal the non-trivial change of order parameter symmetry within the composite core.

As we did in the UN to BN case, one can use the general spinor in Eq. (6.34) to analytically predict the vortex core structures observed when η is a function of the transverse radius $\rho = \sqrt{x^2 + y^2}$. The core can be described by choosing an appropriate function for $\eta(\rho)$ that interpolates between all three phases. In particular, we choose $\eta(\rho) = 3\tanh\big(\rho/2\big) - 1$, which becomes $\eta = -1$ (FM_1^-) at $\rho = 0$ along the vortex core, $\eta = 0$ (cyclic) at $\rho = \tanh^{-1}(1/3)$, and finally $\eta = 2$ (FM_2^+) at large ρ. Thus, this interpolating spinor accurately models the behaviour observed in Fig. 6.5.

Instead of considering only singular vortices, we can also investigate the nonsingular vortex connection given in Eq. (6.36). We choose this as the initial state and choose $\beta = \pi\left[1 + \tanh\big(\rho - 1\big)\right]/2$ to model the required monotonically increasing function. Here we focus only on the cyclic to FM_2 limit, but equivalently the cyclic to FM_1 limit can be chosen by an appropriate choice of p and q that interpolates η between -1 and 0. We perform purely imaginary-time simulations to simulate energy relaxation. We start by discussing the dynamics of the doubly quantised vortex on the cyclic side of the interface, shown in Fig. 6.6. As expected for a doubly quantised vortex line, it very rapidly undergoes a splitting process. In this case, it splits into four one-third vortices, evidenced by the $|\langle\hat{\mathbf{F}}\rangle| = 1$ regions, and a fur-

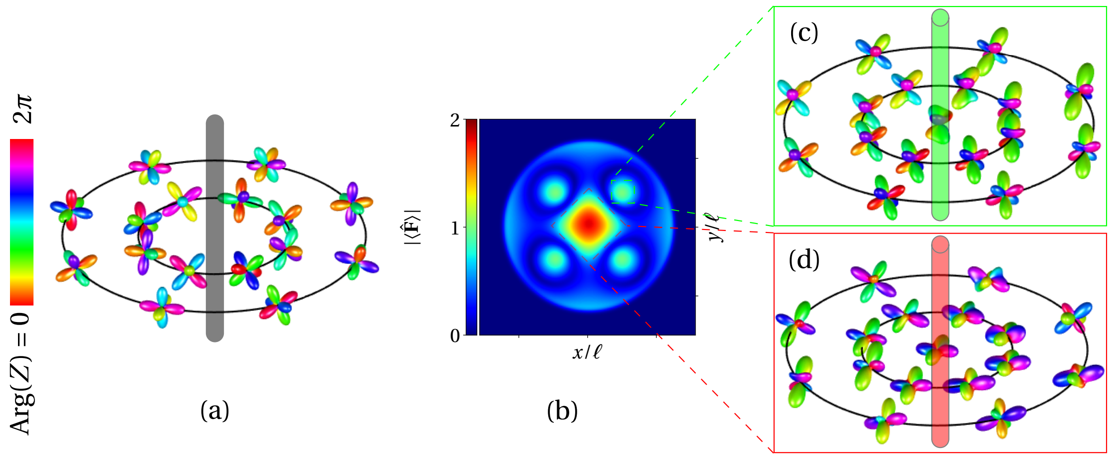

Figure 6.6: Schematic representation of the splitting process occurring on the cyclic side of the interface ($z/\ell < 0$) given by the state in Eq. (6.36). (a): Spherical harmonic representation of the initial doubly quantised vortex line. By traversing a point about the vortex line, the condensate phase is seen to wind by 4π. (b) Transverse cut of $|\langle\hat{\mathbf{F}}\rangle|$ at $z/\ell \approx -3$ after imaginary-time evolution at $\tilde{t} = 1.5$ showing the splitting of the initial doubly quantised vortex into fractional vortices. The one-third and two-third vortices are clearly identified from the $|\langle\hat{\mathbf{F}}\rangle| = 1$ and $|\langle\hat{\mathbf{F}}\rangle| = 2$ regions, respectively. (c) and (d): Spherical harmonic representations about the one-third and two-third vortices, respectively. The spherical harmonics shows the non-trivial change of the order parameter symmetry as we move away from the vortex cores.

ther two-third vortex, evidence by the large $|\langle\hat{\mathbf{F}}\rangle| = 2$ region. The discrepancy of the core size could arise from the different vortices being set by different healing lengths. Analysis of the spherical harmonics in Fig. 6.6c,d shows the non-trivial order parameter symmetry both within and outside the vortex cores. By following the spherical harmonics about the vortex cores, the condensate phase changes by $2\pi/3$ and $4\pi/3$ confirming that these structures are one-third and two-third vortices. Due to the energy relaxation, the one-third vortices quickly leave the condensate. However, the two-third vortex is first observed to undergo a further splitting process in which it splits into two one-third vortices, which then proceed to exit the condensate cloud.

The initial nonsingular vortex on the FM side of the interface also undergoes a complex splitting process, shown in Fig. 6.7. The nonsingular vortex is observed to split into four singular vortices, observed from transverse cuts of $|\langle\hat{\mathbf{F}}\rangle|$. Analysis of the spherical harmonics reveal the non-trivial symmetry within the singular vortex cores. As in the case on the cyclic side, these vortices rapidly leave the condensate due to the energy relaxation. On both sides of the interface the vortex structures are observed to terminate at the interface itself, and do not connect in a way that is observed in the phase vortex to one-third vortex connection (see

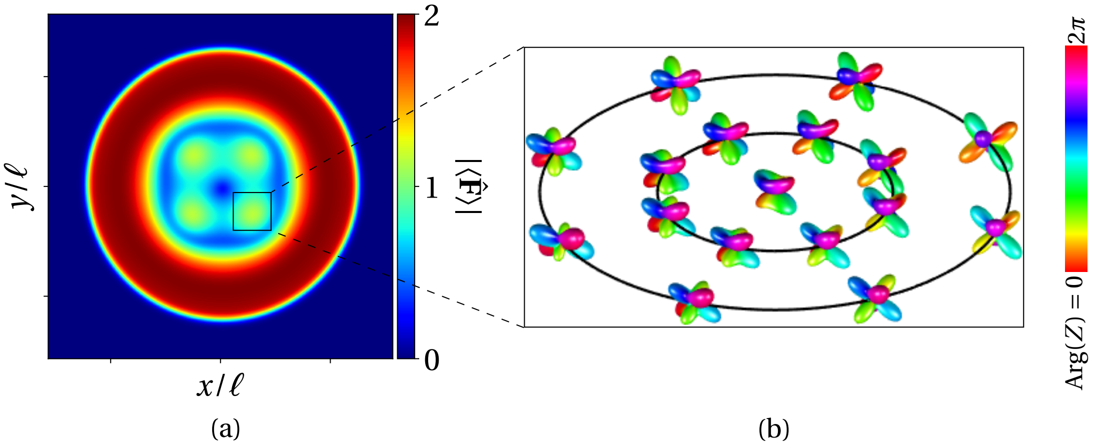

(a) (b)

Figure 6.7: Schematic representation of the splitting process occurring on the FM side of the interface ($z/\ell > 0$) of the state in Eq. (6.36). The initial state on this side of the interface is given explicitly in Eq. (6.37) with Euler angles given in Eq. (6.39). (a): Transverse cut of $|\langle\hat{\mathbf{F}}\rangle|$ at $z/\ell \approx 3$ after complex-time evolution at $\tilde{t} = 1.5$. The singular vortex structures can be seen from the $|\langle\hat{\mathbf{F}}\rangle| \approx 1$ cores. (b): Spherical harmonic representation of the internal structure of the singular vortex, showing the non-trivial symmetry within the core.

Fig. 6.5).

6.4 Conclusions

In this chapter we have presented spin-2 BECs as a medium for investigating topological interface physics. We constructed topological interfaces within the condensate by means of interpolating spinor wave functions which are derived from steady-state solutions to the spin-2 GPEs, which smoothly connect different phases using an interpolation parameter. In each case we constructed multiple different classes of topological defects which either connected smoothly across the interface, or terminated on the interface itself. In particular, we showed how phase, spin, and fractional vortices could be constructed simply from the component phase windings, and how more complicated connections could be constructed by applying a spin rotation to the general interface spinor with appropriate choices for the Euler angles. It was shown that interfaces between the nematic phases allow for monopoles and nonsingular vortices on one side of the interface to smoothly connect to singular line defects on the other side. In addition, interfaces involving the FM phases can be engineered to contain a generalisation of the Dirac monopole in the FM limit, which connects to a singular vortex line in the opposite limit.

Numerical investigations of the UN to BN and cyclic to FM interfaces were also performed. We showed that phase vortices in a UN to BN interface had two distinct parts to their dynamics. The initially overlapping vortex lines quickly spatially separated, arising from an instability at the interface itself. Each vortex then developed composite core structures that contained UN, BN, and cyclic phases, forming a topological interface within the vortex cores themselves. A phase vortex in the BN phase terminating at the interface was also investigated, which was observed to split into a pair of HQVs with FM cores, which also terminated at the interface. In the cyclic to FM interface, we observed a phase vortex in the FM phase smoothly connect to a one-third vortex in the cyclic limit by forming a composite structure that had an inner $|\langle\hat{\mathbf{F}}\rangle| = 1$ core, encased by a surrounding cyclic region, before smoothly interpolating back to the $|\langle\hat{\mathbf{F}}\rangle| = 2$ bulk. Lastly, a connection involving a nonsingular vortex was numerically simulated. We showed that the initial nonsingular structure on the FM side connected smoothly to a doubly quantised phase vortex in the cyclic limit. The nonsingular vortex was then observed to split into four singular structures, whilst the doubly quantised phase vortex split into four one-third vortices, with a large two-third vortex in the centre of the condensate.

CHAPTER 7

CONCLUSIONS & FUTURE WORK

In this Chapter we give an overview of the overarching conclusions of the thesis, in addition to suggesting some avenues for future work.

In Part I we introduced the necessary mathematical framework needed to understand these systems in detail. We started with the scalar system, constructing the full Hamiltonian using a quantum treatment before introducing the mean-field theory and resulting GPEs. Then, we generalised the theory to two-component systems, and derived the miscibility criterion. The theory necessary to understand spinor BECs was introduced, where we constructed the single-particle and interaction Hamiltonians using a quantum treatment, then introduced the mean-field equations along with their reduction to lower dimensions and dimensionless versions. Finally, an overview of the ground states, symmetries, and topologically stable defects that arise in spin-1 and spin-2 systems was introduced. For each ground state we presented two different graphical representations, and then discussed the dynamical properties of certain vortex states arising in these systems.

7.1 The versatility of spinor Bose-Einstein condensates

In this thesis we have shown the robustness of spinor and pseudospin-1/2 systems for investigating a variety of different physics. We showed how the relaxation dynamics of HQVs in pseudospin-1/2 systems exhibit similarities in its spatial properties compared to similar studies concerning scalar vortices in scalar BECs [143, 144], despite being a topologically distinct vortex. However, there was a multitude of differences found in the temporal aspects of the scaling. It was shown that the decay rate of the vortices at early times was strongly correlated to the ratio of the inter- and intra-species interactions, leading to wildly different dynamics at these early times, before the decay rate at later times tended to a universal scaling which has been observed in scalar systems [144].

In addition, we showed how spinor condensates can be used as a test bed to discern more about the scaling laws associated with discontinuous, first-order quantum phase transitions. We presented the broken-axisymmetry to ferromagnetic phase transition as an example, and showed that it did indeed fit the requirements of a first-order transition. We generalised the KZM, and showed how scaling laws that govern the density of defects can still be found despite having a gapless spectrum. Independent of the KZM, we also derived scaling laws for the onset of the decay of the metastable state after the transition point is crossed, which aligned with the predictions of our generalised KZM, further justifying the robustness of our theory.

Finally, we showed that spinor BECs are excellent candidate for investigating topological interface physics due to their rich phase diagrams. In particular, we presented stationary solutions derived from the spinor GPEs that offered interpolating solutions between two distinct ground states dependent on an interpolating parameter. It was also shown how a myriad of different defect states can be connected across the interface, ranging from simple quantised phase vortices to more complicated structures representing generalisations of the Dirac monopole. Our work concluded with mean-field numerical simulations of select examples, and showed vastly different results between the cases, ranging from the formation of composite core structures and splitting of phase vortices in an interface between the uniaxial nematic and biaxial nematic phases, to complex splitting process of nonsingular vortices in a cyclic to ferromagnetic interface.

7.2 Future work

7.2.1 Understanding more about half-quantum vortex dynamics

Our numerical investigation of the relaxation dynamics of HQVs investigated in Chapter 4 revealed interesting behaviour unseen in similar relaxation studies involving scalar condensates [144]. In particular, a clear attractive force between the vortices dominates at sufficiently high γ, which simple point-vortex models have been unable to account for [42, 43], so discerning more about the dynamics of these objects is an active topic. In fact, recent theoretical work has already shed more light on the topic [195]. They showed that the atoms filling the large cores of the HQVs act as a pinning potential, driving the HQVs to collide. This work therefore explains previously observed numerical simulations of HQV dynamics in these systems [42, 43], and provides a better insight into our observed decay laws.

In addition, experimental work has already been conducted investigating the relaxation dynamics of HQVs in a spin-1 BEC [196]. However, corresponding numerical investigations of the decay rate of the vortices has not been carried out, and it would indeed be interesting to see whether there is overlap with our pseudospin-1/2 work.

7.2.2 Quantum phase transitions and metastability

Recently, there has been new interest in understanding quantum phase transitions where metastability plays a crucial role such as in false-vacuum decay [197–200]. However, a lack of theoretical understanding of first-order quantum phase transitions leads to confusion to exactly how the metastable state decays. Our work presented in Chapter 5 presents a theoretical framework for extracting scaling laws associated with first-order quantum phase transitions both for the onset of the decay of the metastable state itself and the density of defects far past the transition point. In addition, the work carried out is applicable in experimentally-relevant parameter regimes, which opens up the avenue of spin-1 BECs being used as emulators to understand the recent interest in false-vacuum decay.

7.2.3 Experimental realisations of topological interfaces

Our work in Chapter 6 already extends the work of Refs. [85–87] by considering topological interfaces between the ground state phases of spin-2 BECs, but can be used as a further stepping stone to understand more about topological interface physics. Interfaces formed within vortex cores has recently been achieved in both spin-1 [88, 89] and spin-2 BECs [54], but current experimental realisations of interfaces formed between bulk regions has remained elusive due to lack of proper experimental techniques. Once an experimental realisation of such an interface is achieved, our work can be used to understand the resulting core structure of defects connected across the interface. Naturally, further numerical studies of more complicated examples, e.g., monopoles, present an avenue for studying the dynamics of such objects when constrained to topological interfaces.

Part III

Appendices

APPENDIX A

NUMERICAL TECHNIQUES

A.1 Dimensionless two-component Gross-Pitaevskii equations

As mentioned in Sec 2.5, dimensionless equations offer numerous benefits, including increased numerical stability and the ease of reformulating calculations into a desired scale and parameter regime. Here we derive the dimensionless two-component GPEs which are stated in Eq. (4.14).

To begin we start with the full 3D dimensional GPEs for a two-component system:

$$i\hbar\frac{\partial\psi_1}{\partial t} = \left(-\frac{\hbar^2\nabla^2}{2m_1} + g_1|\psi_1|^2 + g_{12}|\psi_2|^2\right)\psi_1, \tag{A.1}$$

$$i\hbar\frac{\partial\psi_2}{\partial t} = \left(-\frac{\hbar^2\nabla^2}{2m_2} + g_2|\psi_2|^2 + g_{12}|\psi_1|^2\right)\psi_2. \tag{A.2}$$

Our simulations are performed on space-time grid lattices with a spatial side length of $L = N_s a_s$, where a_s is the lattice spacing and the total number of grid points is given as N_s^d where d is the dimensionality of the system. With these, we make use of the following dimensionless variables

$$\tilde{\mathbf{r}} = \frac{\mathbf{r}}{a_s}, \quad \tilde{g}_j = \frac{2mg_j {a_s}^{2-d}}{\hbar^2}, \quad \tilde{t} = \frac{t\hbar}{2ma_s^2}, \quad \tilde{\psi}_j = \sqrt{a_s^d}\, e^{2i\tilde{t}}\psi_j, \tag{A.3}$$

where $m = m_1 = m_2$. Using the above dimensionless quantities, we can rescale the dimensional variables in Eqs (A.1) - (A.2), which leads to the dimensionless equations

$$i\frac{\partial\tilde{\psi}_1}{\partial t} = \left(-\tilde{\nabla}^2 + \tilde{g}_1|\tilde{\psi}_1|^2 + \tilde{g}_{12}|\tilde{\psi}_2|^2\right)\tilde{\psi}_1, \tag{A.4}$$

$$i\frac{\partial\tilde{\psi}_2}{\partial t} = \left(-\tilde{\nabla}^2 + \tilde{g}_2|\tilde{\psi}_2|^2 + \tilde{g}_{12}|\tilde{\psi}_1|^2\right)\tilde{\psi}_2. \tag{A.5}$$

Now, if we have atomic species where $g_1 = g_2 = g$, then the above equations simplify to (dropping the tildes for notational convenience)

$$i\frac{\partial\psi_1}{\partial t} = \left(-\nabla^2 + g|\psi_1|^2 + \gamma|\psi_2|^2\right)\psi_1, \tag{A.6}$$

$$i\frac{\partial\psi_2}{\partial t} = \left(-\nabla^2 + g|\psi_2|^2 + \gamma|\psi_1|^2\right)\psi_2, \tag{A.7}$$

where $\gamma = g_{12}/g$ is the ratio of inter- to intra-species interaction.

A.2 Symplectic integrators for spinor Bose-Einstein condensates

The numerics of Chapters 5 and 6 are based on second-order symplectic integrators: a type of numerical scheme for Hamiltonian systems. In particular, we make use of the work of Symes *et al.* for both our spin-1 [176] and spin-2 [192] systems. Symplectic integration schemes provide highly accurate solutions for Hamiltonian systems over extended periods of time, making them ideal for studying the long-time dynamics in Chapter 5. In addition, the second-order numerical schemes devised by Symes *et al.* have been shown to be both simpler and more efficient than other second-order composition methods [201], which is critical for compute-heavy 3D simulations as in Chapter 6.

The spinor symplectic integration schemes work by splitting the spinor GPEs into two subsystems. The first is a single-particle-like subsystem, which includes the kinetic energy and the Zeeman terms of the Hamiltonian, which is solved exactly in Fourier Space. The second system comprises the non-linear subsystem, which includes the remaining non-linear terms in the spinor GPEs. Due to the nature of the splitting, this remaining subsystem becomes exactly solvable in position space. Note that the Zeeman terms are assumed to be spatially-uniform (a good approximation in experiments), which allows them to be included in the single-particle-like subsystem. However, if the Zeeman shifts are not spatially-uniform they must instead be included with the non-linear subsystem, which still leads to analytical solutions in the form of Jacobi elliptic functions (see Refs. [176, 192] for details). Finally, though not used in this thesis, the two-way splitting implies that the scheme can be extended using the composition method of Blanes and Moan [202] to fourth-order, should a higher-order symplectic scheme be required.

The numerical methods throughout this thesis have been implemented using the personally-developed Python package *PyGPE* [203]: a CUDA-accelerated library for numerically solving the GPEs for scalar, two-component, spin-1, and spin-2 BEC systems. It supports 1D, 2D, and 3D grid lattices, as well as possessing the ability to run on both CPUs or Nvidia-native GPUs. In addition, it provides tools for data handling, as well as a suite of diagnostics functions useful for handling data from BEC simulations.

APPENDIX B

DERIVATION OF STATIONARY SOLUTIONS IN A SPIN-2 BOSE-EINSTEIN CONDENSATE

B.1 Time-independent spin-2 Gross-Pitaevskii equations

Here we derive stationary solutions to the spin-2 GPEs that provide the interpolating spinor wave functions that are used throughout Chapter 6. Firstly, recall that the stationary solutions of the spin-2 GPEs are obtained by substituting $\psi_m = \sqrt{n}\zeta_m e^{-i\mu t/\hbar}$ into Eqs. (2.84)-(2.86). Assuming a uniform system with $V(\mathbf{r}) = 0$, this results in

$$\mu\zeta_2 = \left(-2p + 4q + c_0 n + 2c_1 n\langle\hat{F}_z\rangle\right)\zeta_2 + c_1 n\langle\hat{F}_-\rangle\zeta_1 + \frac{c_2}{\sqrt{5}} n A_{00}\zeta^*_{-2}, \tag{B.1}$$

$$\mu\zeta_1 = \left(-p + q + c_0 n + c_1 n\langle\hat{F}_z\rangle\right)\zeta_1 + c_1\left(\frac{\sqrt{6}}{2} n\langle\hat{F}_-\rangle\zeta_0 + n\langle\hat{F}_+\rangle\zeta_2\right) - \frac{c_2}{\sqrt{5}} n A_{00}\zeta^*_{-1}, \tag{B.2}$$

$$\mu\zeta_0 = c_0 n\zeta_0 + \frac{\sqrt{6}}{2} c_1\left(n\langle\hat{F}_+\rangle\zeta_1 + n\langle\hat{F}_-\rangle\zeta_{-1}\right) + \frac{c_2}{\sqrt{5}} n A_{00}\zeta^*_0, \tag{B.3}$$

$$\mu\zeta_{-1} = \left(p + q + c_0 n - c_1 n\langle\hat{F}_z\rangle\right)\zeta_{-1} + c_1\left(\frac{\sqrt{6}}{2} n\langle\hat{F}_+\rangle\zeta_0 + n\langle\hat{F}_-\rangle\zeta_{-2}\right) - \frac{c_2}{\sqrt{5}} n A_{00}\zeta^*_1, \tag{B.4}$$

$$\mu\zeta_{-2} = \left(2p + 4q + c_0 n - 2c_1 n\langle\hat{F}_z\rangle\right)\zeta_{-2} + c_1 n\langle\hat{F}_+\rangle\zeta_{-1} + \frac{c_2}{\sqrt{5}} n A_{00}\zeta^*_2. \tag{B.5}$$

Follow the literature of Ref. [96], we make the following assumptions. We can choose the overall phase such that ζ_0 is real and, since the system has SO(2) symmetry about the direction of the applied magnetic field (which we take to be the z-axis), we choose the coordinate system such that $\langle\hat{F}_y\rangle = 0$ without loss of generality, implying $\langle\hat{F}_+\rangle = \langle\hat{F}_-\rangle$. In addition, to simplify further, we consider the specific case where the transverse magnetisation is zero $\langle\hat{F}_\pm\rangle = 0$ which is valid in a system where $q < 0$ such that the system favours atoms in the outer components [see Eq. (2.81)]. Assuming the above, the stationary equations can be transformed into the following simplified set of equations:

$$0 = (-2p + 4q + c_0 n + 2c_1 n\langle\hat{F}_z\rangle - \mu)\zeta_2 + \frac{c_2}{\sqrt{5}} n A_{00}\zeta_{-2}^*, \tag{B.6}$$

$$0 = (2p + 4q + c_0 n - 2c_1 n\langle\hat{F}_z\rangle - \mu)\zeta_{-2} + \frac{c_2}{\sqrt{5}} n A_{00}^*\zeta_2, \tag{B.7}$$

$$0 = (-p + q + c_0 n + c_1 n\langle\hat{F}_z\rangle - \mu)\zeta_1 + \frac{c_2}{\sqrt{5}} n A_{00}\zeta_{-1}^*, \tag{B.8}$$

$$0 = (p + q + c_0 n - c_1 n\langle\hat{F}_z\rangle - \mu)\zeta_{-1} + \frac{c_2}{\sqrt{5}} n A_{00}^*\zeta_1, \tag{B.9}$$

$$0 = \left(c_0 n + \frac{c_2}{\sqrt{5}} n A_{00} - \mu\right)\zeta_0. \tag{B.10}$$

Noting that the above equations are decoupled in three parts, we can construct the following matrix equations relating to Eqs. (B.6)-(B.7) and Eqs. (B.8) - (B.9), respectively, as

$$\begin{pmatrix} 4q + 2\tilde{\beta} - \tilde{\mu} & \tilde{\alpha} \\ \tilde{\alpha}^* & 4q - 2\tilde{\beta} - \tilde{\mu} \end{pmatrix} \begin{pmatrix} \zeta_2 \\ \zeta_{-2}^* \end{pmatrix} = 0, \tag{B.11}$$

$$\begin{pmatrix} q + \tilde{\beta} - \tilde{\mu} & -\tilde{\alpha} \\ -\tilde{\alpha}^* & q - \tilde{\beta} - \tilde{\mu} \end{pmatrix} \begin{pmatrix} \zeta_1 \\ \zeta_{-1}^* \end{pmatrix} = 0, \tag{B.12}$$

with Eq. (B.10) being recast as

$$(\tilde{\alpha} - \tilde{\mu})\zeta_0 = 0, \tag{B.13}$$

where $\tilde{\mu} = \mu - c_0 n$, $\tilde{\alpha} = c_2 n A_{00}/\sqrt{5}$ and $\tilde{\beta} = c_1 n\langle\hat{F}_z\rangle - p$. The stationary solutions are then classified according to the determinant of the coefficient matrices of the above equations. Explicitly, these are

$$D_2 = (4q - \tilde{\mu})^2 - 4\tilde{\beta}^2 - |\tilde{\alpha}|^2, \tag{B.14}$$

$$D_1 = (q - \tilde{\mu})^2 - \tilde{\beta}^2 - |\tilde{\alpha}|^2. \tag{B.15}$$

From these determinants and Eq. (B.13), we can derive stationary solutions that interpolate between different ground states of the spin-2 system.

B.2 Stationary solutions involving interpolating spinors

B.2.1 Uniaxial nematic, biaxial nematic, and cyclic limits

First consider the case $D_1 \neq 0$ and $D_2 = 0$. Then, Eq. (B.12) and $D_1 \neq 0$ implies that $\zeta_1 = \zeta_{-1} = 0$. Here, consider the case that $\tilde{\mu} = \tilde{\alpha}$. Then all three of the $\zeta_{\pm 2}, \zeta_0$ components can be non-zero. From the definition of the longitudinal magnetisation given in Eq. (2.81), we have

$$|\zeta_2| = \sqrt{|\zeta_{-2}|^2 + \frac{\langle \hat{F}_z \rangle}{2}}. \tag{B.16}$$

The normalisation condition states $|\zeta_2|^2 + |\zeta_0|^2 + |\zeta_{-2}|^2 = 1$, which leads to

$$|\zeta_{-2}| = \sqrt{\frac{1 - \zeta_0^2 - \langle \hat{F}_z \rangle /2}{2}}, \tag{B.17}$$

$$|\zeta_2| = \sqrt{\frac{1 - \zeta_0^2 + \langle \hat{F}_z \rangle /2}{2}}. \tag{B.18}$$

Thus, the total spinor now reads

$$\zeta = \begin{pmatrix} e^{i\chi_2}\sqrt{\frac{1-\zeta_0^2+\langle \hat{F}_z\rangle/2}{2}} \\ 0 \\ \zeta_0 \\ 0 \\ e^{i\chi_{-2}}\sqrt{\frac{1-\zeta_0^2-\langle \hat{F}_z\rangle/2}{2}} \end{pmatrix}. \tag{B.19}$$

The substitution of the above spinor into Eq. (B.11) leads to the relations $\tilde{\mu} = 2q - \tilde{\beta}^2/(2q)$ and $\langle \hat{F}_z \rangle = (\tilde{\beta} + p)/(c_1 n)$, where $\tilde{\beta}$ can be calculated from the following equation [96]:

$$\tilde{\beta}^3 + p\tilde{\beta}^2 + 4q[q + 2c_1 n(1 - \zeta_0^2)]\tilde{\beta} + 4pq^2 = 0. \tag{B.20}$$

Let us consider the case $p = 0$, then the above equation transforms to

$$\tilde{\beta}^2 = -4q\left[q + 2c_1 n(1 - \zeta_0^2)\right]. \tag{B.21}$$

Then, since the left-hand side is positive, we derive the condition $|q| > |2c_1 n(1 - \zeta_0^2)|$. Under this condition $\tilde{\beta}$ is determined to be $\tilde{\beta} = 0$ [96], and hence $\langle \hat{F}_z \rangle = 0$. To determine ζ_0 we minimise the energy per particle [96]

$$\epsilon = \sum_{m=-2}^{2} (-pm + qm^2)|\zeta_m|^2 + \frac{1}{2}c_0 n + \frac{1}{2}c_1 n|\langle \hat{\mathbf{F}} \rangle|^2 + \frac{1}{2}c_2 n|A_{00}|^2. \tag{B.22}$$

Substituting Eq. (B.19) and $\langle \hat{F}_z \rangle = 0$ into the above expression yields

$$\epsilon = 4q(1-\zeta_0^2) + \frac{1}{2}c_0 n + \frac{c_2 n}{10}\left| e^{i(\chi_2+\chi_{-2})}(1-\zeta_0^2) + \zeta_0^2 \right|^2 . \tag{B.23}$$

Note that since

$$\tilde{\alpha} = \tilde{\mu} = \frac{c_2 n}{5}\left(e^{i(\chi_2+\chi_{-2})}\sqrt{(1-\zeta_0^2) - \frac{\langle \hat{F}_z \rangle}{4}} + \zeta_0^2 \right), \tag{B.24}$$

which must be real, we require $\chi_2 + \chi_{-2} = 0$ or π. If $c_2 < 0$, then the energy is minimised by $\chi_2 + \chi_{-2} = \pi$. Taking the derivative of Eq. (B.23) with respect to ζ_0 and setting equal to zero leads to the expression for ζ_0:

$$\zeta_0 = \sqrt{\frac{1 + 10q/(c_2 n)}{2}}. \tag{B.25}$$

Substituting ζ_0 back into Eq. (B.19) leads to the final interpolating spinor

$$\zeta^{\text{C-N}} = \begin{pmatrix} i e^{i\chi}\frac{\sqrt{1-10q/(c_2 n)}}{2} \\ 0 \\ \sqrt{\frac{1+10q/(c_2 n)}{2}} \\ 0 \\ i e^{-i\chi}\frac{\sqrt{1-10q/(c_2 n)}}{2} \end{pmatrix}, \tag{B.26}$$

where we have chosen $\chi_{\pm 2} = \pi/2 + \chi$ to satisfy $\chi_2 + \chi_{-2} = \pi$ and χ is an arbitrary phase. This solution continuously becomes the three-component cyclic state when $q = 0$, and the BN (UN) when $q = -c_2 n/10$ $(q = c_2 n/10)$.

Alternatively, when $c_2 < 0$ the energy is minimised by having $\chi_2 + \chi_{-2} = 0$, which instead leads to the interpolating spinor

$$\zeta^{\text{UN-BN}} = \begin{pmatrix} e^{i\chi}\frac{\sqrt{1-10q/(c_2 n)}}{2} \\ 0 \\ \sqrt{\frac{1+10q/(c_2 n)}{2}} \\ 0 \\ e^{-i\chi}\frac{\sqrt{1-10q/(c_2 n)}}{2} \end{pmatrix}, \tag{B.27}$$

which now interpolates between the UN phase at $q = |c_2|n/10$ and the BN phase at $q = -|c_2|n/10$.

B.2.2 Cyclic to ferromagnetic

Consider the case that $D_2 = D_1 = 0$. Then, we have the following system of equations for the determinants

$$0 = (4q - \tilde{\mu})^2 - 4\tilde{\beta}^2 - |\tilde{\alpha}|^2, \tag{B.28}$$

$$0 = (q - \tilde{\mu})^2 - \tilde{\beta}^2 - |\tilde{\alpha}|^2, \tag{B.29}$$

which can be solved to find $\tilde{\mu}$:

$$\tilde{\mu} = \frac{5q^2 - \tilde{\beta}^2}{2q}. \tag{B.30}$$

Then, for the case that $\tilde{\mu} \neq \tilde{\alpha}$ and $q \neq 0$, Eq. (B.13) implies $\zeta_0 = 0$. Now, since we assumed zero transverse magnetisation, Eq. (2.81) leads to

$$2c_1 n(\zeta_2^* \zeta_1 + \zeta_{-1}^* \zeta_{-2}) = 0. \tag{B.31}$$

We can use the matrix Eqs (B.11) and (B.12) to find expressions for ζ_{-1}^* and ζ_{-2} or ζ_2^* and ζ_1 which when substituted into the above equation leads, respectively, to the following equations

$$2c_1 n\zeta_2^* \zeta_1 \left(1 - \frac{\tilde{\beta} + 3q}{\tilde{\beta} - 3q}\right) = 0, \tag{B.32}$$

$$2c_1 n\zeta_{-1}^* \zeta_{-2} \left(1 - \frac{\tilde{\beta} - 3q}{\tilde{\beta} + 3q}\right) = 0, \tag{B.33}$$

where we have substituted $\tilde{\mu}$ according to Eq. (B.30). This implies that, generally, $\zeta_2^* \zeta_1 = \zeta_{-1}^* \zeta_{-2} = 0$. To be consistent with Eqs. (B.11) and (B.12) either $\zeta_1 = \zeta_{-2} = 0$ or $\zeta_2 = \zeta_{-1} = 0$. Here we focus on the former case, since it relates to our discussion in Sec. 6.2.3. The longitudinal magnetisation in Eq. (2.81) implies we now have

$$|\zeta_2| = \sqrt{\frac{\langle \hat{F}_z \rangle + |\zeta_{-1}|^2}{2}}. \tag{B.34}$$

Then, using the normalisation condition $|\zeta_2|^2 + |\zeta_{-1}|^2 = 1$ leads to

$$|\zeta_{-1}| = \sqrt{\frac{2 - \langle \hat{F}_z \rangle}{3}}, \tag{B.35}$$

$$|\zeta_2| = \sqrt{\frac{1 + \langle \hat{F}_z \rangle}{3}}, \tag{B.36}$$

and thus the final interpolating spinor now reads

$$\zeta^{\text{C-FM}} = \frac{1}{\sqrt{3}}\begin{pmatrix} e^{i\chi_2}\sqrt{1+\langle\hat{F}_z\rangle} \\ 0 \\ 0 \\ e^{i\chi_{-1}}\sqrt{2-\langle\hat{F}_z\rangle} \\ 0 \end{pmatrix}. \tag{B.37}$$

Substituting this back into Eqs. (B.11) and (B.12) leads to $\langle\hat{F}_z\rangle = (p-q)/(c_1 n)$. This state now continuously becomes the two-component cyclic state at $\langle\hat{F}_z\rangle = 0$ and the FM_2^+ state at $\langle\hat{F}_z\rangle = 2$.

B.2.3 Ferromagnetic to biaxial nematic

Consider the case $D_2 \neq 0$ and $D_1 = 0$. Then, $D_2 \neq 0$ implies that $\zeta_2 = \zeta_{-2} = 0$. Consider also the case that $\tilde{\mu} \neq \tilde{\alpha}$, then Eq. (B.13) implies that $\zeta_0 = 0$. Now, from the definition of the longitudinal magnetisation given in Eq. (2.81), we have

$$|\zeta_2| = \sqrt{|\zeta_{-2}|^2 + \frac{\langle\hat{F}_z\rangle}{2}}. \tag{B.38}$$

Using the normalisation condition $|\zeta_2|^2 + |\zeta_{-2}|^2 = 1$ then leads to

$$|\zeta_{-2}| = \sqrt{\frac{1-\langle\hat{F}_z\rangle/2}{2}}, \tag{B.39}$$

$$|\zeta_2| = \sqrt{\frac{1+\langle\hat{F}_z\rangle/2}{2}}. \tag{B.40}$$

Thus, the final interpolating spinor now reads

$$\zeta^{\text{FM-BN}} = \begin{pmatrix} e^{i\chi_2}\sqrt{\frac{1+\langle\hat{F}_z\rangle/2}{2}} \\ 0 \\ 0 \\ 0 \\ e^{i\chi_{-2}}\sqrt{\frac{1-\langle\hat{F}_z\rangle/2}{2}} \end{pmatrix}. \tag{B.41}$$

Substituting the above spinor into Eq. (B.11) and using $D_2 = 0$ leads to $\langle\hat{F}_z\rangle = p/[(c_1 - c_2/20)n]$. Note that the above spinor becomes the BN phase at $p = 0$ and $\text{FM}_2^\pm$ for $p = \pm(2c_1 - c_2/10)n$.

BIBLIOGRAPHY

[1] Bose, "Plancks Gesetz und Lichtquantenhypothese", Z. Physik **26**, 178–181 (1924).

[2] A. Einstein, "Quantentheorie des einatomigen idealen Gases", in *Albert Einstein: Akademie-Vorträge*, edited by D. Simon, 1st ed. (Wiley, Dec. 2005), pp. 237–244.

[3] C. J. Pethick and H. Smith, *Bose–Einstein Condensation in Dilute Gases*, 2nd ed. (Cambridge University Press, Sept. 2008).

[4] M. H. Anderson, J. R. Ensher, M. R. Matthews, C. E. Wieman, and E. A. Cornell, "Observation of Bose-Einstein Condensation in a Dilute Atomic Vapor", Science **269**, 198–201 (1995).

[5] K. B. Davis, M. Mewes, M. R. Andrews, N. J. Van Druten, D. S. Durfee, D. M. Kurn, and W. Ketterle, "Bose-Einstein Condensation in a Gas of Sodium Atoms", Phys. Rev. Lett. **75**, 3969–3973 (1995).

[6] C. C. Bradley, C. A. Sackett, J. J. Tollett, and R. G. Hulet, "Evidence of Bose-Einstein Condensation in an Atomic Gas with Attractive Interactions", Phys. Rev. Lett. **75**, 1687–1690 (1995).

[7] J. M. Obrecht, R. J. Wild, M. Antezza, L. P. Pitaevskii, S. Stringari, and E. A. Cornell, "Measurement of the Temperature Dependence of the Casimir-Polder Force", Phys. Rev. Lett. **98**, 063201 (2007).

[8] T. Byrnes, K. Wen, and Y. Yamamoto, "Macroscopic quantum computation using Bose-Einstein condensates", Phys. Rev. A **85**, 040306 (2012).

[9] D. M. Stamper-Kurn, M. R. Andrews, A. P. Chikkatur, S. Inouye, H.-J. Miesner, J. Stenger, and W. Ketterle, "Optical Confinement of a Bose-Einstein Condensate", Phys. Rev. Lett. **80**, 2027–2030 (1998).

[10] T.-L. Ho, "Spinor Bose Condensates in Optical Traps", Phys. Rev. Lett. **81**, 742–745 (1998).

[11] T. Ohmi and K. Machida, "Bose-Einstein Condensation with Internal Degrees of Freedom in Alkali Atom Gases", J. Phys. Soc. Jpn. **67**, 1822–1825 (1998).

[12] M. D. Barrett, J. A. Sauer, and M. S. Chapman, "All-Optical Formation of an Atomic Bose-Einstein Condensate", Phys. Rev. Lett. **87**, 010404 (2001).

[13] H. Schmaljohann, M. Erhard, J. Kronjäger, M. Kottke, S. Van Staa, L. Cacciapuoti, J. J. Arlt, K. Bongs, and K. Sengstock, "Dynamics of F = 2 Spinor Bose-Einstein Condensates", Phys. Rev. Lett. **92**, 040402 (2004).

[14] A. Görlitz, T. L. Gustavson, A. E. Leanhardt, R. Löw, A. P. Chikkatur, S. Gupta, S. Inouye, D. E. Pritchard, and W. Ketterle, "Sodium Bose-Einstein Condensates in the F = 2 State in a Large-Volume Optical Trap", Phys. Rev. Lett. **90**, 090401 (2003).

[15] Q. Beaufils, R. Chicireanu, T. Zanon, B. Laburthe-Tolra, E. Maréchal, L. Vernac, J.-C. Keller, and O. Gorceix, "All-optical production of chromium Bose-Einstein condensates", Phys. Rev. A **77**, 061601 (2008).

[16] M. R. Matthews, B. P. Anderson, P. C. Haljan, D. S. Hall, C. E. Wieman, and E. A. Cornell, "Vortices in a Bose-Einstein Condensate", Phys. Rev. Lett. **83**, 2498–2501 (1999).

[17] J. E. Williams and M. J. Holland, "Preparing topological states of a Bose–Einstein condensate", Nature **401**, 568–572 (1999).

[18] J. R. Abo-Shaeer, C. Raman, J. M. Vogels, and W. Ketterle, "Observation of Vortex Lattices in Bose-Einstein Condensates", Science **292**, 476–479 (2001).

[19] J. Ruostekoski, "Topological phase preparation in a pair of atomic Bose-Einstein condensates", Phys. Rev. A **61**, 041603 (2000).

[20] K. W. Madison, F. Chevy, W. Wohlleben, and J. Dalibard, "Vortex Formation in a Stirred Bose-Einstein Condensate", Phys. Rev. Lett. **84**, 806–809 (2000).

[21] K. W. Madison, F. Chevy, W. Wohlleben, and J. Dalibard, "Vortices in a stirred Bose-Einstein condensate", Journal of Modern Optics **47**, 2715–2723 (2000).

[22] M. Kobayashi and M. Tsubota, "Quantum turbulence in a trapped Bose-Einstein condensate", Phys. Rev. A **76**, 045603 (2007).

[23] R. Numasato, M. Tsubota, and V. S. L'vov, "Direct energy cascade in two-dimensional compressible quantum turbulence", Phys. Rev. A **81**, 063630 (2010).

[24] M. T. Reeves, T. P. Billam, B. P. Anderson, and A. S. Bradley, "Inverse Energy Cascade in Forced Two-Dimensional Quantum Turbulence", Phys. Rev. Lett. **110**, 104501 (2013).

[25] T. P. Billam, M. T. Reeves, B. P. Anderson, and A. S. Bradley, "Onsager-Kraichnan Condensation in Decaying Two-Dimensional Quantum Turbulence", Phys. Rev. Lett. **112**, 145301 (2014).

[26] T. Simula, M. J. Davis, and K. Helmerson, "Emergence of Order from Turbulence in an Isolated Planar Superfluid", Phys. Rev. Lett. **113**, 165302 (2014).

[27] A. W. Baggaley and C. F. Barenghi, "Decay of homogeneous two-dimensional quantum turbulence", Phys. Rev. A **97**, 033601 (2018).

[28] E. A. L. Henn, J. A. Seman, G. Roati, K. M. F. Magalhães, and V. S. Bagnato, "Emergence of Turbulence in an Oscillating Bose-Einstein Condensate", Phys. Rev. Lett. **103**, 045301 (2009).

[29] W. J. Kwon, G. Moon, J.-y. Choi, S. W. Seo, and Y.-i. Shin, "Relaxation of superfluid turbulence in highly oblate Bose-Einstein condensates", Phys. Rev. A **90**, 063627 (2014).

[30] S. W. Seo, B. Ko, J. H. Kim, and Y. Shin, "Observation of vortex-antivortex pairing in decaying 2D turbulence of a superfluid gas", Sci Rep **7**, 4587 (2017).

[31] N. Navon, C. Eigen, J. Zhang, R. Lopes, A. L. Gaunt, K. Fujimoto, M. Tsubota, R. P. Smith, and Z. Hadzibabic, "Synthetic dissipation and cascade fluxes in a turbulent quantum gas", Science **366**, 382–385 (2019).

[32] G. Gauthier, M. T. Reeves, X. Yu, A. S. Bradley, M. A. Baker, T. A. Bell, H. Rubinsztein-Dunlop, M. J. Davis, and T. W. Neely, "Giant vortex clusters in a two-dimensional quantum fluid", Science **364**, 1264–1267 (2019).

[33] S. P. Johnstone, A. J. Groszek, P. T. Starkey, C. J. Billington, T. P. Simula, and K. Helmerson, "Evolution of large-scale flow from turbulence in a two-dimensional superfluid", Science **364**, 1267–1271 (2019).

[34] H. Salman and N. G. Berloff, "Condensation of classical nonlinear waves in a two-component system", Physica D: Nonlinear Phenomena **238**, 1482–1489 (2009).

[35] C.-M. Schmied, T. Gasenzer, and P. B. Blakie, "Violation of single-length-scaling dynamics via spin vortices in an isolated spin-1 Bose gas", Phys. Rev. A **100**, 033603 (2019).

[36] M. Karl, B. Nowak, and T. Gasenzer, "Universal scaling at nonthermal fixed points of a two-component Bose gas", Phys. Rev. A **88**, 063615 (2013).

[37] M. Prüfer, P. Kunkel, H. Strobel, S. Lannig, D. Linnemann, C. M. Schmied, J. Berges, T. Gasenzer, and M. K. Oberthaler, "Observation of universal dynamics in a spinor Bose gas far from equilibrium", Nature **563**, 217–220 (2018).

[38] J. Hofmann, S. S. Natu, and S. Das Sarma, “Coarsening Dynamics of Binary Bose Condensates”, Phys. Rev. Lett. **113**, 095702 (2014).

[39] S. Autti, V. V. Dmitriev, J. T. Mäkinen, A. A. Soldatov, G. E. Volovik, A. N. Yudin, V. V. Zavjalov, and V. B. Eltsov, “Observation of Half-Quantum Vortices in Topological Superfluid He 3”, Phys. Rev. Lett. **117**, 255301 (2016).

[40] U. Leonhardt and G. E. Volovik, “How to create an Alice string (half-quantum vortex) in a vector Bose-Einstein condensate”, Jetp Lett. **72**, 46–48 (2000).

[41] S. W. Seo, S. Kang, W. J. Kwon, and Y.-i. Shin, “Half-Quantum Vortices in an Antiferromagnetic Spinor Bose-Einstein Condensate”, Phys. Rev. Lett. **115**, 015301 (2015).

[42] M. Eto, K. Kasamatsu, M. Nitta, H. Takeuchi, and M. Tsubota, “Interaction of half-quantized vortices in two-component Bose-Einstein condensates”, Phys. Rev. A **83**, 063603 (2011).

[43] K. Kasamatsu, M. Eto, and M. Nitta, “Short-range intervortex interaction and interacting dynamics of half-quantized vortices in two-component Bose-Einstein condensates”, Phys. Rev. A **93**, 013615 (2016).

[44] T. Isoshima, K. Machida, and T. Ohmi, “Quantum Vortex in a Spinor Bose-Einstein Condensate”, J. Phys. Soc. Jpn. **70**, 1604–1610 (2001).

[45] T. Mizushima, K. Machida, and T. Kita, “Axisymmetric versus nonaxisymmetric vortices in spinor Bose-Einstein condensates”, Phys. Rev. A **66**, 053610 (2002).

[46] T. Mizushima, K. Machida, and T. Kita, “Mermin-Ho Vortex in Ferromagnetic Spinor Bose-Einstein Condensates”, Phys. Rev. Lett. **89**, 030401 (2002).

[47] M. Takahashi, V. Pietilä, M. Möttönen, T. Mizushima, and K. Machida, “Vortex-splitting and phase-separating instabilities of coreless vortices in F = 1 spinor Bose-Einstein condensates”, Phys. Rev. A **79**, 023618 (2009).

[48] J. Lovegrove, M. O. Borgh, and J. Ruostekoski, “Energetically stable singular vortex cores in an atomic spin-1 Bose-Einstein condensate”, Phys. Rev. A **86**, 013613 (2012).

[49] J. Lovegrove, M. O. Borgh, and J. Ruostekoski, “Energetic Stability of Coreless Vortices in Spin-1 Bose-Einstein Condensates with Conserved Magnetization”, Phys. Rev. Lett. **112**, 075301 (2014).

[50] J. Lovegrove, M. O. Borgh, and J. Ruostekoski, “Stability and internal structure of vortices in spin-1 Bose-Einstein condensates with conserved magnetization”, Phys. Rev. A **93**, 033633 (2016).

[51] A. E. Leanhardt, Y. Shin, D. Kielpinski, D. E. Pritchard, and W. Ketterle, "Coreless Vortex Formation in a Spinor Bose-Einstein Condensate", Phys. Rev. Lett. **90**, 140403 (2003).

[52] A. E. Leanhardt, A. Görlitz, A. P. Chikkatur, D. Kielpinski, Y. Shin, D. E. Pritchard, and W. Ketterle, "Imprinting Vortices in a Bose-Einstein Condensate using Topological Phases", Phys. Rev. Lett. **89**, 190403 (2002).

[53] Y. Shin, M. Saba, M. Vengalattore, T. A. Pasquini, C. Sanner, A. E. Leanhardt, M. Prentiss, D. E. Pritchard, and W. Ketterle, "Dynamical Instability of a Doubly Quantized Vortex in a Bose-Einstein Condensate", Phys. Rev. Lett. **93**, 160406 (2004).

[54] Y. Xiao, M. O. Borgh, A. Blinova, T. Ollikainen, J. Ruostekoski, and D. S. Hall, "Topological superfluid defects with discrete point group symmetries", Nat Commun **13**, 4635 (2022).

[55] M. Gring, M. Kuhnert, T. Langen, T. Kitagawa, B. Rauer, M. Schreitl, I. Mazets, D. A. Smith, E. Demler, and J. Schmiedmayer, "Relaxation and Prethermalization in an Isolated Quantum System", Science **337**, 1318–1322 (2012).

[56] M. T. Reeves, K. Goddard-Lee, G. Gauthier, O. R. Stockdale, H. Salman, T. Edmonds, X. Yu, A. S. Bradley, M. Baker, H. Rubinsztein-Dunlop, M. J. Davis, and T. W. Neely, "Turbulent Relaxation to Equilibrium in a Two-Dimensional Quantum Vortex Gas", Phys. Rev. X **12**, 011031 (2022).

[57] L. E. Sadler, J. M. Higbie, S. R. Leslie, M. Vengalattore, and D. M. Stamper-Kurn, "Spontaneous symmetry breaking in a quenched ferromagnetic spinor Bose–Einstein condensate", Nature **443**, 312–315 (2006).

[58] R. Barnett, A. Polkovnikov, and M. Vengalattore, "Prethermalization in quenched spinor condensates", Phys. Rev. A **84**, 023606 (2011).

[59] N. Navon, A. L. Gaunt, R. P. Smith, and Z. Hadzibabic, "Critical dynamics of spontaneous symmetry breaking in a homogeneous Bose gas", Science **347**, 167–170 (2015).

[60] L. M. Symes and P. B. Blakie, "Nematic ordering dynamics of an antiferromagnetic spin-1 condensate", Phys. Rev. A **96**, 013602 (2017).

[61] S. Kang, S. W. Seo, J. H. Kim, and Y. Shin, "Emergence and scaling of spin turbulence in quenched antiferromagnetic spinor Bose-Einstein condensates", Phys. Rev. A **95**, 053638 (2017).

[62] I.-K. Liu, J. Dziarmaga, S.-C. Gou, F. Dalfovo, and N. P. Proukakis, "Kibble-Zurek dynamics in a trapped ultracold Bose gas", Phys. Rev. Research **2**, 033183 (2020).

[63] S. Sachdev, *Quantum Phase Transitions*, 2nd ed. (Cambridge University Press, May 2011).

[64] A. Del Campo and W. H. Zurek, “Universality of phase transition dynamics: Topological defects from symmetry breaking”, Int. J. Mod. Phys. A **29**, 1430018 (2014).

[65] B. Damski and W. H. Zurek, “Adiabatic-impulse approximation for avoided level crossings: From phase-transition dynamics to Landau-Zener evolutions and back again”, Phys. Rev. A **73**, 063405 (2006).

[66] B. Damski and W. H. Zurek, “Dynamics of a Quantum Phase Transition in a Ferromagnetic Bose-Einstein Condensate”, Phys. Rev. Lett. **99**, 130402 (2007).

[67] A. Lamacraft, “Quantum Quenches in a Spinor Condensate”, Phys. Rev. Lett. **98**, 160404 (2007).

[68] H. Saito, Y. Kawaguchi, and M. Ueda, “Kibble-Zurek mechanism in a quenched ferromagnetic Bose-Einstein condensate”, Phys. Rev. A **76**, 043613 (2007).

[69] H. Saito, Y. Kawaguchi, and M. Ueda, “Topological defect formation in a quenched ferromagnetic Bose-Einstein condensates”, Phys. Rev. A **75**, 013621 (2007).

[70] M. Vengalattore, S. R. Leslie, J. Guzman, and D. M. Stamper-Kurn, “Spontaneously Modulated Spin Textures in a Dipolar Spinor Bose-Einstein Condensate”, Phys. Rev. Lett. **100**, 170403 (2008).

[71] T. Świsłocki, E. Witkowska, J. Dziarmaga, and M. Matuszewski, “Double Universality of a Quantum Phase Transition in Spinor Condensates: Modification of the Kibble-Żurek Mechanism by a Conservation Law”, Phys. Rev. Lett. **110**, 045303 (2013).

[72] E. Witkowska, J. Dziarmaga, T. Świsłocki, and M. Matuszewski, “Dynamics of the modified Kibble-Żurek mechanism in antiferromagnetic spin-1 condensates”, Phys. Rev. B **88**, 054508 (2013).

[73] M. Anquez, B. A. Robbins, H. M. Bharath, M. Boguslawski, T. M. Hoang, and M. S. Chapman, “Quantum Kibble-Zurek Mechanism in a Spin-1 Bose-Einstein Condensate”, Phys. Rev. Lett. **116**, 155301 (2016).

[74] L. A. Williamson and P. B. Blakie, “Coarsening and thermalization properties of a quenched ferromagnetic spin-1 condensate”, Phys. Rev. A **94**, 023608 (2016).

[75] L.-Y. Qiu, H.-Y. Liang, Y.-B. Yang, H.-X. Yang, T. Tian, Y. Xu, and L.-M. Duan, “Observation of generalized Kibble-Zurek mechanism across a first-order quantum phase transition in a spinor condensate”, Sci. Adv. **6**, eaba7292 (2020).

[76] Y. B. Zel'dovich, I. Y. Kobzarev, and L. B. Okun', "Cosmological consequences of a spontaneous breakdown of a discrete symmetry", Sov. Phys. JETP **67**, 401–409 (1975).

[77] T. W. B. Kibble, "Topology of cosmic domains and strings", J. Phys. A: Math. Gen. **9**, 1387–1398 (1976).

[78] T. Kibble, "Some implications of a cosmological phase transition", Physics Reports **67**, 183–199 (1980).

[79] D. D. Osheroff and M. C. Cross, "Interfacial Surface Energy between the Superfluid Phases of He 3", Phys. Rev. Lett. **38**, 905–909 (1977).

[80] S. Yip and A. J. Leggett, "Dynamics of the He 3 A - B Phase Boundary", Phys. Rev. Lett. **57**, 345–348 (1986).

[81] M. M. Salomaa, "Monopoles in the rotating superfluid helium-3 A–B interface", Nature **326**, 367–370 (1987).

[82] A. P. Finne, V. B. Eltsov, R. Hänninen, N. B. Kopnin, J. Kopu, M. Krusius, M. Tsubota, and G. E. Volovik, "Dynamics of vortices and interfaces in superfluid ^{3} He", Rep. Prog. Phys. **69**, 3157–3230 (2006).

[83] D. I. Bradley, S. N. Fisher, A. M. Guénault, R. P. Haley, J. Kopu, H. Martin, G. R. Pickett, J. E. Roberts, and V. Tsepelin, "Relic topological defects from brane annihilation simulated in superfluid 3He", Nature Phys **4**, 46–49 (2008).

[84] G. E. Volovik, *The Universe in a Helium Droplet* (Oxford University Press, Feb. 2009).

[85] M. O. Borgh and J. Ruostekoski, "Topological Interface Engineering and Defect Crossing in Ultracold Atomic Gases", Phys. Rev. Lett. **109**, 015302 (2012).

[86] M. O. Borgh and J. Ruostekoski, "Topological interface physics of defects and textures in spinor Bose-Einstein condensates", Phys. Rev. A **87**, 033617 (2013).

[87] M. O. Borgh, J. Lovegrove, and J. Ruostekoski, "Imprinting a topological interface using Zeeman shifts in an atomic spinor Bose–Einstein condensate", New J. Phys. **16**, 053046 (2014).

[88] L. S. Weiss, M. O. Borgh, A. Blinova, T. Ollikainen, M. Möttönen, J. Ruostekoski, and D. S. Hall, "Controlled creation of a singular spinor vortex by circumventing the Dirac belt trick", Nat Commun **10**, 4772 (2019).

[89] Y. Xiao, M. O. Borgh, L. S. Weiss, A. A. Blinova, J. Ruostekoski, and D. S. Hall, "Controlled creation and decay of singly-quantized vortices in a polar magnetic phase", Commun Phys **4**, 52 (2021).

[90] G. W. Semenoff and F. Zhou, “Discrete Symmetries and 1 / 3 –Quantum Vortices in Condensates of F = 2 Cold Atoms”, Phys. Rev. Lett. **98**, 100401 (2007).

[91] S.-K. Yip, “Symmetry and inert states of spin Bose-Einstein condensates”, Phys. Rev. A **75**, 023625 (2007).

[92] Y. Kawaguchi and M. Ueda, “Symmetry classification of spinor Bose-Einstein condensates”, Phys. Rev. A **84**, 053616 (2011).

[93] N. D. Mermin, “The topological theory of defects in ordered media”, Rev. Mod. Phys. **51**, 591–648 (1979).

[94] L. P. Pitaevskii, S. Stringari, L. P. Pitaevskii, and S. Stringari, *Bose-Einstein Condensation*, International Series of Monographs on Physics (Oxford University Press, Oxford, New York, Apr. 2003).

[95] P. Ao and S. T. Chui, “Binary Bose-Einstein condensate mixtures in weakly and strongly segregated phases”, Phys. Rev. A **58**, 4836–4840 (1998).

[96] Y. Kawaguchi and M. Ueda, “Spinor Bose–Einstein condensates”, Physics Reports **520**, 253–381 (2012).

[97] D. M. Stamper-Kurn and M. Ueda, “Spinor Bose gases: Symmetries, magnetism, and quantum dynamics”, Rev. Mod. Phys. **85**, 1191–1244 (2013).

[98] L. Symes, “Exact nonlinear dynamics of Spinor BECs applied to nematic quenches”, PhD thesis (University of Otago, 2019).

[99] L. Warszawski and A. Melatos, “Gross–Pitaevskii model of pulsar glitches”, Monthly Notices of the Royal Astronomical Society **415**, 1611–1630 (2011).

[100] A. L. Gaunt, T. F. Schmidutz, I. Gotlibovych, R. P. Smith, and Z. Hadzibabic, “Bose-Einstein Condensation of Atoms in a Uniform Potential”, Phys. Rev. Lett. **110**, 200406 (2013).

[101] C. Ryu, M. F. Andersen, P. Cladé, V. Natarajan, K. Helmerson, and W. D. Phillips, “Observation of Persistent Flow of a Bose-Einstein Condensate in a Toroidal Trap”, Phys. Rev. Lett. **99**, 260401 (2007).

[102] A. Ramanathan, K. C. Wright, S. R. Muniz, M. Zelan, W. T. Hill, C. J. Lobb, K. Helmerson, W. D. Phillips, and G. K. Campbell, “Superflow in a Toroidal Bose-Einstein Condensate: An Atom Circuit with a Tunable Weak Link”, Phys. Rev. Lett. **106**, 130401 (2011).

[103] T. W. Neely, E. C. Samson, A. S. Bradley, M. J. Davis, and B. P. Anderson, “Observation of Vortex Dipoles in an Oblate Bose-Einstein Condensate”, Phys. Rev. Lett. **104**, 160401 (2010).

[104] S. Burger, K. Bongs, S. Dettmer, W. Ertmer, K. Sengstock, A. Sanpera, G. V. Shlyapnikov, and M. Lewenstein, “Dark Solitons in Bose-Einstein Condensates”, Phys. Rev. Lett. **83**, 5198–5201 (1999).

[105] K. Henderson, C. Ryu, C. MacCormick, and M. G. Boshier, “Experimental demonstration of painting arbitrary and dynamic potentials for Bose–Einstein condensates”, New J. Phys. **11**, 043030 (2009).

[106] A. Crubellier, O. Dulieu, F. Masnou-Seeuws, M. Elbs, H. Knöckel, and E. Tiemann, “Simple determination of Na2 scattering lengths using observed bound levels at the ground state asymptote”, Eur. Phys. J. D **6**, 211–220 (1999).

[107] C. V. Ciobanu, S.-K. Yip, and T.-L. Ho, “Phase diagrams of F = 2 spinor Bose-Einstein condensates”, Phys. Rev. A **61**, 033607 (2000).

[108] N. N. Klausen, J. L. Bohn, and C. H. Greene, “Nature of spinor Bose-Einstein condensates in rubidium”, Phys. Rev. A **64**, 053602 (2001).

[109] W. Zhang, S. Yi, and L. You, “Mean field ground state of a spin-1 condensate in a magnetic field”, New J. Phys. **5**, 77–77 (2003).

[110] E. Majorana, “Atomi orientati in campo magnetico variabile”, Il Nuovo Cimento **9**, 43–50 (1932).

[111] F. Bloch and I. I. Rabi, “Atoms in Variable Magnetic Fields”, Rev. Mod. Phys. **17**, 237–244 (1945).

[112] J. Ruostekoski and J. R. Anglin, “Monopole Core Instability and Alice Rings in Spinor Bose-Einstein Condensates”, Phys. Rev. Lett. **91**, 190402 (2003).

[113] S. Kobayashi, M. Kobayashi, Y. Kawaguchi, M. Nitta, and M. Ueda, “Abe homotopy classification of topological excitations under the topological influence of vortices”, Nuclear Physics B **856**, 577–606 (2012).

[114] S.-K. Yip, “Internal Vortex Structure of a Trapped Spinor Bose-Einstein Condensate”, Phys. Rev. Lett. **83**, 4677–4681 (1999).

[115] T. Isoshima and K. Machida, “Axisymmetric vortices in spinor Bose-Einstein condensates under rotation”, Phys. Rev. A **66**, 023602 (2002).

[116] M. O. Borgh and J. Ruostekoski, “Core Structure and Non-Abelian Reconnection of Defects in a Biaxial Nematic Spin-2 Bose-Einstein Condensate”, Phys. Rev. Lett. **117**, 275302 (2016).

[117] F. Zhou, “Quantum Spin Nematic States in Bose–Einstein Condensates”, Int. J. Mod. Phys. B **17**, 2643–2698 (2003).

[118] A.-C. Ji, W. M. Liu, J. L. Song, and F. Zhou, “Dynamical Creation of Fractionalized Vortices and Vortex Lattices”, Phys. Rev. Lett. **101**, 010402 (2008).

[119] M. Kobayashi, Y. Kawaguchi, M. Nitta, and M. Ueda, “Collision Dynamics and Rung Formation of non-Abelian Vortices”, Phys. Rev. Lett. **103**, 115301 (2009).

[120] M. O. Borgh, J. Lovegrove, and J. Ruostekoski, “Internal structure and stability of vortices in a dipolar spinor Bose-Einstein condensate”, Phys. Rev. A **95**, 053601 (2017).

[121] J.-P. Martikainen, A. Collin, and K.-A. Suominen, “Coreless vortex ground state of the rotating spinor condensate”, Phys. Rev. A **66**, 053604 (2002).

[122] T. Mizushima, N. Kobayashi, and K. Machida, “Coreless and singular vortex lattices in rotating spinor Bose-Einstein condensates”, Phys. Rev. A **70**, 043613 (2004).

[123] J.-y. Choi, W. J. Kwon, M. Lee, H. Jeong, K. An, and Y.-i. Shin, “Imprinting Skyrmion spin textures in spinor Bose–Einstein condensates”, New J. Phys. **14**, 053013 (2012).

[124] J.-y. Choi, W. J. Kwon, and Y.-i. Shin, “Observation of Topologically Stable 2D Skyrmions in an Antiferromagnetic Spinor Bose-Einstein Condensate”, Phys. Rev. Lett. **108**, 035301 (2012).

[125] H. T. C. Stoof, E. Vliegen, and U. Al Khawaja, “Monopoles in an Antiferromagnetic Bose-Einstein Condensate”, Phys. Rev. Lett. **87**, 120407 (2001).

[126] C. M. Savage and J. Ruostekoski, “Dirac monopoles and dipoles in ferromagnetic spinor Bose-Einstein condensates”, Phys. Rev. A **68**, 043604 (2003).

[127] V. Pietilä and M. Möttönen, “Creation of Dirac Monopoles in Spinor Bose-Einstein Condensates”, Phys. Rev. Lett. **103**, 030401 (2009).

[128] M. W. Ray, E. Ruokokoski, S. Kandel, M. Möttönen, and D. S. Hall, “Observation of Dirac monopoles in a synthetic magnetic field”, Nature **505**, 657–660 (2014).

[129] M. W. Ray, E. Ruokokoski, K. Tiurev, M. Möttönen, and D. S. Hall, “Observation of isolated monopoles in a quantum field”, Science **348**, 544–547 (2015).

[130] T. Ollikainen, K. Tiurev, A. Blinova, W. Lee, D. S. Hall, and M. Möttönen, “Experimental Realization of a Dirac Monopole through the Decay of an Isolated Monopole”, Phys. Rev. X **7**, 021023 (2017).

[131] T. Mithun, R. Carretero-González, E. G. Charalampidis, D. S. Hall, and P. G. Kevrekidis, “Existence, stability, and dynamics of monopole and Alice ring solutions in antiferromagnetic spinor condensates”, Phys. Rev. A **105**, 053303 (2022).

[132] C. Barenghi and N. G. Parker, *A Primer on Quantum Fluids*, SpringerBriefs in Physics (Springer International Publishing, Cham, 2016).

[133] M. M. Salomaa and G. E. Volovik, “Half-Quantum Vortices in Superfluid He 3 - A”, Phys. Rev. Lett. **55**, 1184–1187 (1985).

[134] N. D. Mermin and T.-L. Ho, “Circulation and Angular Momentum in the A Phase of Superfluid Helium-3”, Phys. Rev. Lett. **36**, 594–597 (1976).

[135] V. R. Chechetkin, “2”, Zh. Eksp. Teor. Fiz **71**, 1463 (1976).

[136] P. W. Anderson and G. Toulouse, “Phase Slippage without Vortex Cores: Vortex Textures in Superfluid He 3”, Phys. Rev. Lett. **38**, 508–511 (1977).

[137] C. F. Barenghi, L. Skrbek, and K. R. Sreenivasan, “Introduction to quantum turbulence”, Proc. Natl. Acad. Sci. U.S.A. **111**, 4647–4652 (2014).

[138] P. Walmsley, D. Zmeev, F. Pakpour, and A. Golov, “Dynamics of quantum turbulence of different spectra”, Proc. Natl. Acad. Sci. U.S.A. **111**, 4691–4698 (2014).

[139] A. J. E. Kreil, D. A. Bozhko, H. Y. Musiienko-Shmarova, V. I. Vasyuchka, V. S. L’vov, A. Pomyalov, B. Hillebrands, and A. A. Serga, “From Kinetic Instability to Bose-Einstein Condensation and Magnon Supercurrents”, Phys. Rev. Lett. **121**, 077203 (2018).

[140] M. Kobayashi and M. Tsubota, “Kolmogorov Spectrum of Quantum Turbulence”, J. Phys. Soc. Jpn. **74**, 3248–3258 (2005).

[141] K. Kasamatsu, M. Tsubota, and M. Ueda, “Vortices in Multicomponent Bose-Einstein Condensates”, Int. J. Mod. Phys. B **19**, 1835–1904 (2005).

[142] J. Schole, B. Nowak, and T. Gasenzer, “Critical dynamics of a two-dimensional superfluid near a nonthermal fixed point”, Phys. Rev. A **86**, 013624 (2012).

[143] B. Nowak, J. Schole, D. Sexty, and T. Gasenzer, “Nonthermal fixed points, vortex statistics, and superfluid turbulence in an ultracold Bose gas”, Phys. Rev. A **85**, 043627 (2012).

[144] M. Karl and T. Gasenzer, “Strongly anomalous non-thermal fixed point in a quenched two-dimensional Bose gas”, New J. Phys. **19**, 093014 (2017).

[145] C. J. Myatt, E. A. Burt, R. W. Ghrist, E. A. Cornell, and C. E. Wieman, “Production of Two Overlapping Bose-Einstein Condensates by Sympathetic Cooling”, Phys. Rev. Lett. **78**, 586–589 (1997).

[146] D. S. Hall, M. R. Matthews, J. R. Ensher, C. E. Wieman, and E. A. Cornell, “Dynamics of Component Separation in a Binary Mixture of Bose-Einstein Condensates”, Phys. Rev. Lett. **81**, 1539–1542 (1998).

[147] A. Villois, G. Krstulovic, D. Proment, and H. Salman, “A vortex filament tracking method for the Gross–Pitaevskii model of a superfluid”, J. Phys. A: Math. Theor. **49**, 415502 (2016).

[148] V. E. Zakharov, V. S. L'vov, and G. Falkovich, *Kolmogorov Spectra of Turbulence I* (Springer Berlin Heidelberg, Berlin, Heidelberg, 1992).

[149] S. Nazarenko, *Wave Turbulence*, Vol. 825, Lecture Notes in Physics (Springer, Berlin, Heidelberg, 2011).

[150] A. C. Newell and B. Rumpf, "Wave Turbulence", Annu. Rev. Fluid Mech. **43**, 59–78 (2011).

[151] A. Mazumdar and G. White, "Review of cosmic phase transitions: their significance and experimental signatures", Rep. Prog. Phys. **82**, 076901 (2019).

[152] I. Chuang, R. Durrer, N. Turok, and B. Yurke, "Cosmology in the Laboratory: Defect Dynamics in Liquid Crystals", Science **251**, 1336–1342 (1991).

[153] P. C. Hendry, N. S. Lawson, R. A. Lee, P. V. McClintock, and C. D. Williams, "Generation of defects in superfluid 4He as an analogue of the formation of cosmic strings", Nature **368**, 315–317 (1994).

[154] C. Bäuerle, Y. M. Bunkov, S. N. Fisher, H. Godfrin, and G. R. Pickett, "Laboratory simulation of cosmic string formation in the early Universe using superfluid 3He", Nature **382**, 332–334 (1996).

[155] V. M. H. Ruutu, V. B. Eltsov, A. J. Gill, T. W. B. Kibble, M. Krusius, Y. G. Makhlin, B. Plaçais, G. E. Volovik, and W. Xu, "Vortex formation in neutron-irradiated superfluid 3He as an analogue of cosmological defect formation", Nature **382**, 334–336 (1996).

[156] S. L. Sondhi, S. M. Girvin, J. P. Carini, and D. Shahar, "Continuous quantum phase transitions", Rev. Mod. Phys. **69**, 315–333 (1997).

[157] A. Polkovnikov, K. Sengupta, A. Silva, and M. Vengalattore, "*Colloquium* : Nonequilibrium dynamics of closed interacting quantum systems", Rev. Mod. Phys. **83**, 863–883 (2011).

[158] Z. Hadzibabic, P. Krüger, M. Cheneau, B. Battelier, and J. Dalibard, "Berezinskii–Kosterlitz–Thouless crossover in a trapped atomic gas", Nature **441**, 1118–1121 (2006).

[159] T. Langen, R. Geiger, and J. Schmiedmayer, "Ultracold Atoms Out of Equilibrium", Annu. Rev. Condens. Matter Phys. **6**, 201–217 (2015).

[160] R. J. Fletcher, M. Robert-de-Saint-Vincent, J. Man, N. Navon, R. P. Smith, K. G. H. Viebahn, and Z. Hadzibabic, "Connecting Berezinskii-Kosterlitz-Thouless and BEC Phase Transitions by Tuning Interactions in a Trapped Gas", Phys. Rev. Lett. **114**, 255302 (2015).

[161] I.-K. Liu, S. Donadello, G. Lamporesi, G. Ferrari, S.-C. Gou, F. Dalfovo, and N. P. Proukakis, "Dynamical equilibration across a quenched phase transition in a trapped quantum gas", Commun Phys **1**, 24 (2018).

[162] W. H. Zurek, "Cosmological experiments in superfluid helium?", Nature **317**, 505–508 (1985).

[163] W. Zurek, "Cosmic strings in laboratory superfluids and the topological remnants of other phase transitions", Acta Phys. Pol. B **24**, 1301–1311 (1993).

[164] W. Zurek, "Cosmological experiments in condensed matter systems", Physics Reports **276**, 177–221 (1996).

[165] S. Donadello, S. Serafini, T. Bienaimé, F. Dalfovo, G. Lamporesi, and G. Ferrari, "Creation and counting of defects in a temperature-quenched Bose-Einstein condensate", Phys. Rev. A **94**, 023628 (2016).

[166] J. Beugnon and N. Navon, "Exploring the Kibble–Zurek mechanism with homogeneous Bose gases", J. Phys. B: At. Mol. Opt. Phys. **50**, 022002 (2017).

[167] J. Dziarmaga, "Dynamics of a Quantum Phase Transition: Exact Solution of the Quantum Ising Model", Phys. Rev. Lett. **95**, 245701 (2005).

[168] B. Damski, "The Simplest Quantum Model Supporting the Kibble-Zurek Mechanism of Topological Defect Production: Landau-Zener Transitions from a New Perspective", Phys. Rev. Lett. **95**, 035701 (2005).

[169] U. Divakaran, A. Dutta, and D. Sen, "Quenching along a gapless line: A different exponent for defect density", Phys. Rev. B **78**, 144301 (2008).

[170] S. Suzuki and A. Dutta, "Universal scaling for a quantum discontinuity critical point and quantum quenches", Phys. Rev. B **92**, 064419 (2015).

[171] M. E. Fisher and A. N. Berker, "Scaling for first-order phase transitions in thermodynamic and finite systems", Phys. Rev. B **26**, 2507–2513 (1982).

[172] S. Uchino, M. Kobayashi, and M. Ueda, "Bogoliubov theory and Lee-Huang-Yang corrections in spin-1 and spin-2 Bose-Einstein condensates in the presence of the quadratic Zeeman effect", Phys. Rev. A **81**, 063632 (2010).

[173] W. H. Zurek, U. Dorner, and P. Zoller, "Dynamics of a Quantum Phase Transition", Phys. Rev. Lett. **95**, 105701 (2005).

[174] R. Barankov and A. Polkovnikov, "Optimal Nonlinear Passage Through a Quantum Critical Point", Phys. Rev. Lett. **101**, 076801 (2008).

[175] S. Mondal, K. Sengupta, and D. Sen, “Theory of defect production in nonlinear quench across a quantum critical point”, Phys. Rev. B **79**, 045128 (2009).

[176] L. M. Symes, R. I. McLachlan, and P. B. Blakie, “Efficient and accurate methods for solving the time-dependent spin-1 Gross-Pitaevskii equation”, Phys. Rev. E **93**, 053309 (2016).

[177] L. Turban and F. Iglói, “Surface-induced disorder and aperiodic perturbations at first-order transitions”, Phys. Rev. B **66**, 014440 (2002).

[178] M. A. Continentino and A. S. Ferreira, “Quantum first-order phase transitions”, Physica A: Statistical Mechanics and its Applications **339**, 461–468 (2004).

[179] M. Nauenberg, “Scaling representation for critical phenomena”, J. Phys. A: Math. Gen. **8**, 925 (1975).

[180] M. Matuszewski, T. J. Alexander, and Y. S. Kivshar, “Excited spin states and phase separation in spinor Bose-Einstein condensates”, Phys. Rev. A **80**, 023602 (2009).

[181] S. S. Mirkhalaf, D. Benedicto Orenes, M. W. Mitchell, and E. Witkowska, “Criticality-enhanced quantum sensing in ferromagnetic Bose-Einstein condensates: Role of readout measurement and detection noise”, Phys. Rev. A **103**, 023317 (2021).

[182] H. Saito, Y. Kawaguchi, and M. Ueda, “Kibble–Zurek mechanism in a trapped ferromagnetic Bose–Einstein condensate”, J. Phys.: Condens. Matter **25**, 404212 (2013).

[183] S.-W. Su, S.-C. Gou, A. Bradley, O. Fialko, and J. Brand, “Kibble-Zurek Scaling and its Breakdown for Spontaneous Generation of Josephson Vortices in Bose-Einstein Condensates”, Phys. Rev. Lett. **110**, 215302 (2013).

[184] F. Pellegrini, S. Montangero, G. E. Santoro, and R. Fazio, “Adiabatic quenches through an extended quantum critical region”, Phys. Rev. B **77**, 140404 (2008).

[185] H. Takeuchi and M. Tsubota, “Boojums in Rotating Two-Component Bose–Einstein Condensates”, J. Phys. Soc. Jpn. **75**, 063601 (2006).

[186] K. Kasamatsu, H. Takeuchi, M. Nitta, and M. Tsubota, “Analogues of D-branes in Bose-Einstein condensates”, J. High Energ. Phys. **2010**, 68 (2010).

[187] T. Kaneda and H. Saito, “Dynamics of a vortex dipole across a magnetic phase boundary in a spinor Bose-Einstein condensate”, Phys. Rev. A **90**, 053632 (2014).

[188] V. Poenaru and G. Toulouse, “The crossing of defects in ordered media and the topology of 3-manifolds”, J. Phys. France **38**, 887–895 (1977).

[189] A. Blinova, R. Zamora-Zamora, T. Ollikainen, M. Kivioja, M. Möttönen, and D. S. Hall, "Observation of an Alice ring in a Bose–Einstein condensate", Nat Commun **14**, 5100 (2023).

[190] M. O. Borgh, M. Nitta, and J. Ruostekoski, "Stable Core Symmetries and Confined Textures for a Vortex Line in a Spinor Bose-Einstein Condensate", Phys. Rev. Lett. **116**, 085301 (2016).

[191] R. Blaauwgeers, V. B. Eltsov, G. Eska, A. P. Finne, R. P. Haley, M. Krusius, J. J. Ruohio, L. Skrbek, and G. E. Volovik, "Shear Flow and Kelvin-Helmholtz Instability in Superfluids", Phys. Rev. Lett. **89**, 155301 (2002).

[192] L. M. Symes and P. B. Blakie, "Solving the spin-2 Gross-Pitaevskii equation using exact nonlinear dynamics and symplectic composition", Phys. Rev. E **95**, 013311 (2017).

[193] F. K. Fatemi, K. M. Jones, and P. D. Lett, "Observation of Optically Induced Feshbach Resonances in Collisions of Cold Atoms", Phys. Rev. Lett. **85**, 4462–4465 (2000).

[194] D. J. Papoular, G. V. Shlyapnikov, and J. Dalibard, "Microwave-induced Fano-Feshbach resonances", Phys. Rev. A **81**, 041603 (2010).

[195] A. Richaud, G. Lamporesi, M. Capone, and A. Recati, "Mass-driven vortex collisions in flat superfluids", Phys. Rev. A **107**, 053317 (2023).

[196] S. W. Seo, W. J. Kwon, S. Kang, and Y. Shin, "Collisional Dynamics of Half-Quantum Vortices in a Spinor Bose-Einstein Condensate", Phys. Rev. Lett. **116**, 185301 (2016).

[197] T. P. Billam, K. Brown, and I. G. Moss, "False-vacuum decay in an ultracold spin-1 Bose gas", Phys. Rev. A **105**, L041301 (2022).

[198] B. Song, S. Dutta, S. Bhave, J.-C. Yu, E. Carter, N. Cooper, and U. Schneider, "Realizing discontinuous quantum phase transitions in a strongly correlated driven optical lattice", Nat. Phys. **18**, 259–264 (2022).

[199] A. Zenesini, A. Berti, R. Cominotti, C. Rogora, I. G. Moss, T. P. Billam, I. Carusotto, G. Lamporesi, A. Recati, and G. Ferrari, *Observation of false vacuum decay via bubble formation in ferromagnetic superfluids*, May 2023.

[200] G. Lagnese, F. M. Surace, S. Morampudi, and F. Wilczek, *Detecting a long lived false vacuum with quantum quenches*, Aug. 2023.

[201] H. Wang, "A time-splitting spectral method for computing dynamics of spinor F=1 Bose-Einstein condensates", International Journal of Computer Mathematics **84**, 925–944 (2007).

[202] S. Blanes and P. Moan, "Practical symplectic partitioned runge–kutta and runge–kutta–nyström methods", J. Comput. Appl. Math. **142**, 313–330 (2002).

[203] M. T. Wheeler, *PyGPE*, version 2.0.0, Jan. 2024.